

**High Precision Spectroscopy of Strontium in an  
Optical Lattice: Towards a New Standard for  
Frequency and Time**

by

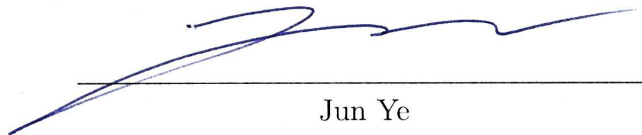
**Martin M. Boyd**

B.S., University of Washington, 2002

A thesis submitted to the  
Faculty of the Graduate School of the  
University of Colorado in partial fulfillment  
of the requirements for the degree of  
Doctor of Philosophy  
Department of Physics

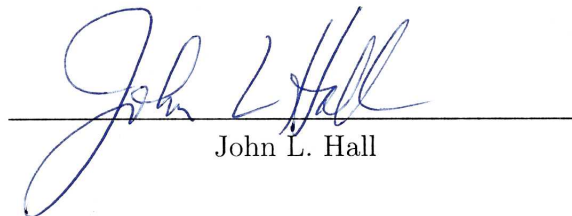
2007

This thesis entitled:  
High Precision Spectroscopy of Strontium in an Optical Lattice: Towards a New  
Standard for Frequency and Time  
written by Martin M. Boyd  
has been approved for the Department of Physics



---

Jun Ye



---

John L. Hall

Date Oct. 1, 2007

The final copy of this thesis has been examined by the signatories, and we find that both the content and the form meet acceptable presentation standards of scholarly work in the above mentioned discipline.

Boyd, Martin M. (Ph.D., Physics)

High Precision Spectroscopy of Strontium in an Optical Lattice: Towards a New  
Standard for Frequency and Time

Thesis directed by Associate Professor Adjoint Jun Ye

Clocks based on optical transitions in ions and atoms are quickly moving to the forefront of the frequency standards field mainly because of the high spectral resolution, and therefore the potential stability and accuracy, which can be achieved. In this thesis a new optical clock based on neutral atoms trapped in an optical lattice is presented, demonstrating spectroscopy of the clock transition free of any lineshape or accuracy degradation due to atomic motion. The system simulates a single trapped ion clock, but allows use of thousands of atoms for improved signal to noise ratio, and clock stability. High accuracy can also be achieved as the lattice can be designed to shift the energy of the two atomic clock states equally, such that the transition frequency is unchanged. Strontium is a natural candidate for such a clock as it offers an extremely narrow optical transition ( $\sim 1$  mHz) based on atomic states which are very insensitive to external fields. The strontium level structure allows efficient laser cooling to  $1 \mu\text{K}$  with diode laser sources, and a convenient wavelength of 813 nm for the zero-differential Stark shift optical lattice. The strontium lattice clock system has allowed observation of high signal-to-noise spectral features with the largest line quality factor ever observed in coherent spectroscopy ( $Q > 2 \times 10^{14}$ ), attesting to the stability of the clock. The effects of nuclear spin in the Sr isotope used are explored in how it pertains to the potential accuracy of the clock. The clock accuracy is evaluated at a fractional level of  $9 \times 10^{-16}$ , representing the first time a neutral atom optical clock has reached an accuracy comparable to the primary Cs fountains. The optical frequency is then

measured using a fs-comb referenced to the NIST Cs standard via a calibrated hydrogen maser. The final frequency value of  $429,228,004,229,874.0(1.1)$  Hz is in excellent agreement with other measurements from labs around the world, and represents one of the most accurate optical frequency measurements to date.

## Dedication

In memory of James Dawson, who got me thinking about the way things work.

and

For Amanda Carpenter, my greatest discovery.

## Acknowledgements

My first scholarly encounter with physics came about somewhat unintentionally. As my sophomore year at Stadium high school began, one of the higher ups had decided that I should relinquish my spot in junior level chemistry to allow a more seasoned student to take the course. The logic was that I was too young, and this other student had apparently enjoyed the class so much the year before, that he desperately needed to take it again before graduating. So they moved me into the senior physics class, and luckily, I was also too young to realize that many students would have considered this a bad thing. After a year of study under the terrific guidance of Jay Eastley, I was hooked. The teachings of Shawn McDougall and Dennis Dale also played a significant role in my early development, as they introduced me to integrals, derivatives and the art of programming.

The next important scientific mentors to enter my life called the University of Washington home. The enthusiasm Norval Fortson had in teaching our freshman class rejuvenated my interest in physics. I recall one lecture in particular, during which Norval described some of the research going on in his laboratory, just one floor below our lecture hall. There was some mention of the search for a permanent electric-dipole-moment (EDM), which if found (or not found) would somehow test the physics of time reversal. Admittedly, I didn't exactly know what an EDM was, but testing time reversal in a lab? This I had to see.

After somehow convincing Norval that I could help in this search, I found myself working in the adjoining lab, under the supervision of Mike Romalis. To

my surprise, it turned out that one of the specialties of the Fortson/Romalis labs was in *not* measuring an EDM. Norval had apparently been not measuring EDMs for years, and other scientists seemed very impressed with that. The picture became clearer when Mike explained to me how laboratory searches of various exotic effects can have a profound impact on newly emerging fundamental physics theories, even (or especially) if the effect is not observed. In my  $\sim 3$  years working afternoons and summers in the lab, Mike taught me a number of essential laboratory skills, building up a foundation for my future scientific endeavors. More important though was this ingrained notion of the value of precision measurement in fundamental physics, as well as a new-found respect for measuring zero. During this same period, I had great interactions with a number of graduate students in the Fortson and Romalis labs. The combined efforts (intentional or not) of Joel Allred, Micah Ledbetter, Clark Griffith, Matt Swallows, Timo Koerber, Reina Maruyama, Amar Andalkar, and Dave Pinegar managed to convince me that graduate school was the thing to do.

While much of my undergrad research was spent aiding in the construction of basement experiments to measure incredibly tiny effects, I also enjoyed my time spent a few floors up, exploring some larger scale (galactic) science with another excellent professor, Julianne Dalcanton. The cosmos had always been of interest to me, and JD's excitement was certainly contagious, but something about all those knobs that needed tweaking in Mike's lab always seemed to pull me back towards the basement.

When I first visited JILA as a prospective graduate student in 2002, I was fortunate enough to receive a lab tour from Jun Ye. Walking into Jun's lab for the first time was an unforgettable experience. While Jun talked excitedly about some sort of frequency revolution that was taking place, my attention was focused mainly on all the experiments crammed into the lab. Coming in to the

visit, I thought I knew a thing or two about lasers. I was wrong, *these* guys knew lasers! Each table in the lab was jam-packed with lasers of all different sorts, including lasers which could emit a whole rainbow of colors (Jun seemed particularly enthusiastic about those ones). I was sold on Boulder, JILA, and Jun, and after some nagging on my part, I managed to sell Jun on me.

Jun has played the most important role in my development as a scientist, and I have greatly enjoyed the journey he has guided me on in the past five years. One of the greatest changes Jun brought about in me is the way I think about science. I'm not sure how he did it, but somehow he changed my mentality from one where participation in science ceased when I left the building, to one where the building was just a convenient place to test or discuss my thoughts from the night before. Jun's generosity is unmatched, as is evident by my excess of frequent flyer miles, and his continued interest in joining the lab poker game. The working atmosphere in the Ye lab is one of excitement, collaboration, and intellectual freedom. I have certainly benefited from all three of these. Jun's ability to successfully pursue so many different cutting edge experiments, in a wide range of fields, continues to inspire and amaze me. He has always treated the lab like a family, and that has not gone unnoticed.

One of the great perks of working in Jun's lab has been the continuous stream of highly talented scientists to interact with. I have benefited greatly over the years from involvement with a number of graduate students, post-docs, and other visiting scientists who have come to work with Jun and Jan. Post-docs Tom Loftus and Tetsuya Ido played a critical role in my early development as a scientist. Both hailing previously from alkaline-earth labs, they provided me with overwhelming expertise on atomic physics, and how to deal with atoms like Sr. Tom and I spent many hours together building the circuits, coils, and the vacuum chamber for the new Sr experiment. His drive and attention to detail



in experimental physics has left a lasting impression on me. Nearly everything I know about diode laser stabilization has come from picking Tetsuya's brain. It is no coincidence that my laser skills improved at the same rate as his English. Interestingly, Tetsuya also proved to be one of the most dominant kick ball players of the modern era. Towards the end of my first year, fellow grad student Andrew Ludlow rejoined the lab (after a short stint in NIST) and we had our Sr team off and running.

Once we had the atoms cooled to an interesting level for clock development, Jason Jones and Kevin Holman joined the fun and brought with them the exciting fs-comb. Under their expert guidance, I spent a few months learning to operate the comb and eventually took Kevin's place as the official frequency counter for the Sr project. I'd like to believe that the joy I saw in Kevin's face during this changing of the guard had something to do with his love of teaching, and not Team Sr's reputation for late night operation (I'd really like to, Kevin). As the Sr project moved towards more precise measurements, Mark Notcutt was lured out of the quiet room to help us build a better clock laser. Andrew took up the challenge of implementing Mark's design at our wavelength, and their success allowed many of the achievements reported in this Thesis. Meanwhile, a new and improved fiberless comb was being integrated into the clock measurements by Seth Foreman, who would become our frequency guru. Tanya Zelevinsky and Sebastian Blatt also joined the late night fun and quickly became significant contributors. Thom Zanon later arrived on the scene, bringing with him plenty of new ideas for our clock.

A big thank you to all those involved in the Sr project! This of course includes the more recent additions which will help Blatt carry the torch: Thanks to Marcio Miranda, Mike Martin, and über-scientist Gretchen Campbell. This also includes John Hall, my academic grandfather who first set in motion many

of these dreams of optical clocks, and along with Alan Gallagher, got the original cool strontium project going at JILA. I've enjoyed many talks with Jan, about both life and science. These days during our chats, I find myself lagging behind his thought process by only one or two steps, a drastic improvement from a few years ago. I'd also like to thank the other current and former members of Jun's group for many pleasant scientific interactions, especially Kevin Moll, Eric Hudson, Mike Thorpe, Darren Hudson, Ben Lev, Xinye Xu, Brian Sawyer, Matt Stowe, Thomas Schibli, Avi Pe'er, and Adela Marian.

Collaboration is a cornerstone of JILA, and my project has certainly been no exception. I am grateful for our fruitful collaborations with the NIST Time and Frequency Division, especially Jim Bergquist, Scott Diddams, Leo Hollberg, Chris Oates, and Tom Parker. Without their numerous contributions, many of the measurements presented in this Thesis would not have been possible. Continued collaboration with Chris Greene's group at JILA has been incredibly valuable over the duration of the Sr experiment. I have also enjoyed interactions with many of the visitors which have temporarily called our group home, including Niels Anderson, Ennio Arrimondo, Xueren Huang, Long-Sheng Ma, and Jan Thomson.

The scientific importance of the technical support provided by the JILA computing, electronics, and instrument shops cannot be overstated. I'd like to thank Terry Brown, James Fung-a-Fat, Mike Whitmore, and Carl Sauer for their numerous contributions in the design and assembly of many of the electronics needed to make our experiment run. Thanks to Joel Fram, Jim McKown, and Mike Paige for all the virus extractions, network and software support, and laptop surgeries. Thanks also goes to Tom Foote and Hans Greene for their mechanical ingenuity which baled me out on a number of occasions. And thanks to David Alchenberger for his work coating the laser diodes used in our setup.

For me, grad school was not only about Sr. I have been very lucky to

have the support of a number of friends in Boulder during my time at JILA. For keeping me sane all these years, I thank Kirk Ullmann, Sebastian Blatt, Zach Walters, Juan Pino, Chris Keller, John Obrecht, John Jost, Russ Stutz, Aaron Leanhardt, Erin White, Carl Sauer, The Ulmers, The Carters, The Holmans, The Joneses, The Molls, The Hudsons, The Salomones, and many others. I also thank my northwest friends Steve Savage, Alex Golubev, Brian Mead, Scott Southard, Eli Troyke, and Ryan Yaden for their multiple journeys to Boulder for hockey, beer, and weddings. I would also like to thank Jay Buchannan and Josh Reis for their friendship and guidance in my earlier years.

Of course, none of this would have been possible without the love and support of my family. I have found that the combination of work ethic and mechanical curiosity handed down to me from my father Joe, and the thirst for a deeper understanding of things, instilled from my mother Marilyn, was a recipe for success in my development as a scientist, and as a person. Thank you Marilyn, and Joe and Nancy, for all your support! My siblings Kate, Scott, Kelly, and Andrew have also played an important role in my development, and it is much appreciated. My sister Kate for example, constantly reminds me of the limitations of scientific thinking when it comes to human society, and is most responsible for the refinement of my debating skills. My support network stretches far into my large extended family, which was never clearer to me than at my wedding, where so many of my relatives made the trip to Boulder. Specifically, I would like to thank the Dawsons for tolerating me for so many summers on the ranch. Working with Jim and Denny on the farm was great fun, and provided me with the confidence and sense of responsibility needed to be successful. Living in both urban and rural communities has taught me to carefully consider both sides of every story, and think critically and independently about issues. I would also like to thank the Carpenter family for so easily accepting me into their lives. Their love of sausage

is both fascinating and terrifying.

Finally, I would like to thank the most important person in my life. Beautiful, intelligent, kind, supportive, hilarious, loving, dedicated, loyal, selfless, and patient are just some of the words Amanda suggested I use to describe her. Indeed she is all of these. I can't imagine my life without her.

## Contents

### Chapter

<b>1</b>	Introduction to Optical Clocks	1
1.1	The Importance of Clocks . . . . .	1
1.1.1	Historical Perspective . . . . .	1
1.1.2	The Atomic Age . . . . .	3
1.1.3	Applications of Atomic Clocks . . . . .	4
1.2	Optical Clocks: Cranking up the $Q$ . . . . .	6
1.2.1	Frequency Combs to the Rescue . . . . .	8
1.2.2	Optical Clock Components . . . . .	9
1.2.3	Optical Clocks Using Clouds of Cold Neutral Atoms . . . . .	10
1.2.4	Optical Clocks Using Single, Trapped Ions . . . . .	11
1.3	Neutral Strontium as a Frequency Standard . . . . .	12
1.3.1	Optical Lattice Clock: Trapped Neutral Atoms . . . . .	13
1.4	Outline of the Thesis . . . . .	15
<b>2</b>	Laser Cooling of Neutral Strontium Atoms	17
2.1	Neutral Strontium: Level Structure and Cooling Transitions . . . . .	18
2.2	Experimental Apparatus . . . . .	23
2.2.1	The Sr Vacuum Chamber Apparatus . . . . .	23
2.2.2	461 nm Light Source . . . . .	25

2.2.3	MOT Repumping Lasers . . . . .	28
2.2.4	689 nm Light source . . . . .	30
2.3	Laser Cooling $^{88}\text{Sr}$ . . . . .	33
2.3.1	Two Stage Cooling Sequence . . . . .	33
2.3.2	Narrow Line Cooling . . . . .	35
2.4	$^{87}\text{Sr}$ Cooling Considerations . . . . .	40
2.4.1	Hyperfine Structure . . . . .	41
2.4.2	Laser Cooling with $J_g = 0$ and $I \neq 0$ . . . . .	43
2.4.3	Repumping Revisited . . . . .	47
2.4.4	A Few Practical Notes . . . . .	48
2.5	On to Spectroscopy ... Almost . . . . .	49
<b>3</b>	<b>Clock Spectroscopy in an Optical Lattice</b>	<b>51</b>
3.0.1	Optical Frequency Measurements in Free Space . . . . .	51
3.0.2	$\vec{k} \cdot \vec{v}$ ... Now What? . . . . .	53
3.1	Stark Cancellation Technique . . . . .	56
3.1.1	One-Dimensional Lattice Potential . . . . .	58
3.1.2	Calculation of the ac Polarizability . . . . .	59
3.1.3	Magic Wavelength: Calculation . . . . .	66
3.2	Spectroscopy in a 1-D Lattice: Theoretical . . . . .	70
3.2.1	Spectroscopy of Atoms Confined in a 1-D Harmonic Potential	71
3.2.2	The Effect of Trap Anharmonicity . . . . .	75
3.2.3	The Effect of Radial Motion on the Sideband Spectrum . .	77
3.2.4	The Effect of Motion on the Rabi Frequency . . . . .	80
3.2.5	Discussion: How should I Design My Trap? . . . . .	87
3.3	Spectroscopy in a 1-D Lattice: Experimental . . . . .	90
3.3.1	The Clock Laser @ 698 nm . . . . .	91

3.3.2	The Optical Lattice Setup . . . . .	95
3.3.3	Measurement of the Magic Wavelength, and Wavelength Sensitivity . . . . .	101
3.3.4	Resolved Sideband Spectroscopy . . . . .	102
3.3.5	Hz-Level Carrier Spectroscopy: Rabi . . . . .	104
3.3.6	Hz-Level Carrier Spectroscopy: Ramsey . . . . .	110
3.4	Discussion . . . . .	112
<b>4</b>	<b>Nuclear Spin Effects in Optical Lattice Clocks</b>	<b>114</b>
4.0.1	“ $^1S_0$ - $^3P_0$ Transition? We Forbid It!”- $\vec{J}$ and $\vec{S}$ . . . . .	114
4.1	State Mixing in the $nsnp$ Configuration . . . . .	115
4.1.1	Calculation of the Mixing Coefficients $\tilde{\alpha}$ , $\tilde{\beta}$ , $\tilde{\alpha}_0$ , $\tilde{\beta}_0$ , and $\tilde{\gamma}_0$	118
4.1.2	Lifetime of the $^3P_0$ State . . . . .	122
4.2	Zeeman Shifts from Magnetic Fields . . . . .	123
4.2.1	The Linear Zeeman Effect: Hyperfine-Induced Differential $g$ -Factor of the Clock Transition . . . . .	124
4.2.2	The Quadratic Zeeman Effect . . . . .	126
4.3	Sublevel-Dependent Light Shifts from the Optical Lattice . . . . .	128
4.3.1	Case I: Linear Polarization and The Tensor Light Shift . . . . .	129
4.3.2	Case II: Circular Polarization and The Vector and Tensor Light Shifts . . . . .	134
4.3.3	Case III: Light Shifts for Arbitrary Light Polarization . . . . .	137
4.3.4	Case IV: Light Shift in the Presence of an External Magnetic Field . . . . .	142
4.3.5	Summary of Nuclear-Spin Related Shifts . . . . .	143
4.4	Experimental Determination of Nuclear Spin Effects . . . . .	146
4.4.1	Precision Measurement of $\delta g$ . . . . .	146

4.4.2	Experimental Limits on the Sublevel-Dependent Light Shifts	154
4.5	Implications For the $^{87}\text{Sr}$ Lattice Clock . . . . .	157
4.5.1	Method I: Degenerate Sublevels . . . . .	158
4.5.2	Method II: Resolved Sublevels and Spin Polarized Samples	159
4.6	Man Made Clock Transition for Bosonic Isotopes . . . . .	163
4.6.1	EIT Clock . . . . .	164
4.6.2	Magnetic Field Induced Clock . . . . .	165
4.6.3	State Mixing at the Magic Wavelength . . . . .	166
4.7	So What Should I Chose? Fermions or Bosons . . . . .	169
<b>5</b>	<b>Accuracy Evaluation of the <math>^{87}\text{Sr}</math> Optical Lattice Clock</b>	<b>172</b>
5.0.1	So What Time Is It? How (un)Certain Are You? . . . . .	172
5.1	Lattice Spectroscopy Accuracy Evaluation . . . . .	175
5.1.1	Interleaved Method for Evaluating Systematics . . . . .	175
5.1.2	Polarizability Effects: Stark Shifts from the Lattice Laser .	178
5.1.3	Polarizability Effects: Stark Shifts from the Probe Laser .	180
5.1.4	Polarizability Effects: Blackbody Radiation Shift . . . . .	181
5.1.5	Characterization of Collision Shifts . . . . .	184
5.1.6	Characterization of Magnetic Effects . . . . .	185
5.1.7	Summary of Clock Systematics . . . . .	188
5.2	Absolute Frequency Measurement of the $^1S_0$ - $^3P_0$ Transition . . . . .	188
5.2.1	The Frequency Comb . . . . .	189
5.2.2	Microwave Reference and Transfer . . . . .	190
5.2.3	Gravitational Correction . . . . .	194
5.2.4	Absolute Frequency Measurement . . . . .	195
5.2.5	An International Effort . . . . .	200
5.3	Outlook for The $^{87}\text{Sr}$ Lattice Clock: Current Progress . . . . .	203



<b>6</b>	<b>On the Horizon</b>	<b>208</b>
6.1	Future $^{87}\text{Sr}$ Clockwork . . . . .	208
6.2	Other Lattice Clock Candidates . . . . .	209
	<b>Bibliography</b>	<b>212</b>

## Tables

### Table

1.1	Clock Transitions . . . . .	13
2.1	Strontium Isotopes . . . . .	18
2.2	Laser Cooling Transitions . . . . .	22
2.3	Sr Hyperfine Parameters Relevant to Laser Cooling . . . . .	41
3.1	Geometric Scaling Factors ( $\widetilde{A}_{ik}/A_T$ ) For Different States and Polarizations . . . . .	61
3.2	Relevant Transition Rates, Frequencies, and Correction Factors for the $5s^2\ ^1S_0$ , $5s5p\ ^3P_0$ and $5s5p\ ^3P_1$ States . . . . .	62
3.3	Fractional light shift for the $^1S_0$ , $^3P_0$ and $^3P_1(m = \pm 1)$ states at the relevant wavelengths . . . . .	69
4.1	Hyperfine Mixing Calculation . . . . .	122
4.2	Zeeman Matrix Elements for Pure ( $^{2S+1}L_J^0$ ) States . . . . .	126
4.3	$^3P_0$ Polarizabilities: Scalar, Vector and Tensor . . . . .	138
4.4	Theoretical estimates of $\delta g$ and $\tau^{^3P_0}$ for $^{87}\text{Sr}$ . . . . .	154
4.5	Measured Field Sensitivities for $^{87}\text{Sr}$ . . . . .	157
4.6	Field Sensitivities For Different Lattice Clock Schemes Using Sr . . . . .	169
5.1	Strontium Lattice Spectroscopy Error Budget . . . . .	188

5.2 Absolute Frequency Measurement Error Budget . . . . . 199

## Figures

### Figure

1.1	Optical clock components . . . . .	10
2.1	Relevant Low Lying Atomic Energy Levels for Sr . . . . .	20
2.2	Vacuum chamber system for laser cooling Sr . . . . .	24
2.3	Blue laser cooling setup . . . . .	27
2.4	Repumping lasers . . . . .	29
2.5	689 nm laser cooling system . . . . .	32
2.6	Two stage laser cooling cycle . . . . .	34
2.7	Red MOT Detuning Dynamics . . . . .	37
2.8	Red MOT Intensity Dynamics . . . . .	38
2.9	Red MOT Temperature Dependence on Detuning and Intensity . . . . .	39
2.10	Hyperfine Structure of The Laser Cooling Transitions . . . . .	42
2.11	MOT operation with hyperfine structure . . . . .	45
3.1	Free space optical frequency measurements . . . . .	52
3.2	Relevant level diagram for light shift calculations . . . . .	56
3.3	Atomic polarizability vs. wavelength for $^1S_0$ and $^3P_0$ . . . . .	64
3.4	Calculated ac Stark shifts for the $^1S_0$ , $^3P_0$ , and $^3P_1$ states for different lattice wavelengths and polarizations . . . . .	65
3.5	Magic Wavelength Calculation For $^3P_0$ and $3P_1$ . . . . .	67

3.6	Schematic of Bound Atom Spectroscopy . . . . .	73
3.7	Theoretical Sideband Spectrum Comparing Harmonic and $\cos^2$ Potentials . . . . .	76
3.8	The effect of radial motion on the sideband lineshape . . . . .	79
3.9	Effect of Longitudinal Motion on the Rabi Frequency . . . . .	82
3.10	Effect of Longitudinal Motion on the Excitation Fraction . . . . .	83
3.11	Effect of Radial Motion on the Rabi Frequency . . . . .	84
3.12	Excitation Probability vs Radial Spectroscopic Parameters . . . . .	86
3.13	ULE Cavity for Clock Stabilization . . . . .	92
3.14	698 nm Clock Laser performance . . . . .	94
3.15	Lattice spectroscopy setup . . . . .	96
3.16	Spectroscopy Sequence For Lattice Spectroscopy . . . . .	100
3.17	Measurement of $\lambda_0$ and the sensitivity to changes in $\lambda_0$ for the $^1S_0$ - $^3P_0$ transition . . . . .	101
3.18	$^1S_0$ - $^3P_0$ Spectroscopy in a 1D lattice: Spectroscopy of the Motional Sidebands . . . . .	104
3.19	$^1S_0$ - $^3P_0$ spectroscopy in a 1D lattice: Carrier Spectroscopy With Degenerate Sublevels . . . . .	106
3.20	High resolution spectroscopy of resolved transitions . . . . .	108
3.21	Ramsey Spectroscopy in an Optical Lattice . . . . .	112
4.1	State Mixing Diagram . . . . .	117
4.2	Nuclear structure of the $^1S_0$ and $^3P_0$ states . . . . .	125
4.3	Magnetic Sensitivity of the $^1S_0$ - $^3P_0$ clock transition . . . . .	127
4.4	$m_F$ -Dependent Polarizability of the $^3P_0$ State for Linear Polarization at 813 nm . . . . .	132

4.5	$m_F$ -Dependent Polarizability of the $^3P_0$ State for Circular Polarization at 813 nm . . . . .	136
4.6	Polarization Dependence of Zeeman Light Shifts . . . . .	140
4.7	Polarization Dependence of Zeeman-like Light Shifts II . . . . .	141
4.8	Setup for Nuclear Spin Studies . . . . .	144
4.9	Spectroscopy of resolved $\pi$ transitions . . . . .	147
4.10	Spectroscopy of resolved $\sigma$ transitions . . . . .	148
4.11	Calculation of Zeeman spectrum for $\sigma$ transitions . . . . .	150
4.12	Measurement of $\delta g$ for different trap depths . . . . .	152
4.13	Measurement of the Tensor Light Shift . . . . .	156
4.14	Spin-Polarized Spectrum . . . . .	161
4.15	Different state mixing schemes for bosonic isotopes . . . . .	167
5.1	High resolution spectroscopy of the $^1S_0$ - $^3P_0$ transition . . . . .	173
5.2	Interleaved measurement scheme for systematic evaluation . . . . .	177
5.3	Lattice Stark shift measurement . . . . .	179
5.4	Density shift measurement . . . . .	185
5.5	Magnetic field calibration . . . . .	187
5.6	Setup for microwave frequency comparisons . . . . .	191
5.7	Unstabilized BRAN phase over 4 days . . . . .	193
5.8	Data record for the 24 hour absolute frequency measurements . . . . .	196
5.9	Absolute frequency measurement of the $^1S_0$ - $^3P_0$ transition . . . . .	198
5.10	International measurement record for Strontium lattice clocks . . . . .	201
5.11	Comparison of the Sr and Hg <sup>+</sup> clock lasers using the BRAN fiber link . . . . .	205
5.12	Sr stability measurement using a H-maser or the NIST Ca optical clock . . . . .	206

## Chapter 1

### Introduction to Optical Clocks

#### 1.1 The Importance of Clocks

##### 1.1.1 Historical Perspective

For thousands of years, the measurement of time has played an essential role in mankind's everyday life. Time keeping and synchronization are required for the success of many important societal activities, including trade, religious ceremonies, and other group gatherings. Agricultural endeavors, and therefore a society's food supply, also rely on monitoring time, as crops must be planted in coordination with the seasons. A natural technique for the measurement of time is to record the motion of celestial bodies such as the position of star constellations in the sky, the rising and setting of the sun, and the phases of the moon. Use of such time scales for societal and agricultural purposes have occurred throughout human history.

Measuring time with astronomical events is a logical and robust technique for synchronizing activities on timescales of months, days, or even hours, however, such slow timescales are not practical for dividing time into the smaller intervals demanded by an increasingly complex society. Hourly precision is insufficient for seemingly simple activities like cooking, let alone for complex scientific measurements. To improve the resolution of time keeping, a periodic event which occurs more frequently is needed, such that time can be divided into smaller intervals.

Because of this need, humans have long pursued alternative ways for time keeping, based on man-made devices.

The beginning of the mechanical era of accurate time keeping is often attributed to the development of the pendulum clock. While man-made clocks (based on water flow for example) had been around for thousands of years, Huygens 1656 invention of the pendulum clock provided a significant improvement in timing precision. The first versions of this clock used the oscillations of a swinging pendulum to keep time with an accuracy of better than one minute over an entire day. By late in the 19th century, the best pendulum clocks could keep time within one second over a duration of 100 days. These high precision mechanical clocks had applications in both science and daily life. Astronomers used high accuracy mechanical clocks to time the movement of planets and stars, allowing accurate mapping of the celestial bodies, which could then be used for science and navigation. These clocks also led to the development of marine chronometers, which provided an accurate navigation system for ships at sea.

Further improvements in time keeping technology came in the early 20th century, as oscillators based on electro-mechanical resonances in quartz crystals were developed. The oscillation period of these systems is much faster than that of pendulum clocks, allowing time to be divided into even smaller intervals and hence improving the precision. The oscillation period of carefully designed quartz systems is so precise that the timing error corresponds to a loss of 1 second in 30 years. These new oscillators also allowed for miniaturization of high accuracy time keeping devices, as is evident in the watch making industry.

While the development of man-made clocks has allowed dramatic and useful improvements in precision timing resolution compared to that of celestial motion, one fundamental limitation remains. The main drawback of mechanical clocks is that they cannot be used as an *absolute* timescale, due to limited reproducibility



in design and implementation. The oscillation period of a pendulum clock, for example, will depend sensitively on the exact length of the pendulum used. Even if clock makers could agree on a fixed length, limited tolerances in length measurement and machining will limit the reproducibility of the oscillation period in different clocks. Because of this limitation, the relatively slow oscillation of celestial bodies, specifically the rotation of the earth, was used as the internationally accepted time standard well into the 20th century. The more precise mechanical clocks are instead operated as local oscillators which could divide time into smaller, more useful intervals, but still had to be calibrated by the slow oscillation period of the astronomical timescale.

### 1.1.2 The Atomic Age

With the discovery of quantum mechanics in the last century came the possibility of using clocks more accurate and more precise than any mechanical or celestial reference previously known to man. The structure of atoms and molecules allows them to emit and absorb electromagnetic radiation by making transitions between predetermined energy levels. The frequency of the radiation is precisely given by the difference in energy of the levels involved in the transition as  $\nu = \Delta E/h$ , where  $h$  is Planck's constant. In many atomic systems, the energy levels are very insensitive to external perturbations, such that the radiation frequency is robust and reliable.

In an atomic clock, the natural frequency of a transition serves as a reference to which a laboratory radiation source can be compared. The oscillator of an atomic clock then consists of two components, a man-made radiation source, and an atomic system which is measured by that source to determine the man-made frequency relative to the atomic frequency governed by quantum mechanics. The beauty of using an atomic frequency standard is that the clock oscillation period

should be independent of the man-made component of the oscillator. Every copy of a given atom is identical, such that a clock built using Cs atoms in Boulder will operate at the same frequency as an independent Cs clock built in Paris, or anywhere in the universe, presuming environmental effects on the atomic energy levels are well understood.

The success of clocks based on atomic Cs in the last century has had a profound impact on science and technology [1, 2]. The unrivaled precision and accuracy in time keeping provided by Cs clocks led to a new definition of time in 1967. The second is now officially defined as "... the duration of 9,192,631,770 periods of the radiation corresponding to the transition between the two hyperfine levels of the ground state of the caesium 133 atom " [3]. The use of atomic clocks has made the second the most accurately realized unit of measurement, such that other units are now being defined in terms of time. The measurement of the speed of light [4] allowed redefinition of the meter in 1983 as "... the length of the path travelled by light in vacuum during a time interval of  $1/299\,792\,458$  of a second" [3].

After more than 50 years of development (nicely summarized in [1]), the Cs fountain clocks of today [5, 6] are now approaching an incredible accuracy level of a few parts in  $10^{16}$ . A clock with such (in)accuracy loses only one second every 100 million years!

### 1.1.3 Applications of Atomic Clocks

Atomic clocks play an important role in wide variety of scientific fields [2]. The precise timing of atomic clocks is used in radio astronomy for Very Long Baseline Interferometry (VLBI), a technique that uses an array of multiple radio telescopes to increase the effective angular resolution of detection. This technology relies on precise synchronization of data signals coming from the individual

telescopes at a level that only atomic clocks can provide. The same technology can also be applied to deep space navigation as a tracking system. Measurements of frequency and time are intimately related to Einstein's theories of special and general relativity. Atomic clocks have so far provided the most stringent tests of these theories via measurements of the orbital period of pulsars and its decay due to emission of gravity waves [7]. Comparison of different atomic clocks allows researchers to test emerging theories which attempt to unite gravitation and quantum mechanics. Such theories leave room for a temporal dependence in fundamental constants, such as the fine structure constant, an effect which can be constrained by comparing different atomic clock frequencies over time [8]. The crustal dynamics of the Earth can also be studied with the aid of atomic clocks, as GPS (discussed below) provides an accurate position measurement system.

Precision spectroscopy, a research area in which clocks are a cornerstone, is a technology driven (or more appropriately, technology *driving*) field. To push the limits of clock performance, new spectroscopic techniques and technologies must constantly be developed, which often leads to new and exciting fields of study. For example, a major motivation for early laser cooling work was to improve the accuracy of atomic spectroscopy and clocks. Today, the study of laser-cooled atoms, molecules, and ions dominates much of atomic physics. The promise of ultra high precision optical clocks fueled the invention of the fs-comb laser [9, 10]. These lasers have revolutionized optical metrology, but also have a wide variety of applications in other fields, including arbitrary waveform generation and time domain exploration of chemical and biological processes. To get a general idea of the importance of clocks in the scientific community, one has to look no further than a list of Nobel laureates in physics, where research related to the development and application of atomic clocks seems to be acknowledged about once per decade.

The precise timing provided by atomic clocks plays an important role in

the lives of non-scientists as well. The Global Positioning System (GPS) [11] is a prime example of the impact that atomic clocks have on our society. Each of the 24 GPS satellites utilizes an onboard atomic clock for precise synchronization of the individual coded signals, allowing accurate positioning of ground based receivers at an amazing level of 1 mm for stationary objects [2]. With a GPS radio communication link, real-time centimeter level accuracy is now possible [11]. The incredible positioning capabilities of GPS have revolutionized navigation, as airplanes, boats, and even some personal vehicles rely on the system to get from point  $A$  to  $B$  safely and efficiently. The positioning system also allows dramatic improvement in surveying and map making, as some traditional limitations such as line-of-sight are eliminated, and the positioning accuracy is unmatched. The atomic clock based timing signals distributed by GPS also have applications in our daily lives. The accurate timing information is used to synchronize large computer networks for banking and the internet, for operation of cell phone networks, and even to manage large-scale power grids.

With the number technological and scientific advances resulting from development of accurate atomic clocks, it is no surprise that researchers are working hard to push the limits of clock accuracy and precision.

## 1.2 Optical Clocks: Cranking up the $Q$

The two main quantities which characterize the performance of a clock are the accuracy and the precision. The accuracy of an atomic clock is determined by how well the measured frequency matches that of the atoms natural frequency. In general, the accuracy will depend on the atomic species used and how well it can be isolated from environmental effects during spectroscopy. The precision of the clock is more commonly referred to as the stability (or instability), which represents the repeatability of the measured clock frequency over a given averaging

time  $\tau$ . The stability is typically expressed as the Allan deviation, in fractional frequency units, given as [12]

$$\sigma_y(\tau) = \frac{\delta\nu(\tau)_{rms}}{\nu} = \frac{\chi}{2\pi Q S/N} \sqrt{\frac{t_c}{\tau}}. \quad (1.1)$$

Here,  $Q (= \nu/\Delta\nu)$  is the line quality factor of the clock transition for a linewidth  $\Delta\nu$ ,  $S/N$  is the signal-to noise-ratio achieved in the measurement cycle time  $t_c$ , and  $\chi$  is a constant of order unity which depends on the transition lineshape used for measurements. For quantum projection noise limited measurements, the  $S/N$  is determined by the number of atoms ( $N_a$ ) used in each measurement, as  $\sqrt{N_a}$ .

From Eq. 1.1 we can see that the most precise clock will have a large  $Q$  value and  $S/N$  ratio. The Cs clock satisfies these criteria as the 9.2 GHz transition can be resolved with a transition width of about 0.5 Hz yielding a  $Q > 10^{10}$ , and a large number of atoms can be used for good  $S/N$ . In state-of-the-art Cs clocks, an impressive (in)stability approaching  $1 \times 10^{-14} \tau^{-1/2}$  has been achieved [13]. The Cs clock transition could, in principle, support a larger line  $Q$  allowing improved stability. However, in current experiments gravity limits the interaction time ( $t$ ) with the atoms to about 1 second, resulting in a Ramsey linewidth  $\delta\nu = 1/(2t) = 0.5$  Hz. Therefore to improve the stability the  $S/N$  must be increased, which for Cs fountains means increasing the atom number as projection-noise-limited measurements have already been achieved [14]. The problem with this tactic is two-fold. For one, the stability depends on the square root of the atom number, such that large increases in  $N_a$  result in only moderate improvements in the stability. Second, atomic collisions are a central concern for the accuracy of the Cs clock [15], such that the improved precision that comes with large atom number may degrade the clock accuracy.

Since we can't dramatically change the linewidth, or the  $S/N$ , in the Cs clock, an alternative option for improved precision and accuracy is to use an atomic

transition with a higher frequency. In this way, a larger  $Q$  can be achieved for the same interaction time, and the clock stability can be improved. Herein lies the motivation for developing atomic clocks based on optical transitions. Changing the clock reference frequency from the microwave region to the optical can provide a  $Q$  enhancement of more than four orders of magnitude [16, 17]. Assuming all other parameters equal, the improvement in the  $Q$  could reduce the needed averaging time to reach a given level of precision by eight orders of magnitude. As the clock precision improves, the accuracy is likely to follow, as systematic frequency shifts can be evaluated with less and less averaging time (read effort). The potential precision and accuracy gains provided by the larger  $Q$  makes clocks based on optical transitions a very attractive system to explore.

### 1.2.1 Frequency Combs to the Rescue

The benefits from optical clocks are no secret, so why have microwave clocks been the focus historically? The problem with optical clock schemes has always been in the readout of the optical frequency, that is, how to make the gears of the clock that can measure the ticks. In the Cs case, the clock frequency is accessible with conventional electronics, making measurement and distribution of the clock signal relatively straight forward. Optical frequencies on the other hand are very difficult to measure, as the oscillation is orders of magnitude faster than electronics can measure. The traditional method for measuring optical frequencies was to develop complex frequency chains which essentially divide down the optical frequency in steps by comparison with a number of other oscillators [4]. This approach was expensive and labor intensive, such that only national standards labs could realistically pursue high accuracy optical frequency measurement.

In the last decade, the development of octave spanning fs-comb lasers has revolutionized the business of optical frequency metrology [18, 19, 20, 21]. Briefly,

in the frequency domain, the output of a fs-laser consists of a large number of lasing modes which are evenly spaced by the frequency at which pulses are emitted from the laser, known as the repetition rate  $f_{rep}$ . Owing to dispersion inside the fs-laser, the frequencies of the comb modes are not exact harmonics of the repetition frequency, instead the entire comb is offset in frequency by a small (microwave) amount  $f_o$ . If  $f_{rep}$  and  $f_o$  are known, then the frequency of the  $n$ th comb mode is given by  $\nu_n = nf_{rep} + f_o$ . This is a powerful relationship as we have expressed an optical frequency  $\nu_n$ , in terms of two microwave frequencies and an integer  $n$ . With all the comb mode frequencies known precisely, an optical clock frequency can be measured via heterodyne beat with the nearest comb mode as  $\nu_{clock} = \nu_n + f_{beat}$ , such that the optical frequency is completely determined by microwave frequencies and an integer. The fs-laser provides a coherent link between the optical and microwave regions of the electromagnetic spectrum, providing a greatly simplified system for measuring optical frequencies with traditional microwave technology.

### 1.2.2 Optical Clock Components

With the fs-comb greatly simplifying the business of high accuracy optical frequency measurement, interest in optical clocks has grown rapidly. The general design of an optical clock is shown in Fig. 1.1. Here, the light emitted from an ultra-stable cw laser acts as the local oscillator (or pendulum) for the clock. However, the laser frequency in general will be sensitive to environment effects, and cannot be used alone as a standard. To ensure the frequency is maintained at a fixed value, the light is used to probe an electromagnetic resonance in an atom (or molecule or ion). This quantum absorption provides a natural frequency marker for the system, as the resonance will nominally depend only on the fundamental properties of the atom. The atomic signal can then be used to determine the difference between the laser frequency and that of the reference atom, allowing

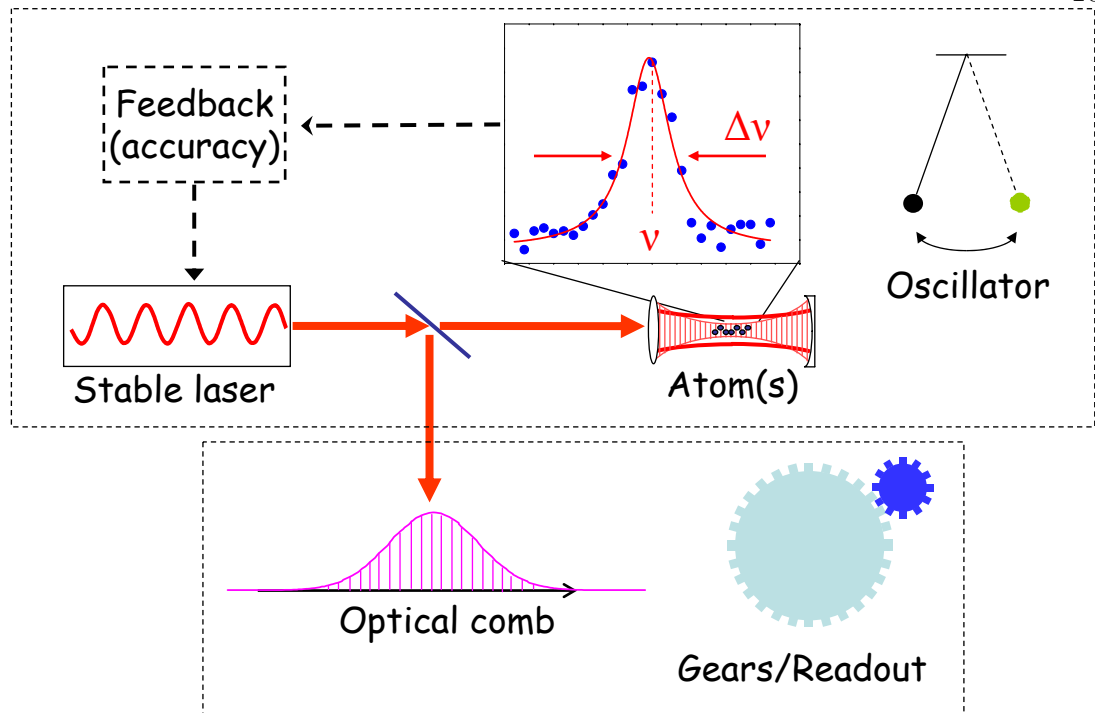


Figure 1.1: Components of an optical clock.

the laser frequency to be monitored and stabilized to the preferred value. The fs-comb provides the gears of the clock, allowing measurement of the laser frequency relative to other high accuracy clocks in either the optical or microwave domain.

The frequency flexibility of the comb technique provides an environment where clock developers can nominally ignore the actual frequency of the clock transition in a given quantum reference, and instead choose a system based on its merit as a potential standard. To make an informed decision on the type of quantum absorber to employ in our clock, we will take a quick look at the different state-of-the-art schemes for high accuracy, high precision, optical clocks.

### 1.2.3 Optical Clocks Using Clouds of Cold Neutral Atoms

Neutral atom optical clocks are a natural extension of the Cs primary standard, as the basic physics of the measurement is the same but the precision is



increased. Alkaline-earth atoms are promising candidates for optical clocks as the level structure allows for laser cooling and provides narrow clock transitions which can be insensitive to frequency shifts from external fields [22, 23]. The most intensively pursued neutral atom optical clock has thus far been based on ballistically expanding clouds of laser-cooled Ca atoms [24, 25]. The reference frequency for this clock is the narrow ( $\sim 300$  Hz)  $^1S_0$ - $^3P_1$  intercombination transition. In this system a stability of  $4 \times 10^{-15}$  at 1 s has been achieved, and the clock inaccuracy has been reduced to  $6.6 \times 10^{-15}$  [24], with good agreement on the measured frequency between different labs [26]. The analogous transition has also been explored in Mg [27] and Sr [28].

Owing to the Doppler effect, the optical spectroscopy in these experiments is sensitive to atomic motion. This effect will likely limit the eventual accuracy of clocks based on clouds of atoms in free fall, at a level worse than that already achieved by the best Cs fountains. In this case, the improved stability comes at a cost of accuracy due to the Doppler shift.

#### 1.2.4 Optical Clocks Using Single, Trapped Ions

Single trapped ions [29, 30, 31, 32, 33, 34, 35] provide a reference free of the Doppler shift problems that hinder free space measurements of neutral atoms. In these systems the ions are tightly trapped in the so-called Lamb-Dicke regime where the ion motion is much smaller than the wavelength of the spectroscopy laser. In this case, the atomic motion has a negligible effect of the transition width, and long interrogation times can be used such that exceedingly large line  $Q$ 's are achieved [16]. The benefits of optical ion clocks are significant, as can be seen in the recent results of the  $\text{Hg}^+$  clock at NIST [29]. Owing to the high line  $Q$ , The  $\text{Hg}^+$  system out-performs the stability of current state of the art Cs clocks, reaching the level of  $4 \times 10^{-15} \tau^{-1/2}$ , even with the reduced  $S/N$  provided by only one atom.

Furthermore the elimination of Doppler effects allows an accuracy superior to the fountain clocks, now at a level below  $7 \times 10^{-17}$ . While the fundamental stability limit for ion clocks is not as good as in neutral atoms, the high accuracy and large line  $Q$  keep the ions at the forefront of optical frequency metrology.

### 1.3 Neutral Strontium as a Frequency Standard

Neutral strontium is an interesting candidate for the development of an optical frequency standard. Strontium has a level structure similar to Ca, resulting in two relevant clock transitions. The  $^1S_0$ - $^3P_1$  transition in Sr is broader than that of Ca, having a linewidth of 7.4 kHz. However, even with the lower  $Q$ , this transition is of interest as the level structure of Sr allows more efficient laser cooling than in the Ca system, such that more atoms are available ( $S/N$ ) and the cloud temperatures are lower. One can therefore expect the stability to be similar to that of the Ca system but with a reduced sensitivity to Doppler shifts. The second clock line of interest is the doubly-forbidden, nuclear spin induced  $^1S_0$ - $^3P_0$  transition in  $^{87}\text{Sr}$ . This transition has a very small linewidth of 1 mHz, and therefore the achievable  $Q$  will only be limited by technical issues such as laser noise, and not by the transition itself, as is the case of the broader intercombination lines. The Sr system is convenient in that all of the lasers for cooling and spectroscopy can be derived from inexpensive diode laser sources, as opposed to many other optical clocks which require more challenging laser wavelengths.

Table 1.1 compares clock parameters of the high-performance clocks discussed here. The  $Q$  values represent the highest achieved values in current experiments, with the  $^{87}\text{Sr}$  result discussed later on in this text. Based on Eq. 5.12, the strontium clock transitions should have excellent stability performance, with the  $^{87}\text{Sr}$  clock potentially outperforming the others on the list.

Table 1.1: Relevant clock stability parameters for the  $^{133}\text{Cs}$ ,  $^{199}\text{Hg}^+$ , and  $^{40}\text{Ca}$  clocks as compared to the two Sr clock transitions. The  $Q$  value represents the best achieved linewidth in the system. In the Cs case the  $Q$  is limited by the interaction time (gravity). In Hg, Ca, and  $^{88}\text{Sr}$  the  $Q$  is limited by the clock state lifetime. In  $^{87}\text{Sr}$  the  $Q$  is limited by oscillator noise. The atom number  $N$  represents the values achieved in current systems. In the final column the stability is given in units of  $\chi\sqrt{\frac{t_c}{\tau}}$ .

Species	Transition	$\nu$	$Q$	$N$	$1/(2\pi Q\sqrt{N})$
$^{133}\text{Cs}$	$^2S_{1/2}(F=3)-^2S_{1/2}(F=4)$	$9.2\times 10^9$	$2\times 10^{10}$	$10^6$	$7\times 10^{-15}$
$^{199}\text{Hg}^+$	$^2S_{1/2}-^2D_{5/2}$	$1.1\times 10^{15}$	$1.6\times 10^{14}$ [16]	1	$7\times 10^{-16}$
$^{40}\text{Ca}$	$^1S_0-^3P_1$	$4.56\times 10^{14}$	$2\times 10^{12}$ [24]	$10^5$	$4\times 10^{-16}$
$^{88}\text{Sr}$	$^1S_0-^3P_1$	$4.34\times 10^{14}$	$6\times 10^{10}$ [36]	$10^6$	$4\times 10^{-15}$
$^{87}\text{Sr}$	$^1S_0-^3P_0$	$4.29\times 10^{14}$	$2.4\times 10^{14}$ [17]	$10^4$	$7\times 10^{-18}$

### 1.3.1 Optical Lattice Clock: Trapped Neutral Atoms

One of the most exciting motivations for pursuing a Sr clock is a new measurement scheme for neutral atom clocks that has recently come to the forefront of optical spectroscopy. Taking a lesson from the high accuracy ion clocks, the neutral atoms can be confined in a tight harmonic potential to eliminate broadening and frequency shifts due to atomic motion. To simulate a harmonic potential, the atoms are trapped in an optical lattice formed by a standing wave light pattern. The trap can be carefully designed such that the light shifts on the clock states are nominally equal and the clock frequency is not perturbed [37]. In Sr, this is achieved by tuning the lattice to a convenient laser wavelength of 813 nm. With this scheme one can combine the best features of neutral atom and trapped ion systems, as Doppler free spectroscopy and long interrogation times are achieved with the large  $S/N$  provided by a neutral atom ensemble. This scheme is particularly well suited for alkaline earth atoms as the clock states are very insensitive to the lattice polarization and other fields. The precision of the lattice clock can be expected to out-perform both ion and free-space atom clocks. The accuracy will

likely exceed that of other neutral atom clocks, including Cs, and may even compete with the accuracy of trapped ion clocks if residual light shifts and collision shifts are manageable.

The proposal and initial theoretical analysis to use Sr in a lattice clock configuration came first from the group of Katori in Tokyo [38, 39]. This was followed shortly after by the first demonstration of optical lattice spectroscopy, using both the  $^3P_1$  [36] and  $^3P_0$  [40] clock transitions. In these initial studies, the magic wavelengths for the two transitions were explored and measured at the sub-nanometer level, and observation of Doppler and recoil free line spectra were reported. Since the initial demonstrations by Katori, a number of groups have begun intensively exploring the lattice clock system, with most of the work to date being performed with different isotopes of Sr and Yb. In the span of only a few years, a number of seminal experimental results have been presented, strengthening the case for lattice clocks as a potential frequency standards.

Most experimental and theoretical work has focused on the issue of clock accuracy. Some experimental highlights towards this end include: confirmation that hyperpolarizability effects will not limit the Sr accuracy at the  $10^{-17}$  level [41], experimental evaluation of the Sr lattice clock frequency systematics below the  $10^{-15}$  level [42, 43], and the excellent agreement of high accuracy Sr clock frequency measurements between three independent laboratories [44, 45, 46, 42, 43]. The theoretical effort has focused mainly on light shift calculations in Sr and Yb [39, 47, 48, 49], as well as nuclear spin related field sensitivities [39, 47, 50]. One of the major systematic effects in the lattice clock system, the clock sensitivity arising from the nuclear spin [50], has motivated development of a number of interesting alternative schemes for lattice clocks where bosonic isotopes (which lack nuclear spin) are used in combination with external fields which induce the otherwise forbidden clock transition [51, 52, 53, 54, 55]. One of these schemes has

already been demonstrated in even isotopes of Yb [56] and Sr [57].

In terms of clock stability, it has been confirmed that the lattice technique does provide nominally motion-free spectroscopy enabling ultrahigh-resolution spectroscopy as in trapped-ion clocks [58]. Record level line  $Q$ 's have recently been demonstrated in Sr, with  $Q$  exceeding  $2 \times 10^{14}$  [17]. Similar results have been achieved in a Yb lattice clock system, reaching  $Q \sim 1 \times 10^{14}$  [59]. These  $Q$  values, and the large atom number ( $\sim 10^4$ ) used in these systems, suggest that 1 second stabilities of  $10^{-17}$  (or lower) could be possible with an adequately pre-stabilized laser.

#### 1.4 Outline of the Thesis

In this thesis the strontium lattice clock system is evaluated as a potential frequency standard. In Chapter 2, a laser cooling apparatus for strontium is presented as a tool for the production of ultra-cold ( $1 \mu\text{K}$ ) strontium samples for clock spectroscopy. Chapter 3 focuses on spectroscopy in a 1D lattice. This includes the design and implementation of a lattice clock setup operating at the “magic” cancellation wavelength. Spectroscopy of confined atoms is explored both theoretically and experimentally. The combination of the lattice confinement and a highly stabilized clock laser allows observation of ultra-narrow spectral features having line  $Q$ 's exceeding  $2 \times 10^{14}$ . With the clock precision under control, the issue of clock accuracy is discussed in the remaining chapters. Specifically, a number of systematic effects relating to the nuclear spin in  $^{87}\text{Sr}$  are investigated in detail in Chapter 4. With these effects well understood, an experimental clock accuracy evaluation is performed in Chapter 5. The systematic errors related to the lattice clock are reduced to below  $10^{-15}$ , similar to the uncertainty of state of the art Cs clocks. The absolute frequency is measured to be  $429,228,004,229,874.0(1.1)$  Hz, and is in excellent agreement with our previous measurement, as well as that of

other groups around the world. The precision and accuracy results presented here speak strongly for the Sr lattice clock as an optical frequency standard, and as a potential system for re-definition of the SI second.

## Chapter 2

### Laser Cooling of Neutral Strontium Atoms

Recent developments in laser cooling and trapping of atoms have opened the doors for a variety of research fields in precision measurement [60]. The MOT (magneto-optical trap) has allowed researchers to study atomic physics at extremely low temperatures while simultaneously increasing the experimental interaction times with the atoms. Access to this ultra-cold atom regime has resulted in tremendous improvements in precision spectroscopy and atomic clock development. Cold trapped atoms have also enabled researchers to reach the ultra-cold, quantum degenerate gas regime creating Bose Einstein Condensates (BEC) [61] and Degenerate Fermi Gases (DFG) [62]. The cold, samples provided by MOT's and laser cooling are becoming an essential tool in many cutting edge research areas of atomic physics.

Alkali atoms have historically been the atoms of choice for laser cooling and trapping due in part to their single unpaired-electron structure, and diode-laser friendly cooling transitions. Atomic Rubidium, for example, was the first atomic BEC, Potassium was the first DFG, while cold Cs atoms are used in the atomic fountain which defines the SI second.

Alkaline earth atoms are relatively new to the playing field, as their more challenging laser requirements for cooling and trapping have limited the pursuit of these systems to comparatively few labs. However, the same two electron

Table 2.1: Naturally occurring isotopes of Sr

Isotope	Nuclear Spin ( $I$ )	Abundance (%)
$^{88}\text{Sr}$	0	82.6
$^{87}\text{Sr}$	9/2	7.0
$^{86}\text{Sr}$	0	9.9
$^{84}\text{Sr}$	0	0.56

level structure that might intimidate the average laser cooler, provides diverse experimental possibilities which are markedly different than in their alkali counter parts.

Some common features of Alkaline earths (and similar atoms such as Yb, Hg) include; a large number of naturally occurring isotopes of both the bosonic and fermionic type; isotopes without nuclear spin (the bosons); strong cycling transitions between states with the same electronic spin; forbidden optical transitions (intercombination), and so on. In the case of Sr, four stable isotopes can be used for cooling experiments. These isotopes are listed in Table 2.1 along with their nuclear spin and natural abundance. The work in our lab has been focused on the most abundant bosonic isotope  $^{88}\text{Sr}$ , and the lone fermionic isotope  $^{87}\text{Sr}$ . As discussed in the introduction, we are after the narrow optical clock transitions in these isotopes. To take advantage of these we need the long interaction time that only ultracold atoms can provide. This chapter is dedicated to the development of such an apparatus for Sr, and exploration of some interesting laser cooling effects that aren't found in a typical Alkali MOT.

## 2.1 Neutral Strontium: Level Structure and Cooling Transitions

The two valence electrons in Sr result in two distinct series of atomic energy levels as the electron spins can be parallel (triplet states) or anti parallel (singlet states) as in atomic helium. The energy levels are described in the usual Russell-



Saunders notation of  $^{2S+1}L_J$  [63], where  $S$  is the total spin of the two electrons (either 0 or 1),  $L$  is the orbital angular momentum of the electrons, and  $J$  is the total angular momentum of the state. The ground state of alkaline atoms is that of the lowest total angular momentum, the  $^1S_0$  state. Here we can already see a departure from the alkalis as the presence of the second electron results in a spin-less ground state (really spin-less if you chose an  $I=0$  isotope). The low lying level structure for Sr is shown in Fig. 2.1. The first excited state in the singlet series  $^1P_1$  is often used for laser cooling experiments in the group II atoms as the transition rate  $\Gamma = 1/\tau$  is quite strong. The triplet series of states contain more variety and the lowest lying  $^3P_J$  manifold contains the states we are most interested in this work. If we assume pure  $LS$  coupling, the three  $5s5p^3P$  states are forbidden to decay to the ground state, and are therefore meta-stable. However we will see in Chapter 4 that the spin-orbit interaction provides a finite lifetime for the  $^3P_1$  state, allowing weak electric dipole transitions to take place. This narrow transition is called an *intercombination* transition and comprises much of the current interest in alkaline earth atoms. A number of relevant transitions from these meta-stable triplet states are shown as they will be relevant as we move along. Notably, the ultranarrow  $^1S_0$ - $^3P_0$  transition we are strongly interested in is only present in the isotope with nuclear spin ( $^{87}\text{Sr}$ ), as the spin-orbit interaction alone is not enough to provide a finite lifetime (see Chapter 4).

With the known level structure in Fig. 2.1 we can begin to explore the laser cooling possibilities for Sr. We gain some insight if we consider the force on the atom in the typical 1D MOT configuration [60]. The MOT is created using counter propagating circularly polarized beams with opposite helicity, in the presence of a magnetic field gradient  $d\vec{B}_x$  along the light propagation axis  $x$ . The force applied to the atom from each beam is given by the product of the photon momentum

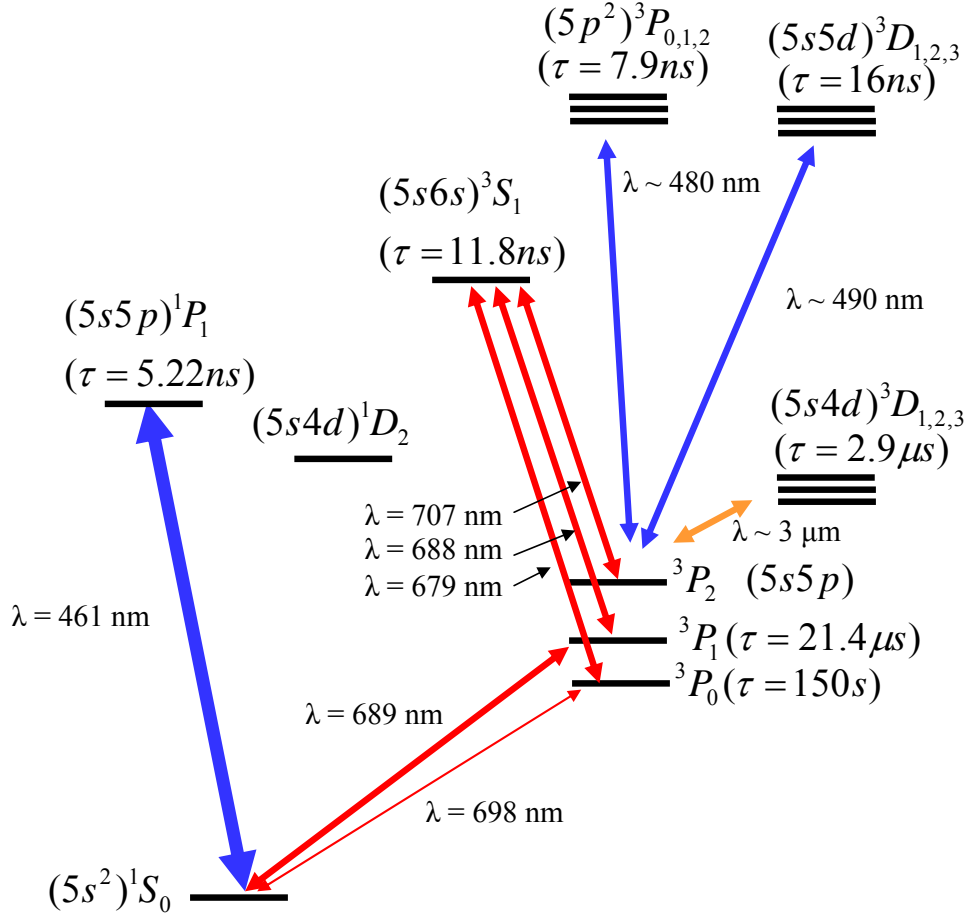


Figure 2.1: Low lying states and electric dipole transitions for atomic strontium (not to scale). The states are labeled by terms  $^{2S+1}L_J$ . The two electron alkaline-earth structure results in both a singlet ( $S=0$ ) and triplet ( $S=1$ ) series of states. Excited state lifetimes are given along with transition wavelengths (in nm). A full list of state lifetimes (or transition rates) is given in Table 3.2 along with references.

$(\hbar k)$  and the photon scattering rate, resulting in a total force

$$F = \hbar k \frac{\Gamma}{2} \left( \frac{s}{1 + s + 4(\Delta - \vec{k} \cdot \vec{v} - g\mu_0 d\vec{B} \cdot \vec{x})^2 / \Gamma^2} - \frac{s}{1 + s + 4(\Delta + \vec{k} \cdot \vec{v} + g\mu_0 d\vec{B} \cdot \vec{x})^2 / \Gamma^2} \right) \quad (2.1)$$

Here  $s = I/I_{sat}$ , where  $I$  is the beam intensity, and  $I_{sat} = \frac{\hbar c \pi}{3\tau \lambda^3}$  is the saturation intensity.  $\Delta/2\pi$  is the laser detuning from the atomic resonance,  $\vec{k}$  is the laser k-vector,  $v$  is the atomic velocity,  $x$  is the atoms position along the x-axis, and  $g\mu_0$  is the magnetic sensitivity of the excited state sublevel. Here the overall sign difference between the

two terms is due to the different propagation directions of the beams, as is the sign difference on the  $\vec{k} \cdot \vec{v}$  term. The magnetic term changes signs because the different light polarizations couple to different  $\pm m_J$  sublevels in the excited state. Since we want to cool the atoms, we would prefer that the scattering force slows atoms. From Eq 2.1 we can see that this will take place via the  $\vec{k} \cdot \vec{v}$  term if the laser frequency is tuned below the atomic resonance frequency. In this case, the scattering force is strongest in the direction opposite the atomic motion and cooling takes place. The magnetic term provides the restoring force for the atoms (the Doppler cooling provides damping but is not enough alone to trap the atoms) as it places a spatial boundary where the detuning and velocity equal the Zeeman shift and the scattering force is maximum.

To estimate the expected feasibility of laser cooling using a given transition, we need to consider some simple quantities in Eq. 2.1 such as the saturation intensity, transition rate, and atomic velocity. Typically one considers a few cooling limits as well, such as the Doppler and recoil limits. The Doppler limit for laser cooling gives the minimum achievable temperature for a given transition, based on the transition rate, as [60]

$$T_{Doppler} = \frac{\hbar\Gamma}{2k_B} \quad (2.2)$$

where here  $\Gamma=2\pi \times \gamma$  where  $\gamma$  is the transition linewidth (full width at half maximum) in Hz. In alkali MOTs the Doppler limit is usually not much of a limit as polarization gradient cooling allows sub-Doppler cooling. In Sr however, this limit is important to consider since the ground state is without structure. A second cooling limit to consider is the recoil temperature limit which arises due to the finite energy shift of the atom when it absorbs a single photon. This limit is given by the atomic mass  $M$  and the cooling wavelength  $\lambda$  as [60]

$$T_{Recoil} = \frac{h^2}{\lambda^2 M} \quad (2.3)$$

A third parameter of interest is the saturation intensity. This value quantifies the required laser intensity for useful cooling and trapping.  $I_{sat}$  depends on the excited

Table 2.2: Laser cooling parameters for different transitions in Sr

Transition	$(\Gamma/2\pi)$	$\lambda$ (nm)	$I_{sat}$	$T_{Doppler}$	$T_{recoil}$	$v_c$
$5s^2\ ^1S_0-5s5p\ ^1P_1$	30.5 MHz	461	40.7 mW/cm <sup>3</sup>	720 $\mu$ K	1.02 $\mu$ K	14 m/s
$5s^2\ ^1S_0-5s5p\ ^3P_1$	7.40 kHz	689	3.0 $\mu$ W/cm <sup>3</sup>	180 nK	460 nK	5.0 cm/s
$5s5p\ ^3P_2-5s4d\ ^3D_3$	53.9 kHz	2923	290 nW/cm <sup>2</sup>	1.3 $\mu$ K	25 nK	1.6 m/s
$5s5p\ ^3P_2-5s5d\ ^3D_3$	8.7 MHz	497	10.2 mW/cm <sup>2</sup>	230 $\mu$ K	890 nK	4.3 m/s

state lifetime, and the cooling wavelength as

$$I_{sat} = \frac{hc\pi}{3\tau\lambda^3} \quad (2.4)$$

A final consideration is the capture velocity for a given transition. If atoms are moving fast enough that the Doppler shift  $\vec{k} \cdot \vec{v}$  is larger than the transition width, then the atom will be tuned out of resonance, reducing the scattering force, and allowing it to escape the cooling beam. The cooling beam can therefore only repel atoms moving with  $v_c \leq \Gamma/k = \gamma\lambda$ . This can also be expressed as a maximum capture temperature using the relation  $T = v^2M/k$ .

Table 2.2 summarizes these parameters for the possible cooling transition in the lowest lying states of Sr. The first transition of interest is the strong  $^1S_0-^1P_1$  transition. Although the wavelength is not terribly convenient, and the Doppler limit is relatively large, the capture velocity for this transition is very large at 14 m/s ( $T = 2$  K). Looking at the intercombination transition, we can see why forbidden lines begin to become interesting. Here the Doppler limit is in the sub- $\mu$ K range because of the narrow linewidth. Thus simple Doppler cooling on a narrow line can be an attractive way to reach ultracold temperatures. The draw back of this transition is the low capture velocity of 5 cm/s ( $T_c = 30 \mu$ K). The two transitions from the meta-stable  $^3P_2$  state are interesting in that the magnetic structure should allow sub-Doppler cooling. This is especially interesting for the three micron transition which has a very small recoil limit.

## 2.2 Experimental Apparatus

In this section we describe the Sr cooling apparatus used in this work. We present the laser systems required for cooling the atoms to  $1\mu\text{K}$ , as well as the vacuum chamber setup. Although one would like to cool using only the narrow intercombination transition, the photon scattering rate is simply too low to capture thermal atoms. We therefore use a two stage cooling process in our experiments where we first load the atoms in to a standard MOT operating on the strong  $^1S_0$ - $^1P_1$  transition where they are pre-cooled to a few mK, and then transfer the atoms to a second stage cooling MOT operating on the weak  $^1S_0$ - $^3P_1$  transition where they are cooled to the  $\mu\text{K}$  level. Before we get to the cooling results, we will discuss the vacuum chamber, and laser systems used for these experiments.

### 2.2.1 The Sr Vacuum Chamber Apparatus

The pre-cooling MOT is loaded using a Zeeman-slowed atomic Sr beam, with the apparatus shown in Fig. 2.2. The atomic beam is generated by an effusive oven which is heated to a temperature of  $575\text{ }^\circ\text{C}$ . A nozzle at the output of the oven acts as a collimator and is heated to  $850\text{ }^\circ\text{C}$ . The atomic beam is then transversely cooled by a 2-dimensional  $461\text{ nm}$  optical molasses detuned from the  $^1S_0$  -  $^1P_1$  resonance by  $-10\text{ MHz}$ . The molasses laser beams have an aspect ratio of 15:1 along the atomic beam propagation axis to maximize the interaction time between the atoms and the collimating beams. Separate cooling beams are used for the horizontal and vertical axes, with each path containing  $\sim 7\text{ mW}$  of power.

After the collimation stage, the atomic beam passes through a  $6.4\text{ mm}$  diameter mechanical shutter which allows us to turn on and off the atomic beam during experiments. A gate valve also allows the oven to be isolated from the rest of the vacuum system. After exiting the transverse cooling region, the atomic

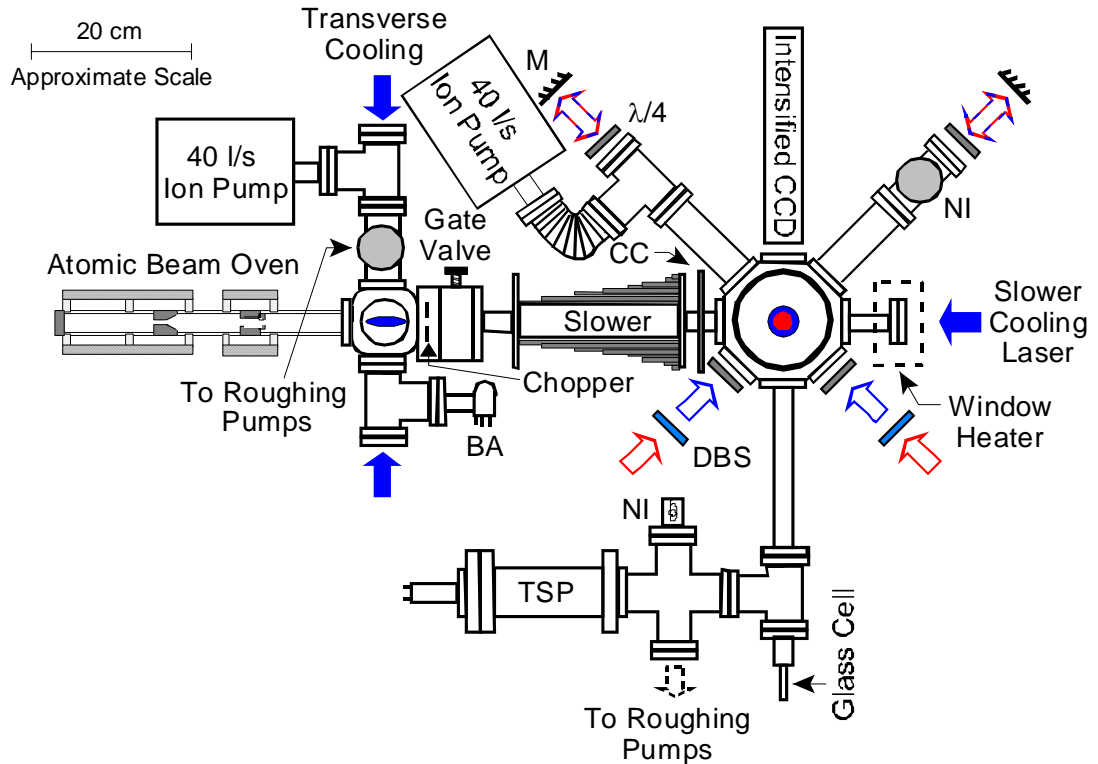


Figure 2.2: Vacuum chamber system for laser cooling Sr. The chamber is divided into three main sections. In the first section, a diffusive oven creates a collimated beam of neutral strontium atoms. Upon leaving the oven, the beam is collimated transversely by a two dimensional transverse cooling setup. After the collimation the beam passes into section two of the system via a differential pumping tube. Here, the atoms pass through a Zeeman slower coil, where they are slowed from 500 m/s to 30 m/s for loading into the MOT. Exiting the slower, the slow atoms are collected in the singlet MOT where they are pre-cooled before transfer to the intercombination MOT for cooling to  $1\mu\text{K}$ . The third section of the chamber contains a glass cell for experiments in an ultra high vacuum environment ( $\sim 10^{-10}$  Torr), and is not used in this work.

beam enters a water cooled 20 cm long constant deceleration  $\sigma^-$  Zeeman slower [64] with a peak magnetic field of  $\sim 600$  G, corresponding to a capture velocity of 500 m/s. A compensation coil reduces the slower field in the MOT region to less than 100 mG. The field is further zeroed with use of three sets of Helmholtz pairs. The 461 nm Zeeman slower cooling laser is detuned from the  $^1S_0 - ^1P_1$  resonance by -1030 MHz, contains 60 mW of power, and is roughly collimated. It enters the

apparatus through a viewport opposite the atomic beam. To prevent corrosion of the viewport window, an optical quality  $z$ -cut sapphire flat is used. The sapphire is AR coated on the side facing away from the atomic beam and transmits 92% of the light. The window is heated to 200 °C to prevent deposits, and physically forms part of the vacuum seal [65].

The trapping chamber has two large (6") view ports along the axis of gravity, and eight 2 3/4" ports in the plane of the optical table, two of which are used for the Zeeman slower. The vacuum windows are fused silica, and have been AR coated with a broadband coating optimized for transmission at 461 and 689 nm. The oven and trapping sections of the chamber are each evacuated by 40 l/s ion pumps and occasionally by a titanium sublimation pump (TSP), although the latter had a marginal effect on the pressure. The two chambers are separated by a 6.4 mm diameter, 45 mm long differential pumping tube just before the gate valve. Typical vacuum levels in the oven and trapping region during experiments are  $2 \times 10^{-8}$  Torr and  $1.5 \times 10^{-9}$  Torr. The MOT anti-Helmholtz coils are oriented such that the axial magnetic field gradient,  $dB_z = 50$  G/cm, lies along gravity, and the current in the coils is regulated with a Hall probe and servo system. The current set point (and field gradient) is computer controlled and can be switched on and off or between different values in  $\sim 1$  ms. For detection and imaging of the atoms in various experiments, atomic fluorescence is monitored in a number of ways. The atom cloud is simultaneously imaged onto a standard ccd camera, a blue sensitive photo diode, a photo-multiplier tube (PMT), and an intensified ccd imaging system.

### 2.2.2 461 nm Light Source

The light source for the 461 nm radiation is shown in Fig. 2.3. Due to the large saturation intensity of the cycling transition ( $41$  mW/cm<sup>2</sup>) an intense

light source is required to provide the light for the slower, transverse cooling, and MOT beams. With adequate diode laser sources unavailable at 461 nm, we instead employ second harmonic generation (SHG) to produce the blue light. Light at 922 nm is generated by an AR coated, grating stabilized, external cavity diode laser (ECDL) system oriented in the Littman-Metcalf geometry [66]. The free running linewidth of this master laser is  $< 300$  kHz and the available output power, after passing through two 30 dB optical isolators, is typically 45 mW. The light is used to injection lock a tapered amplifier diode chip, which then provides up to 1.6 W at 922 nm. The light is collimated and passed through two additional 30 dB isolators, before being spatially filtered with a short piece of single mode fiber. In the end up to 900 mW of light, in a gaussian TEM<sub>00</sub> mode, is available for the SHG.

The 461 nm light is produced by frequency doubling the 922 nm light using a KNbO<sub>3</sub> crystal in a linear build up cavity configuration [67]. The cavity configuration is very simple and robust consisting only of an curved input/output coupler, which is transmissive in the blue and reflects 94% of the IR, and the doubling crystal, which acts as the end mirror due to a high reflective coating for both colors on the back face. The front face of the SHG crystal is AR coated for both colors. The potassium niobate crystal is a-cut and phase matching is achieved with temperature tuning, at a temperature of  $\sim 150$  °C. The master laser frequency is modulated at 30 MHz via the laser diode current and the doubling cavities are locked (using a PZT on the output coupler cavity mirror) to the 922 nm cavity transmission signal. For input powers less than 350 mW, the conversion efficiency is  $\sim 50\%$  (usable blue power outside the cavity), but for larger fundamental powers the output beam develops mode structure and becomes unstable. Since we have ample power in the IR, we simply built two doubling cavities which provide 180 mW and 130 mW each at 461 nm. The frequency of the blue light is stabilized to



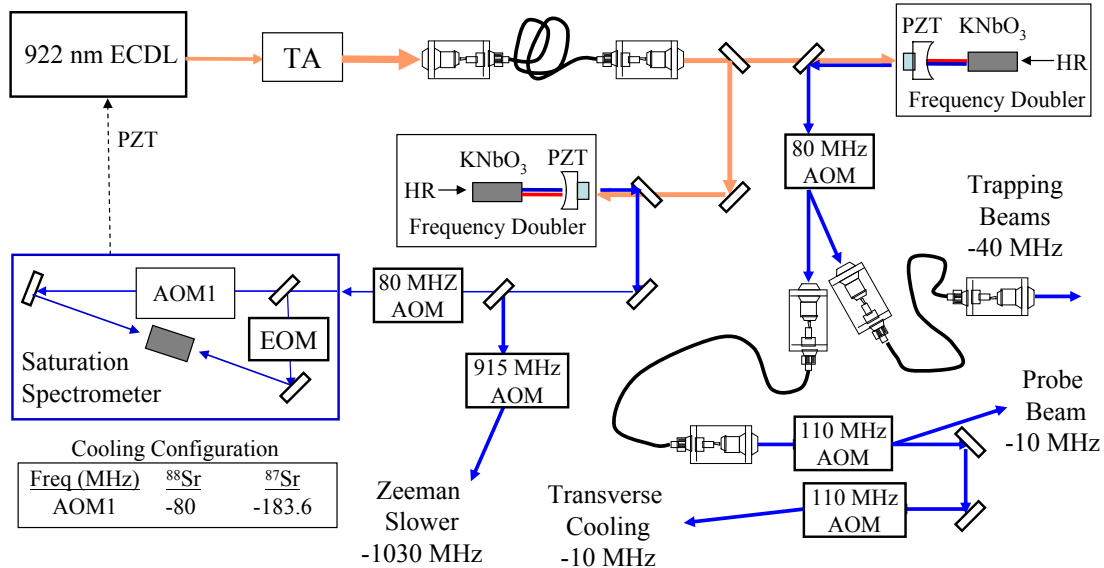


Figure 2.3: The 461nm light source. A master ECDL at 922nm injects a tapered amplifier (TA) which generates up to 1.6 W for SHG. Two linear doubling cavities are used for the SHG, each providing  $\sim 150$  mW. The first cavity generates the light which is used for the Zeeman slower, and the saturation spectrometer which controls the master laser frequency. The second doubler provides light for the trapping beams, transverse cooling and a strong detection beam. To switch the 461 nm system between  $^{88}\text{Sr}$  and  $^{87}\text{Sr}$  the AOM frequency within the spectrometer is changed from 80 MHz to 183.6 MHz.

a  $^{88}\text{Sr}$  saturated absorption spectrometer which results in a detuning of -120 MHz from the  $^1S_0$ - $^1P_1$  transition for light coming from the two doublers. The spectrometer error signal is used to control the PZT of the master laser to stabilize the frequency of the system. Different AOMs within the spectrometer are used to change the optical frequency of the blue system for isotope selection.

The Zeeman slower beam is derived from the output of the first SHG cavity by taking the -1 order diffraction of a 915 MHz AOM. The slower beam typically contains 60 mW. The second SHG cavity provides the light for the trapping beams, transverse cooling, and a near resonant probe beam. To ensure a good mode profile these beams are filtered by a short SMPM fiber. The trapping beams are detuned by -40 MHz and have a  $1/e^2$  diameter of  $\sim 3$  cm. The MOT beams are

retro-reflected such that only three beams are needed. The total power in the two horizontal and one vertical MOT beams are 8, 8, and 3 mW respectively. All 461 nm beams in the setup are intensity stabilized using the AOM modulation depth, and are switched on and off using the AOMs and mechanical shutters.

### 2.2.3 MOT Repumping Lasers

Due to the presence of the low lying  $^1D_2$  state, the singlet cooling transition is not completely closed. Figure 2.4 shows the decay path from  $^1P_1$ , which eventually leads to atoms being shelved into the  $^3P_2$  state. This loss mechanism limits the total atom number in the blue MOT, as the MOT lifetime (in seconds) can be estimated given the decay rates as [68]

$$\tau = 1.56 \times 10^{-3} \left( 1 + \frac{1 + 4(\Delta/\Gamma)^2}{s} \right). \quad (2.5)$$

For the trapping beam parameters described above, the saturation is typically 0.5, leading to a MOT lifetime of around 20 ms. This short lifetime will limit the number of atoms loaded into the MOT, and should be addressed.

To re-pump the  $^3P_2$  atoms to the  $^1S_0$  state, we drive the  $^3P_2$ - $^3S_1$  transition (707 nm) to pump the atoms into the  $^3P_1$  state, which eventually decays to the ground state. To prevent optical pumping to the long lived  $^3P_0$  state we also excite the  $^3P_0$ - $^3S_1$  transition (679 nm). The 679 nm and 707 nm lasers are grating stabilized diode lasers in the Littman configuration. The ECDL configuration provides sufficient frequency stabilization (in terms of laser linewidth) for the repumping transitions, which have MHz level linewidths. Instead of locking the lasers to an atomic signal [69], the optical frequency is controlled using a transfer cavity technique. Each laser is locked to a reference cavity which is simultaneously locked to a commercial  $I_2$  stabilized HeNe laser. The cavities are locked to the HeNe by measurement of the transmission (side lock) and feedback to a PZT on

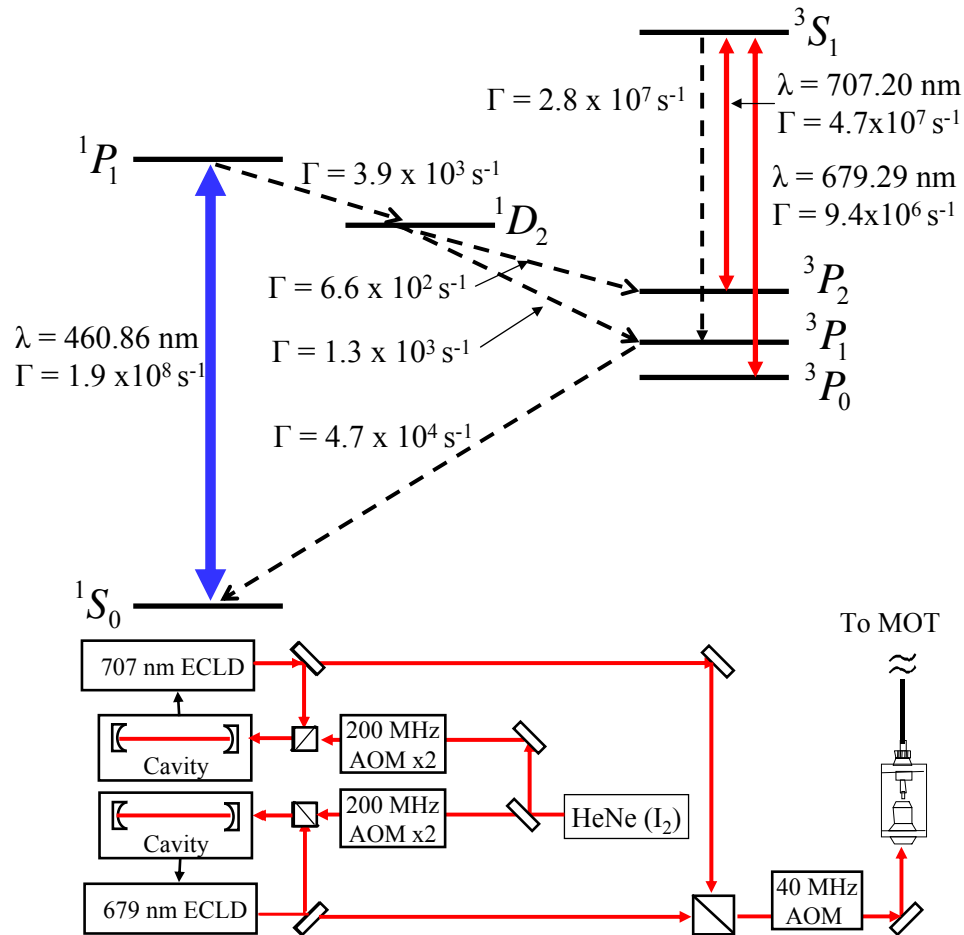


Figure 2.4: Repumping scheme for the blue MOT. Decay to the  $^1D_2$  state from the  $^1P_1$  state limits the number of atoms in the blue MOT as they can decay to the meta-stable  $^3P_2$  state. To prevent this loss mechanism the atoms can be re-pumped into the ground state by exciting the  $^3P_2$ - $^3S_1$  and  $^3P_0$ - $^3S_1$  transitions as shown. To stabilize the repumping lasers, transfer cavities are used which can be locked to a commercial iodine stabilized HeNe laser which provides excellent long term stability. The relative cavity frequency can be changed with double pass AOMs in between the HeNe and the cavity.

one of the cavity mirrors. The correct frequencies of the 707 nm and 679 nm beams are realized by first tuning the lasers manually by looking at the enhanced blue MOT signal. The cavity length is then tuned over a few free spectral ranges until the fringes at 633 nm and the re-pump wavelength roughly coincide. At this point the cavity is locked to the HeNe fringe, and the ECDL is locked to

the cavity. Fine tuning of the absolute frequency of the repumps is then done by tuning double-passed AOMs between the HeNe source and the cavities. This procedure is typically done once per day, after which the lasers can be relocked to the cavity without careful frequency tuning. After passing through a single-mode polarization-maintaining optical fiber, the co-propagating 707 nm and 679 nm laser beams are expanded to a  $1/e^2$  diameter of  $\sim 1$  cm and delivered to the  $^1S_0 - ^1P_1$  MOT, co-aligned with the MOT beams. The 707 nm (679 nm) beam contains 1 mW (2.5 mW) of power, resulting in an predicted optical re-pumping time of  $< 1$  ms.

Interestingly, the leak in the MOT efficiently populates the  $^3P_2$  state with mK temperature atoms, which can be quite useful for some experiments as the state can be magnetically trapped (for  $m_J = 1, 2$ ), while the  $^1S_0$  state cannot [70]. This results in some interesting possibilities as the atoms can be stored in the magnet trap provided by the MOT field [68, 71, 72, 73, 74, 75, 76, 77]. We find that nearly  $10^8$  atoms can be loaded in this way, and the magnetic trap lifetime exceeds 1 s. Thus we can expect the blue MOT lifetime to be extended to similar timescales if the repumping scheme is employed.

#### 2.2.4 689 nm Light source

The 689 nm light source has more stringent requirements for frequency stabilization than the other laser systems, as the cooling transition width is only 7.4 kHz. Aside from the linewidth requirements, the 689 nm system is fairly simple, as very inexpensive diodes (\$50) are available commercially at 685 nm (although without AR coating). The complete laser system (shown in Fig. 2.5) is based on a grating stabilized master ECDL with an AR coated diode tuned to 689.4 nm. The laser is stabilized to a high finesse cavity ( $\sim 3000$ ) using an EOM to modulate the laser frequency for the Pound-Drever-Hall locking scheme [78]. The cavity

is isolated from environmental perturbations in a number of ways. The cavity is suspended by two thin wires inside a temperature stabilized can that is evacuated to  $< 10^{-6}$  Torr, and mounted on vibration damping material. For further stability, the cavity is completely passive. The electronic feedback provided by the cavity lock has a bandwidth of  $\sim 250$  kHz where the high frequency feedback is coupled directly to the laser current and the lower frequency signal controls the PZT in the ECDL for slow drift. Locking the laser to the cavity provides a measured linewidth of less than 300 Hz, more than sufficient for cooling on the  $^3P_1$  line. To ensure the laser frequency is accurate and well controlled on slow timescales, the laser is tuned relative to the cavity by double-passing the 689 nm light using a 1 GHz AOM. The set point frequency for the AOM is determined from measurement of the master laser frequency using a signal from a saturated absorption spectrometer based on the  $^{88}\text{Sr } ^1S_0\text{-}^3P_1(m=0)$  resonance. The spectrometer signal controls the GHz AOM frequency, and locks the laser system to 40 MHz above the resonance.

Two slave lasers are then phase locked to the master by stabilizing the beat frequency between the master and slave to a pre-determined frequency for the experiment of interest. For the  $^{88}\text{Sr}$  cooling, only Slave *A* is needed and the beat frequency is fixed to -120 MHz, which results in a total detuning of -80 MHz from the cooling transition. The slave is then double passed through a 40 MHz AOM such that the light is (nearly) resonant with the cooling transition. The AOM is used for switching, but also allows modulation of the laser frequency during the laser cooling stage. For  $^{87}\text{Sr}$  cooling the second slave is required (see below) for efficient cooling trapping. In this case Slave *A* is the stirring laser and the appropriate frequency for the beat with the master is +101.64 MHz. While Slave *B* is the trapping laser, which is stabilized at -1.2 GHz relative to the master. Note that using this master/slave combination instead of AOMs to control the

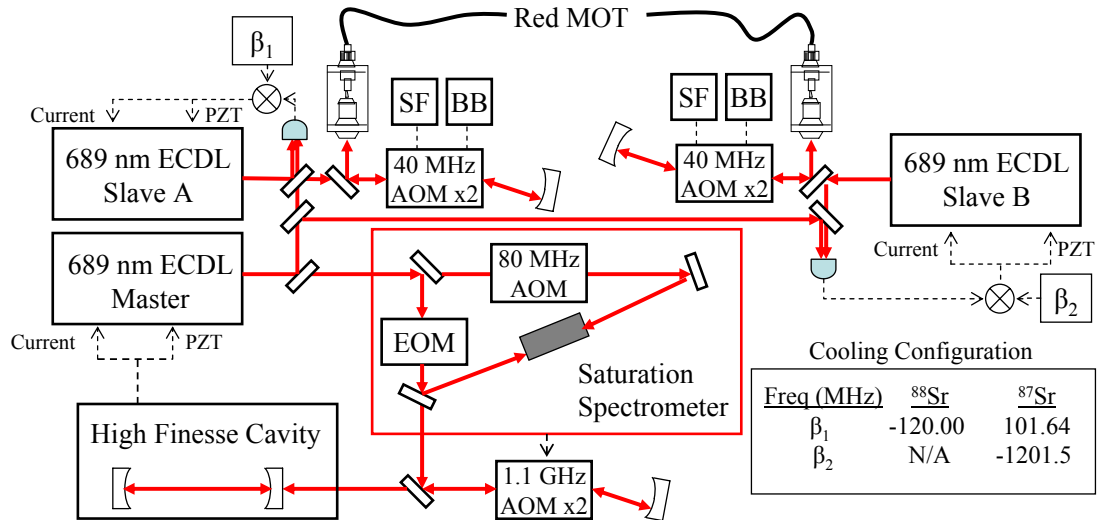


Figure 2.5: Laser system for narrow-line cooling at 689 nm. A master ECDL laser is locked to a high finesse cavity, resulting in line width below 300 Hz. To control the absolute frequency of the laser, a spectrometer is used which control the laser frequency offset from the cavity via a 1.1 GHz AOM. Due to power considerations, a second ECDL (Slave A) is phase locked to the master by stabilization of a heterodyne beat between the two lasers. The slave light is double passed through a 40 MHz AOM which provides switching, broad band (BB) frequency modulation, and single frequency (SF) mode for the cooling discussed below. When  $^{87}\text{Sr}$  is used in experiments, a second slave laser is locked to the master to allow the two color cooling scheme discussed below. The frequency  $\beta$  of the offset locks are given for the different isotopes.

frequency allows easy changes to accommodate cooling and trapping of different isotopes, as only the phase lock frequency (and sign) need to be changed on Slave A. This also provides more optical power for cooling experiments than a single laser setup combined with AOMs. The two slave lasers are then coupled to the chamber table using SMPM fibers. Upon exiting the fiber, the 689 nm light (up to 5 mW at each frequency) is combined such that the two frequencies are spatially overlapped and have the same polarization. The beam size is expanded to a  $1/e^2$  diameter of 5.2 mm. The red light is then co-aligned with the 461 nm trapping beams using dichroic mirrors. Dual wavelength waveplates ( $3\lambda/4$  at 461 nm and  $\lambda/4$  at 689 nm) with two inch apertures are used to set the MOT beam

polarization.

## 2.3 Laser Cooling $^{88}\text{Sr}$

In this section, we briefly summarize some of the important features of cooling Sr on both the strong and narrow transition. A complete exploration of the mechanical and thermodynamical narrow line laser cooling properties for the Sr system have been presented elsewhere by our group [71, 79, 80], and a number of others [81, 82].

### 2.3.1 Two Stage Cooling Sequence

In the first cooling stage, atoms are continuously loaded from the atomic beam into a blue MOT operating on the  $^1S_0$ - $^1P_1$  transition. With the Zeeman slower and transverse cooling laser beams present, the typical blue MOT lifetime, population, and temperatures are 20 ms,  $3 \times 10^7$ , and  $\sim 2.5$  mK, respectively. Even without the repumps we see that the cycling transition is “closed enough” to allow a significant atom number in the trap. When the re-pump lasers are introduced, the  $^1S_0$  -  $^1P_1$  MOT population and lifetime are enhanced by  $10\times$  and  $15\times$  respectively, with both values likely limited by atomic beam induced trap loss.

With the atoms pre-cooled to the mK level, we are ready to cool on the narrow intercombination transition. The two stage cooling cycle used here is shown in Fig. 2.6. After the pre-cooling stage, the 461 nm light is switched off and the atomic beam is blocked with the mechanical shutter, and the MOT gradient is reduced to 3 G/cm. At this point the 689 nm cooling light is switched on, however the Doppler profile of the strontium atoms is still above 1 MHz. To ensure spectral coverage of all the atoms, the 689 light is frequency modulated (using the 40 MHz double pass AOM in Fig. 2.5) to broaden the laser spectrum

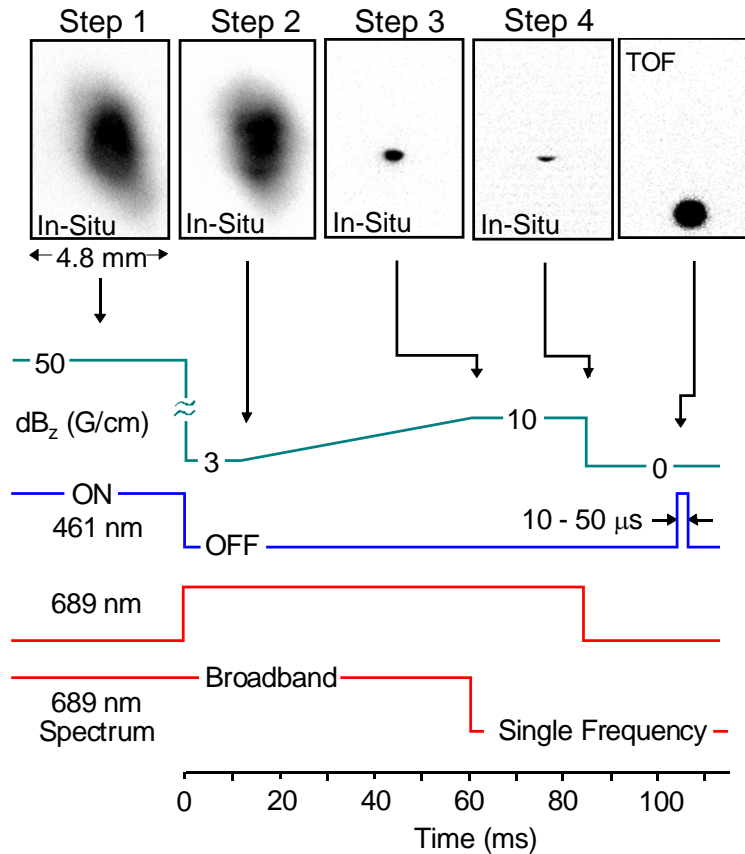


Figure 2.6:  $^{88}\text{Sr } ^1S_0 - ^3P_1$  MOT timing diagram. Images at the top show the atomic cloud at various stages of the cooling and compression process. From left to right, the first four images show in-situ distributions of the cloud at various points in the cooling cycle, while the last frame gives a time-of-flight (TOF) image taken after 25 ms of free expansion from the  $\delta = -520$  kHz,  $s = 75$  single-frequency MOT. The green line represents the operational mode of the anti-Helmholtz and relevant field gradient in G/cm. The blue line gives the timing for the blue trapping beam (on/off). The first red line gives the timing for the red trapping beams (on/off) while the bottom red line shows the timing for modulation of the red laser spectrum. For the  $^{87}\text{Sr}$  system, the cooling cycle is slightly altered as discussed in the text.

to a few MHz. At this stage, the atom temperature is roughly  $100 \mu\text{K}$  and about half of the original mK atoms are captured. The field gradient is then ramped to 10 G/cm resulting in compression of the atom cloud and further cooling to  $10 \mu\text{K}$ . The cooling lasers are then switched to single frequency mode for operation of the narrow line MOT. The temperature and atom number of the final atomic sample



depend on the single frequency stage laser detuning and intensity (see 2.3.2). The resulting atom temperature at the end of the MOT stage is typically  $1\mu\text{K}$ , and the total transfer efficiency from the blue MOT to the red MOT can be as large as 50%. The red MOT lifetime is  $\sim 1$  s, and the atomic density is  $10^{11}$ – $10^{12}$   $\text{cm}^{-3}$ . Note that the atom transfer efficiency from the broad band cooling state to the single frequency MOT depends strongly on the modulation parameters as shown in [71].

### 2.3.2 Narrow Line Cooling

Laser cooling on a narrow transition provides a system where a number of cooling features, not easily observed for the standard strong transitions which nearly every laser cooling experiment has been based on [60], can be explored. One example of this is the importance of gravity. For strong transitions, such as the singlet line in this work, the maximum scattering force from the cooling beams ( $\hbar k\Gamma/2$ ) is about five orders of magnitude larger than the force of gravity ( $F = Mg$ ). Conversely, for the narrow  $^1S_0$ - $^3P_1$  transition, the light scattering force is only about 16 times larger than gravity. Therefore, gravity, which can safely be ignored in traditional experiments, becomes a significant effect for narrow line cooling. In the case of light alkaline earth atoms with weaker intercombination lines (e.g. Ca, Mg), the cooling force is weak enough that the force of gravity dominates and Doppler cooling is not possible, such that other cooling schemes are required [83, 84]. Another significant difference is the importance of the photon recoil on cooling dynamics. For broad transitions we have the situation  $\Gamma_E/\omega_R \gg 1$ , where  $\Gamma_E = \Gamma\sqrt{1+s}$  is the power broadened transition linewidth and  $\omega_R/(2\pi) = \frac{\hbar k^2}{4\pi M}$  is the photon recoil frequency. For the Sr intercombination line (ignoring saturation) the ratio  $\Gamma/\omega_R = 1.6$ . We therefore expect the recoil to be an important feature in low saturation narrow-line cooling. The use of a narrow transition allows

exploration of three drastically different cooling regimes with the same physical setup. Here we will follow the regime classification used in Ref. [71].

In cooling regime (I), we assume strong saturation ( $s \gg 1$ ) and a large detuning, such that  $\Delta \gg \Gamma_E \gg \Gamma$ . In this regime, atoms at a given position in the trap experience photon scattering for only one of the beams (along each axis) at the spatial positions which satisfy  $\Delta/2\pi = \vec{k} \cdot \vec{v} + \mu_0 dB_x x$ . The atoms can be thought of as trapped between hard wall boundaries, as opposed to the traditional dispersion shaped force curve in strong cooling. Here, gravity also plays an essential role as the trapped atoms can be expected to sag to vertical positions where the Zeeman shift balances  $\Delta$ . If the laser detuning is reduced below  $\Gamma_E$  (or if the the power broadened linewidth is made larger than the detuning), the cooling is described in regime (II) where  $\Delta < \Gamma_E \gg \Gamma$ . In this case the cooling is expected to behave as in a typical strong transition and the scattering force will provide a dispersion shaped feature. The effect of gravity is expected to be negligible as the scattering force, determined by  $\Gamma_E$  is large. The most exotic cooling regime studied is that of regime (III) where  $\Gamma_E = \Gamma \sim \omega_R$ . In this case the relevant energy scale is that of a single photon recoil. Consequently, quantum scattering, as opposed to the semi-classical scattering described by Eq. 2.1 govern trap dynamics [85].

Fig. 2.7 details the mechanical cooling dynamics in regime (I) for various detunings, with  $s=250$ . In panel (a) the scattering force is calculated as a function of position (assuming zero velocity for convenience) for the horizontal cooling axis at different detunings. Here we see that for large detunings, the atoms essentially see no scattering in the central trapping region. Instead they interact with a single beam at each end of the trap. Panel (b) shows the significance of gravity as the force (and potential energy) in the trap is altered in the vertical direction. The inclusion of the gravitational potential results in a potential minimum in the

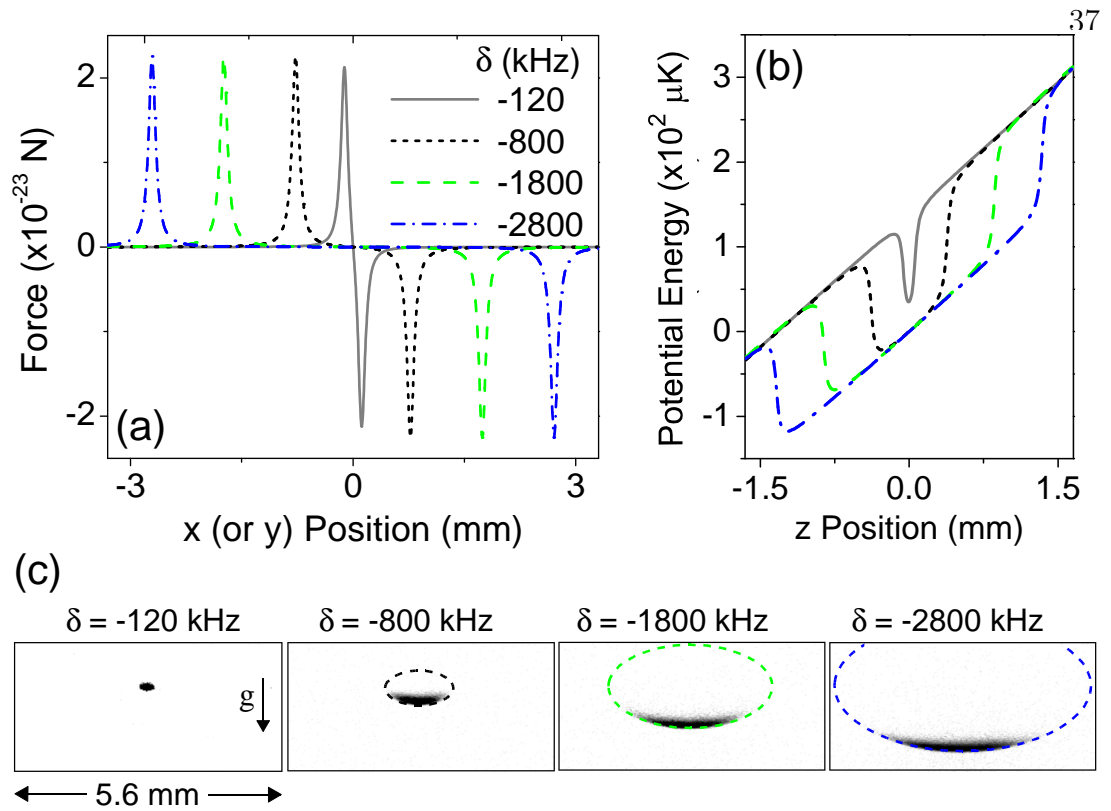


Figure 2.7: Red MOT detuning dynamics. (a) Scattering force is plotted for different detunings assuming  $s=248$ . For large detunings, the MOT beams operate independently as hard wall boundaries while for small detunings the force has a dispersion shape. The effect of gravity (b) is significant for this system as the gravitational potential alters the trapping potential such that the atoms are trapped in the potential created by only one of the vertical beams. (c) in situ MOT images showing the effect of gravity on the MOT dynamics. For large detuning, the atoms are located at the lower resonant boundary (dashed lines) determined by the field and laser detuning. In this case it is possible to operate the MOT (once loaded) without the downward propagating laser beam. As the detuning is reduced, the system begins to resemble a traditional MOT.

trap near the resonant position of the lower beam. Therefore the atoms will be localized at the lower bound of the trap. This effect is shown in panel (c) where in-situ images of the MOT are taken at various detunings. As seen in (a) and (c), when the detuning is decreased, the cooling begins to resemble that expected in regime (II).

A similar effect is seen in Fig. 2.8 where the intensity is varied over a wide

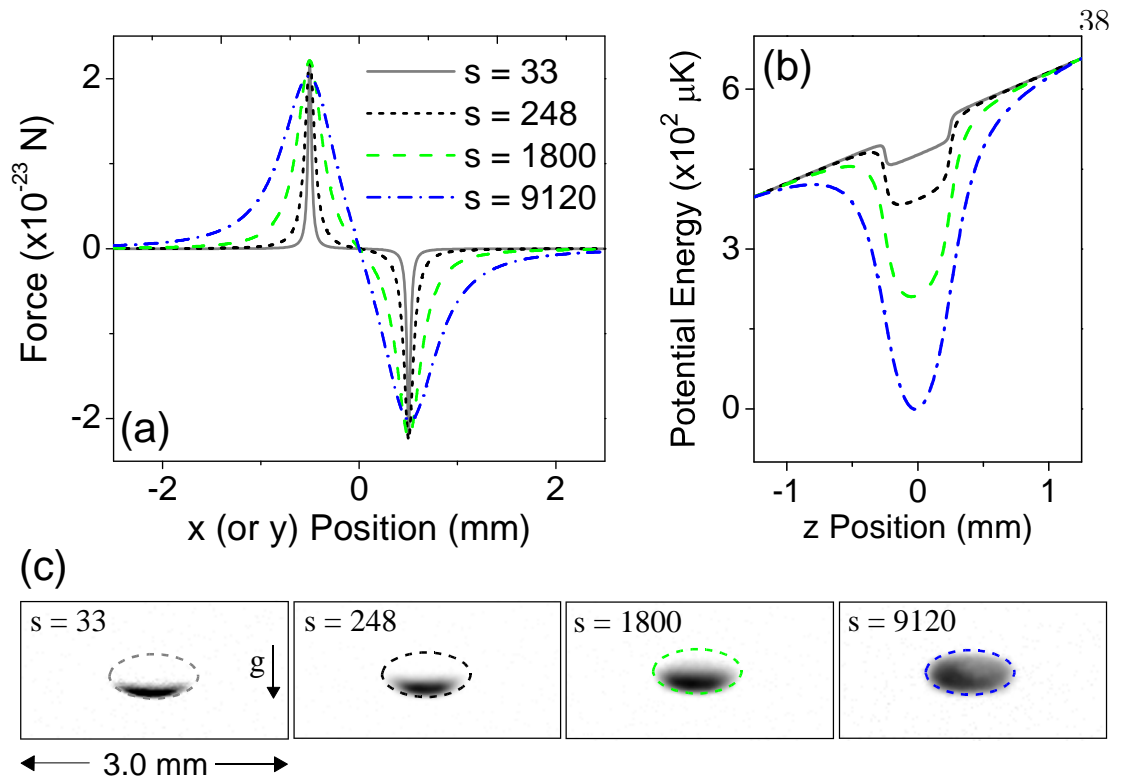


Figure 2.8: Red MOT intensity dynamics. (a) shows the position dependence of the light scattering force for different intensities with  $\delta = -520$  kHz. For low intensities we again see the single beam hard wall properties of the MOT, indicative of regime (I) discussed in the text. As the saturation parameter is increased, the cooling conditions evolve into the standard semiclassical cooling described by regime (II). The effect of gravity (b) on the potential energy is reduced as the beam intensity is increased. The transition from regime (I) to (II) is shown in the MOT images (c).

range with a fixed detuning of -520 kHz. For low saturation intensities, we are in regime (I) where gravity is important and the MOT provides a “box” trapping potential. As  $\Gamma_E$  is increased to large values compared to the detuning, the force and potential energy curves become similar to cooling on a standard transition. This is evident in the images in panel (c) which show the transition from regime (I) to regime (II) as the intensity is increased.

The effect of gravity in regime (I) is also seen in the atom temperature. For normal cooling, we expect a strong detuning dependence on the atom temperature.

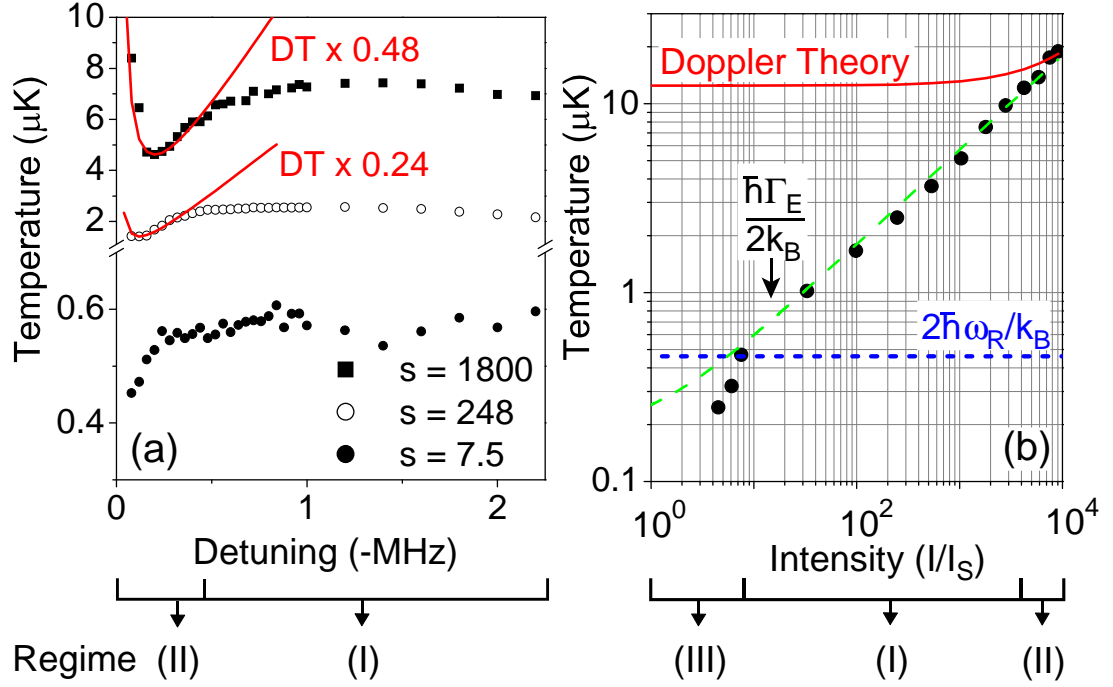


Figure 2.9: The dependence of the red MOT temperature on laser detuning and intensity. (Left) MOT temperature vs. detuning at different intensities. For large detunings, the temperature is independent of the detuning. This is because gravity keeps the atoms held against the upward going beam resonance, such that the photon scattering rate is constant. At small detunings, the temperature dependence on detuning is reminiscent of standard Doppler cooling, but with a lower absolute temperature scale. Note that for low saturation, the recoil temperature is reached. (Right) Temperature dependence on intensity for a fixed detuning of -520 kHz. For large intensities, the temperature is in agreement with Doppler theory. As the intensity is reduced, the regime (I) temperature dependence is lower than Doppler theory predicts at this detuning, and is instead determined by the traditional Doppler limit (green line). As the intensity is reduced below the saturation intensity, the cooling results in temperatures of half the recoil temperature

In narrow-line cooling regime (I) however, the detuning doesn't change the photon scattering rate, it only changes the position of the trap boundary. Therefore the temperature of the atoms is independent of detuning over a large range, as shown in Fig. 2.9 (left panel). This effect was first observed in [81] and has some important consequences as it allows manipulation of the MOT geometry independent of the atomic temperature. In this figure we show the dependence of

the atom temperature on detuning for different intensities. For small detuning, we are closer to regime (II) and the expected  $\delta$ - and  $s$ -dependent temperature minima are observed, although with values globally smaller than standard Doppler theory predictions. The standard recoil limit  $T_{Recoil}$  is achieved at the lower intensity. For large detuning on the other hand we see that the temperature is completely independent of detuning, and instead only depends on the saturation parameter, or more specifically  $\Gamma_E$ .

The right panel of Fig. 2.9 shows the intensity dependence of atom temperature for a fixed detuning of -520 kHz. For large intensities, the temperature agrees well with standard Doppler theory. As the intensity is decreased into region (I), the atom temperature deviates from the predicted value (for the given detuning) and follows the traditional Doppler limit of  $\hbar\Gamma_E/2k_B$ . Therefore we can conclude from these two plots that in region (I)  $\Gamma_E$  sets the limit on the temperature, independent of detuning. For the smallest intensities, we enter regime (III) where the recoil energy becomes important and quantum mechanical cooling is expected. Here we observe temperatures as low as 250(20) nK, in good agreement with the predicted half recoil limit in quantum cooling [85]. This sub-recoil cooling has recently been verified in Sr experiments in Florence [86].

## 2.4 $^{87}\text{Sr}$ Cooling Considerations

In the spectroscopic work presented in this thesis, we will report on experiments with cold  $^{87}\text{Sr}$  as it is the isotope with the narrow clock transition. The hyperfine structure, present in only the  $^{87}\text{Sr}$  isotope, results in some additional effects which must be taken into consideration for laser cooling.

Table 2.3: Relevant hyperfine parameters for the laser cooling and repumping states in  $^{87}\text{Sr}$ . <sup>a</sup> The  $g$  factor for the  $^1S_0$  and  $^3P_0$  states is determined by the nuclear  $g$ -factor,  $g_I$  (see Chapter 4) which results in a much smaller sensitivity of  $\sim 200 \text{ Hz/G} \times m_F$

State	$A(\text{MHz})$	$Q(\text{MHz})$	$F$	$g_F$
$^1S_0$	0	0	9/2	0 <sup>a</sup>
$^1P_1$	-3.4(4) [87]	39(4) [87]	7/2	-2/9
			9/2	4/99
			11/2	2/11
$^3P_0$	0	0	9/2	0 <sup>a</sup>
$^3P_1$	-260.084 [88]	-35.658 [88]	7/2	-1/3
			9/2	2/33
			11/2	3/11
$^3P_2$	-212.765 [89]	67.34 [89]	5/2	-6/7
			7/2	-1/7
			9/2	2/11
			11/2	51/143
			13/2	6/13
$^3S_1$	-542 [90]	-0.1(5) [90]	7/2	-4/9
			9/2	8/99
			11/2	4/11

### 2.4.1 Hyperfine Structure

The presence of nuclear spin ( $I$ ) provides additional structure to the states shown previously in Fig. 2.1, as each  $^{2S+1}L_J$  state will contain multiple levels denoted by quantum number  $F$  (with sublevels  $m_F$ ), where  $\vec{F} = \vec{I} + \vec{J}$ . For  $J$  smaller than  $I$ , as is the case for the relevant states here, the angular momentum coupling results in  $2J+1$  values for  $F$  in a given  $^{2S+1}L_J$  state. The hyperfine states are shifted in energy (from the assumed  $^{2S+1}L_J(I=0)$  state) by [63]

$$\Delta E_{HFS}/h = \frac{A}{2}K + \frac{Q}{2} \frac{\frac{3}{4}K(K+1) - I(I+1)J(J+1)}{I(2I-1)J(2J-1)} \quad (2.6)$$

where  $A$  and  $Q$  are the magnetic dipole and electric quadrupole (often written as  $B$ ) interaction constants, and  $K = (F(F+1) - I(I+1) - J(J+1))$ . Table 2.3 lists the interaction constants for the states relevant for laser cooling and repumping

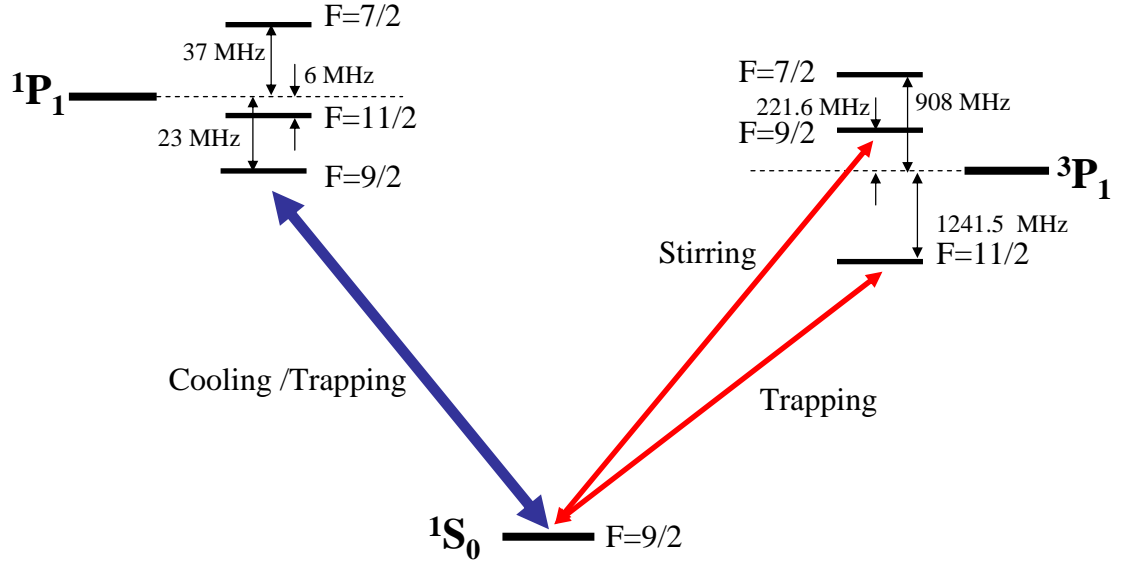


Figure 2.10: Hyperfine Structure of the laser cooling transitions used in this work. The two excited states are split into levels having  $F=7/2$ ,  $9/2$ , and  $11/2$ . The relevant frequencies are shown, along with the two color narrow-line cooling scheme discussed in the text.

in this work. Also shown are the  $g_F$  factors relevant for each state, where the Zeeman shift of the magnetic sublevels  $m_F$  is given by  $\delta\nu \simeq m_F g_F \mu_0 B$ . Here we assume the effect of the nuclear  $g$  factor is negligible, and the Bohr magneton is  $\mu_0 \simeq 1.4 \times 10^6$  Hz/G.

The resulting level structure for the  $1S_0$ ,  $1P_1$ , and  $3P_1$  cooling states is shown in Fig. 2.11. The effect of the hyperfine interaction on the ground state is negligible. Since  $J=0$ , only one energy level is present, which has  $F = 9/2$ . Due to the large nuclear spin, the ground state now consists of ten magnetic sublevels. The Zeeman sensitivity of these states is very small, determined only by the nuclear magnetic moment, yielding a shift sensitivity of  $\sim 200$  Hz/G  $\times m_F$ , which is orders of magnitude smaller than the sensitivity of the  $J = 1$  excited states (roughly given by the proton-electron mass ratio). The effect on the  $1P_1$  state is more pronounced. The state is split into three levels, having  $F=7/2$ ,  $9/2$ , and  $11/2$ , each state having  $2F+1$   $m_F$  sublevels. Since the  $A$  and  $Q$  coefficients



are small, the energy spacing between these levels is on the same order as the transition linewidth of 31 MHz. For cooling, one needs to use a transition with  $F_e = F_g + 1$ , so the  $F=11/2$  state is of interest to us. Note that due to the small hyperfine shift, any cooling on the  $F=11/2$  will undoubtedly result in some excitation to the  $F = 9/2$  state. In the  $^3P_1$  state the coupling constants are much larger, such that the three  $F$  levels are detuned from each other by hundreds of MHz. The large splitting and narrow linewidth of the transition ensure that these levels can be excited completely independently.

#### 2.4.2 Laser Cooling with $J_g = 0$ and $I \neq 0$

For alkali atoms, the hyperfine structure doesn't change the MOT action significantly, but for alkaline earth atoms the use of a  $J = 0$  ground state has a dramatic effect. To explore the difference, we will consider an example case of a MOT operating cooling transition between  $F=3/2$  and  $F=5/2$  states (we consider here a lower value of  $F$  than the real Sr case to reduce the complexity of Fig. 2.11).

In traditional alkali MOTs, the ground ( $g$ ) and excited ( $e$ ) states have similar  $g_F$  factors ( $g_e$  and  $g_g$ ), such that in the presence of a magnetic field, the resonant frequency for a given polarization is nearly independent of the ground state sublevel populated by the atom. This situation is shown in the first panel of Fig. 2.11. To design a 1D MOT using such a transition, we apply an inhomogeneous magnetic field of  $B = ax$  where  $a$  is a proportionality constant and  $x$  is the position from the center of the trap. Counter propagating laser beams, detuned below the atomic resonance frequency and having opposite helicity, then provide a restoring force for atoms leaving the trap as shown in Fig. 2.11(b). If atoms move in the  $-x$  direction, the magnetic field gets larger and more negative, such that eventually the  $\Delta m_F = +1$  transitions are resonant, and the atom absorbs photons from the  $\sigma^+$  beam and is pushed back towards the center of the

trap. Atoms moving away from the center in the  $+x$  direction will experience the same effect from the  $\sigma^-$  beam. Since the ground and excited state  $g$ -factors are similar (with the small difference resulting in the slightly different slopes in the plot), the restoring feature of the MOT is independent of the ground state  $m_F$  that the atom is in, and it acts in the same way as the traditional  $J = 0 - J = 1$  MOT without hyperfine structure.

In alkaline-earth MOTs, the ground state  $g$  factor is determined only by the nuclear spin, and hence is typically three orders of magnitude smaller than that of the excited state. As shown in Fig. 2.11 (a), this results in a strong  $m_F$ -dependence for the transition frequency in the presence of magnetic fields. In fact, in some cases the sign of the frequency shift even changes. If we draw the same MOT design as in the alkali case (lower left panel of the figure) we find that  $x$  position for absorption depends strongly on the ground state sublevel. To see how this can affect the MOT we consider the case in the lower right panel where an atom is in the  $m_F = +3/2$  ground state. This atom can only absorb a photon which moves it to the  $m_F = 5/2$  or  $m_F = 1/2$  states. Due to the small ground state  $g$  factor, the sign of the zeeman shift of these two transition options both have the same sign (compared to the alkali case where they always had opposite signs). This degrades the MOT action in two ways, first if we assume the atom is in the  $-x$  region, it is possible to absorb photons from either beam such that the atoms can be forced out of the MOT. However, the probability of absorption from the wrong beam is reduced if one considers Clebsch-Gordan coefficients (in Sr for the stretched state for example, the ratio is 55:1 for likelihood to be pushed in the MOT). So we see that the MOT does not operate purely on the position dependant resonance condition, but also requires help from the CG coefficients which are most preferential for trapping in the stretched states. The second effect we notice is that if the atom is in the  $m_F = +3/2$  state in the  $+x$  region, there is

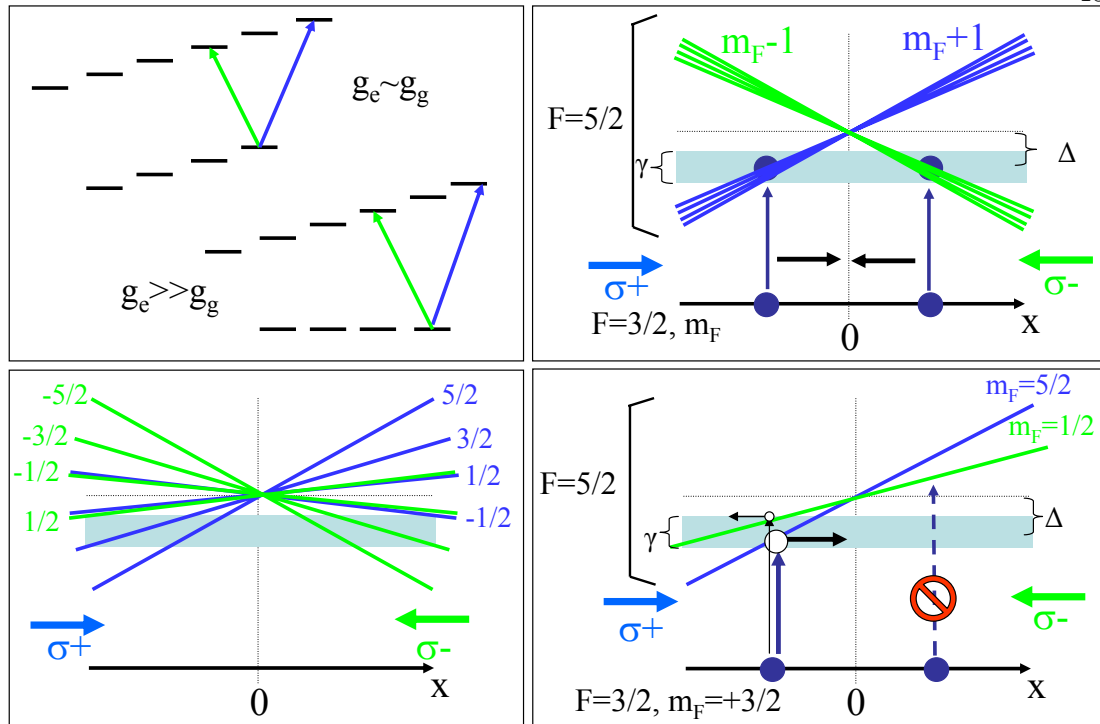


Figure 2.11: Comparison of MOT operation for a  $F = 3/2 - F = 5/2$  cooling transition with  $g_e \sim g_g$  and  $g_e \gg g_g$ . The upper right panel shows 1D MOT operation for a traditional cooling transition where the state  $g$  factors are similar, where  $\gamma$  is the transition width,  $\Delta$  is the detuning, and the magnetic field is  $B=ax$ . The green lines represent positions of the excited state sublevels which can be excited with  $\sigma^-$  radiation ( $\Delta m_F = -1$ ), while the blue lines give the positions of the sublevels which can be excited with  $\sigma^+$ . Since the  $g$ -factors are similar, the field dependence of the transition resonances are similar and the MOT action operates independently of the ground state sublevel. The condition  $g_e \gg g_g$  (lower left panel) shows a different feature as the slope (frequency/field) of the different resonances depend strongly on the ground state sub-level the atom is in, in some cases even changing sign. The lower right panel shows an example how this effects the MOT operation. An atom in the  $m_F=+3/2$  ground state can only make transitions to the excited  $+5/2$  and  $+1/2$  sublevels. Due to small ground state  $g$ -factor, both of these states have the sign of magnetic sensitivity such that they will both be resonant with the MOT beams in the  $-x$  region. Owing to a stronger Clebsch-Gordan coefficient for the  $\sigma^+$  transition, the atom is still pushed back towards the trap center. In the  $+x$  region however, there are no states resonant with the laser beam for the  $m_F=3/2$  state, so the atom is lost. State randomization from optical pumping eliminates this problem for strong transitions as the population is rapidly cycled between different states, some of which will satisfy the trapping condition. For the narrow transition discussed here, the optical pumping is in-efficient, and a second “stirring” laser is required.

no chance for resonant absorption, and the atom is free to leave the trap. So in this simple picture, we have the situation where the atom is well trapped if in the stretched state on one side, and not trapped at all on the other side of the trap.

In a more realistic case, for example a strong cooling transition, enough photons are scattered that we can expect fast randomization of the ground state population distribution. Thus the original stretched state atom can quickly be pumped to a different state, and the MOT trapping mechanism will still work well on both sides of the trap. In our narrow-line cooling on the other hand, the photon recoil shift is comparable to the transition width, so the atom only stays on resonance with the trapping beam for a few scattering events, and the population is not efficiently randomized.

This effect was first observed by the Tokyo group [91] as they found that the  $^{87}\text{Sr}$  red MOT lifetime was nearly ten times shorter than that of the red MOT  $^{88}\text{Sr}$ . To combat it, they employed a two color MOT on the intercombination line. Since the  $^1S_0(F = 9/2) - ^3P_1(F = 11/2)$  cooling is inefficient for optical pumping, one can apply additional light near the  $^1S_0(F = 9/2) - ^3P_1(F = 9/2)$  resonance. This state has a smaller  $g$ -factor than the  $F = 11/2$  state which allows the optical pumping to take place over a larger spatial area in the MOT, because the resonance position is less sensitive to the size of the field. While a  $\Delta F = 0$  transition does not provide any trapping, this additional laser does provide cooling and sufficient optical pumping to allow the  $^1S_0(F = 9/2) - ^3P_1(F = 11/2)$  MOT to operate more efficiently. Therefore the MOT can be operated using two colors, one trapping frequency near the  $F = 11/2$  line, and one “stirring” frequency.

Although we have not explored the  $^{87}\text{Sr}$  narrow-line cooling at the level of detail of the  $^{88}\text{Sr}$  results above, we have found that we can cool  $10^5$  atoms to as low as  $2 \mu\text{K}$  in agreement with the results of [91]. In our system the cooling cycle is only slightly changed when switching between isotopes. When cooling

the fermions, we find the MOT number is optimized when the timing sequence in Fig. 2.6 is altered such that the broad band, field ramp, and single frequency cooling times are extended to 60 ms, 100 ms, and 55 ms each. We also find that the initial and final red MOT gradient fields should be reduced to 1 G/cm and 3 G/cm respectively. The longer cooling times attest to the fact that the cooling is less efficient, and the lower optimum magnetic field is expected as it reduces the magnetic effect discussed here.

While the hyperfine structure does alter the cooling process for the intercombination line, it does not present a real road block to experiments with the isotope as the second 689 nm laser is only 1.5 GHz away from the trapping laser. This gap can be bridged with either an AOM or with a phase locked system as shown in Fig. 2.5. Furthermore, the slightly higher temperature here can be reduced by cooling on the narrow transition while holding the atoms in an optical lattice [91]. For the clock experiments in this work, the results are more than sufficient.

### 2.4.3 Repumping Revisited

Another effect that should be considered when cooling  $^{87}\text{Sr}$  is the efficiency of the repumping scheme. The hyperfine structure provides five  $F$  states in  $^3P_2$  and three in the  $^3S_1$  state such that we can expect the repumping process to pump a significant number of atoms into states which are not resonant with the repumping light. We estimate that more than 80% of the atoms which decay from  $^1P_1 \rightarrow ^1D_2 \rightarrow ^3P_2$  end up in the  $F = 13/2$  state. One can therefore tune the 707 nm laser to the  $^3P_2(F = 13/2) \rightarrow ^3S_1(F = 11/2)$  transition for pumping but inevitably some atoms will decay back to the lower  $F$  states of  $^3P_2$ . In practice we find that the blue MOT enhancement is at most factor of four in the  $^{87}\text{Sr}$  MOT when the re-pumpers are used, compared to a factor of 10 in the bosonic MOT.

To improve the repumping we employ the technique of the Paris group [41] where the repumping lasers are scanned during the Blue MOT. Since the  $^3P_2$  and  $^3S_1$   $F$  states are spread over a few GHz, the repumping lasers must be scanned over a significant range. This is performed by continuously scanning the ECDL laser current and cavity mirror PZT. The laser frequency is scanned over 5 GHz at a modulation frequency of  $\sim 5$  kHz. The PZT in the ECDL is scanned over 500 MHz at a frequency of 800 Hz. Although the lasers are not single mode over the entire scanning cycle, by scanning both the current and the PZT one can find parameters where the repumping is significantly more efficient than in the fixed-frequency case, resulting in enhancement factors as large as 20 in the atom number, and 10 in the trap lifetime. Furthermore the laser system is simplified as the lasers do not need to be locked to a cavity. For the results in this thesis, however, we used the cavity locking scheme as we had not yet implemented the scanning method.

#### 2.4.4 A Few Practical Notes

A few other details of interest were discovered in our  $^{87}\text{Sr}$  cooling experiments. To optimize the blue MOT number, it was necessary to offset the MOT position from the slowed atomic beam, suggesting collisions with the  $^{88}\text{Sr}$  atoms (comprising  $> 80\%$  of the slowed beam) can limit the  $^{87}\text{Sr}$  MOT. With the beam offset, we found that the transverse cooling and repumping gave more enhancement than in the  $^{88}\text{Sr}$  case where the atomic beam passed directly through the MOT. In the  $^{88}\text{Sr}$  experiments [71, 79] we found that the MOT number had a ceiling which was likely limited by collisions with the atomic beam, or possibly collisions between MOT atoms. So it is not surprising that the enhancement factors are larger in the  $^{87}\text{Sr}$  MOT (by a factor of 2 for repumping and a factor of 2-3 for the transverse cooling) which has more than an order of magnitude less atoms

and is offset from the beam. While the exact source of the MOT limitation needs further study, we point it out as an important detail to be considered in designing future  $^{87}\text{Sr}$  experiments.

Another practical issue to consider is the relatively small frequency difference between the strong cooling transitions in the  $^{88}\text{Sr}$  and  $^{87}\text{Sr}$  isotopes. Isotope selection in the blue MOT involves simply changing the spectrometer AOM frequency (and hence that of all the blue light) to account for the small isotopic shift of the strong cooling line. With the detuning for the  $^{87}\text{Sr}$  MOT trapping beams set to -40 MHz from the  $F=11/2$  line, the detuning for the  $^{88}\text{Sr}$  atoms is only -91.8 MHz, or  $\Delta/\Gamma \sim 3$ . Because of this, a significant amount of fluorescence is observed from the bosonic atoms passing through the MOT region, and we are likely to trap both isotopes in the MOT. Therefore care must be taken in experiments where a pure  $^{87}\text{Sr}$  sample is desired, or even in simple tasks like calibrating the number of atoms. In our experiments, the pre-cooled atoms pass through a pseudo-isotopic filter before any measurements are made. This is achieved naturally by second stage cooling on the  $^3P_1$  line where the isotope shift is orders of magnitude larger than the transition width and detuning. Note that we have verified that scanning the repump lasers does enhance the red MOT number so we can be sure that the blue MOT enhancement is not just a result of enhancing the  $^{88}\text{Sr}$  contributions to the MOT signal (although that could still be contributing).

## 2.5 On to Spectroscopy ... Almost

With ultracold atoms in hand, we are ready to move on to some high precision spectroscopy of the clock transition. In the remaining chapters the cold atoms go through one more step in the preparation stage discussed here, as they need to be loaded into an optical lattice trap. The design and operation of our trap is reserved for the next Chapter (Section 3.3.2). In brief, loading of the lattice

is done simultaneously with the entire cooling cycle, resulting in  $10^4$   $^{87}\text{Sr}$  atoms (or  $10^5$   $^{88}\text{Sr}$  atoms). The presence of the relatively shallow lattice trap ( $\sim 7 \mu\text{K}$  in this work) does not deteriorate the final atom temperature significantly as we typically measure it to be  $2 \mu\text{K}$ . With that said, we have our cold atomic ruler ready to measure those precision laser ticks, so lets get started!



## Chapter 3

### Clock Spectroscopy in an Optical Lattice

#### 3.0.1 Optical Frequency Measurements in Free Space

With samples of  $\mu\text{K}$  atoms in hand, we can begin the quest for a Sr optical frequency standard. In our earlier work [28], cold  $^{88}\text{Sr}$  was used for a high accuracy clock evaluation of the  $^1S_0$ - $^3P_1$  transition. In this experiment, a  $2\ \mu\text{K}$  atom cloud was probed in free space using light derived from the 689 nm master laser. The resulting absorption spectrum for the  $\sim 10^6$  atoms is shown in Fig. 3.1. Here we find that the observed transition width is limited to 45 kHz due to Doppler broadening which results from the gaussian velocity distribution of the atoms. In this study, it was found that atomic motion limited not only the achievable  $Q$ , but the accuracy as well. Doppler shifts of the resonant frequency,  $2\pi\delta\nu = \vec{k} \cdot \vec{v}$ , due to atomic motion relative to the propagation of the probe beam resulted in a number of systematic effects. During spectroscopy, the atoms are not trapped so gravity causes the atom cloud to fall. If the probe beam  $\vec{k}$  vector has a component along the axis of gravity, the measured frequency will be shifted. Therefore it is paramount that the probe beam is well collimated and aligned perpendicular to the axis of gravity. If spectroscopy with a single beam is performed, the measurement will also be sensitive to cloud drifts along the laser axis. In our experiment, it was found that the atom cloud drifts horizontally at about 1 mm/s due to the intensity imbalance of the MOT trapping beams. This small drift results in a

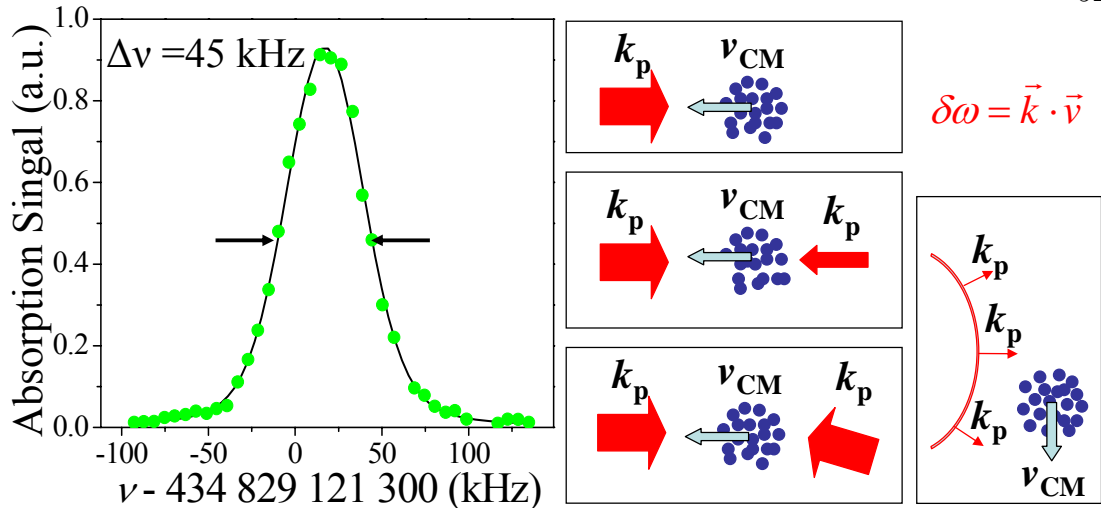


Figure 3.1: (left) Absorption spectrum for the  $^1S_0\text{-}^3P_1$  transition in free space. The line width (FWHM) is 45 kHz, limited by Doppler broadening. (right) The dangers of Doppler. Here a few ways that the Doppler shift can cause frequency errors are shown. If a single beam is used the inevitable motion of the atom cloud relative to the beam shifts the resonant frequency. Counter propagating beam configurations can reduce the sensitivity but one must be careful in considering the relative tilt angle between the two beams as well as the relative intensity. The curvature of the probe can also cause frequency shifts which will not be canceled by the counter-propagating beam configuration.

rather large shift of  $\delta\nu=1.5$  kHz. To eliminate this first order Doppler shift, and that of gravity, a counter-propagating probe set-up is used such that the average Doppler shift for the two beams is zero. However, to ensure that the Doppler shift is well canceled, the intensity of the two beams needs to be well calibrated, and the beams need to be co-aligned with high precision. While the use of counter propagating probes can reduce residual Doppler shifts, finite beam curvature can also cause a problem, as illustrated in Fig. 3.1. As the atoms fall, they sample the  $k$  vector of the lower part of the beams which can cause an offset of the same sign for both probe beams.

In the end, by carefully collimating the probe beams ( $R > 50$  m), controlling the beam angle relative to gravity ( $<1$  mRad), the mutual tilt angle of the two

probes ( $< 50 \mu\text{Rad}$ ), and the intensity imbalance ( $< 2.5 \%$ ), the Doppler limitations for spectroscopy were reduced to 26 Hz, allowing an absolute frequency measurement relative to the NIST Cs-fountain with a final accuracy of  $\sim 30$  Hz, or  $7 \times 10^{-14}$  [28].

Unfortunately the same effect that allows cooling and mechanical control of our atoms, the Doppler effect, results in a number of limitations on the clock performance in terms of both accuracy and stability. The line  $Q$ , for example, was limited by the Doppler broadening from motion of the atoms and by the interaction time constraint from free fall induced by gravity. While the resonance width could be further reduced by using Ramsey spectroscopy or saturation techniques, the Doppler shifts arising from MOT drift velocities and probe laser wavefront-curvature and misalignment are discouraging. These issues have been explored extensively in the Ca system [24, 25] and, with great care, can be controlled at the 1 Hz level. Since the laser cooling for Sr provides lower temperatures than those typically employed in the Ca clock and therefore Doppler systematics could eventually be reduced to a lower level. However, evaluation of these systematics will be more difficult since the Sr transition linewidth is more than ten times larger than in Ca. Even with the orders of magnitude improvement in line  $Q$  that the Ca and Sr measurements provide compared to the Cs clock transition, the Doppler sensitivity proves a difficult roadblock to reaching the accuracy of Cs fountains. To push the limits of neutral atom based optical standards it seems a different approach is needed.

### 3.0.2 $\vec{k} \cdot \vec{v} \dots$ Now What?

Trapped ion systems [29], on the other hand, have recently surpassed the accuracy and stability provided by the Cs fountains, a triumphant validation of this new business of optical clocks. Neutral atom folk can't help but peek over

the fence at the greener pastures of trapped ions, and wonder “*Do we really need all that  $\sqrt{N}$ ?*”. After all, the recent  $\text{Hg}^+$  results from NIST have shown that the huge line  $Q$  provided by optical clocks compensates for the lack of  $S/N$  since the stability of the single atom optical clocks now out performs that of their microwave counterparts which typically utilize  $\sim 10^5$  atoms.

The key feature of the ion clocks is the Lamb-Dicke [92] confinement provided by the trap itself. One obvious advantage provided by a trapped specimen is the long interrogation time which eliminates transit-time broadening issues. More important is the altered absorption spectrum of an atom in a harmonic potential. Free space atoms absorb light at a frequency  $\nu = \nu_c + \vec{k} \cdot \vec{v}/(2\pi) + \nu_R$ , with the last two terms resulting in Doppler broadening, and frequency offsets and uncertainties, including the photon recoil. In a deep Harmonic potential however, the absorption spectrum goes as  $\nu = \nu_c \pm \Delta n \Omega/(2\pi)$  where  $\Omega/(2\pi)$  is the trap oscillation frequency. The motional levels in the harmonic trap are represented by  $n$ . We’ll get to what exactly “deep” means below, the point is that the confining potential provides a textbook harmonic oscillator system where the possible energy of the atomic motion is quantized. Therefore atoms can only absorb light at frequencies where the above relation is satisfied for  $\Delta n = 0, \pm 1, \pm 2 \dots$ . The resulting absorption spectrum is one which is not broadened or shifted by the atomic motion, but instead the motion modulates the spectrum, resulting in a strong carrier ( $\Delta n = 0$ ) transition with small sidebands located at integer multiples of the trap frequency [93, 94, 95]. The problem of atomic motion is then transformed to one of line pulling from the motional sidebands which in most systems is negligible at the relevant level of accuracy.

So, do we have to give up our  $\sqrt{N}$  for the advantage of a recoil and Doppler free spectrum? No, like any good neighbor, we want that green motion-free grass in our yard, but as a complementary feature in our existing landscaping philos-

ophy. For neutral atoms the problem boils down to creating a deep harmonic potential without perturbing the clock states. For ensembles of neutral atoms, the traditional route for deep harmonic confinement is to hold the atoms in a standing wave pattern of laser light, known as an optical lattice. In these systems perturbation of the energies of the clock states is unavoidable as the trapping mechanism operates by providing a position dependant shift of the state energies. Although the dynamic polarizabilities (or equivalently the ac Stark shift) of the two clock states have a dramatically different form, we can take advantage of the fact that they each depend on the wavelength and polarization of the trapping light. The task is then reduced to the design of a trap at a “magic” wavelength (and appropriate polarization) such that the clock states experience identical perturbations and can be measured in a pseudo Stark-shift-free environment.

This wavelength tuning mechanism was first proposed as a way to increase the coherence time in cavity QED experiments by trapping atoms in a “Stark-Free” lattice to simulate ion systems [37], and also as a technique for efficient loading of dipole traps for laser cooling experiments [96]. The idea was then generalized to the field of optical clocks by Katori [39], specifically using Sr as a test case for the technique. The design and implementation of a Sr optical lattice clock is the main focus of this chapter. In section 3.1 the ac Stark shifts of the  $^1S_0$ ,  $^3P_0$ , and  $^3P_1$  states are examined in order to determine the cancelation wavelength and polarization sensitivity for the two Sr clock transitions. A detailed theoretical exploration into the spectroscopic features of trapped atoms is presented in section 3.2 as a further aid to optimizing the trap design. Finally, section 3.3 gives the details of our experimental setup and spectroscopic results including calibration of  $\lambda_m$ , measurement of motion effects in the trap, and the ultra-narrow Doppler and recoil free spectrum provided by the lattice confinement.

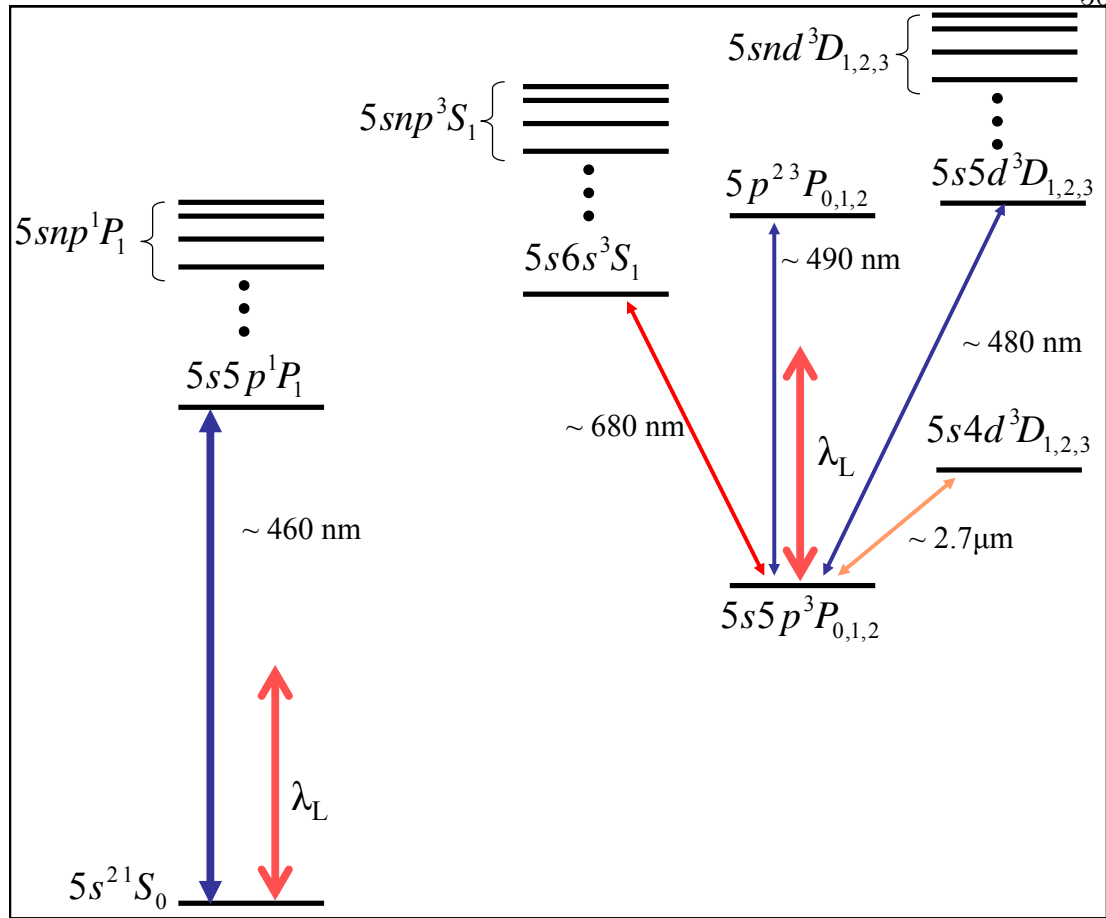


Figure 3.2: Level diagram of relevant states for the light shift. The Lattice light couples the ground state to the excited singlet state, with the largest effect coming from the first excited  $^1P_1$  state. The triplet clock states are coupled to the  $^3S$ ,  $^3D$ , and  $5p^2 3P$  states. The dominant interaction for the triplet states is given by the specific levels shown.

### 3.1 Stark Cancellation Technique

Strontium (and other alkaline earth(like) atoms such as Mg, Ca, Yb, and Hg) is a natural candidate for the lattice clock. The two-electron level structure (see Fig. 3.2) results in nearly independent series of singlet and triplet states such that the Stark shift of the clock states can be tuned semi-independently. Consider first the ground state  $5s^2 1S_0$  which, ignoring weak intercombination transitions, is coupled only to excited  $5snp 1P$  states by the lattice. For all lattice wavelengths

longer than 461nm (the lowest lying excited state transition wavelength), we have the situation of a red-detuned trap, in which the ac Stark shift will always be negative and the atoms will be trapped at the anti-nodes of the standing wave. The upper clock state,  $5s5p^3P_{1,0}$ , is markedly different as three series of triplet states are coupled by the trapping laser, specifically the  $5sns^3S$  and  $5snd^3D$  series, and the  $5p^2^3P$  states. The Stark shift for the  $S$  and  $P$  state contributions will be negative for all wavelengths above 700 nm. However, the low lying  $5s4d^3D$  state will contribute a positive shift for wavelengths below 2600 nm. In the wavelength range 700-2600 nm there must be a sign change in the polarizability and Stark shift of the  $5s5p^3P$  state while the  $5s^2^1S_0$  polarizability changes very little of the same range. Since we can tune the magnitude and sign of the  $^3P$  shift independently from that of the  $^1S_0$  state and rely on nearby resonances in the  $^3P$  polarizability for the needed amplitude swings we are all but guaranteed the existence of a magic crossing point. For the lattice confined neutral atoms to be a practical clock scheme, we would like it to satisfy a few key criteria at a trap depth  $U_T=U_0$ :

1.  $\lambda_m$  is a practical wavelength, and the required frequency stability on the laser is reasonable.
2. One can perform spectroscopy in the Lamb-Dicke limit ( $\nu_{Trap} > \nu_{Recoil}$ ) and in the resolved sideband limit ( $\nu_{Trap} > \gamma_{Clock}$ ).
3. One can efficiently load atoms into the lattice ( $U_0 > k_B T$ )
4. Negligible scattering rate for lattice photons at  $\lambda_m$  and  $U_0$ .
5. Negligible polarization dependence of the polarizability at  $\lambda_m$  and  $U_0$
6. Negligible quadratic Stark shift at  $\lambda_m$  and  $U_0$ .

The only way to sort out the practical trap design issues is to directly calculate the ac Stark shift and magic wavelength for our lattice configuration. So let's get to it!

### 3.1.1 One-Dimensional Lattice Potential

The Stark shift,  $\Delta\nu$ , of an energy level  $i$  in the presence of an electric field with amplitude  $\mathbf{E}$  is given by [97]

$$h\Delta\nu = -\frac{1}{2}\alpha_i|\mathbf{E}|^2 \quad (3.1)$$

where  $\alpha_i$  is the polarizability of the atomic state  $i$ . For a 1D optical lattice geometry the potential is described by a longitudinal standing wave with a gaussian distribution in the radial dimension, given by [98]

$$U(r, z) = 4U_m e^{-\frac{2r^2}{w(z)^2}} \cos^2(2\pi z/\lambda_L). \quad (3.2)$$

Here  $U_m = P\alpha_i/(\pi c\epsilon_0 w(z)^2)$  where  $P$  is the average laser power of the incoming beam,  $w(z)$  is the beam waist at a longitudinal distance  $z$  from the focus of the beam,  $r$  is the radial distance from the beam center, and  $\lambda_L$  is the laser wavelength. The potential can be approximated by a harmonic trap in both the longitudinal and radial dimensions yielding vibrational frequencies at the trap waist ( $z \approx r \approx 0$ )

$$\begin{aligned} \nu_r &= \frac{1}{2\pi} \sqrt{\frac{1}{M} \left( \frac{\delta^2 U(r, z)}{\delta r^2} \right)_{r, z=0}} = \frac{1}{2\pi w_0^2} \sqrt{\frac{16\alpha_i P}{c\epsilon_0 M \pi}} \\ \nu_z &= \frac{1}{2\pi} \sqrt{\frac{1}{M} \left( \frac{\delta^2 U(r, z)}{\delta z^2} \right)_{r, z=0}} = \frac{1}{2\pi w_0 \lambda} \sqrt{\frac{32\pi\alpha_i P}{c\epsilon_0 M}}. \end{aligned} \quad (3.3)$$

Unfortunately describing the trap dynamics in terms of intensity and beam waist carries some ambiguity as often in the literature terms such as 'peak' and 'average' intensity are used loosely, and similarly for the waist. So we would prefer to characterize the trap by less ambiguous parameters. From equations 3.2 and 3.3 we can also write the trap depth  $U_T$  in terms of the longitudinal trap frequency

$$U_T = \nu_z^2 \frac{M^2 \lambda_L^4}{h^2} E_R \quad (3.4)$$



where  $E_R = \hbar^2/(2M\lambda_L^2)$  is the recoil energy associated with the lattice photon. Writing the potential in this way is natural as the longitudinal trap frequency can be measured unambiguously and all other parameters in Eq. 3.4 are well defined. Note also that the ratio of the trap frequencies,

$$\frac{\nu_z}{\nu_r} = \frac{\sqrt{2\pi}w_0}{\lambda_L}, \quad (3.5)$$

yields information about the waist without knowledge of  $P$  or  $\alpha_i$ . This can be very useful for checking for example, polarizability calculations or the position of the atoms relative to minimum waist of the lattice.

### 3.1.2 Calculation of the ac Polarizability

For a complete description of the trap properties, the remaining issue is to evaluate the polarizability of the clock states. In the presence of a laser field of frequency  $\omega_L$ , the dynamic dipole polarizability of a state  $i$  involves the sum over the dipole interaction between state  $i$  and excited states  $k$  given as [99]

$$\alpha_i(\omega_L) = 2e^2 \sum_k \frac{\hbar\omega_{ik} |\langle \phi_k | \mathfrak{D} | \phi_i \rangle|^2}{\hbar^2(\omega_{ik}^2 - \omega_L^2)}. \quad (3.6)$$

Here,  $e$  is the electron charge,  $\hbar\omega_{ik}$  is energy difference between states  $i$  and  $k$ , and  $\hbar\omega_L$  is the energy of the lattice photon. The dipole matrix element  $|\langle \phi_k | \mathfrak{D} | \phi_i \rangle|^2$  can be written in terms of transition rates  $A_{ik}$  using the fact that

$$A_{ik} = \frac{e^2}{4\pi\epsilon_0} \frac{4\omega_{ik}^3}{3\hbar c^3} |\langle \phi_k | \mathfrak{D} | \phi_i \rangle|^2. \quad (3.7)$$

Combination of equations 3.6 and 3.7 yields

$$\alpha_i(\omega_L) = 6\pi\epsilon_0 c^3 \sum_k \frac{A_{ik}}{\omega_{ik}^2(\omega_{ik}^2 - \omega_L^2)} \quad (3.8)$$

which depends only on the lattice frequency, the transition rates between states  $i$  and  $k$ , and their corresponding energy difference  $\hbar\omega_{ik}$ . One then needs only the

measured  $A_{ik}$  values and state energies to perform the calculation. Typically, the literature reports the total transition rate  $A_T$  from a given excited state to the fine structure manifold below, or equivalently as a lifetime of the excited state  $1/A_T$ . In either case, one must be careful in consideration of what branching ratio of the interaction corresponds to the single state of interest. One also needs to take into account the polarization dependence of the coupling strength. For a given excited state with quantum numbers  $S$ ,  $L_k$ ,  $J_k$ , and a lifetime  $1/A_T$ , we find that the fraction of the interaction  $\widetilde{A}_{ik}/A_T$ , for a state with quantum numbers  $S$ ,  $L_i$ ,  $J_i$ , is given by

$$\frac{\widetilde{A}_{ik}}{A_T} = \frac{(2J_i + 1) \left\{ \begin{matrix} J_i & J_k & 1 \\ L_k & L_i & S \end{matrix} \right\}^2}{\sum_{J=|L_i-S|}^{|L_i+S|} (2J + 1) \left\{ \begin{matrix} J & J_k & 1 \\ L_k & L_i & S \end{matrix} \right\}^2} \sum_{m_k=-J_k}^{J_k} (2J_k + 1) \left( \begin{matrix} J_i & 1 & J_k \\ m_i & p & -m_k \end{matrix} \right)^2 \quad (3.9)$$

Here the matrices with curly brackets are the Racah 6- $j$  symbols and the matrices with parenthesis are the Wigner 3- $j$  symbols. The first term in Eq. 3.9 gives the fraction of the coupling strength between the excited state and a given lower state. For example, in the case of the  $5s5p$  triplet states, the ratio term gives the interaction strength for a single fine structure level (say  ${}^3P_0$ ), divided by the sum of the interaction for all of the fine structure levels ( ${}^3P_0$ ,  ${}^3P_1$ , and  ${}^3P_2$ ). The second term differentiates between magnetic sublevels  $m_i$  of the ground state, as the interaction is summed over the excited state magnetic levels for a given light polarization  $p$ . Since the total transition rate, or lifetime of the excited state is usually the available quantity in the literature, this total geometric ratio tells us how to scale the interaction for a particular state of interest. Table 3.1 gives the result of Eq. 3.9 for the states of interest, specifically the geometric scaling for the  ${}^1S_0$ ,  ${}^3P_0$ , and  ${}^3P_1(m = \pm 1, 0)$  clock states interaction with the excited  ${}^1P_1$ ,  ${}^3S_1$ ,  ${}^3D_{1,2}$ , and  $5s^2{}^3P_{0,1,2}$  states for linear ( $p = 0$ ) and circular ( $p = \pm 1$ ) polarization. The individual contributions from single states are given, as well as the sum of the contributions from the entire fine-structure manifold, with the latter allowing

Table 3.1: Geometric Scaling Factors ( $\widetilde{A}_{ik}/A_T$ ) For Different States and Polarizations

Ground State and Pol.	Excited State								
	$^1P_1$	$^3S_1$	$\sum ^3P$	$^3P_0$	$^3P_1$	$^3P_2$	$\sum ^3D$	$^3D_1$	$^3D_2$
$^1S_0(m = 0; p = 0, \pm 1)$	1	–	–	–	–	–	–	–	–
$^3P_0(m = 0; p = 0, \pm 1)$	–	1/9	1/3	–	1/3	–	5/9	5/9	–
$^3P_1(m = 0; p = 0)$	–	–	1/2	1/3	–	1/6	1/2	–	1/2
$^3P_1(m = 0; p = \pm 1)$	–	1/6	1/4	–	1/8	1/8	7/12	5/24	3/8
$^3P_1(m = \pm 1; p = 0)$	–	1/6	1/4	–	1/8	1/8	7/12	5/24	3/8
$^3P_1(m = \pm 1; p = \mp 1)$	–	1/6	1/2	1/3	1/8	1/24	1/3	5/24	1/8
$^3P_1(m = \pm 1; p = \pm 1)$	–	–	1/4	–	–	1/4	3/4	–	3/4

simplification of the calculation when the fine-structure energy splitting is ignored. The dashes in the table signify that for the given states and polarization, electric dipole interaction is forbidden (naturally taken into account by the 3- $j$  symbol).

The geometric scaling factors do not include the fact that the  $5s5p$  states are non-degenerate due to the fine structure splitting. In principle, the ratio term in Eq. 3.9 should have been modified to include the energy (actually coming in as  $\hbar\omega^3$ ) of each lower levels resulting in a small departure of the purely geometric value at the few percent level. The size of this correction depends on the relative size of the energy difference between the upper and lower state, and the fine structure splitting in the  $5s5p$  states. The final value of  $A_{ik}$  needed to evaluate the polarizability is then given by total transition rate  $A_T$ , the geometric scaling factors  $\widetilde{A}_{ik}/A_T$  in Table 3.1, and a small energy dependent correction  $\zeta(\omega_{ik})$  given as

$$A_{ik} = \zeta(\omega_{ik}) \frac{\widetilde{A}_{ik}}{A_T} \times A_T. \quad (3.10)$$

Values for  $\zeta(\omega_{ik})$  are tabulated in Table 3.2 for both the  $^3P_0$  and  $^3P_1$  clock states, for different excited triplet states.

To calculate the wavelength dependent polarizability, we then simply combine Eq. 3.10 with Eq. 3.8, and are left with the task of finding energies and

Table 3.2: Relevant Transition Rates, Frequencies, and Correction Factors for the  $5s^2\ ^1S_0$ ,  $5s5p\ ^3P_0$  and  $5s5p\ ^3P_1$  States

	$5s^2\ ^1S_0$	$5s5p\ ^3P_0$		$5s5p\ ^3P_1$		
Upper State	$\omega_{ik}$ ( $2\pi \times THz$ )	$\omega_{ik}$ ( $2\pi \times THz$ )	$\zeta$	$\omega_{ik}$ ( $2\pi \times THz$ )	$\zeta$	$A_T$ ( $\times 10^6\ s^{-1}$ )
$5s6s\ ^3S_1$	—	2.77	1.071	2.74	1.043	$85^b$
$5s7s\ ^3S_1$	—	4.36	1.045	4.32	1.027	$17.5^a$
$5s8s\ ^3S_1$	—	4.98	1.039	4.95	1.024	$8.22^a$
$5s9s\ ^3S_1$	—	5.30	1.036	5.27	1.022	$4.52^a$
$5s10s\ ^3S_1$	—	5.49	1.035	5.45	1.021	$2.77^a$
$5p^2\ ^3P_0$	—	—	—	3.90	1.000	$127^c$
$5p^2\ ^3P_1$	—	3.97	1.036	3.94	1.017	$127^c$
$5p^2\ ^3P_2$	—	—	—	3.99	1.043	$127^c$
$5s4d\ ^3D_1$	—	0.724	1.053	0.689	0.9489	$0.345^d$
$5s4d\ ^3D_2$	—	—	—	0.700	1.077	$0.345^d$
$5s5d\ ^3D_1$	—	3.90	1.010	3.86	0.9909	$61^c$
$5s5d\ ^3D_2$	—	—	—	3.87	1.014	$61^c$
$5s6d\ ^3D_1$	—	4.78	1.008	4.75	0.9926	$26.7^a$
$5s6d\ ^3D_2$	—	—	—	4.75	1.012	$26.7^a$
$5s7d\ ^3D_1$	—	5.19	1.008	5.16	0.9932	$14.2^a$
$5s7d\ ^3D_2$	—	—	—	5.16	1.011	$14.2^a$
$5s8d\ ^3D_1$	—	5.42	1.007	5.38	0.9935	$8.5^a$
$5s8d\ ^3D_2$	—	—	—	5.38	1.010	$8.5^a$
$5s9d\ ^3D_1$	—	5.56	1.007	5.52	0.9937	$5.5^a$
$5s9d\ ^3D_2$	—	—	—	5.52	1.010	$5.5^a$
$5s5p\ ^1P_1$	4.09	—	—	—	—	$190.5^e$
$5s6p\ ^1P_1$	6.43	—	—	—	—	$1.86^f$
$5s7p\ ^1P_1$	7.33	—	—	—	—	$3.19^a$
$4d5p\ ^1P_1$	7.76	—	—	—	—	$12^a$
$5s8p\ ^1P_1$	7.76	—	—	—	—	$14.9^a$
$5s9p\ ^1P_1$	8.00	—	—	—	—	$11.6^a$
$5s10p\ ^1P_1$	8.16	—	—	—	—	$7.6^a$
$5s11p\ ^1P_1$	8.28	—	—	—	—	$4.88^a$

<sup>a</sup> [100] <sup>b</sup> [36] <sup>c</sup> [101] <sup>d</sup> [102] <sup>e</sup> [103] <sup>f</sup> [104]

lifetimes (or transition rates) from the literature. Since it is difficult to find data for higher  $n$  states, we truncate the sum at about  $n=10$ . This should be a good approximation for the polarizability since the contribution of the excited states drops off as  $1/(\omega_{ik}^2(\omega_{ik}^2 - \omega_L^2))$ . However, we should note that we are then ignoring

the effect of the continuum states which can have a significant contribution to the static polarizability ( $\omega_L \rightarrow 0$ ). Frequency differences  $\omega_{ik}$ , derived from [105], are given in table 3.2 in units of  $2\pi \times 10^{15}$  Hz, along with the relevant transition rates  $A_T$  in units of  $10^6 \text{ s}^{-1}$ .

Many of  $A_T$  values have been calculated by Greene [100] and are used here. For the lowest lying excited states, which have the most significant effect on the polarizability at optical frequencies, experimental data is used when available. Preference is given to data in which direct lifetime measurements are reported, as opposed to ratios of oscillator strengths or line strengths, to avoid ambiguity in convention and notation. For the  $^1S_0$  calculation, recent photoassociation data [103] provides an accurate determination of the lifetime of the first  $^1P_1$  state which dominates the ground state polarizability. For the  $^3P_0$  and  $^3P_1$  states, accurate and direct lifetime measurements are available for the  $5p^2\ ^3P$  [101],  $5s4d\ ^3D$  [102], and  $5s5d\ ^3D$  [101] states. The lowest lying  $^3S_1$  state which provides a significant portion of the total light shift for the triplet states is more of a problem, as a number of measurements (summarized in [100]) based on relative oscillator strengths or lifetimes are in disagreement. Recent light shift measurements by Ido [36] on the  $^3P_1$  state seem the most reliable, providing the value  $A_T=8.5 \times 10^7 \text{ s}^{-1}$ .

With the completion of Tables 3.1 and 3.2 we can now calculate the polarizability for the different clock states. The polarizability for  $^1S_0$  and  $^3P_0$  is plotted as a function of wavelength in Fig. 3.3. The result is given in atomic units, for wavelengths between 200 nm and 5  $\mu\text{m}$ . The most interesting region for this work is that of the 700-1000 nm range where the  $^3P_0$  polarizability gently crosses that of the  $^1S_0$  curve. This is exactly the kind of feature we were looking for in the polarizability, as the crossing (or *magic*) wavelength occurs in an area accessible by commercial lasers, and is far enough away from any resonance features that the clock sensitivity to deviations from the magic wavelength should be small.

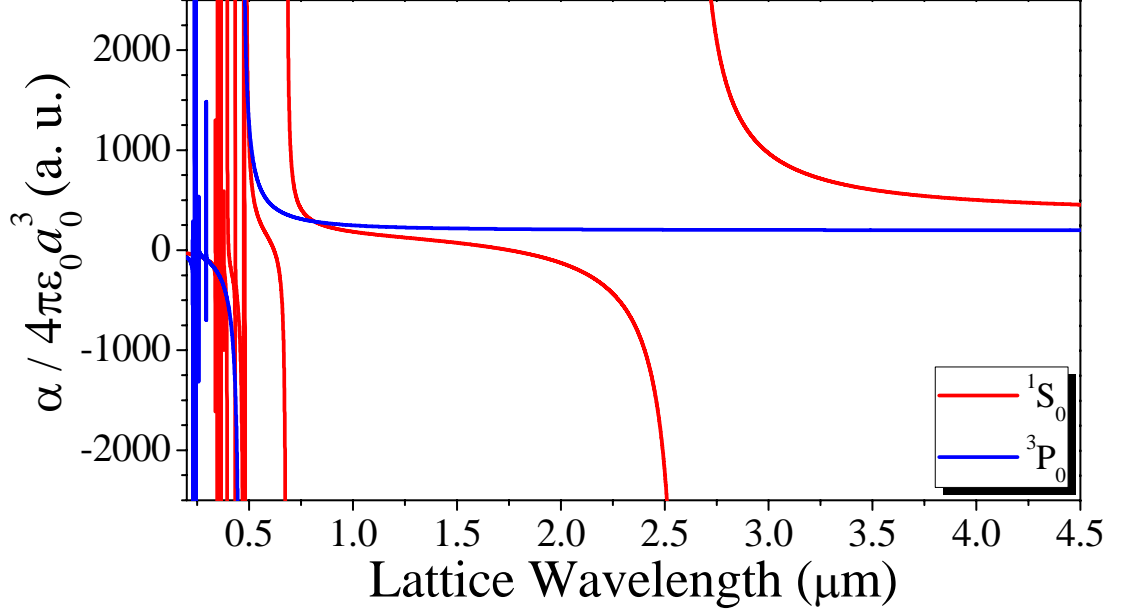


Figure 3.3: Wavelength dependence of the atomic polarizability. The polarizability is calculated for the  $^1S_0$  (blue) and  $^3P_0$  (red) states using the data in Tables 3.2 and 3.1. The result is scaled by a factor of  $1/(4\pi\epsilon_0 a_0^3)$  so that the polarizability is given in atomic units.

Since we have the polarizability, we can now look at the magnitude of the ac Stark shift for a given laser intensity. For convenience, we will do all of our calculations at the approximate parameters we use in the experimental sections of this work. For a laser power of  $P=150$  mW, which is focused to a waist of  $w_0=65$   $\mu\text{m}$  and retro-reflected for a lattice configuration, the Stark shift  $U$  is given from Eq. 3.2. Figure 3.4 gives the wavelength dependence of the resulting Stark shift in kHz for the clock states of interest in this work. The data is plotted for different  $m_J$  values and different lattice polarizations. In the calculation thus far, we have not included any hyperfine structure, so the  $^1S_0$  and  $^3P_0$  states only have an  $m_J = 0$  state and  $^3P_1$  has  $m_J = 0, \pm 1$ . Inclusion of the hyperfine structure is discussed in the next chapter (Section 4.3).

For the  $^3P_0$  and  $^1S_0$  we find again that there is a magic crossing point around 800 nm which is of interest for our lattice clock. Since both clock states

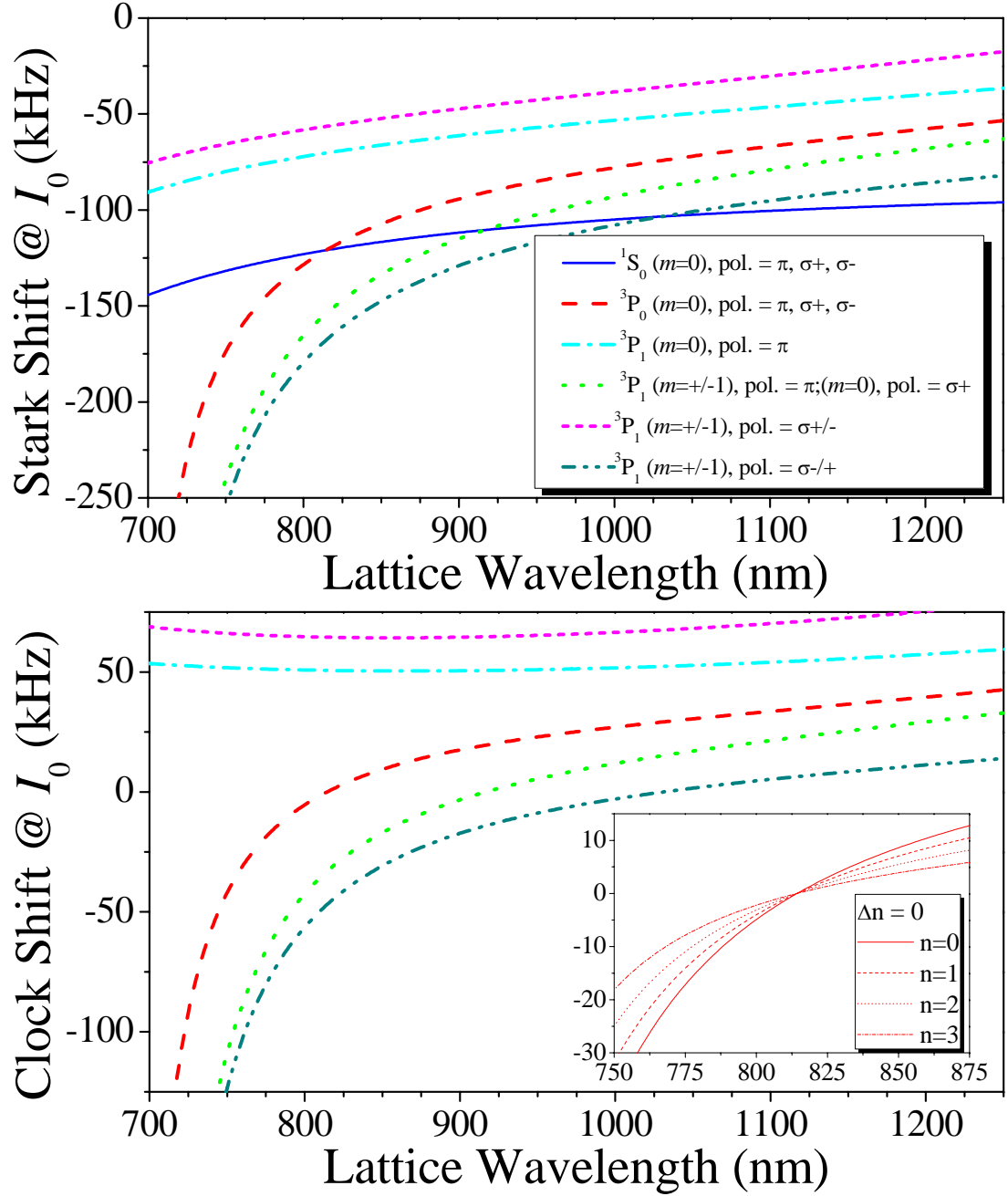


Figure 3.4: Wavelength and dependent ac Stark shift for the  $^1S_0$ ,  $^3P_0$ ,  $^3P_1(m=0)$ , and  $^3P_1(m=\pm 1)$  states for different lattice polarizations. The top panel give the shift for a lattice with input power  $P=150$  mW focused to a waist of  $65 \mu\text{m}$ . The second panel gives the differential shift for the triplet states relative to the ground state. The key in the upper panel applies to both graphs. The inset gives the clock shift for carrier ( $\Delta n = 0$ ) transitions originating from different harmonic oscillator states is discussed in the text.

are  $J=0$ , we find no polarization dependence on the Stark shift. This is in strong contrast to the  ${}^3P_1$  case. We find for example that the  $m_J$ -dependence in  ${}^3P_1$  is so strong, that in the case of  $\pi$ -polarized trapping light the  $m_J=\pm 1$  states have a magic wavelength crossing in the wavelength region shown and the  $m_J=0$  state does not. This strong dependence of the shift on  $|m_J|$  is due to the tensor component of the light shift, which provides a  $m_J^2$ -dependent effect. From the figure, we can see that for the  ${}^3P_1$  state the tensor shift is on the same order of magnitude as the scalar ( $m_J$ -independent) component. The  ${}^3P_1$  state also has a significant vector ( $m_J$ -dependent) light shift in the case of circular polarization as can be seen in the figure. A detailed discussion of tensor and vector light shifts is given in Section 4.3 when we introduce nuclear spin to the problem. For now we simply note that although a magic crossing does exist for the  ${}^3P_1$  state if the appropriate  $m_J$  and polarization are used, the large size of the tensor and vector light shifts make this case undesirable for the ultimate clock because of the significant sensitivity to light polarization. From this point on in this work we will thus be pursuing the  ${}^3P_0$  clock state which shows no vector or tensor light shift of electronic-spin origin. We will see later that the nuclear spin does result in some state dependent shifts, however these effects are orders of magnitude smaller than those affecting the  ${}^3P_1$  state.

### 3.1.3 Magic Wavelength: Calculation

The crossings points of the polarizability are of the most interest for this work. Figure 3.5 shows the Stark-free crossing points of the two most relevant lattice clock possibilities. The left panel shows that the crossing of  ${}^1S_0$  and  ${}^3P_0$  takes place at just below 815 nm, while the second panel shows the crossing of the  ${}^1S_0$  and  ${}^3P_1(m_J = \pm 1)$  states for linear polarization near 917 nm. Both of these results are in excellent agreement with the experimental values of 813.428(1) nm



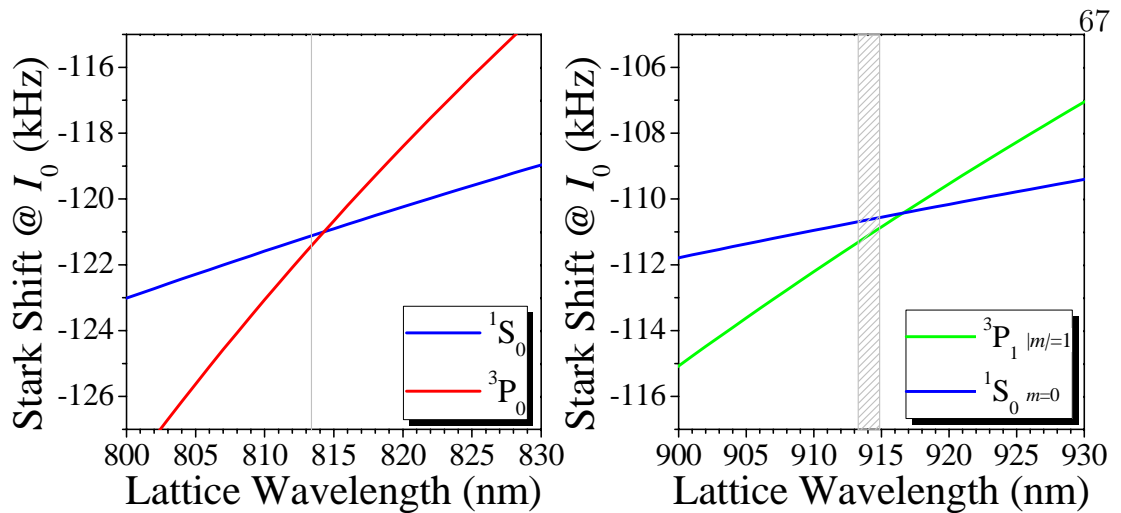


Figure 3.5: Calculation of the Stark shift crossing points for laser power of 150 mW and a waist of  $65 \mu\text{m}$ . The left panel gives the shift of the  $^3P_0$  and  $^1S_0$  state, while the right panel gives result for the  $^3P_1(m = \pm 1)$  state with linear polarization. In each case the experimental value is shown as a grey bar with the width representing the experimental uncertainty. Changing the  $A_T$  value for the first  $^3S_1$  state by 0.5% to  $84.6 \times 10^6 \text{ s}^{-1}$  changes the calculated magic wavelengths to 813.4 and 914.7 nm, falling within the experimental errors shown

[58, 44, 41, 42] and 914(1) nm [36] suggesting that the polarizability calculation is fairly accurate.

In principle one can use the measured magic wavelengths to try and back out more accurate lifetimes of the excited states. This is in fact how the  $^3S_1$   $A$ -coefficient was estimated in Ref. [36]. Since we have two measured magic wavelengths now we could push that method further and try and fit both the  $^3S$  and another lifetime (say the  $5s4d^3D$  state) to the experimental data. However, we can see this method could be problematic because in our calculation we find that using the  $A$ -coefficient from [36] does not exactly yield the correct magic wavelength. The likely reason for this is the use of slightly different oscillator strengths in the polarizability calculation, as well as the inclusion of the fine structure splitting correction factor in our code.

Before we try and tweak any state lifetimes we can first learn which ones

are more important by looking at the relative contributions that the first few levels have to the total light shift. Table 3.3 gives this data for the  $^1S_0$ ,  $^3P_0$ , and  $^3P_1(m = \pm 1)$  states at the relevant magic wavelengths as well as at  $10 \mu\text{m}$ , which is where the black-body radiation (BBR) spectrum is centered for  $T=300$  K. From the table we can see for the clock states that one state is dominant at the magic wavelength,  $^1P_1$  for the ground state and  $^3S_1$  for the triplet clock states. We therefore expect the magic crossing point to be most sensitive to these two values. Another interesting thing to note is that the first  $^3D$  state provides a significant portion of the light shift in the BBR regime, suggesting that it will be important for future experiments to accurately measure the lifetime of that state. Ideally one would like to constrain the  $^3D$  lifetime by the magic wavelength measurements. For example, since the  $^1P_1$  state lifetime is known with high accuracy, one can let the  $^3S$  and  $^3D$  lifetimes be free parameters in the polarizability calculation and solve for the result that predicts both magic wavelengths within the measured uncertainties. The problem with this tactic is that near the magic wavelength, the  $^3D$  contribution is fairly small (in fact it is not even in the top three for shifts) so tweaking that parameter to induce a small polarizability change at the trapping wavelength will likely not be effective in reducing the uncertainty of the  $^3D$  lifetime unless the lifetimes of the more dominant states are known with higher precision. Furthermore, that small tweak will have a large effect on the BBR Stark shift value, so you can see we are heading down a dangerous road.

Since our calculation here is so close to both experimental values, we have tried to improve the agreement by just changing the  $A$  value for  $^3S_1$  since that was the one value which was not based on lifetime measurements. We find that for  $A_T=84.6 \times 10^6 \text{ s}^{-1}$ , for example, we get magic wavelengths of 813.4 nm and 914.7 nm which are in perfect agreement with the experimental data. So how do we interpret this value? The one thing our calculation did not include is

Table 3.3: Fractional Light shift for the  $^1S_0$ ,  $^3P_0$  and  $^3P_1(m = \pm 1)$  states at the relevant wavelengths. Value represent the size of the light shift from the excited state in question, compared to the total light shift given as a percentage. Values are also included for a wavelength of  $10 \mu\text{m}$  which is relevant for estimating clock shifts due to black body radiation.

	$^1S_0$			$^3P_0$		$^3P_1$	
	813nm	914nm	$10\mu\text{m}$	813nm	$10\mu\text{m}$	914nm	$10\mu\text{m}$
$5s6s\ ^3S_1$	—	—	—	92	59	94	66
$5s7s\ ^3S_1$	—	—	—	0.1	0.2	0.2	0.2
$5s4d\ ^3D$	—	—	—	-1.3	27	-1.8	24
$5s5d\ ^3D$	—	—	—	3.7	5.2	3.6	4.1
$5p^2\ ^3P$	—	—	—	4.3	6.1	2.9	3.4
$5s5p\ ^1P$	96	95	94	—	—	—	—
$5s6p\ ^1P$	0.1	0.1	0.2	—	—	—	—

the effect of the continuum states. So it's possible that this is not an improved measurement of any transition rate, because we may just be compensating for the lack of continuum states in the calculation by boosting the strength of one of the transitions (the calculation in [36] also ignores the continuum). For now we just conclude that it is the best rate for predicting the magic wavelengths, and it is in agreement with the experimental values that vary between  $6.7\text{-}9.2 \times 10^7 \text{ s}^{-1}$ .

As we can calculate the magic wavelength for the two clock transitions, we can also calculate the clock sensitivity to wavelength fluctuations. For the  $^1S_0\text{-}^3P_0$  state we find that for our trap depth of  $U_T=120 \text{ kHz}$ , or in terms of lattice recoils  $U_T=35 E_R$ , the wavelength sensitivity for deviations from the magic wavelength is  $\sim 0.35 \text{ kHz/nm}$ . Or in terms of an arbitrary lattice depth given in units of  $E_R$ , the shift coefficient is  $10 \text{ Hz}/(\text{nm } E_R)$ . From here we can set the precision needed for the lattice laser frequency stabilization for a given system to reach an accuracy of  $10^{-18}$  (0.5 mHz) at the level of  $5 \times 10^{-5}/U_T$  for  $U_T$  given in units of  $E_R$ . For our trapping potential the resulting limit is at the  $1.5 \times 10^{-6}$  level, meaning lattice frequency stabilization at the MHz level is more than sufficient. This is an amazing level of suppression and should be trivial to achieve with current laser

technology. The sensitivity for the  $^3P_1$  transition is even smaller by about a factor of two.

A final thought on the magic wavelength issue is to consider choosing a different crossing where the trap is blue detuned. In a blue detuned trap the atoms are repelled from strong intensity zones and are trapped in nodes of the standing wave. This could be advantageous in that the actual Stark shift of the atoms is small compared to the red-detuned case, and therefore may be easier to control. This might be important if some of the polarization issues discussed in the next chapter limit the accuracy of the clock. From our polarizability calculation we find such a crossing at 389 nm which is not unthinkable as a laser wavelength. At the highest intensity point, for similar power (150 mW) and waist (65  $\mu\text{m}$ ) as before, the Stark shift is similar in magnitude to the red detuned case  $\sim +150$  kHz, while the wavelength sensitivity is larger (but still nice) at 10 kHz/nm. These number should be dramatically less in practice since the atoms will be repelled from the highest intensity point. The drawbacks to this scheme include more complicated generation of the trapping light, and that to implement a trap one has to go directly to a 3D lattice since the atoms will be radially ejected from the trap in a 1D system. It will be interesting to see if the Stark shifts in the red-detuned magic wavelength lattice get difficult enough to prompt exploration of such a system.

### 3.2 Spectroscopy in a 1-D Lattice: Theoretical

We now turn our focus to a theoretical discussion of the properties we can expect for spectroscopy of atoms trapped in the lattice. This will be essential for the design of a lattice clock system as a number of important effects depend on trap depth, atom temperature, beam alignment and so on. In this section we discuss the absorption profile of bound atoms which is well known from trapped

ion experiments, and generalize it to our specific case of a 1D trap defined by a standing wave laser.

### 3.2.1 Spectroscopy of Atoms Confined in a 1-D Harmonic Potential

For an atomic transition with linewidth  $\Gamma_a$  and frequency  $\omega_0$ , the absorption signal for atoms trapped in a 1D harmonic potential with trap energy levels  $E_{n_i}$ , and with probability distribution among the  $n$  sublevels  $P(n_i)$  is given by [94, 93]

$$S \propto \sum_{n_j, n_i} P(n_i) \frac{|\langle n_j | e^{ik_z z} | n_i \rangle|^2}{1 + \frac{4}{\Gamma_a^2} (\omega_0 - \omega_L + (E_{n_j} - E_{n_i})/h)^2}, \quad (3.11)$$

where  $\omega_L$  is the frequency of probe laser traveling along the  $z$  axis described by a traveling plane wave  $e^{ik_z z}$ . The positions of the energy levels are given by

$$E_n = h\nu_z \left( n + \frac{1}{2} \right). \quad (3.12)$$

with  $\nu_z$  being the trap frequency as before. Typically, we assume the Lamb-Dicke condition that the product of the probe wave vector  $\vec{k} = 2\pi/\lambda_p$  and the characteristic oscillator length  $z_0 = \sqrt{\hbar/4\pi M\nu_z}$  is much less than one. This essentially parameterizes the motion of the atom in the trap as compared to the wavelength of the probing light  $\lambda_p$ . In the Lamb-Dicke regime, the matrix element in Eq 3.11 can be found by expanding the exponent to first order and expanding the  $z$  operator in terms of  $z_0$  and the usual raising ( $a^\dagger$ ) and lowering ( $a$ ) operators such that we find for the matrix element

$$\begin{aligned} \langle n_j | e^{ik_z z} | n_i \rangle &\approx \langle n_j | 1 | n_i \rangle + \langle n_j | ik_z z | n_i \rangle = \delta_{n_i, n_j} + ik_z z_0 \langle n_j | a + a^\dagger | n_i \rangle \\ &= \delta_{n_i, n_j} + ik_z z_0 (\sqrt{n_i} \delta_{n_i+1, n_j} + \sqrt{n_i+1} \delta_{n_i-1, n_j}) \end{aligned} \quad (3.13)$$

If we then square the matrix element we find that only three terms remain, giving

$$|\langle n_j | e^{ik_z z} | n_i \rangle|^2 = \delta_{n_i, n_j}^2 + \eta_z^2 \left( n_i \delta_{n_i+1, n_j}^2 + (n_i + 1) \delta_{n_i-1, n_j}^2 \right) \quad (3.14)$$

Where we have defined the product  $k_z z_0$  as the Lamb-Dicke parameter  $\eta_z$

$$\eta_z \equiv k_z z_0 = \frac{1}{\lambda_p} \sqrt{\frac{h}{2M\nu_z}} = \sqrt{\frac{\nu_{\text{recoil}}}{\nu_z}} \quad (3.15)$$

which we can see also parameterizes the trap depth in comparison to the recoil frequency for absorption of the probe light.

For a general value of  $k_z$  and  $z_0$  (or  $\eta_z$ ) the solution to the matrix element is also well known [93] as

$$\langle n_j | e^{ik_z z} | n_i \rangle = e^{-\frac{1}{2}(\eta_z)^2} \sqrt{\frac{n_{<}!}{(n_{<} + \Delta n)!}} (i\eta_z)^{\Delta n} L_{n_{<}}^{\Delta n}[(\eta_z)^2], \quad (3.16)$$

where  $n_{<}$  is the lower of the two motional states,  $\Delta n$  gives the change in motional quantum, and  $L_{n_{<}}^{\Delta n}[(\eta_z)^2]$  is the generalized Laguerre polynomial. This reduces to the results of Eq. 3.14 if it is assumed  $\eta_z \ll 1$ .

If we combine Eq. 3.14 with Eq. 3.11 we can begin to understand what the absorption spectrum for a trapped atom will look like. In the Lamb-Dicke regime we will have only three non-zero situations where absorption can take place. For simplicity we will first consider the case of a single atom in the  $n_i$  motional state and the  $^1S_0$  electronic state, in a harmonic potential which is identical for the two clock states. This situation is shown schematically in Fig. 3.6 for a  $\cos^2$  potential with an atom in the  $n_i = 1$  motional state. For excitation where  $\Delta n = n_j - n_i = 0$  (known as a carrier transition), only the delta function in the first term of Eq. 3.14 survives and the atoms will absorb light at the frequency  $\omega_L = \omega_0$  and be moved to the excited  $^3P_0$  state. Therefore we will have a narrow absorption feature at the natural frequency of the transition. Two other features will be present in the absorption spectrum due to the  $\delta_{n_i+1, n_j}$  and  $\delta_{n_i-1, n_j}$  terms in the matrix element. For the first of these two cases, the absorption results in an increase of the motional quantum number  $n_i$  by 1, and the position of the resonance is shifted from the atomic frequency by  $\nu_z \times (n_i + 3/2) - \nu_z \times (n_i + 1/2) = \nu_z$ . From Eq. 3.14 we can see

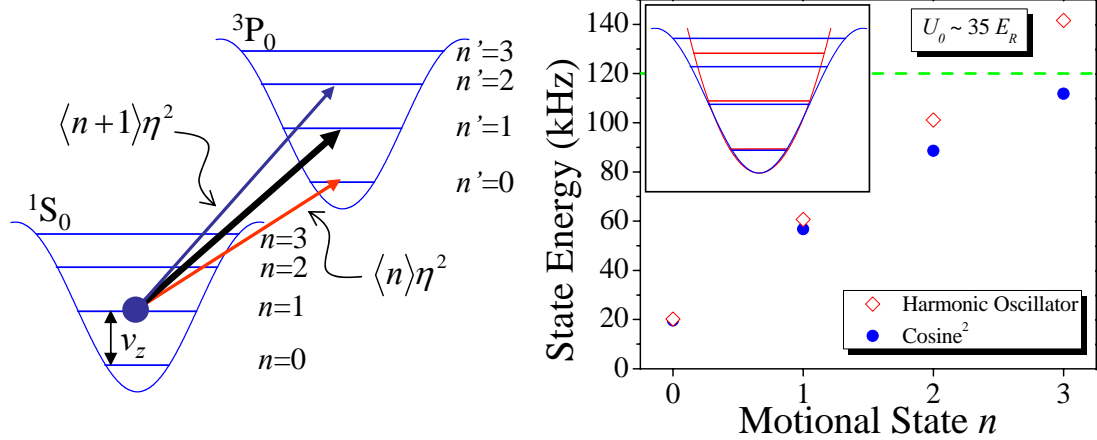


Figure 3.6: Schematic of lattice spectroscopy (left) shows a ground state atom in a bound motional state  $n=1$ . In the Lamb-Dicke regime we expect to see three absorption features. The strongest transition is the one where the motional state does not change ( $\Delta n = 0$ ), known as the carrier transition. Transitions where  $\Delta n = -1$ , known as red side bands are suppressed by a factor of  $\eta^2 n$  compared to that of the carrier transition. Transitions where  $\Delta n = +1$ , known as blue side bands are suppressed by a factor of  $\eta^2 (n+1)$ . The right panel shows the effect of trap anharmonicity on the spacing of the motional states in the lattice. The red diamonds are given for a trap depth of  $U_T = 35 E_R = 120$  kHz which is assumed to be purely harmonic. The blue circles show the position of the energy levels for the more realistic  $\cos^2$  potential of the same depth provided by calculations in [106].

that the relative strength of this spectral feature compared to that of the carrier transition is given by  $\eta_z^2 (n_i + 1)$ . The  $\delta_{n_i-1, n_j}$  term in the matrix element results in a similar feature where this time the motional quantum number is reduced by 1, and the resonance is at a frequency  $-\nu_z$  with relative strength  $\eta^2 n_i$ . These two features are referred to as motional sidebands and from here out are referred to as blue ( $\Delta n = 1$ ) and red ( $\Delta n = -1$ ) sidebands due to the relative frequency of the features compared to the central carrier transition. If we are in the Lamb-Dicke regime, the trap frequency is large compared to the recoil frequency. If we also assume the clock transition is narrow compared to the trap frequency, then we are in the resolved sideband regime of spectroscopy where the motional sideband are completely resolved from the carrier.

In the Lamb-Dicke and resolved sideband regimes we have some significant spectroscopic advantages as compared to free space spectroscopy. In free space, the absorption feature depends strongly on the temperature of the atoms and includes the effect of recoil. In the lattice case, the temperature of the atomic sample determines the distribution among the oscillator states in the trap. From our analysis above, we found that the frequency of the carrier transition does not depend on the state  $n_i$ , whereas the motional sideband features do. Although the sideband features will have a temperature dependence, they are suppressed by a factor of  $\eta_z^2$  and are at a large detuning compared to the transition width. Therefore the effect of atomic motion on the carrier transition should be very small, reduced to an issue of potential line-pulling effects. We can then expect that if the carrier transition is used, we will be able to perform spectroscopy nearly free of any Doppler or recoil effects. The magic wavelength concept is crucial for practical implementation of this idea because we are relying on the fact that the trap frequencies (which we saw depend on the Stark shift) are the same in the ground and excited state. If the trap potentials are different, then the carrier frequency will depend on the motional state  $n_i$  as

$$\Delta\nu(\lambda, n_i) = \Delta\nu(\lambda) + \Delta\nu_z(\lambda) \times (n_i + 1/2) \quad (3.17)$$

where  $\Delta\nu(\lambda)$  is the differential Stark shift of the clock states at a wavelength  $\lambda$ , and  $\Delta\nu_z(\lambda)$  is the differential trap frequency for the clock states. The inset of Fig. 3.4 shows this effect as the clock shift for carrier transitions from different ground states  $n$  are shown as a function of trapping wavelength. From the figure we can understand that deviation from  $\lambda_m$  results not only in frequency shift, but also in line shape deformation when multiple levels are populated.



### 3.2.2 The Effect of Trap Anharmonicity

So far we have assumed that the trap is purely harmonic. Of course we know a purely harmonic potential is un-physical here because the trap is not infinitely deep. In actuality, the standing wave pattern is a  $\cos^2$  potential having some anharmonic characteristics which affect the absorption spectrum and should be considered here. The main effect of the anharmonicity is to modify the energy of the quantized motional states in the trap. This effect has been explored elsewhere [106, 107, 108] in detail, here we will only give the final result for the assumed trapping depth of  $35E_R$ . The right panel of Fig. 3.6 shows the calculation of the energy of the motional states in kHz, for a purely harmonic (red diamonds) and a  $\cos^2$  (blue circles) potential. For the first two ladder states, we find that the harmonic approximation is very good, as can be expected because the  $\cos^2$  potential is well approximated by a harmonic potential for small deviations from the potential minimum. As we look at larger  $n$  states, the disagreement begins to show up. In fact, in this case we find that there is actually one less bound state for the  $\cos^2$  potential than that of the harmonic potential. Given the deviation from a harmonic potential, we expect that the absorption spectrum must be altered. For the carrier transition, as long as the magic wavelength condition is met, we do not expect any change in the spectrum because the ground and excited trapping potentials will still be identical. The positions of the motional sidebands on the other hand depend on the difference in the trap frequency  $\nu_z$  for the different  $n$  levels. In the harmonic case the difference in energy for neighboring  $n$  states is independent of  $n$ , simply given by  $\nu_z$ . In the more realistic anharmonic case, the energy difference depends on how deep in the potential the state  $n$  is, and Therefore the detuning of the motional sideband will depend on the  $n$  level that the atom is in.

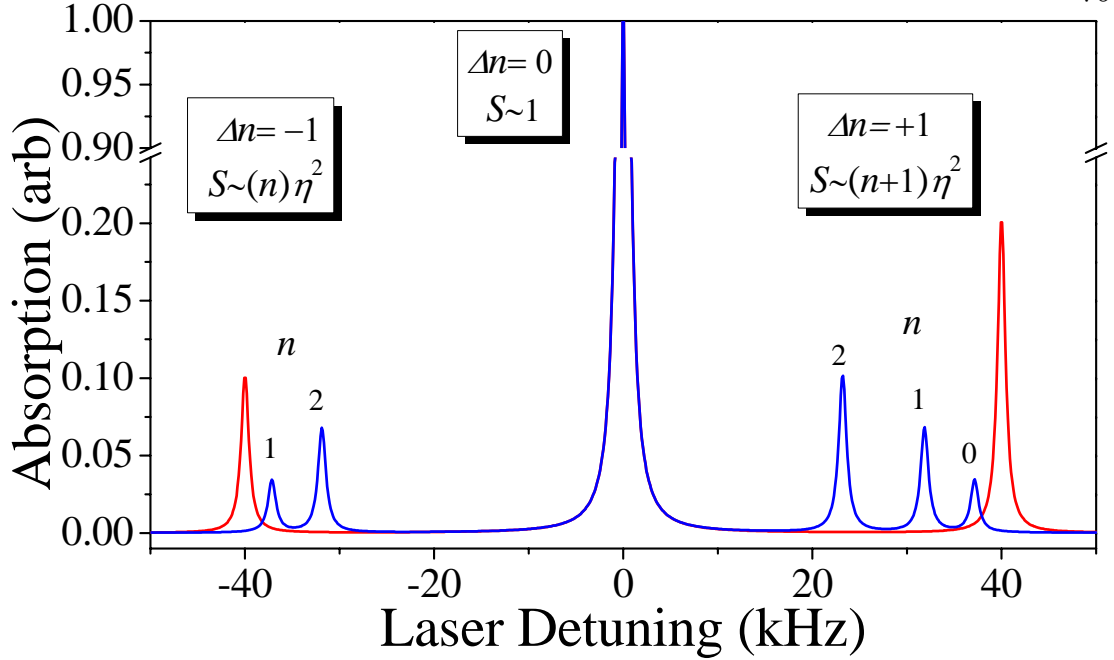


Figure 3.7: The effect of trap anharmonicity on the absorption spectrum of bound atoms. The graph shows the simulated absorption spectrum for three atoms in a trap of depth  $U_T=35E_R$  with one atom in each of the first three  $n$  states. For the harmonic potential (red curve) the motional sidebands are degenerate. For the  $\cos^2$  potential (blue curve), the anharmonicity breaks the degeneracy and multiple side bands are observed. The carrier feature is unchanged by the anharmonicity.

Figure 3.7 gives an example of this difference between purely harmonic and anharmonic absorption spectra. Here we consider the case where we have three atoms in the potential, one in each of the first three ( $n=0,1,2$ ) motional states. For the harmonic spectrum (red curve), we find that motional sidebands will be located at  $\pm 40$  kHz, suppressed in amplitude (relative to the carrier signal) by a common factor of  $\eta_z^2 \simeq 0.1$ . The red sideband amplitude is also scaled by the average value of  $n$  which in this case is 1. The blue sideband is scaled by the average value of  $n+1$ , so it is twice as strong as the red sideband for the case described here. It is expected that for atoms near the ground state of the trap, the blue side band feature will be stronger than that of the red side band. This is easily understood if one considers that for an atom in the ground state there

is no lower energy bound state in the potential, so the red sideband vanishes. In the anharmonic case, the positions of the sidebands depend on the motional state, so we see a number of absorption features. This should not affect the carrier line shape as long as the frequency separation between the carrier and first motional sideband is large compared to the carrier width. Analysis of the sideband spectrum on the other hand, a useful tool for characterizing trap properties and atom temperature, does become more complex in an anharmonic potential.

For the remainder of this section we will assume that the harmonic approximation is good enough for describing the physics of lattice spectroscopy. For sufficiently cold atoms, this is certainly a valid assumption.

### **3.2.3 The Effect of Radial Motion on the Sideband Spectrum**

Up to this point, we have neglected the effect of the radial motion (described by Eq. 3.3) on the spectroscopic properties of the lattice clock system. The radial motion does in fact alter the absorption spectrum of the confined atoms significantly. Here we will consider the effect of radial motion on the sideband spectrum, in the next subsection we will also see how the radial degree of freedom affects the Rabi excitation spectrum of the carrier.

The atoms in our trap are tightly confined in the longitudinal direction of the lattice, however in the radial direction the confinement is much weaker, due to the gaussian profile of the laser beam (See Eqs. 3.2 and 3.3). The effect of interest in this subsection is that the atoms can move radially in the trap, which changes the trap intensity that the atoms see as a function of radial position. Therefore the atoms will see a different longitudinal trap frequency depending on their radial position in the trap. Once again we find that at the magic wavelength, the carrier signal is not affected by this motion because the effect will be identical in the two clock states. The longitudinal sidebands however are sensitive to this motion

because their frequency position depends on the local trap intensity. Since any radial motion from the center of the trap reduces the intensity seen by the atom, we expect that the motion results in asymmetric broadening of the sideband feature towards the carrier. The size of which will depend on the average excursion of the atoms in the trap, or more specifically, the trap parameters and atom temperature.

For our assumed trap parameters of  $P=150$  mW and  $w_0=65$   $\mu\text{m}$ , the radial trap frequency at the magic wavelength is given by Eq. 3.3, yielding  $\nu_x \simeq 125$  Hz. With the known trap frequency, we can calculate the  $1/e^2$  waist of the atom distribution,  $w_{\text{atoms}}$ , for a given temperature  $T$  as  $w_{\text{atoms}}=2\sqrt{\langle x^2 \rangle}$  where  $\sqrt{\langle x^2 \rangle}$  is the length scale of the trap oscillation given by

$$\sqrt{\langle x^2 \rangle} = x_0(2\langle n_x \rangle + 1) \quad (3.18)$$

As before  $x_0 = \sqrt{\hbar/2M(2\pi\nu_x)}$ . For an ensemble of atoms in the trap the average  $n$  value in the  $x$  direction is simply determined by a Boltzman distribution as

$$\langle n_x \rangle = \sum_{n_x} P(n_x) n_x = \frac{\sum_{n_x=0}^{\infty} n_x e^{-n_x h\nu_x/k_B T}}{\sum_{n_x=0}^{\infty} e^{-n_x h\nu_x/k_B T}}. \quad (3.19)$$

To estimate the absorption signal of the blue sideband in the presence of the radial motion we use the following expression

$$S \propto \frac{\sqrt{2}}{\sqrt{\pi} w_{\text{atoms}}} \int_{-\infty}^{\infty} \frac{\gamma N_a e^{-2x'^2/w_{\text{atoms}}^2}}{(\nu_L - \nu_z e^{-x'^2/w_0^2})^2 - \gamma^2} dx'. \quad (3.20)$$

Here we have a convolution of the Lorentzian absorption profile for a transition width  $\gamma$ , and the atomic distribution with a  $1/e^2$  waist  $w_{\text{atoms}}$ . The numerator of the integral takes into account the portion of the total atom number  $N_a$  which contributes to the signal for a given position along the  $x'$  axis. The first term in the denominator is an effective detuning of the laser frequency  $\nu_L$  from position of the sideband resonance, which takes into account the fact that the frequency of the resonance depends on the position of the atom  $x'$  within the gaussian distribution

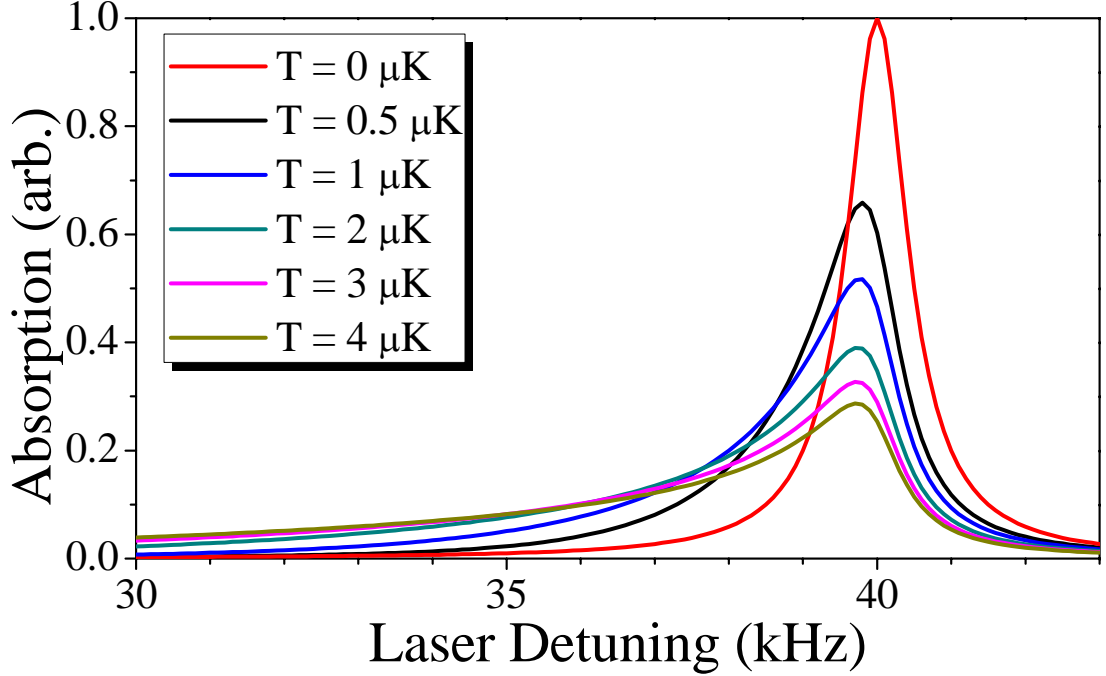


Figure 3.8: The effect of Radial Motion on the Sideband Lineshape. The absorption profile for a single blue sideband, given by Eq. 3.20 with  $w_0=65\mu\text{m}$ ,  $\nu_z=40$  kHz, and  $\nu_x=125$  Hz, for different radial temperatures. As the radial temperature of the atoms increases, the atoms sample positions of the lattice with lower trap intensity and Therefore a smaller longitudinal trap frequency. The result is an asymmetric broadening which gets quite drastic as the temperature rises. Here a transition width of 500 Hz is assumed for presentation purposes.

of the laser with waist  $w_0$ . We have assumed that the probe laser waist is large compared to all other dimensions in the problem such that the probe intensity is constant for all regions of the trap. Note that the reason the argument in the exponential term in the denominator is missing the usual factor of two (given that  $w_0$  is the  $1/e^2$  laser waist) is because the frequency of the sideband resonance depends on the square root of the light intensity. Using Eq. 3.20 we can then plot the absorption signal for our trap having  $\nu_z=40$  kHz,  $\nu_x=125$  Hz, and  $w_0=65$   $\mu\text{m}$ . This is done in Fig. 3.8 where we have plotted the absorption spectrum of the longitudinal blue sideband for different temperatures (and hence  $\langle n_x \rangle$  and  $w_{\text{atoms}}$  values) assuming a transition width of 500 Hz for convenience. The figure

shows that for the trap parameters here, a radial temperature of only a few  $\mu\text{K}$  results in significant asymmetric broadening of the sideband. Note that even in the limit that the radial temperature goes to zero, some asymmetry remains since  $w_{\text{atoms}} \rightarrow x_0$  as  $T \rightarrow 0$ .

Another sideband effect to consider here is that the radial motion in the trap also results in red and blue motional sidebands at the radial trap frequency of 125 Hz. This could be of great concern for the carrier as these absorption features are much closer than the longitudinal sidebands. Fortunately, as we will see in the next subsection, these peaks will be strongly suppressed in a carefully designed setup.

### 3.2.4 The Effect of Motion on the Rabi Frequency

The final effect we will consider in this theoretical spectroscopy section is the effect that atomic motion has on the ability to excite all of the atoms in a sample. Thus far in all of our absorption profiles we have assumed that the trapped atoms can absorb the probe photons with unity efficiency such that 100% of the atoms can be excited by a single spectroscopic pulse. It turns out that this is not true in practice for a number of reasons. To explore how well we can excite the population to the  $^3P_0$  state we need to first consider how the excitation fraction depends on different trap parameters. In free space, the probability for excitation  $P_e$  of an atom for a probe resonant with the clock transition is given by a simple expression

$$P_e = \sin^2 \left( \frac{\Omega_c t}{2} \right) \quad (3.21)$$

where  $\Omega_c^2 = (I_p/2I_{\text{sat}}) \times (2\pi\gamma)^2$  is the Rabi frequency of the clock transition,  $t$  is the spectroscopic pulse duration, and we have assumed that all decoherences such as excited state lifetime are negligible for the region of interest. From this expression

it is simple to calculate the needed probe intensity for a given probe time to excite 100% of the population by setting  $\Omega_c t = \pi$ .

For bound atoms in a 3D potential, the situation is a bit more complicated as the quantum states  $n$  come into play. The Rabi frequency for example is given by [93]

$$\Omega = \Omega_c \langle n' | e^{i\vec{k}\cdot\vec{x}} | n \rangle = \Omega_c |\langle n'_x | e^{ik_x x} | n_x \rangle| |\langle n'_y | e^{ik_y y} | n_y \rangle| |\langle n'_z | e^{ik_z z} | n_z \rangle|. \quad (3.22)$$

For the carrier transition ( $\Delta n = 0$ ) using Eq. 3.16, this simplifies to

$$\Omega_{\Delta n=0} = \Omega_c e^{-\frac{(\eta_x^2 + \eta_y^2 + \eta_z^2)}{2}} L_{n_x}^0 [(\eta_x)^2] L_{n_y}^0 [(\eta_y)^2] L_{n_z}^0 [(\eta_z)^2] \quad (3.23)$$

Where we have used Lamb-Dicke parameters for a laser propagating along  $\hat{k}$ , probing an atom in motion along the axis  $\hat{i}$ , defined as

$$\eta_i = \cos(\hat{k} \cdot \hat{i} + \delta\theta) \frac{1}{\lambda_p} \sqrt{\frac{\hbar}{2M\nu_i}}. \quad (3.24)$$

In our situation we have a probe aligned along the  $z$ -axis such that  $\hat{k} \cdot \hat{x} = \hat{k} \cdot \hat{y} = \frac{\pi}{2}$  and  $\hat{k} \cdot \hat{z} = 0$ . The second term in the cosine argument ( $\delta\theta$ ) allows for a small mismatch between the spectroscopy and motional axes due to beam misalignment or differential focusing of the probe and lattice beams. If we assume that we are probing along the strong confinement axis provided by the standing wave pattern, then we have  $\eta_z \simeq \frac{1}{\lambda_p} \sqrt{\frac{\hbar}{2M\nu_z}}$ . The weak confinement is provided by the gaussian shape of the lattice beam and results in radially symmetric motion with a frequency  $\nu_r$ . Our solution above (Eq. 3.23) for the Rabi frequency is for an atom bound independently in  $x$ ,  $y$ , and  $z$  so we need to include some additional assumptions to more accurately describe our real system. First, we make a simple approximation that the  $x$  and  $y$  trap frequencies are roughly given by the true radial trap frequency such that  $\eta_x = \eta_y \simeq \eta_r = \frac{\delta\theta}{\lambda_p} \sqrt{\frac{\hbar}{2M\nu_r}}$ . Second, we constrain the possible state occupation as  $n_x = n_y \simeq n_r$  to reflect the real situation where

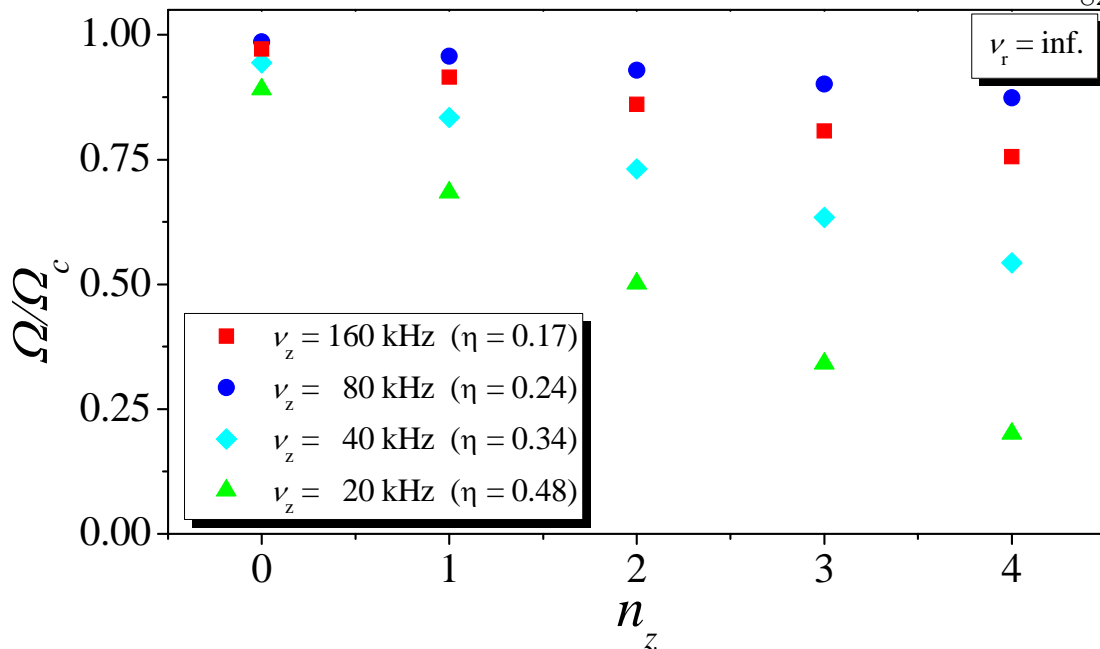


Figure 3.9: The effect of longitudinal motion on the Rabi frequency is shown by plotting the Rabi frequency as a function of  $n_z$  for different trap depths. Here we have assumed a purely 1D system.

the atom occupation is given only by the states  $n_z$  and  $n_r$ . In this way we can use the well known solution given in Eq. 3.23 for a three dimensional bound atom but described, albeit as an approximation, in terms of the trap frequency and quantum states of our quasi 2D system.

From Eq. 3.23 we can see that the Rabi frequency for a bound atom will depend on the trapping parameters, such as longitudinal and radial trap frequencies, as well as the quantum state of motion. To explore how the Rabi frequency scales with these various trap properties we first return to the simple 1D case where the radial contributions are ignored. Figure 3.9 gives the bound atom Rabi frequency (as a fraction of the free space Rabi frequency) for different trap states  $n_z$  and different trap frequencies (or equivalently Lamb-Dicke parameters). The figure shows quite clearly that the Rabi frequency has a significant dependence on  $n$ , which gets less pronounced as the trap gets deeper. Note also how even



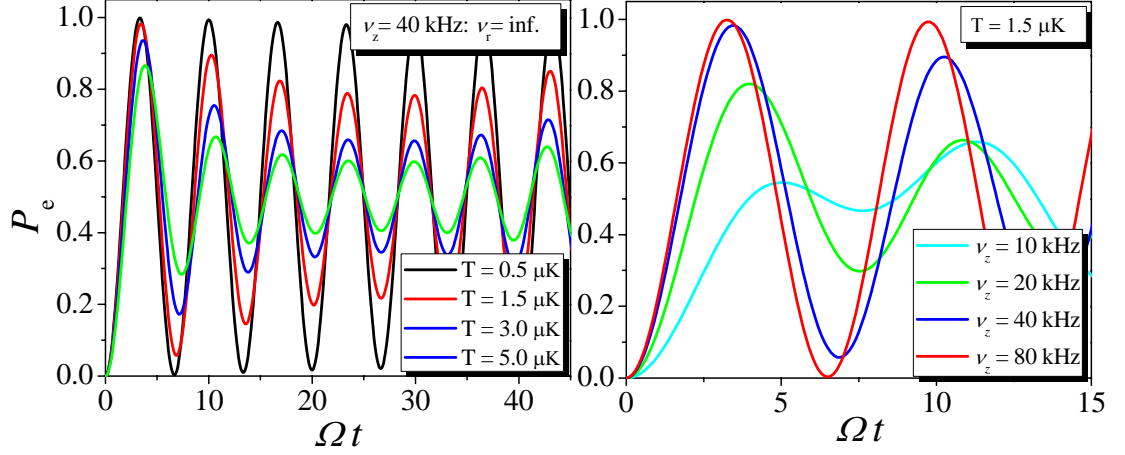


Figure 3.10: The effect of atomic motion on the excitation fraction. In the left panel the excitation probability is shown versus the product  $\Omega t$  to show the usual Rabi-flopping diagram which allows optimization of the pulse time and intensity to reach the desired excitation fraction. The excitation is shown for our typical trap parameters and different temperatures. The right panel show the resulting excitation for a fixed temperature of  $1.5 \mu\text{K}$  but for varying trap frequencies.

for the deepest bound state  $n = 0$  the fraction never quite gets to 1 because of the non-zero Lamb-Dicke parameter (i.e. some of the excitation must go into the change in motional quanta if  $\eta > 0$ ).

Turning our attention to an ensemble of bound atoms, since we do see a strong  $n$  dependence for the conditions we expect in our experiment ( $\nu_z = 40 \text{ kHz}$ ), we know that the expression for the excitation fraction of a free space ensemble is insufficient to describe atoms populating the various  $n$  levels. We therefore must sum the contribution of the different  $n$  dependent Rabi frequencies weighted by the thermal distribution of atoms  $P(n)$  in the given states  $n$  (here we only include one population factor for the transverse motion because we have previously assumed that  $n_x = n_y \simeq n_r$  is fixed for our trap description). The excitation probability is then given by

$$P_e = \sum_{n_z} \sum_{n_r} P(n_z) P(n_r) \sin^2 \left( \frac{\Omega \Delta_{n=0} t}{2} \right) \quad (3.25)$$

Instantly we can see that the total ensemble excitation fraction will depend on

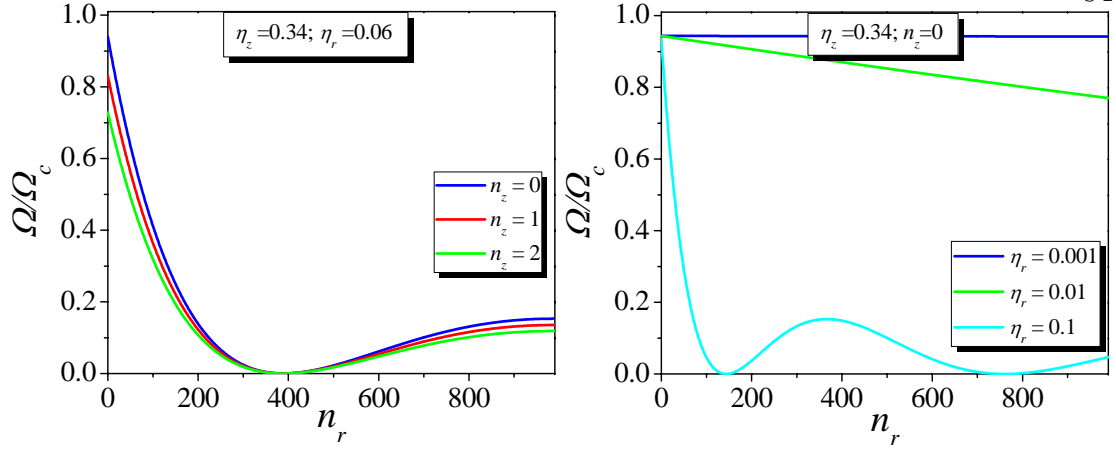


Figure 3.11: The effect of radial motion on the Rabi frequency is shown in the left panel as a function of  $n_r$  for the first three longitudinal motion states. The calculation is done assuming our typical longitudinal trap frequency of 40 kHz, and a radial Lamb-Dicke parameter is assumed to be 0.06. The right panel shows the  $n_r$  dependence of the Rabi frequency for atoms in the  $n_z = 0$  ground state, for different Lamb-Dicke parameters for the radial axis. From here we can see that reducing  $\eta_r$  either by beam alignment or radial trap frequency can drastically reduce the motional dephasing of the Rabi frequencies.

trap temperature as well as trap depth. The excitation probability is plotted in Fig. 3.10 to show this effect, where we again consider the 1D case only. In the first panel, the excitation probability is plotted for a trap depth of  $35E_R$  for different ensemble temperatures. The calculation shows that for a fixed trap depth, the contrast of the standard “Rabi-flopping” fringes is reduced as the temperature is increased. Again, this is due to the fact that the atoms are filling up more  $n$  levels as the temperature increases, such that the Rabi frequencies become different and dephase the oscillatory pattern. The second panel shows a similar effect takes place when the trap depth is varied for a fixed temperature of  $1.5 \mu\text{k}$ . In both graphs we must conclude that keeping the temperature cold enough to only populate the first  $n_z$  state would be ideal if we want to keep our possible excitation fraction large.

Now that we have a feel for how the temperature and trap depth can play

an important role, we consider the more complicated case by including the effect of radial motion. We again need to see how the Rabi frequency depends on different parameters, which now will depend not just on the motional state, but also on the Lamb-Dicke parameter in the radial direction determined by the  $k$ -vector misalignment angle  $\delta\theta$ . We assume that care is taken in aligning the probe along the lattice axis such that  $\delta\theta$  is small, and that the misalignment angle is somewhat of a global factor that accounts for both beam overlap and focusing issues. Figure 3.11 gives the dependence of the Rabi frequency for different situations using Eq. 3.23 and our assumptions that  $\eta_x = \eta_y \simeq \eta_r$  and  $n_x = n_y \simeq n_r$ . The first panel assumes our standard designed trap frequencies of 40 kHz and 125 Hz, as well as a misalignment angle of about 10 mRad ( $\eta_x = \eta_y = \eta_r = 0.06$ ). The Rabi frequency is plotted as a function of  $n_r$  for different values of  $n_z$ . The second figure shows the  $n_r$  dependence of the Rabi frequency (assuming the  $n_z = 0$  state) for different radial Lamb-Dicke parameters. As the Lamb-Dicke parameter gets smaller, either by alignment or increased trap frequency, the dependence of  $\Omega$  on  $n_r$  is relaxed.

With the  $n$  dependence of the Rabi frequency sorted out we can return to Eq. 3.25 to see the effect on an ensemble of atoms in the lattice. We can evaluate how the excitation fraction depends on parameters such as temperature and radial trap frequency, and beam misalignment. Here we assume our standard longitudinal trap frequency of 40 kHz and vary the other parameters in the system. We assume for simplicity that the radial and axial temperatures are the same. The top panel of Fig. 3.12 gives the excitation fraction plot for our trap parameters with  $T = 1.5 \mu\text{K}$  for different misalignment angles. Once again we see a dephasing of the expected Rabi-flopping due to the atomic motion. From this calculation we see that alignment to better than 1 mRad is desirable for our trap parameters. However, in a realistic situation it may be difficult to guarantee such a strict

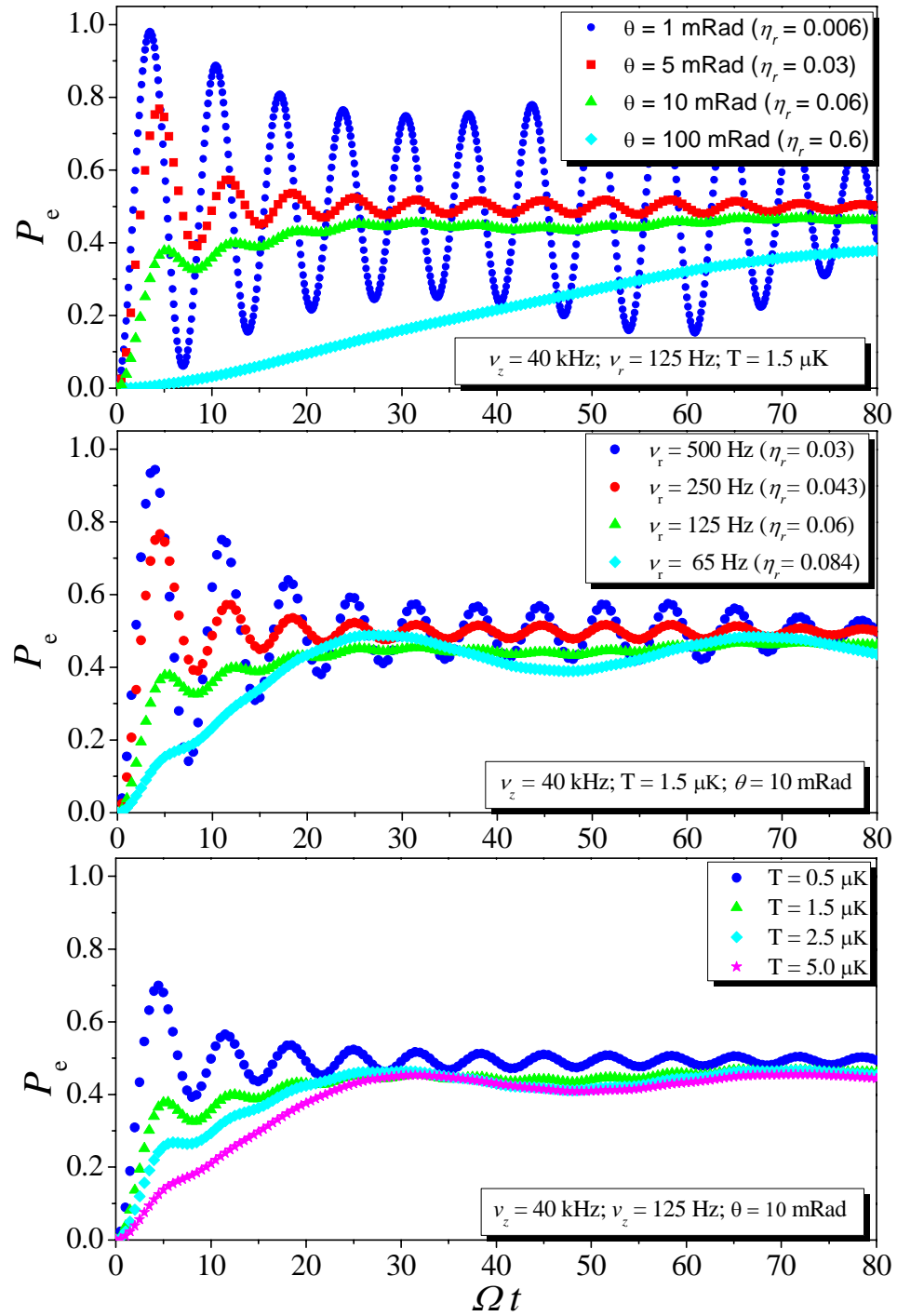


Figure 3.12: Effect of radial motion on the excitation fraction for various trap parameters. The fixed parameters in the calculation are given in the lower box of each panel. In all plots the radial and longitudinal temperatures are assumed equal.

constraint on alignment and focusing. If we instead constrain the misalignment angle to 10 mRad, we can see if it is possible to have a good excitation fraction by controlling the atom temperature or trap depth. The middle panel in the figure shows how the excitation can be improved for our fixed longitudinal frequency and misalignment ( $\theta=10$  mRad), by increasing the radial trap frequency. We see that as the trap gets deeper in the radial direction, the effect of the misalignment is lessened. The final graph shows the importance of the ensemble temperature on the excitation. From the figure we see that if we are to use our prototype trap parameters and  $\theta=10$  mRad, it is important that the temperature of the sample be kept as low as possible. Note we have not included any decoherence in the calculation due to the excited state lifetime, the laser spectrum, or the trap lifetime. The decay to 0.5 is instead a result of destructive interference. Interestingly the beating of the different Rabi frequencies often results in a revival of the fringe pattern at longer times.

### 3.2.5 Discussion: How should I Design My Trap?

Now that we have looked into some specifics of our lattice, we can re-visit the questions we posed earlier to see if the scheme is a viable one for our proposed optical lattice clock for the  $^1S_0$ - $^3P_0$  transition with a trap depth of  $U_T=35E_R$ .

1. *Is  $\lambda_m$  is a practical wavelength, and is the required frequency stability reasonable?*

We found that the magic wavelength for the transition is at 813 nm which is a wavelength easily accessible by either a Ti:Sapphire laser or a diode laser system with tapered amplifiers. Output power of hundreds of mW from these lasers is common. The sensitivity of the clock shift to wavelength errors was found to be 350 Hz/nm at our trap depth, such that the trapping laser needs to be stabilized to about 1 MHz to keep the clock shifts below  $10^{-18}$ . The level of stabilization is

trivial compared to other lasers in the system, and will not be a concern. ✓

2. *Can we perform spectroscopy in the Lamb-Dicke limit ( $\nu_{Trap} > \nu_{Recoil}$ ) and in the resolved sideband limit ( $\nu_{Trap} > \gamma_{Clock}$ )?*

At our trap depth, the trap frequency is about 10 times larger than the recoil frequency, such that the Lamb-Dicke condition is satisfied. The longitudinal sidebands are well resolved so we can expect a Doppler-and recoil-free absorption spectrum. For the radial motion, the trap frequency is smaller than the recoil frequency, and the sidebands are only 125 Hz away from the carrier. Fortunately, if we align our probe laser along the lattice axis, the Lamb-Dicke parameter for the radial motion is suppressed by a factor of  $\delta\theta$ , which can be a few mRad, such that the radial sidebands can be suppressed relative to the carrier signal by orders of magnitude. We will see in the experimental section, that the carrier will be narrower than 100 Hz such that we are still in the resolved sideband regime. ✓

3. *Can we efficiently load atoms into the lattice ( $U_0 > k_B T$ )?*

Our trapping depth of  $35E_R$  can be expressed as a temperature of about  $7 \mu\text{K}$ . From our narrow line cooling results we can expect the atoms sample to be in the  $1 \mu\text{K}$  range, easily trapped by the lattice potential. ✓

4. *Is the absorption rate for lattice photons at  $\lambda_m$  and  $U_0$  an issue?*

The concern here is that the atoms could scatter lattice photons which can heat the atoms out of the trap and limit the trap lifetime. Since we want a long lifetime for resolving narrow lines, this effect is important to consider. The photon scattering rate is related to the trap depth [109] and can be estimated by

$$\Gamma_{sc} = \frac{\Gamma}{\Delta} \frac{U}{\hbar}. \quad (3.26)$$

For a trap depth of  $35 E_R$  the corresponding scattering rate for atoms in the  $^1S_0$  state is estimated to be  $0.09 \text{ s}^{-1}$ . Therefore for our trapping depth the lifetime limitation from photon scattering can be expected to be tens of seconds, exceeding

the coherence time of state of the art lasers. ✓

*5. Is the light shift polarization dependence at  $\lambda_m$  and  $U_0$  significant?*

In this chapter we have found that for the  $^3P_0$  transition there is no polarization dependence of the light shift. In the next chapter we explore how the hyperfine structure does introduce a small sensitivity to polarization. In practice, there are ways to eliminate this effect as we shall see, so for now we can assume the problem is under control ✓

*6. Is the fourth order Stark shift at  $\lambda_m$  and  $U_0$  negligible?*

So far we have not discussed the possibility of higher order light shifts which scale as  $U_T^2$ . These can be a concern for the magic wavelength concept as they result in an additional shift that depends on the trap. The influence of possible two-photon transitions from the clock states lead to a hyperpolarizability which provides shift proportional to  $U_T^2$ . Specifically for the  $^3P_0$  states, there are two of these transitions near the magic wavelength, the first is the  $^3P_0$ - $5s7p^1P_1$  transition at 813.36 nm, which is forbidden to leading order but is very close to the magic wavelength, and the second is the  $^3P_0$ - $5s4f^3F_2$  transition at 818.57 nm which is a completely allowed two photon transition. The effect of the hyperpolarizability has been explored theoretically [39, 48] and experimentally [41, 43] elsewhere and will not be discussed in detail in this work. The best available experimental limits [43] for the size of this effect is a frequency shifts of  $4.5(4.5) \mu\text{Hz}/((U_T/E_R)^2)$  which for our trap depth results in a shift of at most 10 mHz. Since this effect can be characterized by varying the trap depth one expects it will not be a limit for reaching mHz clock accuracy. ✓

Our trap seems to satisfy all of the criteria set up in the beginning of this chapter for a clock, however, these are by no means the best trap parameters to perform experiments with. Instead, they simply correspond to the values which are used in the experimental system we use in the rest of this work. From our

discussion of Rabi frequency effects, we might desire a deeper trap to eliminate some of the dephasing problems we found. This could also help to reduce any possible line-pulling effects from motional sidebands, although at the level of  $10^{-17}$  it appears unimportant. One can go to significantly deeper traps by using a smaller waist or larger beam power, as long as the hyperpolarizability effect is kept in mind as it will increase as the square of the trap depth. For shallower traps, one can also reduce the Rabi dephasing by implementing extra laser cooling for the trapped atoms [91] such that the  $\langle n \rangle$  is reduced. Another effect not discussed here is the effect of site to site tunneling between lattice wells. If a trap is too shallow, one expects tunneling between different wells which can result in decoherence, and even lineshape asymmetry limiting both the  $Q$  and accuracy of the clock. These effects are discussed in [110], and are not expected to affect the lattice clock for depths of  $10E_R$  and higher, if a vertically oriented lattice is used.

The best trap parameters for the clock will eventually depend on the largest systematic in the frequency evaluation. The trap will likely be designed to minimize the effects which are the most difficult to calibrate. Our best guess for now is that we would like to avoid any hyperpolarizability effects so we chose a relatively shallow trap.

### 3.3 Spectroscopy in a 1-D Lattice: Experimental

We have now built up a good understanding of what trap parameters are desirable for our lattice clock experiment. In this section we describe the implementation of the optical lattice clock, as well as a number of spectroscopic measurements. We report on measurements of the magic wavelength and sensitivity to deviations from that value. We explore the effect of atomic motion in the lattice by directly exciting the motional sidebands. Finally we push the system to the limit in terms of line  $Q$ , to see just how well the lattice clock will work for a



high precision clock. An experimental accuracy evaluation is reserved for a later chapter, after we have explored the consequences of hyperfine structure in detail.

### 3.3.1 The Clock Laser @ 698 nm

To take advantage of our expected Doppler free line  $Q$  and the ridiculously small natural linewidth of 1 mHz for the clock transition, we need to eliminate all sources of decoherence in our spectroscopy system. From our analysis in the previous sections, it seems the lattice technique solves the motional decoherence issues for the atomic sample, at least for time scales smaller than the trap lifetime. The remaining issue then is the interaction of the atomic sample with the clock laser. The oscillator noise can effect clock performance in a number of ways. The most obvious effect is that the achievable line  $Q$  in a clock will be limited by the laser linewidth. It is in fact desirable to operate the clock at a  $Q$  larger than the inherent laser noise so that the spectrum is repeatable and the  $S/N$  is not affected by the laser noise. The laser drift can also cause a problem if the free running oscillator drift is similar to the width of the absorption profile for the relevant time scales of the experiment. During clock operation, the free running laser noise typically determines the short-term stability until time scales where the cold atom signal steers the laser. Even at longer time scales, however the Dick effect [111] becomes important, as high frequency laser noise can be aliased down to very low frequencies since the laser is only corrected by the atoms at regular intervals and not continuously. In light of all of these effects it is crucial to develop a laser with both a narrow intrinsic linewidth as well as small frequency drift and low instability. Development of such an oscillator to probe the Sr clock transition at 698 nm has therefore been one of the central focuses of work in our lab. This topic could fill an entire chapter (or even thesis) but since this author has not been the driving force for this particular part of our lattice clock development,

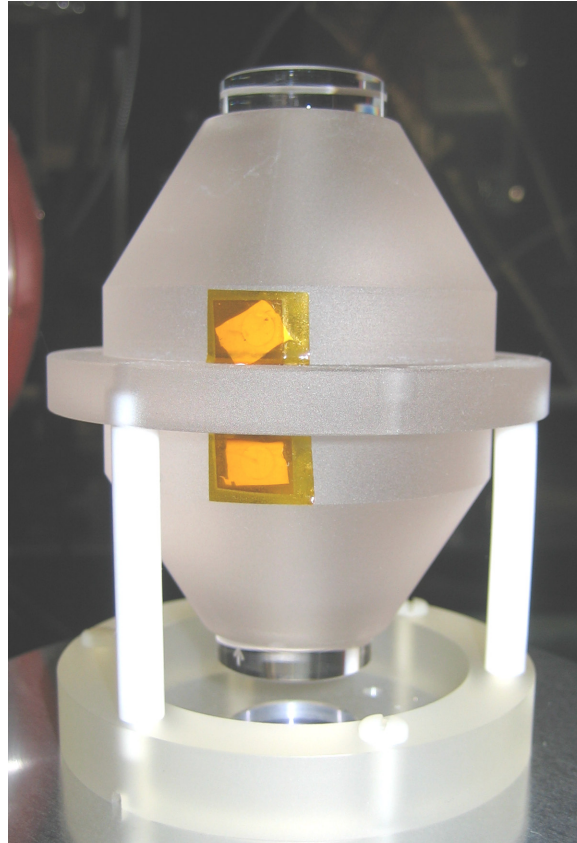


Figure 3.13: Image of the ULE cavity used for stabilization of our clock laser at 698 nm.

only the general features of the laser are described here. Full details of the laser system are discussed in detail elsewhere [112].

To create the clock laser, a grating-stabilized diode laser at 698 nm is locked to a high-finesse ( $\sim 200,000$ ) ultra-low-expansion (ULE) cavity, with a free spectral range of 2 GHz, using the Pound-Drever-Hall technique [78]. This configuration allows stabilization of the laser frequency to below the mHz level relative to the frequency defined by the optical cavity. The problem then boils down to designing the reference cavity in such a way as to minimize mechanical shaking and expansion which will end up as frequency noise and drift on the clock laser. The ULE material is chosen to make the reference cavity for two reasons. First, the

coefficient for thermal expansion of ULE glass can be zero near room temperature which helps to keep the drift in the length of the cavity small, and equivalently the frequency drift of the laser. The second reason for choosing ULE glass is more subtle. Thermal mechanical noise in the cavity material, mirrors, and mirror coatings has recently been brought to attention as a major limiting effect in the stability of the laser [113, 114]. For a non-zero temperature, the material in the mirrors for example undergoes Brownian motion causing deformation of the material, which causes the resonant frequency of the cavity to fluctuate. The strength of the effect depends on the geometry of the cavity and the mechanical  $Q$  of the material, where it can be understood that higher  $Q$  values are better for suppressing this effect because mechanical resonances will be sharper, having less effect at low frequencies. ULE has a higher  $Q$  than zerodur which is also commonly used for cavities. The  $Q$  of ULE is smaller than another common material, fused silica, but with fused silica the coefficient for thermal expansion is much larger than ULE at room temperature. Low frequency mechanical vibrations are another very serious concern for cavity design. To even get to the point where thermal noise becomes an issue, the vibrations must be addressed. Our cavity is mounted in a vertical orientation in order to reduce fluctuations of the cavity length due to vibrations [115]. The cavity is under vacuum and mounted on a compact, passive vibration-isolation table, and is shown in Fig. 3.13.

The clock laser performance has been characterized in a number of ways, including direct comparison of two similar systems at 698 nm, comparison to highly stabilized lasers at other colors using the fs-comb, and by precision atomic spectroscopy (discussed in the upcoming sections of this chapter). Figure 3.14 summarizes the performance of the clock laser as determined by direct comparison between the two 698nm systems via heterodyne beat. The beat reveals narrow linewidths sometimes below 300 mHz for integration times of a few seconds. The

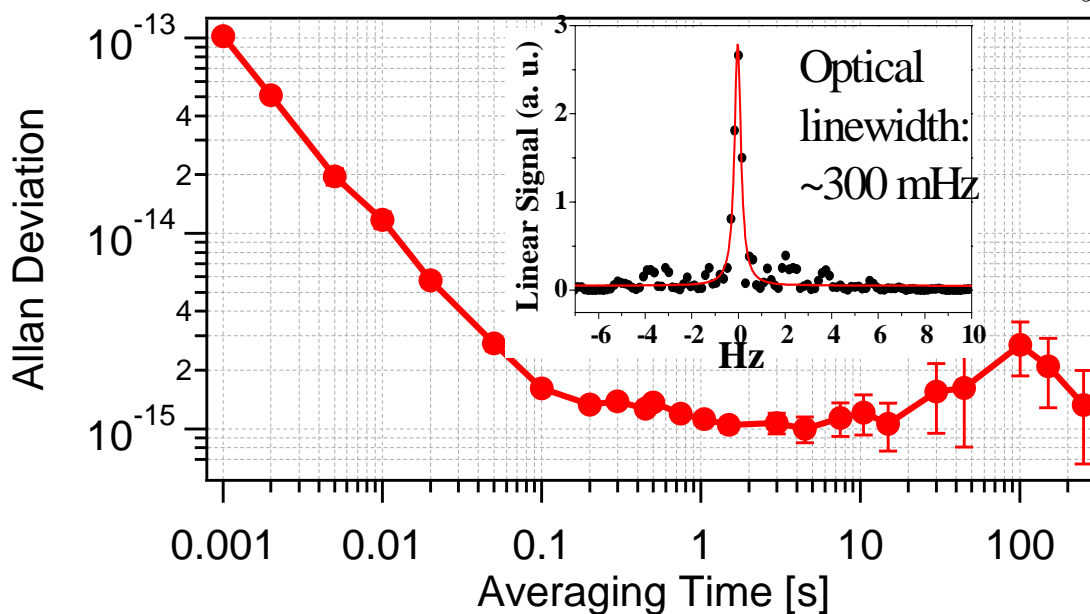


Figure 3.14: The graph shows the Allan deviation of a heterodyne beat between two similar 698 nm systems (linear drift removed). The 1 s stability is at  $1 \times 10^{-15}$  consistent with the thermal noise limit of the cavity. The inset shows the narrow beat between the two oscillators for a resolution bandwidth (RBW) of 333 mHz. The beat linewidth is 340 mHz, suggesting the measurement is RBW limited. If we assume the two lasers contribute equal noise we can estimate the linewidth in this case is less than 250 mHz. Multiple measurements with the same conditions show that the beat linewidth is typically between 340 and 450 mHz. For integration times of 60 seconds, the beat broadens to nearly 2 Hz.

Allan deviation shown reveals that the fractional frequency noise of the beat is  $1 \times 10^{-15}$  at 1 s, consistent with the expected limit set by thermal-mechanical noise in the cavity mirrors and mirror coatings. The drift of the laser is typically less than 1 Hz/s. This is still on the large side if we hope to scan out Hz level lines. To further suppress the drift we monitor the laser frequency relative to a hydrogen maser via the fs-comb. We then apply a frequency ramp to an AOM in the clock laser system to compensate for the drift relative to the maser. This works well for long times scales (many 100s of seconds), typically allowing us to reduce the long-term linear drift to 100 mHz/s. At shorter timescales of course the maser information is too noisy to be useful for any laser correction (that's what the Sr

will be for!!!).

With the sub-Hz linewidth shown here we are in great shape for lattice spectroscopy and clock operation. For longer integration times of tens of seconds the beat between our lasers is still less than 2 Hz so we should expect that we can see spectral features of similar widths from our atoms if all other decoherence processes are controlled.

### 3.3.2 The Optical Lattice Setup

Here we describe the setup used for optical lattice spectroscopy. The main change from the setup discussed in Chapter 2 is the addition of the lattice and spectroscopy laser to the system. The general features of the apparatus are summarized in Fig. 3.15. The light for the standing wave is generated by a CW Ti:Sapphire laser operating at a wavelength of 813.4280(5) nm, monitored by a high precision wavemeter. To improve the spatial mode, the light is spatially filtered by transmission through a single-mode polarization maintaining (SMPM) optical fiber. At the output of the fiber the light is collimated by a microscope objective and passed through a linear polarizer which should provide pure linear polarization at the level of a part in  $10^4$ . The light is then transmitted through a long-wave-pass dichroic mirror which allows the probe laser to be co-aligned with the lattice. The beams are then passed through a second high quality polarizer to ensure the polarization axes are the same. The two beams are focused at roughly the position of the MOT with an AR coated achromatic doublet where the beam sizes before the lens have been chosen such that at the focus, the lattice waist is roughly three times smaller than that of the probe. This ensures that the intensity profile (and hence Rabi frequency) of the probe beam is constant over the lattice. A curved mirror ( $R \simeq 20\text{cm}$ ), which reflects the lattice and transmits (90%) the probe wavelength, then retro-reflects the trapping laser such that the standing-

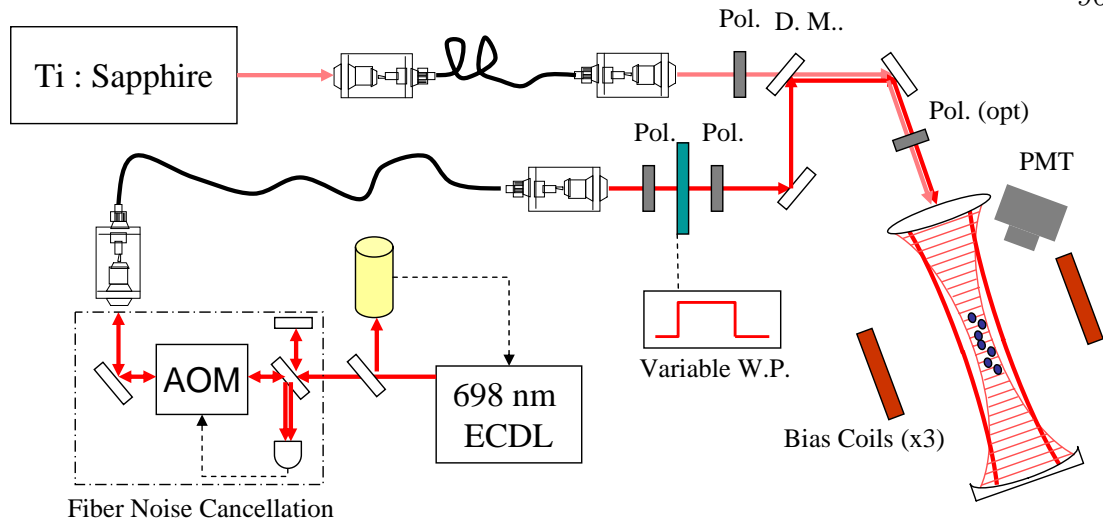


Figure 3.15: Diagram of the experimental setup used for spectroscopy of lattice confined atoms. The 813 nm light is generated by a CW Ti:sapphire laser and is brought to the atoms with a single-mode polarization-maintaining (SMPM) fiber. It is then passed through a high quality linear polarizer before being focused into the trap by an achromatic doublet. The clock laser (discussed in the previous section) is transferred to the atoms SMPM fiber as well but in this case special care is taken to eliminate fiber noise. The clock light is first split into a local and outgoing beam. The outgoing beam passes through an 80 MHz AOM and the first order diffracted light is passed through the optical fiber. At the atom end of the fiber, some of the light is reflected back through the fiber by the fiber tip. This light passes back through the AOM and the first order diffraction is compared to the original local copy. The beat between the two beams (now at 160 MHz) is used to stabilize the transfer. Note that since the light passes through both the fiber and AOM twice the light is stabilized at both ends of the fiber. The clock laser is switched on and off using a liquid crystal waveplate instead of the usual AOM to maintain the spatial mode profile and keep the fiber stabilization on continuously. The clock and lattice lasers are combined with a dichroic mirror and pass through a second polarizer together. For some experiments the second polarizer is removed such that the probe and lattice lasers can have orthogonal polarization. Pol.=Linear polarizer, D.M.= dichroic mirror, ECDL=external cavity diode laser, AOM=acousto-optic modulator, W.P.=half wave plate, PMT=photo multiplier tube.

wave is formed. The position and alignment of the curved mirror is optimized by ensuring that the trapping light returns through the fiber. The relevant lens system is designed for a lattice waist of  $35 \mu\text{m}$ .

The available power at the output of the lattice fiber is 350 mW, unfortu-

nately our vacuum window coatings transmit only 75% at 813 nm so the amount of retro-reflected light the atoms will see is only 150 mW. If we want to estimate the expected trap depth then we should use 150 mW as the single pass power in Eq. 3.2. We then have the situation of a standing wave based on 150 mW, as well as a traveling wave of about 100 mW. Since the peak intensity of a standing wave is four times larger than that of a traveling wave we can estimate that this 100 mW should actually only change the trap depth by about 10% and hence we ignore it. With  $P=150$  mW and  $w_0=35\mu\text{m}$  we can expect a trap depth of  $120 E_R$ . We will see in the next section that the measured waist, based on trap frequencies, is  $65 \mu\text{m}$ , yielding a trap depth of  $35 E_R$ . Since the work in this thesis was completed, the cause of this discrepancy has been found to be due to misalignment between the waist and the atom cloud.

The clock laser described above is on a separate table than the atom trapping apparatus and therefore must be also be transferred via optical fiber. The transfer process can be a problem for lasers stabilized to this level, as stretching and shaking of the fiber causes a Doppler effect for the transmitted light. We find for example that for a 10 m fiber the linewidth of the clock light is broadened to a few hundred Hz. To combat this effect we stabilize the fiber transfer interferometrically using an AOM by comparing light reflected from the output of the fiber tip with a local copy at the clock laser table [116, 117]. In the experiment the clock laser is switched on and off using a combination of polarizers and a liquid crystal wave plate which can rotate the polarization by 90 degrees on demand. In this way we can keep the fiber noise stabilization on at all times. After the shutter the light is combined with the lattice with the dichroic mirror discussed above.

To load atoms into the lattice we take a fairly straightforward approach and simply leave the trapping beam overlapped with the MOT for the entire cooling sequence discussed in Chapter 2. Since the strong cooling transition is based on

a broad transition, the Stark shift provided by the lattice has no effect on the blue MOT properties. The second stage cooling on the other hand is based on a narrow transition such that Stark shifts on the order of 100 kHz will have an effect on the cooling process. While this will likely reduce the cooling efficiency, it can actually be advantageous as the cold atoms which pass through the lattice region, will become detuned from the MOT beams and will remain trapped in the lattice, creating an effective “dark spot” MOT. In practice, we optimize the atom number in the lattice by varying the detuning and intensity of the red MOT lasers, resulting in  $10^4$  atoms in the lattice. In doing so we end up at trapping parameters which are not optimized for the transfer from the blue MOT to the red MOT. This is easily understood if one remembers how both the physical size and atom number of the red MOT were largest for large trap detuning [71, 79]. The lattice volume on the other hand is small so to optimize the number in the lattice smaller MOT detunings are used to make the MOT volume small at the cost of Blue MOT to Red MOT transfer efficiency. In future measurements a hybrid protocol can be developed where the red MOT parameters are optimized for initial MOT to MOT transfer and then the detuning can be changed actively to load the lattice. From scaling arguments it seems if such an approach is taken one can expect an order of magnitude enhancement in atom number.

Now, since we are interested in long coherence time, we must consider the lifetime of the atoms in the lattice. Possible trap lifetime limitations include inelastic collisions with background gas, scattering of lattice photons (we have already discussed this limit and it is negligible), and trap intensity fluctuations which can cause heating of the atoms [98, 107, 108]. In the apparatus described here the typical background gas pressure in the vacuum chamber of  $< 1 \times 10^{-9}$  Torr is not expected to limit the trap lifetime at the 1 second timescale. Early experiments with the optical lattice revealed that the lifetime was  $\sim 700$  ms. By



adding intensity stabilization via measurement of the lattice reflection off of one of the vacuum windows and feedback to an AOM before the single mode fiber, the lattice lifetime was extended beyond 1 second. Atomic structure effects must also be carefully considered for our goal of achieving a narrow resonance width. The nuclear spin in  $^{87}\text{Sr}$  provides additional broadening mechanisms as the 10  $m_F$  sublevels in each clock state can have different sensitivity to external fields. Specifically, the state mixing provided by the hyperfine interaction results in a differential  $g$ -factor between the two clocks states yielding a first order Zeeman shift of  $109 m_F \text{ Hz/G}$  (this is discussed in detail in the next chapter). Therefore the magnetic fields in the experiment must be controlled at the mG level. For this reason 3 pairs of Helmholtz coils (one pair oriented on each axis) are used to eliminate stray magnetic fields.

After the laser cooling stage, the  $10^4$  atoms are ready for spectroscopy. Our spectroscopy scheme is the following (see Fig 3.16). The cold ground state atoms are first excited to the  $^3P_0$  clock state with a pulse of length  $t_R$  from the clock laser. The length of time for the pulse depends on the desired spectral resolution for a given experiment, as for a square pulse we expect a Rabi ( $\text{sinc}^2$ ) line shape with a fourier limited full width half maximum (FWHM) in Hz given by  $\Delta\nu_{FWHM} \simeq 0.89/t_R$ . After the spectroscopy probe, a shelved detection scheme is used where the remaining ground state atoms are irradiated with a beam slightly red detuned from the strong  $^1S_0$ - $^1P_1$  cycling transition. The scattered photons from this process are collected with a photo multiplier tube (PMT) for measurement of the ground state atom number. This process boils the ground state atoms out of the trap, however any atoms excited by the clock laser will remain. We then measure the  $^3P_0$  population, by first applying the repumping lasers to drive the atoms back to the  $^1S_0$  state, followed by a second blue pulse on the cycling transition for population detection. (Note that one should take care during the re-

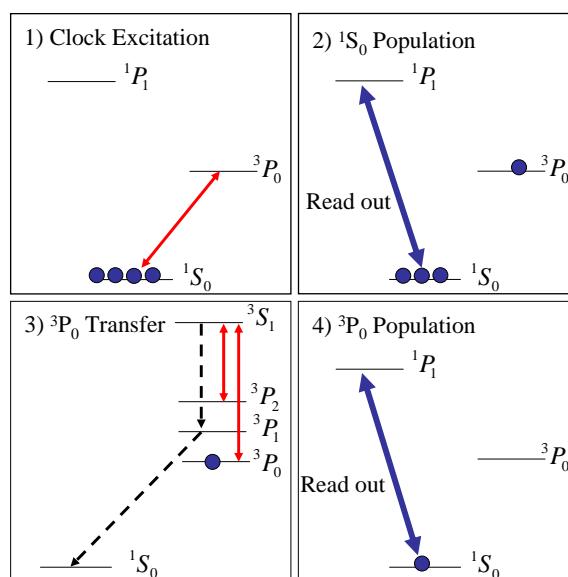


Figure 3.16: Spectroscopy sequence used for observing the clock transition. 1) After the laser cooling sequence, the 698 nm laser provides excitation light for the atoms. 2) After the spectroscopy pulse, the ground state population is detected by cycling photons on the strong  $^1S_0$ - $^1P_1$  transition, and collecting them with a nearby PMT. These atoms are lost from the lattice. 3) The atoms which were excited to the  $^3P_0$  state are then pumped back to ground state by means of a few ms pulse of the repumping lasers. 4) The  $^3P_0$  population can now be measured in the same way that the original ground state population was measured.

pumping stage, in that if some  $B$ -field is applied during clock excitation it should be shut off to ensure the repumping lasers are still on resonance with all of the sublevels. IF the repumping lasers are being scanned then it is not important.) After the two measurements there are no remaining atoms in the trap so atoms must be re-cooled and loaded into the lattice for each frequency step of the probe laser.

Measuring both the excited and ground state population may seem redundant, but actually for practical reasons it is important. In our system for example, we find that the number of atoms available for spectroscopy fluctuates by 5-10% from shot to shot. Therefore if one uses the ground state measurement to look for a weak signal it can be washed out by the baseline fluctuation. In the excited

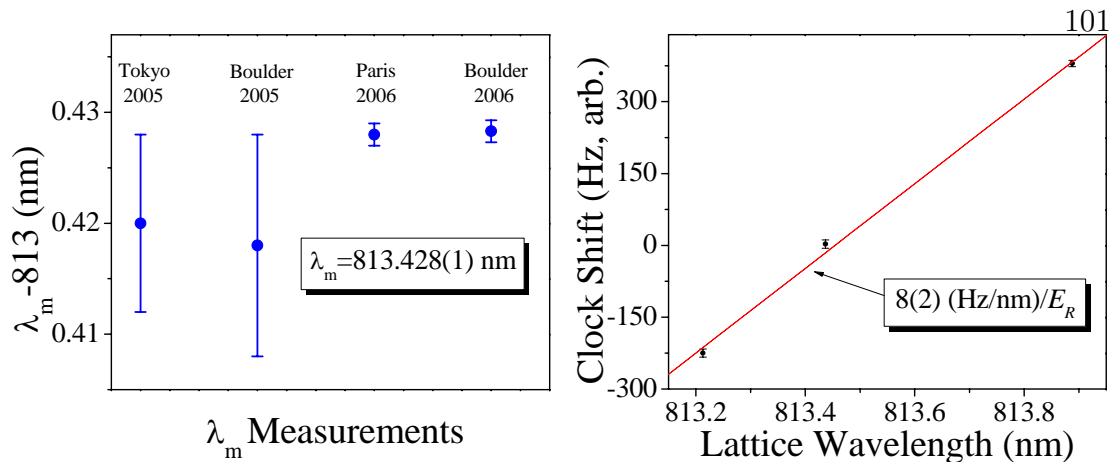


Figure 3.17: (Left) Recent measurements of the magic wavelength ( $\lambda_m$ ) made by our group, as well as the Tokyo and Paris groups. The most recent measurement from our group is discussed later on in this work. The result is 813.4283(12)nm. (Right) Measurement of the clock sensitivity to lattice wavelength for a 110  $E_R$  lattice operating near  $\lambda_m$ . The resulting slope is  $8(2)(\text{Hz/nm})/(U_T/E_R)$ , which for our typical depth of 35  $E_R$  means a stabilization of the lattice wavelength of only  $\sim 1$  MHz is required for 1 mHz accuracy in the clock frequency.

state on the other hand, the baseline is zero (or close to it depending on how many stray photons reach the detector) since no atoms are there when the excitation is absent, so we are much more sensitive to small excitations. The ground state measurement is still very useful though because the combination of the two can be used to normalize the excitation signal to eliminate  $S/N$  problems caused by shot to shot atom number fluctuation. This normalization is not done here, but will become important as one pushes the clock stability towards the quantum limit. For the  $10^4$  atoms used here for example, a  $S/N$  of 100 can be expected if all other technical noise is removed.

### 3.3.3 Measurement of the Magic Wavelength, and Wavelength Sensitivity

A quick aside on the issue of magic wavelength before we get to spectroscopy results. The first step to take in developing the lattice clock system is to mea-

sure the magic wavelength of the transition. This is done by measuring how the transition frequency varies for different trap depths and wavelengths. A high precision measurement of the magic wavelength is discussed in Chapter 5 along with our accuracy evaluation of the clock, for now we will just summarize the results that have been obtained recently. The magic wavelength for the  $^1S_0$ - $^3P_0$  transition has by now been measured with high precision by three groups, first in Tokyo[58], then Boulder[44], followed by a measurement from the Paris group[41]. The results are plotted in the left panel of Fig 3.17 along with a follow up measurement from our group [42] which will be discussed later on. We can see from the figure that the agreement between the three groups is quite good, with the most recent measurements yielding a value of 813.428(1). The second plot gives a measurement of the sensitivity of the clock transition frequency to small deviations from the magic wavelength. This data (here taken with a trap depth of  $U_T=3U_0 \simeq 110E_R$ ) yields a slope of 0.9 kHz/nm, which corresponds to a sensitivity of 8 (Hz/nm)/( $U_T/E_R$ ) which is good agreement the estimate from our theory section of 10 (Hz/nm)/( $U_T/E_R$ ). From this point forward it is assumed that all spectroscopy is performed with a trap wavelength of 813.4280(5).

### 3.3.4 Resolved Sideband Spectroscopy

With the spectroscopy system ready to go, we first apply a large probe laser intensity to observe the transition. In doing so we see the expected absorption features we discussed in the theory section. Figure 3.18 shows the absorption spectrum for the lattice confined atoms at our typical depth  $U_T=35E_R$  when the transition is very strongly saturated. In the case of strong saturation we can observe not only the carrier transition with the expected excitation fraction of 0.5, but the sideband features as well. We can extract some key information from spectra such as this. For example, the sharp edge of the blue (higher frequency)

sideband give a good estimate of the longitudinal trap frequency, which from the figure we can see is approximately 40 kHz, or equivalently  $\eta_z=0.33$ . The longitudinal temperature of the atom sample can be estimated from the relative heights of the blue and red sidebands. We see for example that the relative strengths of the two are about 5:1 which tells us that  $(\langle n \rangle + 1)/\langle n \rangle = 5$  and Therefore  $\langle n \rangle = 0.25$ , which leads to a temperature of 1.2  $\mu\text{K}$  if we assume a harmonic potential. The line shape deformation of the sideband can also tell us about the radial temperature of the atom sample. The second panel in the figure shows the excitation of the radial sidebands. To observe the radial sidebands we have to intentionally mis-align the probe beam from the lattice axis to increase the Lamb-Dicke parameter  $\eta_r$ . Here we can see that the radial trap frequency is 125 Hz. With the misalignment comes a reduced maximum excitation for the carrier as expected. In the typical operation of our spectroscopy system it is estimated that the radial sidebands are suppressed by at least a factor of 25 from the carrier transition. Note that the two graphs are not the same data set, although the trapping potential was unchanged between them. These trap frequency values have been confirmed by independent measurements where a parametric oscillation technique was used [98].

With the measured trap frequencies we can extract the waist of the trap by the relation given in Eq. 3.5. In this case we find the waist  $w_0$  is 65  $\mu\text{m}$ . The ratio of the trap frequencies is a useful way to back out the waist as it does not depend on the light power, or polarizability calculation, so it is robust against rogue factors of two. As discussed above, the reason for a waist of 65  $\mu\text{m}$  instead of the designed waist of 35  $\mu\text{m}$  was eventually found to be misalignment between the actual location of the waist and the atom cloud. Given this measured waist we can check our calculations by using the measured power of 150 mW and Eq. 3.3 and we find that using our polarizability code, the predicted trap frequency is

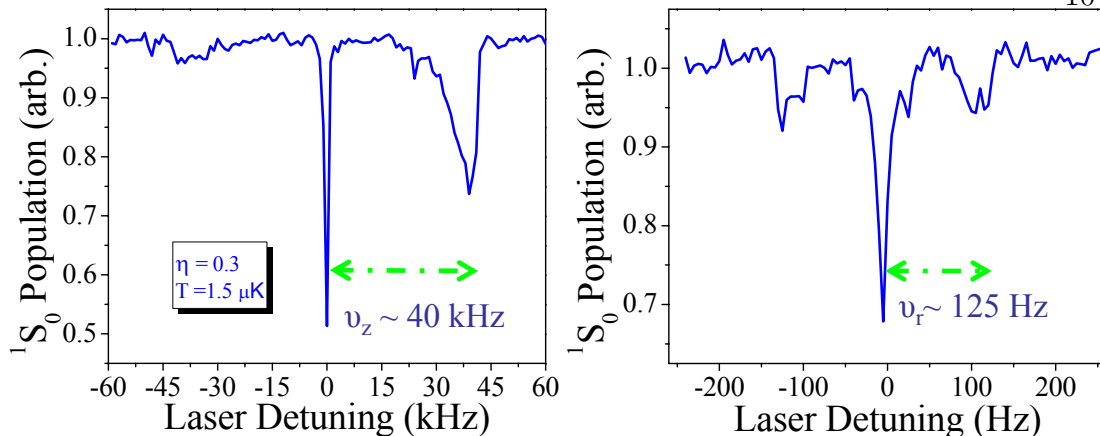


Figure 3.18: Spectroscopy of the clock transition in the optical lattice. When the clock transition is strongly saturated, the motional sidebands are observed. From these spectra we can extract the trap parameters such as motional frequency, and Lamb-Dicke parameter, as well as the atom temperature.

indeed 40 kHz.

### 3.3.5 Hz-Level Carrier Spectroscopy: Rabi

The narrow central feature in Fig. 3.18 is of the greatest interest for clock development. This carrier transition ( $\Delta n = 0$ ) provides a remarkably large line  $Q$  which is not affected by atomic motion in the resolved sideband limit. For saturation intensities below unity (where we expect to operate to get the narrowest line), the longitudinal sidebands amplitudes are found to be at the percent level, while the radial sideband are estimated to be at least a factor of ten smaller. In this case our absorption spectrum is a single strong feature at the clock transition frequency with a width determined by the Fourier limit, or other broadening mechanisms.

Figure 3.19 shows a high resolution scan of the clock transition when a 400 ms spectroscopy pulse is used. The probe laser intensity has been reduced below saturation such that the line is not broadened. Here we see the remarkable result we have been working for, the peak is extremely narrow, having a linewidth

(FWHM) of just 4.5 Hz. This is a  $Q$  of  $9.5 \times 10^{13}$ ! If we compare this lineshape to a free space measurement at a similar temperature, as in Fig. 3.1, we see that we have reduced the resonance width four orders of magnitude by confining the atoms. If we assume that our  $S/N$  can eventually reach the quantum projection noise limit of  $\sqrt{N}$ , then for our  $10^4$  atoms we could expect the atoms to provide a 1 s stability below  $1 \times 10^{-16}$ . This is an order of magnitude better than our state of the art laser can even handle. The  $S/N$  shown in the plot is closer to 10:1 than 100:1, this is a technical limit in that we have not performed any normalization of the atom number so we are limited by the shot-to-shot atom number fluctuation. We also point out that the data is a single scan across the resonance and not from a number of averages. While trapped ion systems can achieve similar  $Q$ 's, the signal to noise is so poor that to create a spectrum as shown in Fig. 3.19 one needs to average tens or hundreds of scans together, although we should note that the total time is not too different since in our current experiment we spend most of our time cooling ( $\sim 700$  ms). In the case, where the system is optimized for stability (i.e.  $S/N$ ,  $Q$ , and duty cycle), there is no question that the  $10^4$  atoms will out perform a single ion with the same  $Q$ , even if we consider that the probe time for ions may be shorter due to a higher transition frequency.

From the spectrum we can extract some additional information about how our system is performing. The first thing to note is that the lineshape does not agree with what we would expect. For a square pulse of  $t_R=400$  ms we expect a  $\text{sinc}^2$  lineshape with a FWHM of  $0.89/t_R = 2.2$  Hz. Instead we find that the lineshape is best fit by a Lorentzian profile with a 4.5 Hz width. An external broadening mechanism must be present. Some possible sources of this include laser noise, lattice lifetime, and lattice wavelength, but these have been checked independently as discussed above. A more likely reason is that the hyperfine structure in  $^{87}\text{Sr}$  provides ten  $m_F$  sublevels in each of the clock states which are

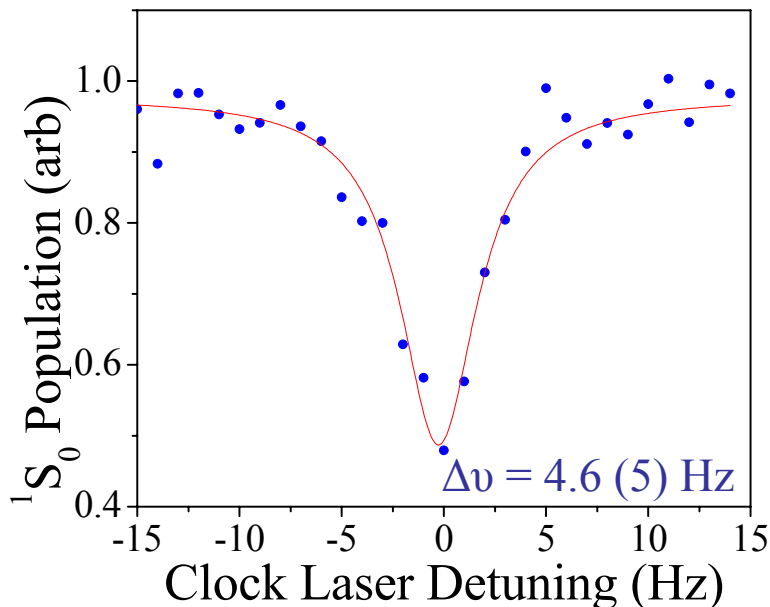


Figure 3.19: High resolution spectroscopy of the carrier transition for weak probe powers. When the probe intensity is reduced below saturation, the carrier feature reveals a very narrow line shape with a FWHM of 4.5(6) Hz ( $Q = 9 \times 10^{13}$ ). Here the width is limited by stray magnetic fields which result in a linear Zeeman shift for the  $m_F$  sublevel of the clock transition. The excitation fraction is limited by differing Rabi frequencies between  $m_F$  levels and the motional dephasing effects discussed in this chapter.

sensitive to external fields. As we will see in the next chapter, the two clock states have slightly different sensitivity to magnetic fields such that a small linear Zeeman shift exists. So we can expect that the broadening in Fig. 3.19 is due to stray magnetic fields at the few mG level. The hyperfine interaction also provides the possibility for vector and tensor light shifts due to the lattice beam which are smaller than the zeeman effect but could still be contributing (see section 4.3). The amplitude of the signal is also an interesting issue, although not shown here, we have found that turning up the probe power does not increase the excitation fraction by a significant amount. While we expect some degradation due to motional effects, a second effect is that the Clebsch-Gordon coefficients are very different for the different  $m_F$  sublevels, such that if the probe intensity



is optimized for excitation (or linewidth) of one  $m_F$  transition, other transitions will not be optimized. Therefore we expect some additional dephasing of the Rabi frequency when degenerate sublevels are used.

To really test the performance of the lattice clock system then it seems we should use resolved sublevels to eliminate any broadening from  $m_F$ -dependent field sensitivities, or any Rabi dephasing. To probe a single transition we apply an external magnetic field of a few hundred mG orthogonal to the lattice propagation axis, and parallel to the polarization of the lattice. The field is sufficient to provide a frequency splitting between neighboring transition of about 50 Hz. We then focus on a single transition, in this case the  $m_F=5/2$ . Until now, we have been using the  $^1S_0$  population measurements to record our spectra since the signals have been large. However, in this case we expect the population to be evenly distributed among the sublevels, such that if we excite only one transition our signal can suffer by a factor of 10, and will be washed out in the  $^1S_0$  measurement by the 10% atom number fluctuation. So we instead use the  $^3P_0$  population measurement to record the spectra. To test our maximum achievable  $Q$  we use an even longer probe time of 480 ms which should provide a Fourier limit to the achievable width of 1.8 Hz. Figure 3.20 summarizes the results when spectroscopy is performed in this way. The first panel shows a lineshape with a width of 1.9(2) Hz that does show the expected  $\text{sinc}^2$  profile for Fourier broadening. From this graph we conclude that by eliminating the  $m_F$  dependent broadening, we can achieve fourier limited linewidths of 1.8 Hz in the system. Thus our system provides a incredible line  $Q$  of  $2.4 \times 10^{14}$ . This value exceeds even that provided by the best ion clock [16] by 50%, and is to our knowledge, the largest  $Q$  ever recorded for coherent spectroscopy.

So why not increase the probe time and push further? Well, as the other two spectra in the figure show, at this narrow width, reproducibility starts to become an issue. We show three sample spectra that are achieved on a resolved sublevel

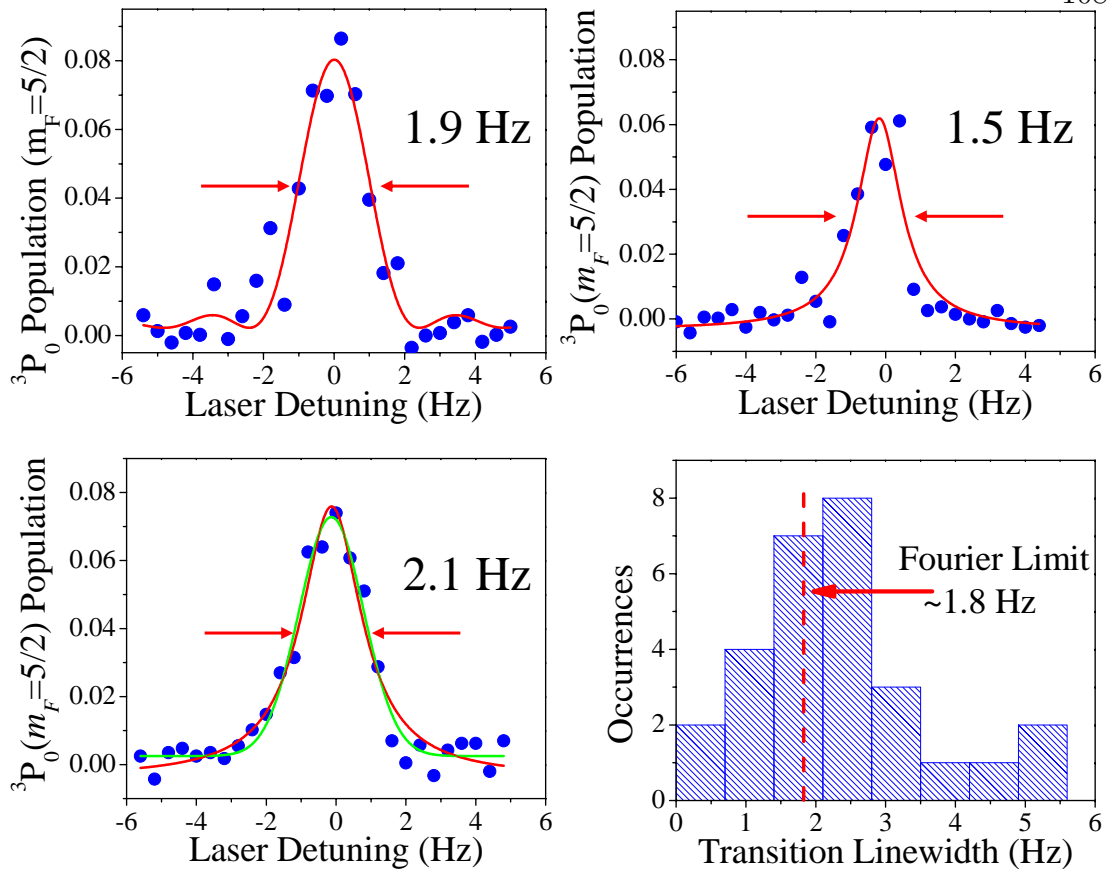


Figure 3.20: High resolution Spectroscopy using the resolved  $m_F=5/2$  state in the presence of a magnetic field. Single sublevel spectroscopy eliminates the effect of Zeeman broadening allowing exploration of the true limit of our spectroscopic precision. Here a probe time of 480ms (1.8 Hz Fourier limit) is used and lineshapes with  $Q > 2 \times 10^{14}$  are observed. In some cases the lines are Fourier limited. For the most part the repeatability, shown as a histogram, is limited by the clock laser with the mean lorentzian linewidth value of the 28 measurements being 2.2 Hz.

with the intent of discussing the reproducibility of the lineshape. The lower panel for example is more lorentzian in nature suggesting some small additional broadening. A lorentzian fit (red) to the data yields a slightly broadened linewidth FWHM of 2.1(2) Hz. A gaussian fit of the same data (green) yields a FWHM of 2.1(1) Hz. The upper right panel shows a line shape with a width smaller than the Fourier limit, likely due to the sharp drop off on the right side of the peak. The three spectra shown were all taken under identical experimental conditions.

The bottom right panel summarizes the linewidths of 28 such spectra taken over the course of about 2 hours. All linewidth values represent lorentzian fits. The high line Q is obviously reproducible as the data is peaked near the Fourier limit, with a mean value (determined by the raw data, not the histogram shape which for small data sets can change as the binning changes) of 2.2 Hz ( $Q = 2 \times 10^{14}$ ). This mean value suggests that going to longer probe times will not help reduce the average linewidth significantly (in fact we have tried this and it did not) as there is an apparent additional broadening mechanism of  $\sqrt{2.2^2 - 1.8^2} = 1.3$  Hz (on average).

In the resolved transition spectroscopy, the most likely source of additional broadening and fluctuations in Fig. 3.20 is the probe laser. We have seen with independent measurements of our two clock lasers that for integration times of 60 s the beat sometimes broadens to nearly 2 Hz. Our measurements here take roughly 30 seconds so one could imagine that over that time scale the laser noise could contribute broadening at the Hz level. Furthermore the spread in the linewidths could be due to residual laser drift which could broaden or reduce the linewidth depending on the relative drift and scan directions. Mechanical vibrations of our spectroscopy layout may also be contributing to the width, as we have seen that the path length shakes a bit when the MOT coils are cycled on an off. Although we know this doesn't degrade the lattice lifetime at the 500 ms timescale, it could result in a residual Doppler broadening if the position of the lattice sites moves relative to the probe laser. Site to site tunneling could also be a source of decoherence.

With the resolved sublevel spectrum we can return to the issue of excitation fraction discussed above. Here we see that only 7-8% of the atoms are excited by the probe laser. If we assume that the population is evenly distributed, only 10% of the atoms were actually in the  $m_F=5/2$  ground state so with resolved

sublevels our excitation fraction is up to around 75%. Since we have removed the dephasing effect that originates from the  $m_F$  dependence of the Rabi frequency, we can assume the limit of 75% originates from the atomic motion effects discussed in the theoretical section. The 25% loss of contrast here is well worth the incredible line  $Q$  the lattice technique allows.

### 3.3.6 Hz-Level Carrier Spectroscopy: Ramsey

Before we are finished with the topic of precision spectroscopy, we will turn our attention to “that other way” of doing things, Ramsey Spectroscopy. For clouds of atoms in free space, Rabi spectroscopy is not very practical for achieving the highest precision. For a cloud of 1  $\mu$ K Sr atoms for example, one will be limited by two effects, the Doppler width of about 40 kHz, and the limited spectroscopy pulse time due to gravity. In the Ca clock system, the Doppler limit on the  $Q$  is eliminated by employing a counter-propagating beam Ramsey spectroscopy [118, 119] setup, enabling widths of a few hundred Hz [24]. The line shape for an atomic resonance when Ramsey’s method is used consists of a  $\text{sinc}^2$  Rabi lineshape with width given by  $0.89/t_R$  (where  $t_R$  is the pulse times), multiplied by a sinusoidal fringe pattern with a period given by  $1/(t_R + t_F)$  and a fringe width of half of that, where  $t_F$  is the free evolution time between the separated pulses (See Fig. 3.21). The central fringe of the Ramsey spectrum is centered on the atomic transition frequency and can be used for metrology. In standard Ramsey spectroscopy the pulse length is set to give a Fourier-limited Rabi envelope equal to the Doppler width of the atoms. Depending on the temperature, this might mean that large probe intensities are needed to excite the atoms, which can result in clock shifts. Fortunately, experimental geometries can be used in which the Doppler width does not affect the Ramsey fringe width, but it does affect the number of fringes which can make central fringe identification difficult. For our Sr

atoms in free space (with a 40 kHz Doppler profile), we would have to deal with more than 10,000 fringes if we wanted a 2 Hz fringe width. Yikes!!!

For our bound atoms on the other hand, there is no Doppler width, so we can use long weak pulses in the Ramsey sequence and drastically reduce the number of fringes in the spectral pattern as well as any light shifts from the probe. Ideally for these measurement one uses a  $\Omega t = \pi/2$  pulse for the Ramsey experiment for the best possible fringe contrast. In the lattice then we should stick to resolved sublevels to keep the Rabi frequency as uniform as possible. Figure 3.21 shows a Ramsey measurement using a pulse sequence with  $t_R=20$ ms and  $t_F=25$  ms, where the pulse intensity has been optimized for maximum fringe contrast. Here we find a narrow fringe pattern with an oscillation period of 20.8(3) Hz corresponding to a fringe width of 10.4(2) Hz. The expected period and width for the times above are 22 Hz and 11 Hz respectively. From the figure, one can see that, in the lattice, identification of the central fringe is trivial since we can use long Rabi pulses in the sequence. The right panel of the figure shows a Ramsey spectrum at the resolution limit of our spectroscopy system. Here a pulse sequence of  $t_R=80$  ms and  $t_F=200$  ms are used and the fringe width of 1.7(1) Hz is achieved, consistent with the predicted value of 1.8 Hz.

A Ramsey sequence certainly adds complexity to the clock system as compared to a single Rabi pulse. It does have its advantages though if one considers the width of the spectral feature which can be achieved in a given measurement time. In Ramsey spectroscopy the central fringe width is given by  $\Delta\nu_{Ramsey} = 1/(2(t_R + t_F))$  while in the single pulse case it is given by  $\Delta\nu_{Rabi} = 0.89/t_R$ . Therefore, if one wants a 10 Hz signal for example, the single pulse fourier limit is about 80 ms, while in the case of Ramsey spectroscopy the equivalent width can be achieved with a 45 ms free evolution time. In this light, it could be advantageous in future work to use the Ramsey method for clock operation as a way to

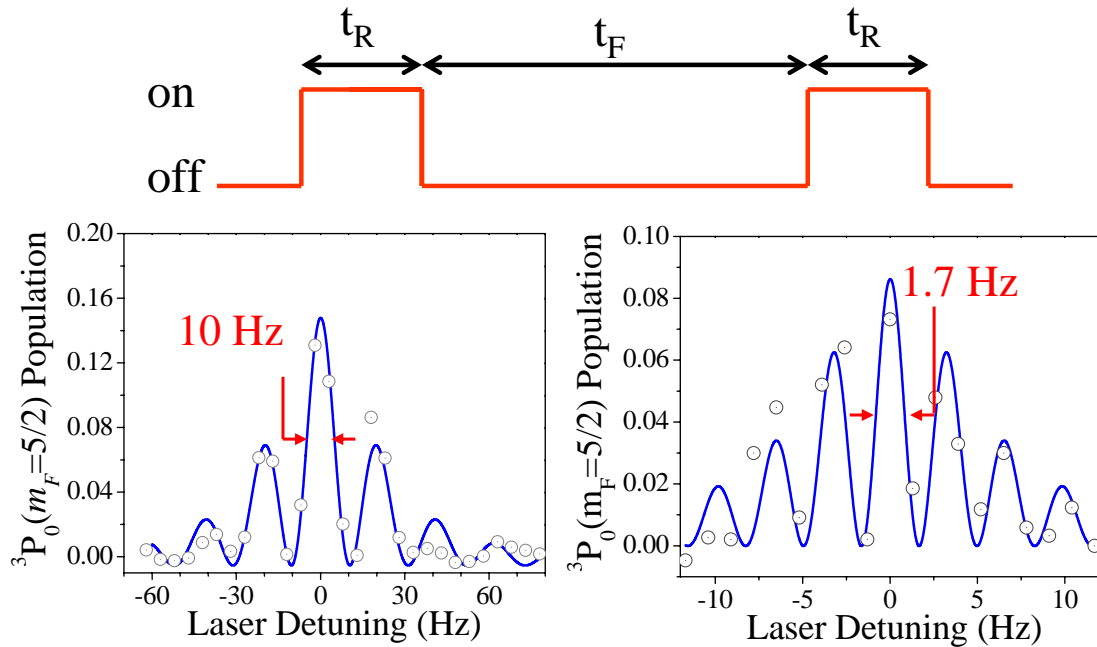


Figure 3.21: Ramsey spectroscopy of the  $^1S_0$ - $^3P_0$  transition in an optical lattice. Ramsey spectroscopy may be a useful alternative to Rabi spectroscopy as narrower features can be observed for the same probe time. The left panel shows such a measurement for a pulse length  $t_R$  of 20 ms and a free evolution time  $t_F = 25$  ms resulting in a spectral feature with a fringe width of 10.4(2) Hz. Note the obvious central fringe identification. The right panel shows a Ramsey fringe where we have pushed the width as narrow as our system allows (as is apparent from the data), with  $t_R = 80$  ms and  $t_F = 200$  ms. The fringe width of 1.7(1) Hz agrees with the expected width (1.8 Hz).

reduce the total cycle time of the experiment. Ramsey spectroscopy can also be used to reduce the fringe width below the limitation resulting from effects such as natural linewidth of the transition or lifetime of atoms in the lattice, although one would expect a degradation of fringe contrast in these cases.

### 3.4 Discussion

Based on the work in this chapter, it seems clear that by using carefully designed optical fields to confine the atoms we can achieve a large  $Q$  competitive with (or in this case slightly larger than) the best trapped ion systems, but

with the significantly enhanced signal to noise ratio of a neutral atom cloud. For the precision side of the clock development, we are assured that the lattice clock system is the real deal. The big question now is whether or not the lattice confinement can be achieved experimentally without degrading the accuracy of the clock. This issue is explored in detail in the remaining chapters.

## Chapter 4

### Nuclear Spin Effects in Optical Lattice Clocks

#### 4.0.1 “ $^1S_0$ - $^3P_0$ Transition? We Forbid It!”— $\vec{J}$ and $\vec{S}$

It looks like the lattice clock will be a success after all. We can achieve record level line  $Q$ 's by eliminated Doppler effects, and the magic wavelength principle seems to work well. But wait, there are a few things that should be making you uneasy right about now. You must be asking yourself: 1) “ $^1S_0$ - $^3P_0$ ? isn't that transition forbidden by the angular momentum selection rules I know and love!” 2) “What was the origin of that broadening in figure 3.19? I thought the magnetic sensitivity of the clock states should be identical.” 3) “If the lattice clock is a success, then why are there  $\sim 50$  more pages of text before you measure the clock frequency?”. The answer to all three of these valid questions is “the nuclear spin”.

It turns out, the presence of nuclear spin in  $^{87}\text{Sr}$  results in a number of remarkable effects which are important to consider for the lattice clock, including the finite lifetime of the  $^3P_0$  state, the magnetic sensitivity of the clock transition, and a small light shift sensitivity of the Zeeman sublevels. Nearly all of the important effects result from state mixing of the  $^3P_0$  state by hyperfine interaction effects. In this chapter, the state mixing is discussed in terms of the origin of the  $^1S_0$ - $^3P_0$  clock transition as well as a basis for evaluating external field sensitivities to explore the potential accuracy of the lattice clock system. In the sections that



follow, nuclear-spin related shifts of the clock states due to both magnetic fields and the lattice trapping potential are discussed. The theoretical development is presented for a general alkaline-earth type structure, using  $^{87}\text{Sr}$  as an example (Fig. 4.1), so that the results can be applied to other species with similar level structure, such as Mg, Ca, Yb, Hg, Zn, Cd,  $\text{Al}^+$ , and  $\text{In}^+$ . Following the theoretical discussion is a detailed experimental investigation of these nuclear spin related effects in  $^{87}\text{Sr}$ , and a comparison to the theory section. At the end of this chapter we take a second look at the feasibility of an optical lattice clock, once the effects of nuclear spin are well understood.

#### 4.1 State Mixing in the $nsnp$ Configuration

To describe the two-electron system in intermediate coupling, we follow the method of Breit and Wills [120] and Lurio [121] and write the four real states as expansions of pure spin-orbit (LS) coupling states,

$$\begin{aligned}
 |^3P_0\rangle &= |^3P_0^0\rangle \\
 |^3P_1\rangle &= \tilde{\alpha}|^3P_1^0\rangle + \tilde{\beta}|^1P_1^0\rangle \\
 |^3P_2\rangle &= |^3P_2^0\rangle \\
 |^1P_1\rangle &= -\tilde{\beta}|^3P_1^0\rangle + \tilde{\alpha}|^1P_1^0\rangle.
 \end{aligned} \tag{4.1}$$

Here the intermediate coupling coefficients  $\tilde{\alpha}$  and  $\tilde{\beta}$  represent the strength of the spin-orbit induced state mixing between singlet and triplet levels, and can be determined from experimentally measured lifetimes of  $^1P_1$  and  $^3P_1$  as is discussed in the next section. This mixing process results in the weakly allowed  $^1S_0$ - $^3P_1$  transition (spin-forbidden by angular momentum selection rules for pure LS states), and has been used for a variety of experiments spanning different fields of atomic physics, including many discussed already in this thesis. In recent years, these intercombination transitions have provided a unique testing ground for studies of

narrow-line cooling in Sr [80, 91, 79, 71, 82] and Ca [83, 84], as well as the previously unexplored regime of photoassociation using long lived states [122, 123, 124]. These transitions have also received considerable attention as potential optical frequency standards [24, 25, 28], owing mainly to the high line  $Q$  and insensitivity to external fields. Fundamental symmetry measurements, relevant to searches of physics beyond the standard model, have also made use of this transition in Hg [125].

In most of the naturally occurring alkaline-earth isotopes, the nuclear spin is zero, so the complexity of the level structure essentially ends with the spin-orbit interaction. The absence of hyperfine structure in these bosonic isotopes is beneficial to many of these fields as the simple level structure lends itself to straightforward comparisons between experiment and theory. The  $^3P_0$  state on the other hand is not affected by the spin-orbit interaction. Thus in the  $I = 0$  isotopes, the  $^1S_0$ - $^3P_0$  clock transition is completely forbidden. To explain the existence of the electric dipole transition we observed in  $^{87}\text{Sr}$  ( $I = 9/2$ ) we need to consider the effect of the hyperfine interaction.

The hyperfine interaction (HFI) in the fermionic isotopes does provide an additional state mixing mechanism between states having the same total spin  $F$ , mixing the pure  $^3P_0$  state with the  $^3P_1$ ,  $^3P_2$  and  $^1P_1$  states.

$$|^3P_0\rangle = |^3P_0^0\rangle + \tilde{\alpha}_0|^3P_1\rangle + \tilde{\beta}_0|^1P_1\rangle + \tilde{\gamma}_0|^3P_2^0\rangle \quad (4.2)$$

The HFI mixing coefficients  $\tilde{\alpha}_0$ ,  $\tilde{\beta}_0$ , and  $\tilde{\gamma}_0$  ( $2 \times 10^{-4}$ ,  $-4 \times 10^{-6}$ , and  $-1 \times 10^{-6}$  respectively for  $^{87}\text{Sr}$ ) can be related to experimental values such as the hyperfine splitting in the  $P$  states, the fine structure splitting in the  $^3P$  states, and the coupling coefficients  $\tilde{\alpha}$  and  $\tilde{\beta}$  [120, 121]. They are calculated explicitly in the next section. The  $^3P_0$  state can also be written as a combination of pure states using

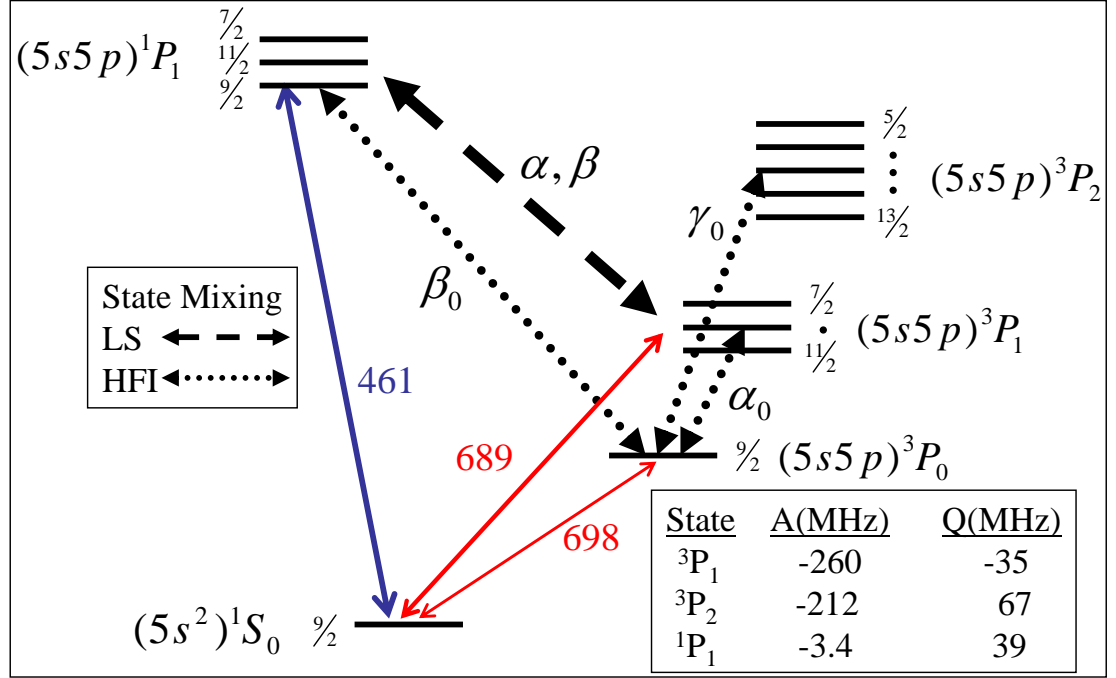


Figure 4.1: Simplified  $^{87}\text{Sr}$  energy level diagram (not to scale). Hyperfine structure sublevels are labeled by total angular momentum  $F$ , and the magnetic dipole ( $A$ ) and electric quadrupole ( $Q$ , equivalent to the hyperfine  $B$  coefficient) coupling constants are listed in the inset. State mixing of the  $^1P_1$  and  $^3P_1$  states due to the spin-orbit interaction is shown as a dashed arrow. Dotted arrows represent the hyperfine induced state mixing of the  $^3P_0$  state with the other  $F = 9/2$  states in the  $5s5p$  manifold.

Eq. 4.1,

$$|^3P_0\rangle = |^3P_0^0\rangle + (\tilde{\alpha}_0\tilde{\alpha} - \tilde{\beta}_0\tilde{\beta})|^3P_1^0\rangle + (\tilde{\alpha}_0\tilde{\beta} + \tilde{\beta}_0\tilde{\alpha})|^1P_1^0\rangle + \tilde{\gamma}_0|^3P_2^0\rangle. \quad (4.3)$$

From Eq. 4.3 we can see that the state mixing due to both the spin-orbit and hyperfine interactions play a role in modifying the  $^3P_0$  wave function by including admixtures of the other states in the  $5s5p$  manifold. This result will be crucial to evaluating a number of effects in the lattice clock including  $^3P_0$  lifetime and the sensitivity to external fields, as it provides a convenient basis of pure LS states for evaluation. The level structure and state mixing discussed here are summarized in a simplified energy diagram, shown in Fig. 4.1, which gives the relevant atomic structure and optical transitions for the  $5s5p$  configuration in  $^{87}\text{Sr}$ .

#### 4.1.1 Calculation of the Mixing Coefficients $\tilde{\alpha}$ , $\tilde{\beta}$ , $\tilde{\alpha}_0$ , $\tilde{\beta}_0$ , and $\tilde{\gamma}_0$

Before we get to the effects of state mixing on the lattice clock, we need to calculate the various mixing coefficients so we can decide just how important each effect is. The intermediate coupling coefficients  $\tilde{\alpha}$  and  $\tilde{\beta}$  are typically calculated from measured lifetimes and transition frequencies of the  $^1P_1$  and  $^3P_1$  states and a normalization constraint  $\tilde{\alpha}^2 + \tilde{\beta}^2 = 1$ . From Eq. 4.1 we can evaluate the lifetime of each state by evaluating the electric dipole matrix element for transitions to the  $^1S_0$  state. For example, using angular momentum selection rules we find for the  $^3P_1$  state  $1/\tau_{3P_1} \propto \omega_{3P_1}^3 \tilde{\beta}^2 |\langle ^1S_0 | \mathcal{D} | ^3P_1 \rangle|^2$ , and the expression for  $\tau_{1P_1}$  is similar with  $\tilde{\beta} \rightarrow \tilde{\alpha}$  and  $\omega_{3P_1} \rightarrow \omega_{1P_1}$ . From those two expressions we can eliminate the matrix element and solve for the mixing coefficients from the measured lifetimes resulting in the expression

$$\frac{\tilde{\alpha}^2}{\tilde{\beta}^2} = \frac{\tau_{3P_1}}{\tau_{1P_1}} \left( \frac{\nu_{3P_1}}{\nu_{1P_1}} \right)^3. \quad (4.4)$$

The energies are well known and the state lifetimes have recently been measured to better than a percent in photoassociation experiments to be  $\tau_{1P_1} = 5.22(3)$  ns [103] and  $\tau_{3P_1} = 21.4(1)$   $\mu$ s [122], resulting in  $\tilde{\alpha} = 0.9996$  and  $\tilde{\beta} = -0.0286(3)$ .

The HFI mixing coefficients  $\tilde{\alpha}_0$ ,  $\tilde{\beta}_0$ , and  $\tilde{\gamma}_0$  are due to the interaction between the pure  $^3P_0$  state and the spin-orbit mixed states in Eq. 4.1 having the same total angular momentum  $F$ . They are defined as

$$\begin{aligned} \tilde{\alpha}_0 &= \frac{\langle ^3P_1, F=I | H_A | ^3P_0^0, F=I \rangle}{\nu_{3P_0} - \nu_{3P_1}} \\ \tilde{\beta}_0 &= \frac{\langle ^1P_1, F=I | H_A | ^3P_0^0, F=I \rangle}{\nu_{3P_0} - \nu_{1P_1}} \\ \tilde{\gamma}_0 &= \frac{\langle ^3P_2, F=I | H_Q | ^3P_0^0, F=I \rangle}{\nu_{3P_0} - \nu_{3P_2}}. \end{aligned} \quad (4.5)$$

Here  $H_A$  and  $H_Q$  are the magnetic dipole and electric quadrupole ( $Q$ , more traditionally written as  $B$ ) contributions of the hyperfine Hamiltonian  $H_{\text{HFI}}$ , given as

$$H_{\text{HFI}} = H_A + H_Q = A \vec{I} \cdot \vec{J} + Q \frac{\frac{3}{2} \vec{I} \cdot \vec{J} (2\vec{I} \cdot \vec{J} + 1) - IJ(I+1)(J+1)}{2IJ(2I-1)(2J-1)}. \quad (4.6)$$

Evaluation of the matrix elements in Eq. 4.5 is non-trivial due to the radial components

of the integral which is exceedingly difficult to calculate for many electron atoms such as Sr. A standard technique for calculating the matrix elements is to relate unknown radial contributions of the wave functions to the measured hyperfine magnetic dipole ( $A$ ) and electric quadrupole ( $Q$ ) coefficients. Calculation of the matrix elements in this way is known as the Breit-Wills (BW) theory and it is discussed in detail in Refs. [120, 121, 87, 126, 35]. Here we only outline the calculation. The hyperfine mixing coefficients ( $\tilde{\alpha}_0$ ,  $\tilde{\beta}_0$ , and  $\tilde{\gamma}_0$ ) can be solved from expressions in Ref. [121, 127] as sums of various radial contributions, known as single-electron hyperfine  $a$  and  $b$  coefficients. The  $a$  and  $b$  coefficients are labeled by superscripts  $TT$ ,  $ST$ , and  $SS$  which denote the origin of the radial integral. The label  $TT$  for example signifies a radial integral between two triplets states, while  $ST$  represents the coefficient for an integral between a singlet and triplet state, and so on. There are also three types of  $a$  coefficients, labeled by subscripts  $s$ ,  $1/2$ , and  $3/2$ , corresponding to different pieces of the hyperfine interaction. Also included are two relativistic corrections,  $\eta'$  and  $\xi'$  of order unity which have been calculated in Ref. [87] for a number of alkaline-earth elements. The result of the matrix element evaluation is

$$\begin{aligned}
\tilde{\alpha}_0 &= \frac{\sqrt{I(I+1)}}{E_{3P_0} - E_{3P_1}} \left[ \frac{\tilde{\alpha}}{\sqrt{6}} \left( a_s^{TT} - a_{1/2}^{TT} - \frac{5}{8} \xi' a_{3/2}^{TT} \right) + \frac{\tilde{\beta}}{2\sqrt{3}} \left( -a_s^{ST} + a_{1/2}^{ST} - \frac{5}{4} \xi' a_{3/2}^{ST} \right) \right] \\
\tilde{\beta}_0 &= \frac{\sqrt{I(I+1)}}{E_{3P_0} - E_{1P_1}} \left[ \frac{-\tilde{\beta}}{\sqrt{6}} \left( a_s^{TT} - a_{1/2}^{TT} - \frac{5}{8} \xi' a_{3/2}^{TT} \right) + \frac{\tilde{\alpha}}{2\sqrt{3}} \left( -a_s^{ST} + a_{1/2}^{ST} - \frac{5}{4} \xi' a_{3/2}^{ST} \right) \right] \\
\tilde{\gamma}_0 &= \frac{1}{E_{3P_0} - E_{3P_2}} \sqrt{\frac{(I+1)(2I+3)}{I(2I-1)}} \frac{\eta'}{4} b_{3/2}^{TT}
\end{aligned} \tag{4.7}$$

The BW theory allows calculation of the  $a$  and  $b$  coefficients using measured

hyperfine splittings  $A$  and  $Q$  of the  $5s5p$  states given by

$$\begin{aligned}
 A_{3P_1} &= \tilde{\alpha}^2 \left( \frac{a_s^{TT}}{4} + \frac{5}{12} \left( 1 - \frac{\xi'}{2} \right) a_{3/2}^{TT} + \frac{a_{1/2}^{TT}}{3} \right) + \tilde{\beta}^2 \left( \frac{5}{6} \left( 1 + \frac{\xi'}{4} \right) a_{3/2}^{SS} + \frac{a_{1/2}^{SS}}{6} \right) \\
 &\quad + 2\tilde{\alpha}\tilde{\beta} \frac{\sqrt{2}}{3} \left( -\frac{3}{4} a_s^{ST} + \frac{5}{4} \left( 1 - \frac{\xi'}{8} \right) a_{3/2}^{ST} - \frac{a_{1/2}^{ST}}{2} \right) \\
 A_{1P_1} &= \text{same as } A_{3P_1} \text{ with } \tilde{\alpha} \rightarrow -\tilde{\beta} \text{ and } \tilde{\beta} \rightarrow \tilde{\alpha}
 \end{aligned} \tag{4.8}$$

$$A_{3P_2} = \frac{a_s^{TT}}{4} + \frac{3a_{3/2}^{TT}}{4}$$

$$Q_{3P_2} = b_{3/2}^{TT}$$

The  $b_{3/2}$  term is trivial if the quadrupole splitting in the  ${}^3P_2$  state is known, and calculation of  $\tilde{\gamma}_0$  using Eq. 4.7 is then complete. The  $a$  terms however are too numerous to be constrained by the measured magnetic dipole terms. Fortunately some of the  $a$  terms are related and we can reduce the number of unknown terms using the following relations[87, 126]

$$\begin{aligned}
 a_s^{SS} &= \lambda_s a_s^{ST} = \lambda_s^2 a_s^{TT} \\
 a_{3/2}^{SS} &= \lambda_p a_{3/2}^{ST} = \lambda_p^2 a_{3/2}^{TT} \\
 a_{1/2}^{SS} &= \lambda_p a_{1/2}^{ST} = \lambda_p^2 a_{1/2}^{TT} \\
 a_{1/2}^{TT} &= 5\theta' a_{3/2}^{TT}
 \end{aligned} \tag{4.9}$$

Where  $\theta'$  is another relativistic factor, and  $\lambda_s$  and  $\lambda_p$  are proportionality constants that relate  $a$  coefficients between different singlet and triplet contributions to the radial integrals.

In the original BW-Theory, it is assumed that the  $a$ -coefficients have no dependence on the singlet or triplet component of the matrix element, and therefore  $\lambda_s$  and  $\lambda_p$  are equal to one and the superscripts on the  $a$  coefficients are not needed. In this case Eqs 4.7–4.9 are drastically simplified and the measured hyperfine  $A$  values are enough to easily evaluate the final hyperfine mixing parameters. The problem then boils down to using the measured  $A$  values to solve for  $a_{3/2}$  and  $a_s$ . In the case of Sr we can also use the value of  $a_{3/2} = -24.8$  MHz from [87] for further simplification and  $a_s$  can be directly calculated using the  $A$  value for the  ${}^3P_1$  state along with Eqs 4.8 and 4.9. In this way

we find that  $a_s = -768$  MHz, leading to  $\tilde{\alpha}_0 = 2.37(1) \times 10^{-4}$  and  $\tilde{\beta}_0 = -4.12(1) \times 10^{-6}$ , where the uncertainty is due to the uncertainty in the  $^1P_1$  and  $^3P_1$  lifetimes. Using the known  $^3P_2$   $Q$  value we also find that  $\tilde{\gamma}_0 = -1.38(1) \times 10^{-6}$ .

The BW theory has been shown to be reliable for predicting the properties of the triplet states in the  $5s5p$  manifold. However, an accurate description of the singlet state requires a modified BW theory (MBW) [127, 87, 126]. For example, if we use the values for  $a_s$  and  $a_{3/2}$  calculated above, in the BW framework ( $\lambda_p = \lambda_s = 1$ ) we can predict the hyperfine  $A$ -factor for the  $^1P_1$  state using Eq. 4.8 to be  $-32.7(2)$  MHz. The experimental value on the other hand is  $-3.4(4)$  MHz [87]. The  $\lambda$  factors in Eq. 4.9 are introduced as a MBW theory to eliminate such discrepancies as they allow for a difference between radial integrals between singlet and triplet states. This is important for accurate calculation of the mixing parameters and hyperfine splitting, especially for  $\tilde{\beta}_0$  and  $A_{1P_1}$ , which depend more strongly on the  $\lambda$  parameters than  $\tilde{\alpha}_0$  or  $A_{3P_1}$  (since  $\tilde{\alpha} \gg \tilde{\beta}$ ). Note that the evaluation of  $b_{3/2}^{TT}$  (and thus  $\tilde{\gamma}_0$ ) is unchanged in the MBW calculation as the  $^3P_2$  state is a pure triplet state, not mixed with any singlet components by the spin-orbit interaction.

In the case of the MBW theory, when we substitute Eq. 4.9 into Eq. 4.8 we are in the situation of having 4 unknowns ( $\lambda_s, \lambda_p, a_{3/2}^{TT}$ , and  $a_s^{TT}$ ) and three equations. Fortunately one of the free parameters can be calculated independently (if the quadrupole coefficients  $Q$  are known) by the formula

$$\lambda_p = \sqrt{\frac{\frac{3(Q_{1P_1} + Q_{3P_1})}{Q_{3P_2}} - \frac{1}{2} + 2\eta'}{1 + 2\eta'}}. \quad (4.10)$$

such that we can solve for the remaining free parameters from the measured hyperfine splitting values  $A_{3P_1}$ ,  $A_{1P_1}$ , and  $A_{3P_2}$ . From this calculation we find  $a_{3/2}^{TT} = -20.7$  MHz,  $a_s^{TT} = -789$  MHz,  $\lambda_s = 1.20$ , and  $\lambda_p = 0.750$ . The resulting mixing coefficients are  $\tilde{\alpha}_0 = 2.56(1) \times 10^{-4}$  and  $\tilde{\beta}_0 = -5.5(2) \times 10^{-6}$  where this time the dominant source for uncertainty is the uncertainty in  $A_{1P_1}$ . Table 4.1 summarizes the results of the BW and MBW calculations performed here, including the values for  $A$ ,  $Q$ ,  $\eta'$ ,  $\xi'$ , and  $\theta'$  that are used.

Table 4.1: Hyperfine Mixing Calculation

<i>Values used in Calculation</i>		
$\tilde{\alpha} = 0.9996, \tilde{\beta} = -0.0286(3),$		
$A_{3P_1} = -260.084 \text{ MHz}, Q_{3P_1} = 35.658 \text{ MHz},$		
$A_{3P_2} = -212.765 \text{ MHz}, Q_{3P_2} = 67.340 \text{ MHz},$		
$A_{1P_1} = -3.4(4) \text{ MHz}, Q_{1P_1} = 39(4) \text{ MHz},$		
$\xi' = 1.018, \eta' = 1.044, \theta' = 1.125$		
<i>Calculation Results</i>		
Parameter	BW Theory	MBW Theory
$a_{3/2}^{TT} \text{ (MHz)}$	-24.8	-20.7
$a_s^{TT} \text{ (MHz)}$	-768	-789
$\lambda_p$	1	0.750
$\lambda_s$	1	1.20
$b_{3/2}^{TT} \text{ (MHz)}$	67.3	67.3
$\tilde{\alpha}_0 (\times 10^4)$	2.37(1)	2.56(1)
$\tilde{\beta}_0 (\times 10^6)$	-4.12(1)	-5.5(1)
$\tilde{\gamma}_0 (\times 10^6)$	-1.38(1)	-1.38(1)

We will save an interpretative discussion of the difference between these two calculations for the end of this chapter, after we have some experimental results in hand. Until then, the magnitudes calculated here will prove valuable in our theoretical discussion of the effects this state mixing has on the lattice clock.

#### 4.1.2 Lifetime of the $^3P_0$ State

Now that we have a good idea of the  $^3P_0$  wave function in the presence of state mixing, we can begin to calculate parameters of interest for the clock transition. Without the hyperfine interaction, the  $^1S_0$ - $^3P_0$  transition is only allowed via a E1M1 two photon decay, which has a lifetime of nearly 1000 years [128]. While a clock transition with a natural linewidth of only a few *pico*-Hz sounds exciting, realistically the system is not possible for a clock. This is because the required probe power to broaden and observe the transition will be significant for realistic interrogation times of a few seconds, causing unmanageably large ac Stark shifts of the clock states. For this reason we need to rely on isotopes with nuclear spin



such that the hyperfine interaction is present.

To calculate the lifetime of the  ${}^3P_0$  state in Eq. 4.3 we can simply evaluate the electric dipole interaction between it and the  ${}^1S_0$  state, yielding  $\tau_{3P_0} \propto (\omega_{3P_0}^3 |\langle {}^1S_0 | \mathcal{D} | {}^3P_0 \rangle|^2)^{-1}$ . The matrix element can be simplified using angular momentum selection rules such that  $\langle {}^1S_0 | \mathcal{D} | {}^3P_0 \rangle = (\tilde{\alpha}_0 \tilde{\beta} + \tilde{\beta}_0 \tilde{\alpha}) \langle {}^1S_0 | \mathcal{D} | {}^1P_1^0 \rangle$ . We see then that the two state mixing mechanisms discussed in the previous sections provide a non-zero electric dipole transition arising from a small admixture of the  ${}^1P_1^0$  state. Once again we can avoid matrix element evaluation by noting that the  ${}^3P_1$  lifetime depends on the same matrix element as  $\tau_{3P_1} \propto (\omega_{3P_1}^3 \tilde{\beta}^2 |\langle {}^1S_0 | \mathcal{D} | {}^1P_1^0 \rangle|^2)^{-1}$ . Then the  ${}^3P_0$  lifetime is given in terms of the measured  ${}^3P_1$  lifetime as

$$\tau_{3P_0} = \left( \frac{\omega_{3P_1}}{\omega_{3P_0}} \right)^3 \frac{\tilde{\beta}^2}{(\tilde{\alpha}_0 \tilde{\beta} + \tilde{\beta}_0 \tilde{\alpha})^2} \tau_{3P_1}. \quad (4.11)$$

From the mixing coefficients in the previous section, the result is  $\tau_{3P_0} = 152(2)$  s for the BW theory and  $\tau_{3P_0} = 110(1)$  s for the MBW theory. The transition linewidth is therefore between 1-1.5 mHz putting a fundamental limit on the achievable line  $Q$  of  $\sim 3 \times 10^{17}$ . This width is out of reach of current state of the art experiments but the linewidth is small enough to leave plenty of room for improvement on the precision side, while being large enough that in current experiments the required probe power is small, only causing shifts at about the 10 mHz level, which can be well characterized. Note that the life time depends almost equally on the two hyperfine mixing parameters  $\tilde{\alpha}_0$  and  $\tilde{\beta}_0$ , while the mixing with the  ${}^3P_2$  state is not important.

## 4.2 Zeeman Shifts from Magnetic Fields

With the obvious advantages in spectroscopic precision of the  ${}^1S_0$ - ${}^3P_0$  transition in an optical lattice, the sensitivity of the clock transition to external field shifts is a central issue in developing the lattice clock as an atomic frequency standard. To evaluate the magnetic sensitivity of the clock states, we continue to follow the treatment of Ref. [121] for the intermediate coupling regime described

by Eqs. 4.1-4.3 in the presence of a weak magnetic field.

We have also explored the Zeeman shifts using a more general treatment for the case of intermediate fields elsewhere [50], where we found that the results for the clock states are identical to the weak field approach taken here below, even for fields as large as  $10^4$  G. Interestingly, we also found that an analytic form can be written for the field dependence of the general alkaline earth  $^1S_0$ ,  $^3P_0$ ,  $^1P_1$ , and  $^3P_1$  state, similar to the traditional Breit-Rabi formula for alkali atoms. These formulas are presented in [50] and are too cumbersome to be given here.

#### 4.2.1 The Linear Zeeman Effect: Hyperfine-Induced Differential $g$ -Factor of the Clock Transition

The Hamiltonian for the Zeeman interaction in the presence of a weak magnetic field  $B$  along the  $z$ -axis is given as

$$H_Z = (g_s S_z + g_l L_z - g_I I_z) \mu_0 B. \quad (4.12)$$

Here  $g_s \simeq 2$  and  $g_l = 1$  are the spin and orbital angular momentum  $g$ -factors, and  $S_z$ ,  $L_z$ , and  $I_z$  are the  $z$ -components of the electron spin, orbital, and nuclear spin angular momentum respectively. The nuclear  $g$ -factor,  $g_I$ , is given by  $g_I = \frac{\mu_I(1-\sigma_d)}{\mu_0|I|}$ , where  $\mu_I$  is the nuclear magnetic moment,  $\sigma_d$  is the diamagnetic correction and  $\mu_0 = \frac{\mu_B}{h}$ . Here,  $\mu_B$  is the Bohr magneton, and  $h$  is Planck's constant. For  $^{87}\text{Sr}$ , the nuclear magnetic moment and diamagnetic correction are  $\mu_I = -1.0924(7)\mu_N$  [129] and  $\sigma_d = 0.00345$  [130] respectively, where  $\mu_N$  is the nuclear magneton. In the absence of state mixing, the  $^3P_0$   $g$ -factor would be identical to the  $^1S_0$   $g$ -factor (assuming the diamagnetic effect differs by a negligible amount for different electronic states), equal to  $g_I$ . However since the HFI modifies the  $^3P_0$  wave function, a differential  $g$ -factor,  $\delta g$ , exists between the two states. This can be interpreted as a paramagnetic shift arising due to the distortion of the electronic

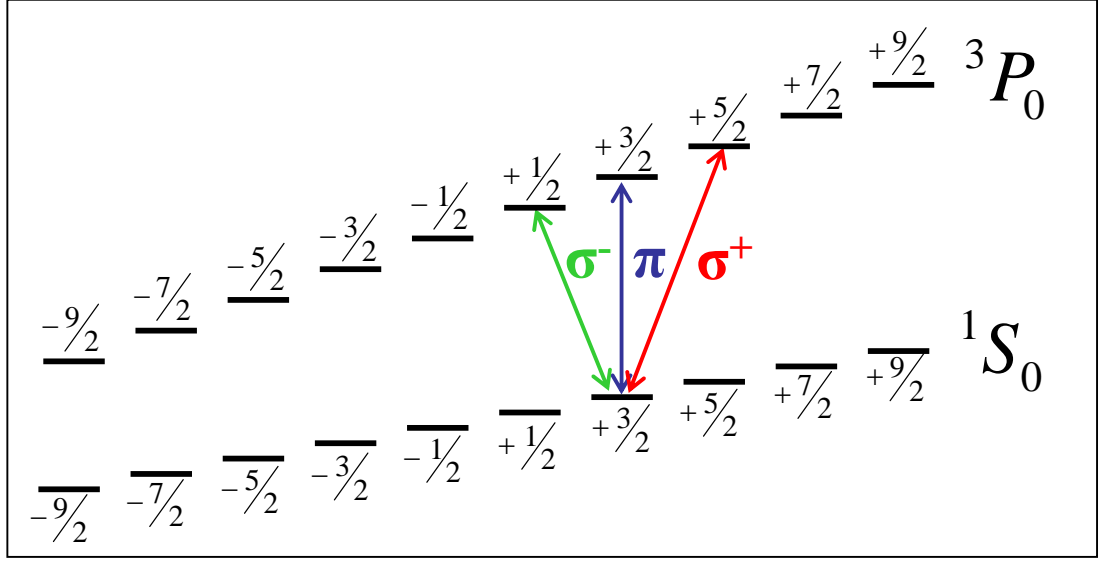


Figure 4.2: Nuclear structure of the  $^1S_0$  and  $^3P_0$  clock states in the presence of a small bias field. The large nuclear spin ( $I = 9/2$ ) results in 28 total transitions, and the labels  $\pi$ ,  $\sigma^+$ , and  $\sigma^-$  represent transitions where  $m_F$  changes by 0, +1, and  $-1$  respectively. The HFI state mixing modifies the  $^3P_0$   $g$ -factor, making the magnitude about 60% larger than that of  $^1S_0$ .

orbitals in the triplet state, and hence the magnetic moment [126].  $\delta g$  is given by

$$\delta g = g^{3P_0} - g_I = -\frac{\langle ^3P_0 | H_Z | ^3P_0 \rangle - \langle ^3P_0^0 | H_Z | ^3P_0^0 \rangle}{m_F \mu_0 B}. \quad (4.13)$$

Using Eq 4.3, the Zeeman matrix elements [121] provided in Table 4.2, and ignoring terms of order 2 or higher in the hyperfine mixing coefficients we find

$$\delta g = -\left(\tilde{\alpha}_0 \tilde{\alpha} - \tilde{\beta}_0 \tilde{\beta}\right) \sqrt{\frac{8}{3I(I+1)}}. \quad (4.14)$$

The mixing results in a modification of the  $^3P_0$   $g$ -factor of  $\sim 60\%$ . Note that the sign in Eq. 4.14 differs from that reported in [126, 35] due to our choice of sign for the nuclear term in the Zeeman Hamiltonian (opposite of that found in Ref. [121]). The resulting linear Zeeman shift  $\Delta_B^{(1)} = -\delta g m_F \mu_0 B$  of the  $^1S_0$ - $^3P_0$  transition is simply given by the mixing calculation yielding  $109.1(1) \times m_F$  Hz/G for the BW theory and  $117.9(5) \times m_F$  Hz/G for the MBW calculation. This linear Zeeman shift (shown schematically in Fig. 4.2) is considered a very important

Table 4.2: Zeeman Matrix Elements for Pure ( $^{2S+1}L_J^0$ ) States

<b>Relevant Elements for the <math>^3P_0</math> State:</b>	
$\langle ^3P_0, F = I   H_Z   ^3P_0, F = I \rangle$	$= -g_I m_F \mu_0 B$
$\langle ^3P_0, F = I   H_Z   ^3P_1, F' = I \rangle$	$= (g_s - g_l) m_F \mu_0 B \sqrt{\frac{2}{3I(I+1)}}$
$\langle ^3P_0, F = I   H_Z   ^3P_1, F' = I + 1 \rangle$	$= (g_s - g_l) \mu_0 B \sqrt{\frac{((I+1)^2 - m_F^2)(4I+6)}{3(I+1)(4(I^2+1)-1)}}$
$\langle ^3P_0, F = I   H_Z   ^3P_1, F' = I - 1 \rangle$	$= (g_s - g_l) \mu_0 B \sqrt{\frac{(I^2 - m_F^2)(4I-2)}{3I(4I^2-1)}}$

systematic effect for the development of lattice clocks, as stray magnetic fields can broaden the clock transition (deteriorate the stability) if multiple sublevels are used. Furthermore, imbalanced population among the sublevels or mixed probe polarizations can cause frequency errors due to line shape asymmetries or shifts. As opposed to the lifetime calculation, the Zeeman sensitivity depends strongly on the  $^3P_1$  mixing and only weakly on the  $^1P_1$  effect ( $|\tilde{\alpha}_0 \tilde{\alpha} / \tilde{\beta}_0 \tilde{\beta}| > 10^3$ ).

#### 4.2.2 The Quadratic Zeeman Effect

The second order Zeeman shift  $\Delta_B^{(2)}$  must also be considered for development of accurate frequency standards. The two clock states are both  $J = 0$  so the shift arises from levels separated in energy by the fine-structure splitting, as opposed to the more traditional case of alkali(-like) atoms where the second order shift arises from nearby hyperfine levels. The shift of the clock transition is dominated by the interaction of the  $^3P_0$  and  $^3P_1$  states since the ground state is separated from all other energy levels by optical frequencies. Therefore, the total Zeeman shift of the clock transition  $\Delta_B$  is given by

$$\Delta_B = \Delta_B^{(1)} + \Delta_B^{(2)} = \Delta_B^{(1)} - \sum_{F'} \frac{|\langle ^3P_0, F, m_F | H_Z | ^3P_1, F', m_F \rangle|^2}{\nu_{^3P_1, F'} - \nu_{^3P_0}}. \quad (4.15)$$

The frequency difference in the denominator is mainly due to the fine-structure splitting and is nearly independent of  $F'$ , and can therefore be pulled out of the

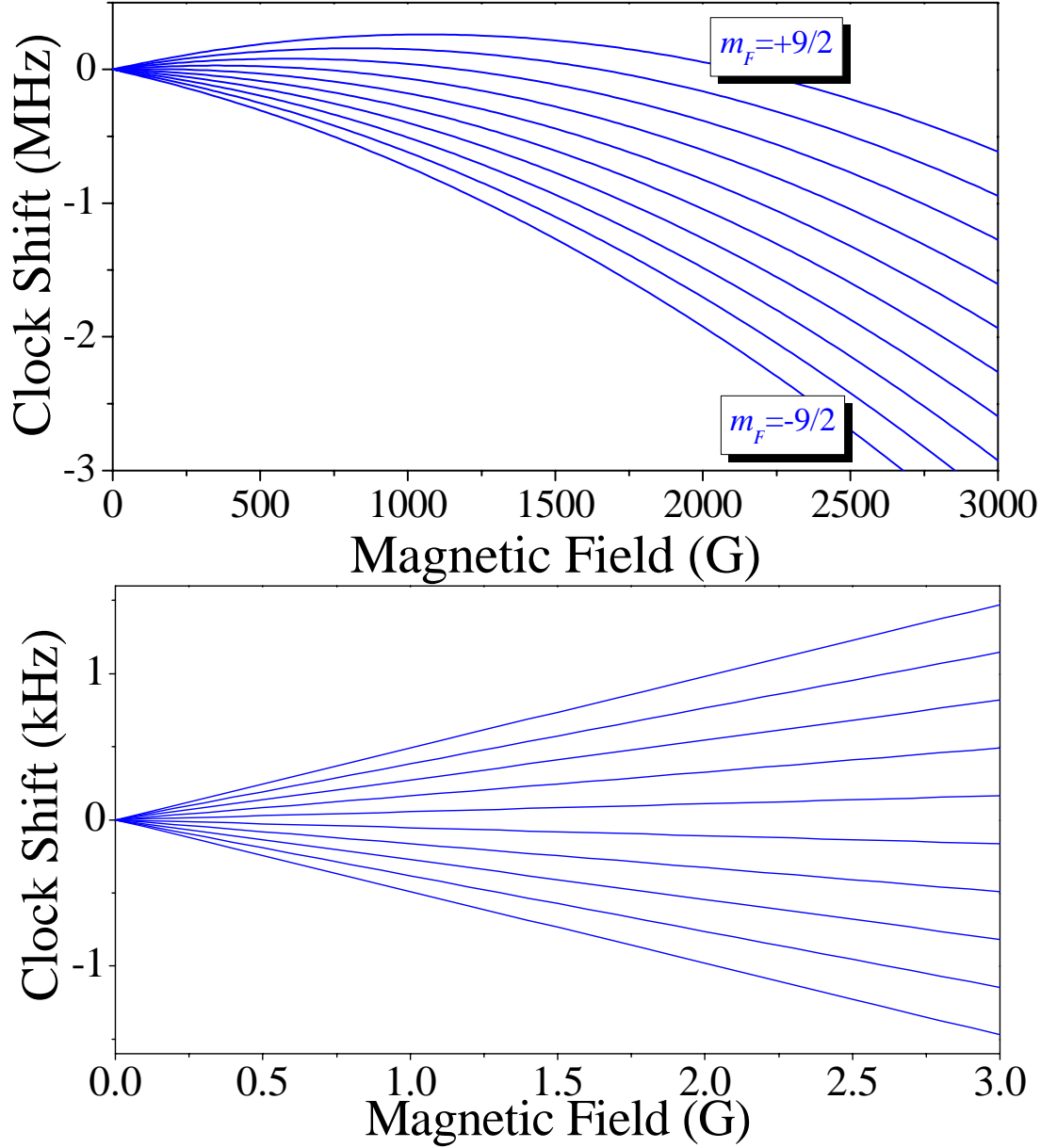


Figure 4.3: A Breit-Rabi-like diagram for the  $^1S_0$ - $^3P_0$  clock transition is shown with  $\delta g\mu_0 = -109$  Hz/G and  $\Delta_B^{(2)} = -0.233$  Hz/G<sup>2</sup>. The top panel gives the shifts of the different sublevels for fields up to 3000 G. The lower panel shows a close up of the shift for a smaller range of fields, more relevant to our experiments. This shows the linear nature of the clock shifts at the fields relevant for the measurements described in the text. Note that the results here are unchanged if we include the Zeeman and hyperfine interaction simultaneously in the Hamiltonian.

summation. In terms of the pure states, and ignoring terms of order  $\tilde{\alpha}_0, \tilde{\beta}_0, \tilde{\beta}^2$ ,

and smaller, we have

$$\Delta_B^{(2)} \simeq -\tilde{\alpha}^2 \frac{\sum_{F'} |\langle {}^3P_0^0, F, m_F | H_Z | {}^3P_1^0, F', m_F \rangle|^2}{\nu_{3P_1} - \nu_{3P_0}} = -\frac{2\tilde{\alpha}^2 (g_l - g_s)^2 \mu_0^2}{3(\nu_{3P_1} - \nu_{3P_0})} B^2, \quad (4.16)$$

where we have used the matrix elements given in Table 4.2 for the case  $F = 9/2$ . From Eq. 4.16 the second order Zeeman shift (given in Hz for a magnetic field given in Gauss) for  ${}^{87}\text{Sr}$  is  $\Delta_B^{(2)} = -0.233B^2$ . This is consistent with the results obtained in Ref. [53] and [57] for the bosonic isotope. Inclusion of the hyperfine splitting into the frequency difference in the denominator of Eq. 4.15 yields an additional term in the second order shift proportional to  $m_F^2$  which is more than  $10^{-6}$  times smaller than the main effect, and therefore negligible. Notably, the fractional frequency shift due to the second order Zeeman effect of  $5 \times 10^{-16} \text{ G}^{-2}$  is nearly  $10^8$  times smaller than that of the Cs [6, 5] clock transition, and more than an order of magnitude smaller than that present in  $\text{Hg}^+$  [29],  $\text{Sr}^+$  [31, 32], and  $\text{Yb}^+$  [33, 34] ion optical clocks.

A Breit-Rabi like diagram is shown in Fig. 4.3, giving the shift of the  ${}^1S_0$ - ${}^3P_0$  transition frequency for different  $m_F$  sublevels (assuming  $\Delta m = 0$  for  $\pi$  transitions), as a function of magnetic field.

### 4.3 Sublevel-Dependent Light Shifts from the Optical Lattice

In this section we consider the effect of the confining potential in terms of the energy shifts of the nuclear sublevels. Our polarizability calculations in Chapter 3 show that the light shift for the  ${}^3P_1$  state (in  ${}^{88}\text{Sr}$  depends strongly on the sublevel  $m_J$ , and the light polarization. For linearly polarized light for example the shift for the  $|m_J|=1$  states is quite different than that of the  $m_J=0$  state (See Fig. 3.4). This is because of the tensor component of the polarizability, which provides shifts proportional to  $m_J^2$ . For the  $J=0$  clock states the tensor shift vanishes (only a  $m_J=0$  state exists) as does the polarization sensitivity. The hyperfine interaction

however provides opportunity for  $m_F$  and polarization dependent shifts that must be considered. Also, the nuclear structure does result in tensor ( $\propto m_F^2$ ) and vector ( $\propto m_F$ ) light shift terms in the atomic polarizability, which depend on the orientation of the relevant electric and magnetic fields. While these effects are expected to be quite small for  $J=0$  states, their magnitudes are important to consider for development of an accurate clock.

### 4.3.1 Case I: Linear Polarization and The Tensor Light Shift

To evaluate the light shift of the clock transition magnetic sub-levels caused by the trapping beam, we first investigate the tensor component of the atomic polarizability. The usual form for the light shift of an  $|F, m_F\rangle$  state is given by [131]

$$\begin{aligned} h\Delta\nu &= -\frac{1}{2}\alpha_i E^2 \\ &= -\left(\alpha^{\text{sc.}} + \alpha^{\text{ten.}} \frac{3m_F^2 - F(F+1)}{F(2F-1)} \frac{3\cos^2\phi' - 1}{2}\right) \frac{E^2}{2} \end{aligned} \quad (4.17)$$

where we have separated out the scalar ( $\alpha^{\text{sc.}}$ ) and tensor ( $\alpha^{\text{ten.}}$ ) components of the polarizability explicitly. The scalar term is common for all sublevels, while the tensor term affects the sublevels with both a common offset, and an  $|m_F|$ -dependent term, with the relative sizes of these two tensor parts determined by  $F$ . The magnitude of the tensor shift also depends on the angle  $\phi'$  between the trap polarization axis and the quantization axis (in this section, we assume that no other external fields are present, such that the lattice geometry defines the quantization axis). In the absence of other fields, a linear polarized beam results in the quantization axis along the light polarization, resulting in  $\phi'=0$  or equivalently  $(3\cos^2\phi' - 1)/2=1$ .

General expressions for the polarizabilities (in terms of reduced matrix elements and angular momentum factors) can be found elsewhere [131, 48] making

the calculation straight forward for a general  $|F, m_F\rangle$  state. The expression for the tensor polarizability is identically zero for states with  $F = 0, 1/2$ . This is easily understood if one considers that in both of these cases there is only one value of  $|m_F|$ . At this point, if your choice of atoms for the lattice clock is  $^{171}\text{Yb}(F=1/2)$  you can skip to the next subsection, for the rest of us let's calculate it!

Unfortunately for us (but fortunately for our accuracy evaluations) the usual expression for the tensor polarizability is insufficient to describe our clock states with  $J=0$  as it is indeterminant. While we could throw our hands up at the situation and call it zero, as much of the literature does (for reasonable reasons), deep down we know there must be some tensor shift with all that hyperfine structure around. For more insight into the issue we can go back to our original expression for the total polarizability given previously as

$$\alpha_i(\omega_L) = 6\pi\epsilon_0 c^3 \sum_k \frac{A_{ik}}{\omega_{ik}^2(\omega_{ik}^2 - \omega_L^2)} \quad (4.18)$$

Now that the hyperfine structure is involved, our original expression for  $A_{ik}$  must be modified and the sum above must be over all states  $J$  and  $F$ . After some angular momentum reduction on our previous expression, the result for  $A_{ik}$  is similar to that in Eq. 3.9 with the usual additional factor of  $(2F_i + 1)(2F_k + 1)\left\{ \begin{matrix} J_i & I & F_i \\ F_k & 1 & J_k \end{matrix} \right\}^2$  along with an appropriate  $3J$  symbol for the  $m_F$  dependence.

$$\frac{\widetilde{A}_{ik}}{A_T} = \frac{(2J_i + 1)(2J_k + 1)\left\{ \begin{matrix} J_i & J_k & 1 \\ L_k & L_i & S \end{matrix} \right\}^2}{\sum_{J=|L_i-S|}^{|L_i+S|} (2J + 1)\left\{ \begin{matrix} J & J_k & 1 \\ L_k & L_i & S \end{matrix} \right\}^2} (2F_k + 1)(2F_i + 1)\left\{ \begin{matrix} J_i & I & F_i \\ F_k & 1 & J_k \end{matrix} \right\}^2 \sum_{m_k=-F_k}^{F_k} \left( \begin{matrix} F_i & 1 & F_k \\ m_i & p & -m_k \end{matrix} \right)^2 \quad (4.19)$$

If we sum Eq. 4.19 over the hyperfine structure of an excited state to determine the geometric scaling factor for  $^3P_0$ , we find that the result is identical to that in Table 3.1 in which the hyperfine structure was ignored (as expected). So we are right back where we started with no  $m_F$  dependent shift for  $^3P_0$ . However, if we include the fact that the hyperfine interaction also changes the relevant transition frequencies ( $\omega_{ik}$ ), then we will have an  $F_k$  dependent frequency which breaks the



symmetry and does in fact result in a  $m_F^2$  dependence. This method of including the hyperfine splitting was also used in the original lattice clock proposal of Katori [39]. Note that this is not a contradiction of our previous statement that the tensor polarizability is undefined for  $J=0$ , the derivation used for the other result simply ignores a small correction due to the hyperfine level shifts because it is negligibly small in most cases [132].

To estimate the size of this effect, we note that the tensor shift of the clock transition should be dominated by the shift of the  $^3P_0$  state because of the relative size of the hyperfine splitting in the excited triplet states, as compared to that of the  $^1P_1$  state. Ideally we would like to include the hyperfine splitting of all of the excited states for the  $^3P_0$  shift, but the limited availability of experimental hyperfine data leads to settling for just the  $^3S_1$  state [90]. This is still a reasonable approximation for the tensor shift since that state provides a significant fraction of the total  $^3P_0$  light shift at the magic wavelength. The total polarizability is calculated (at 813 nm) using Eq. 4.19 and 4.18 along with the data in Table 3.2, with the term for the lowest lying  $^3S_1$  set to include the hyperfine splitting (HFS) for different values of  $F_k$ . The result is plotted (green circles) in the upper panel of Fig. 4.4 for different ground state  $m_F$  values. For comparison, the result without the hyperfine splitting is shown as black squares. The hyperfine energy correction does in fact result in an  $m_F^2$  dependent polarizability. To extract the tensor polarizability the data is fit to Eq. 4.17 (with  $\phi'=0$ ) resulting in  $\alpha^{\text{ten.}} = -1.6 \times 10^{-7}$  a.u..

Another interesting calculation is to consider the effect that the hyperfine state mixing has on the tensor light shift of the  $^3P_0$  state. In the previous sections of this chapter we showed that state mixing is *THE* important consideration for a number of effects, suggesting we take that into account for our polarizability calculation. We can therefore also try an additional approach where we instead

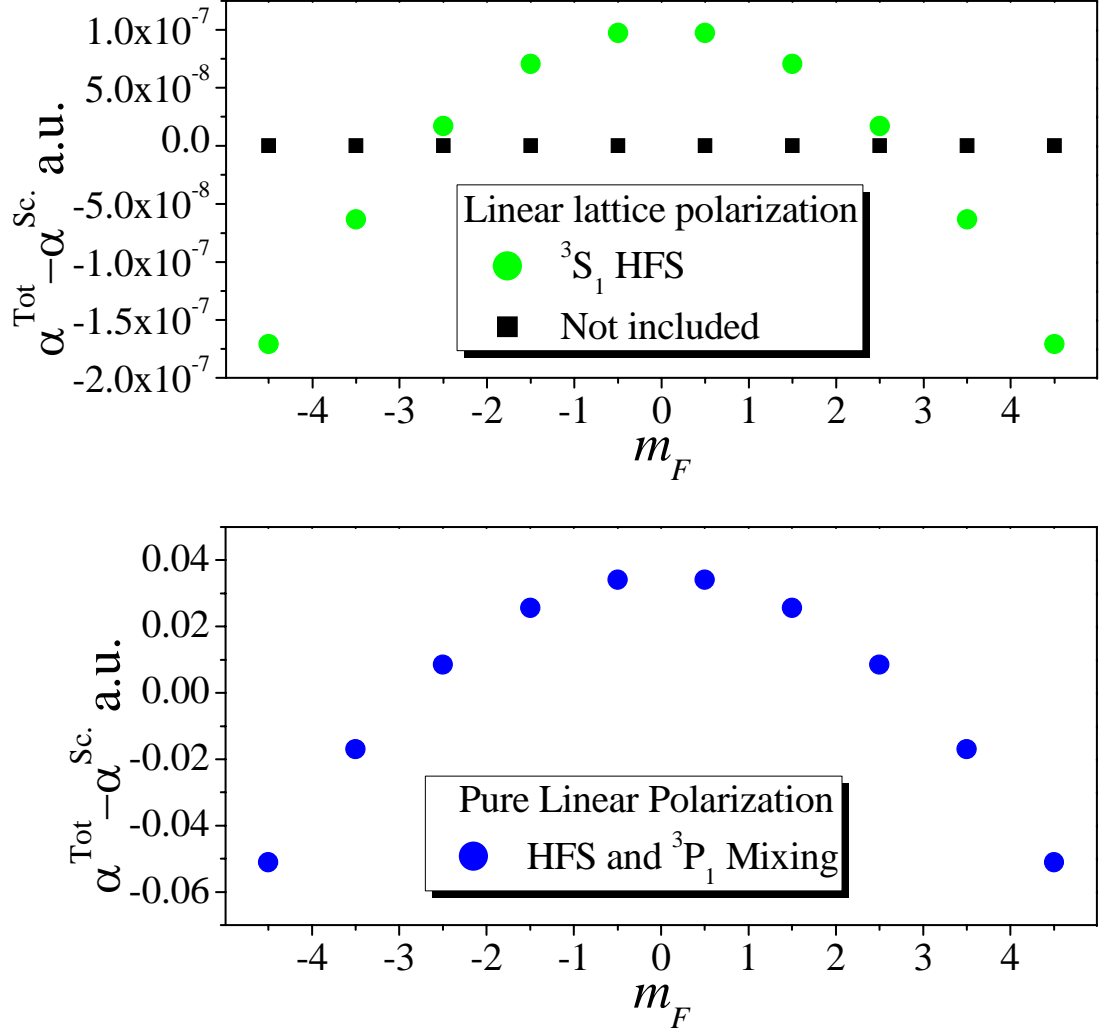


Figure 4.4: The upper panel shows the result of the polarizability calculation in atomic units for purely linear polarized light both with (green circles) and without (black squares) including the hyperfine energy shifts in the  ${}^3S_1$  state. The scalar polarizability ( $\alpha^{\text{Sc.}}$ ) is subtracted off of the total polarizability for convenience. From the data we find that the scalar portion of the polarizability is not effected by the hyperfine correction, but the tensor component is increased from zero to  $\alpha^{\text{ten.}} = -1.6 \times 10^{-7}$  a. u.. The lower panel shows the result of the polarizability calculation if the  ${}^3P_1$  state mixing is included. Here we find that both the scalar and tensor component are altered. The scalar component is altered by less than 0.1% (beyond the precision of our earlier scalar calculations). The tensor component is drastically altered, increasing by orders of magnitude compared to the hyperfine splitting calculation, to  $\alpha^{\text{ten.}} = -0.051$  a.u..

calculate the  ${}^3P_0$  polarizability by taking into account the mixing with the  ${}^3P_1$

( $F = 9/2$ ) state. In light of the results in Fig. 3.4 for the  ${}^3P_1$  state with linear polarization, where the tensor shift has a similar magnitude as the scalar shift, this is worth looking into even with the small reduction factor from the state mixing. We then calculate the total polarizability for the state  $|\phi_i\rangle = |{}^3P_0\rangle \simeq |{}^3P_0^0\rangle + \tilde{\alpha}_0|{}^3P_1, F = 9/2\rangle$  by the relation

$$\begin{aligned} \alpha_i(\omega_L) &= \frac{2e^2}{\hbar} \sum_k \frac{\omega_{ik} |\langle \phi_k | \mathfrak{D} | \phi_i \rangle|^2}{(\omega_{ik}^2 - \omega_L^2)} \\ &= \frac{2e^2}{\hbar} \sum_k \frac{\omega_{ik}}{(\omega_{ik}^2 - \omega_L^2)} \left( |\langle \phi_k | \mathfrak{D} | {}^3P_0 \rangle|^2 + \tilde{\alpha}_0^2 |\langle \phi_k | \mathfrak{D} | {}^3P_1, F = 9/2 \rangle|^2 \right. \\ &\quad \left. + 2\tilde{\alpha}_0 |\langle {}^3P_0 | \mathfrak{D} | \phi_k \rangle \langle \phi_k | \mathfrak{D} | {}^3P_1, F = 9/2 \rangle| \right) \end{aligned} \quad (4.20)$$

The first term in the summation in Eq. 4.20 simply yields the  ${}^3P_0$  polarizability calculated previously. If we ignore the energy difference between the  ${}^3P_0$  and  ${}^3P_1$  states, then the second term is simply the  ${}^3P_1(F = 9/2)$  polarizability, scaled down by the nuclear spin mixing coefficient squared. These first two terms can then be calculated using the polarizability defined in Eqs. 4.18 and 4.19, and  $\tilde{\alpha}_0 = 2.4 \times 10^{-4}$ . As we saw above, the first term does not contribute any tensor component unless the HFS energy splitting is included. For the second term we find the tensor component of the  ${}^3P_1(F = 9/2)$  polarizability is -125 a.u., yielding a contribution of  $-5.0 \times 10^{-6}$  a.u. for the tensor polarizability of the  ${}^3P_0$  state. We therefore see that the state mixing can provide a larger tensor contribution than the hyperfine energy correction. The third term in Eq. 4.20 (the cross term) can provide an even larger contribution to the tensor shift since it only has one order of  $\tilde{\alpha}_0$ . To estimate the contribution for this term we again ignore the  $5s5p$  fine structure and relate the matrix elements to atomic lifetimes using Eq. 3.7, 4.19, and 4.18. We find that inclusion of this larger mixing term further increases the tensor polarizability by a few orders of magnitude compared to the other terms.

The results of the complete polarizability calculation are shown in the lower

panel of Fig. 4.4. The polarizability of the different  $m_F$  sublevels is plotted for pure linear polarization, including the effect of the  $^3S_1$  HFS, the  $\tilde{\alpha}_0^2$  mixing term, and the larger mixing cross term. The state mixing results in a small change in the static polarizability (negligible at our calculation accuracy), but more importantly, the tensor component is dramatically larger than it was in the calculation where only the hyperfine splitting was included. A fit of the data yields  $\alpha^{\text{ten.}} = -0.051$  a.u..

We will find later on in this chapter, that the estimated contribution from the mixing cross term in Eq. 4.20 is actually too large given the experimental data. This could be because of our approximation used, or the ignoring of the other state mixing contributions such as  $^3P_2$ , which has a smaller mixing coefficient but should have a significant tensor shift due to the larger  $J = 2$ . Even if we ignore the large cross term, we still find enhancement in the tensor component from state mixing suggesting that for accurate calculation of the tensor light shift, the state mixing from the hyperfine interaction must be accounted for. The calculation here predicts that state mixing provides a tensor shift significantly larger than that in Katori's original proposal [39]. It also contradicts the suggestion in the Yb proposal (Ref. [47]) that the tensor shift will vanish. Obviously with the contradictions in different calculations, it will be essential to measure the effect.

### 4.3.2 Case II: Circular Polarization and The Vector and Tensor Light Shifts

For pure linearly polarized light we are finished with the issue of sublevel dependent light shifts. But, in the real world we know our laser light will have some small admixture of circular polarization so we would like to see how that affects the different sublevels. We will first look at light shifts for a pure circularly polarized beam, and then consider general polarizations in the next subsection.

For pure circular polarization (still in the absence of other fields), the total light shift is given by

$$h\Delta\nu = - \left( \alpha^{\text{Sc.}} + \alpha^{\text{vect.}} \frac{m_F}{2F} \xi - \alpha^{\text{ten.}} \frac{3m_F^2 - F(F+1)}{2F(2F-1)} \right) \frac{E^2}{2} \quad (4.21)$$

where  $\alpha^{\text{vect.}}$  is the vector (or axial) polarizability, and  $\xi$  is the degree of ellipticity of the light field. For pure circular (linear) polarization,  $\xi=+/-1$  ( $\xi=0$ ). The vector light shift can be simply described as an effective magnetic field  $d\vec{B}$  along the propagation axis, with the magnitude of  $d\vec{B}$  determined by the atomic properties, light intensity, and  $\xi$ . The tensor term from Eq. 4.17 is still present in the light shift, but now the quantization axis is defined by the light propagation axis such that  $\phi'=\pi/2$  and  $(3\cos^2\phi' - 1)/2 = -1/2$ . Because of the change in quantization axis, the tensor light shift is smaller than in the linear polarized case by a factor of 2, and will have an opposite sign.

Once again we find ourselves in a situation where we cannot rely on the standard formulas for  $\alpha^{\text{vect.}}$  and  $\alpha^{\text{ten.}}$  since  $J=0$ . We take the same approach as in the previous subsection and calculate two effects on the polarizabilities. First, we calculate the polarizability by including the  $^3S_1$  hyperfine splitting, again using Eq. 4.18, this time with circular polarization ( $p=1$ ). Once again we find that if the hyperfine splitting is not included, the vector polarizability is zero. With the splitting included, the result is shown in Fig. 4.5 as green triangles. Fitting the data using Eq. 4.21, we find  $\alpha^{\text{vect.}}=1.49\times 10^{-2}$  a.u. and  $\alpha^{\text{ten.}}=-1.6\times 10^{-7}$  a.u.. As expected, the tensor polarizability is identical to what we calculated before for the HFS approximation, so the geometrical factors are correct (a nice consistency check).

As we did before, we can also include the  $^3P_1$  state mixing to calculate the polarizability. Looking again at the results of Fig. 3.4, the  $^3P_1$  vector polarizability should be similar in size to the tensor polarizability. Unlike with the tensor

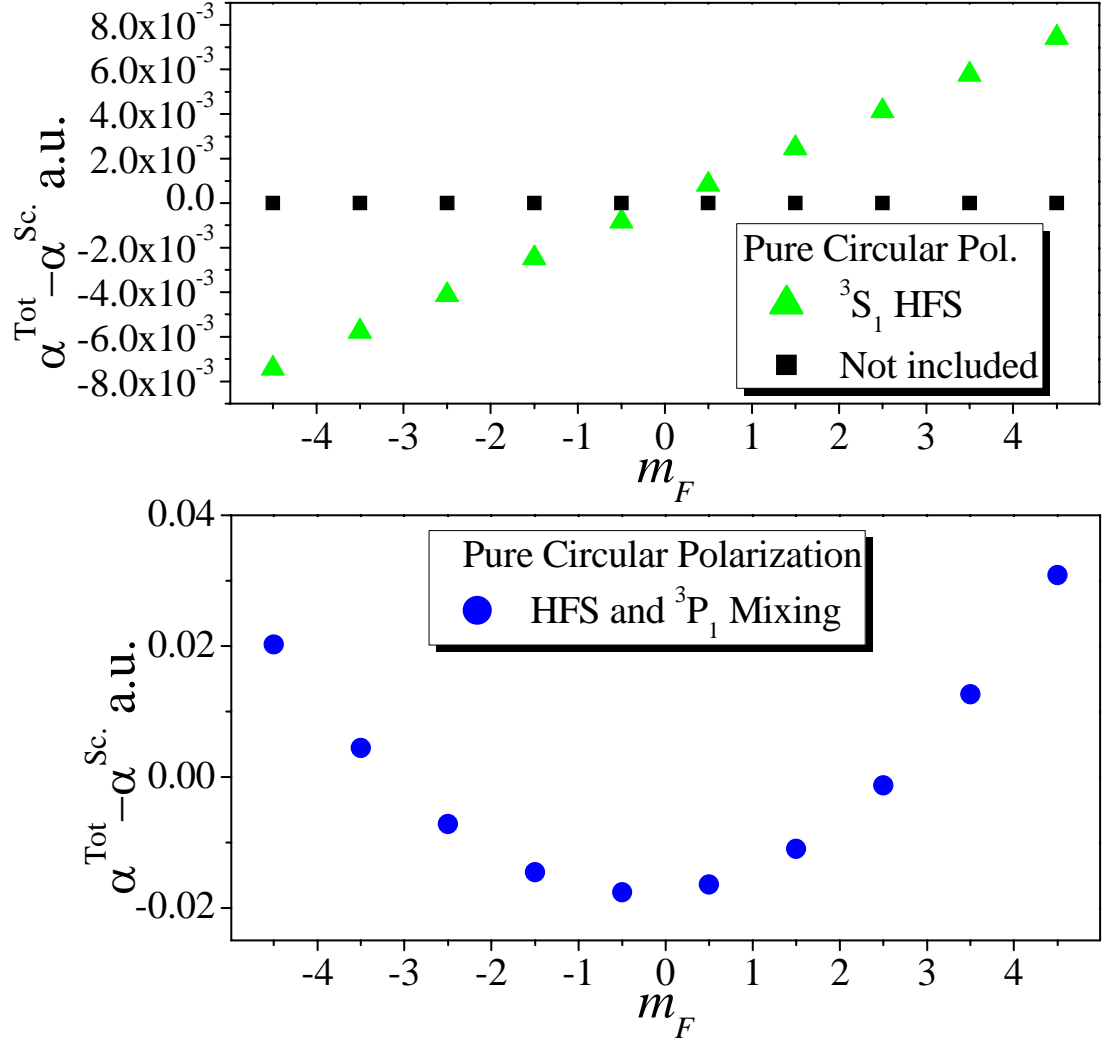


Figure 4.5: Results of the polarizability calculation of the  $^3P_0$   $m_F$  states. If state mixing and hyperfine energy splitting is ignored (black squares), the vector and tensor components are zero, resulting in identical polarizations for different  $m_F$  states. If the hyperfine splitting is included (green triangles), vector and tensor components arise with magnitude 0.0149 a.u. and  $-1.6 \times 10^{-7}$  a.u. respectively. If we also include the  $^3P_1$  state mixing along with the hyperfine splitting (lower panel), the tensor term drastically increases to -0.051 a.u., while the vector term is slightly reduced to 0.0106 a.u..

component, the vector shift of the  $^3P_0$  state originating from the hyperfine splitting is larger than any vector component the mixing can provide. The calculation agrees with this logic, as we find the  $^3P_1(F = 9/2)$  vector polarizability is -57.5 a.u., leading to values of  $\alpha^{\text{vect.}} = -2.3 \times 10^{-6}$  a.u. and  $\alpha^{\text{ten.}} = -5.0 \times 10^{-6}$  a.u. for

the  ${}^3P_0$  state using the  $\tilde{\alpha}_0^2$  mixing term. The contribution is even larger for the mixing cross term (by roughly a factor of  $\tilde{\alpha}_0$ ). The lower panel of Fig. 4.5 shows the polarizability calculation if the HFS and two state mixing terms are included. A fit to the data using Eq. 4.21 yields  $\alpha^{\text{vect.}}=1.06\times 10^{-2}$  a.u. and  $\alpha^{\text{ten.}}=-0.051$  a.u.. Once again we find the state mixing provides a larger tensor shift, however in the case of the vector shift, the hyperfine splitting in the excited states appears to be the dominant effect. In Ref. [47] it was found that in Yb the vector contribution from the state mixing was larger than that from the HFS in the excited states. This is not necessarily inconsistent with our results here as we found the contributions to be of the same order, the difference could simply boil down to differences in the atomic parameters.

From analysis of these two special cases, we can see that for a truly accurate calculation of these different polarizability values, one needs to carefully take into account the hyperfine energy correction to all the excited states, as well as the state mixing caused by the nuclear spin. While the calculations here give reasonable estimates for these values, more complete analysis will be necessary for comparison with future experimental data.

### 4.3.3 Case III: Light Shifts for Arbitrary Light Polarization

With estimates for the various polarizabilities of  ${}^3P_0$  in hand, the sublevel-dependent light shift calculation (still assuming the  ${}^3P_0$  state dominates the effect) can be completed for the case of either pure circular or pure linear polarization as we can use Eq. 4.21 or 4.17. The polarizability values are given in Table 4.3, organized by the effect considered for each calculation.

For the general case of elliptical polarization, discussion of the light shift is complicated by the fact that in the two extreme cases (pure linear or circular) the quantization axis is defined along different axes. To calculate the polarization

dependence we have to take a more general approach where the full light shift hamiltonian is evaluated for a given degree of circular  $\xi$  or linear  $l = \sqrt{1 - \xi^2}$  polarization. Following the derivation of Ref. [48], where we assume the absence of other external fields, the diagonal matrix elements  $w_{m_F, m'_F}$  representing the circular polarization light shift case are given by

$$w_{m_F, m'_F} = -\frac{1}{2} \left( \alpha^{\text{Sc.}} + \frac{m_F}{2F} \alpha^{\text{vect.}} - \frac{3m_F^2 - (F(F+1))}{2F(2F-1)} \alpha^{\text{ten.}} \right). \quad (4.22)$$

For pure circular polarization ( $\xi = \pm 1, l = 0$ ), the light shift matrix is diagonal and we recover the result in Eq. 4.21 where the quantization axis is defined by the light propagation direction. If the light contains some mixture of linear polarization ( $\xi \neq \pm 1, l \neq 0$ ) the matrix is no longer diagonal and the quantization axis is not well defined. We then introduce off diagonal contributions given by

$$w_{m_F \pm 2, m'_F} = -\frac{3\sqrt{1 - \xi^2} \sqrt{(F \pm m_F + 1)(F \pm m_F + 2)(F \mp m_F - 1)(F \mp m_F)}}{4(2F - 1)(2F)} \alpha^{\text{ten.}}. \quad (4.23)$$

In the case when pure linear polarization is used, inclusion of these off diagonal elements in the hamiltonian exactly reproduces the result in Eq. 4.17 where the quantization is defined by the light polarization. Using the matrix elements above, we can calculate the energy shifts for a general polarization, characterized by  $\xi$ , as long as the polarizabilities are known. Here we are mostly interested in the shifts of the Zeeman sublevels relative to the scalar shift common to all states,

Table 4.3:  ${}^3P_0$  Polarizabilities: Scalar, Vector and Tensor

${}^3P_0$  Polarizabilities calculated at 813nm.

Parameter	${}^3S_1$ HFS	$\tilde{\alpha}_0^2$ Mixing Term	${}^3S_1$ HFS, $\tilde{\alpha}_0^2$ and $\tilde{\alpha}_0$ Mixing Terms
$\alpha^{\text{ten.}}$	$-1.6 \times 10^{-7}$ a.u.	$-5.0 \times 10^{-6}$ a.u.	-0.051 a.u.
$\alpha^{\text{vec.}}$	0.0149 a.u.	$-2.3 \times 10^{-6}$ a.u.	0.0106 a.u.
$\alpha^{\text{Sc.}}$	282 a.u.	282 a.u.	282 a.u.



so we will ignore  $\alpha^{\text{Sc.}}$ . We will consider two cases: first we calculate the polarization dependent light shift assuming the HFS is the only interaction, resulting in  $\alpha^{\text{ten.}}=-1.6\times 10^{-7}$  a.u. and  $\alpha^{\text{vect.}}=0.0149$  a.u. from the previous subsections. Second, we will use the polarizability found when the state mixing is included with the HFS yielding  $\alpha^{\text{ten.}}=-0.051$  a.u. and  $\alpha^{\text{vect.}}=0.0106$  a.u.. These two cases allow us to explore the polarization sensitivity in different regimes where in one case the vector shift is dominant and in the other, the tensor shift is dominant. While we expect the second calculation to be more complete, our measurements in a later section show that the upper limit for the tensor contribution is an order of magnitude smaller than the calculation predicts. Since the complete polarizability calculation is apparently not very accurate it is useful to consider both cases until more exact polarizability values have been measured.

The  $^3P_0$  state has  $F=9/2$ , so you'll have to forgive me for diagonalizing the 10 by 10 light shift matrix numerically to solve for the energy shifts. The top panel of Fig. 4.6 shows the result for the HFS polarizability parameters in Table 4.3, as  $\xi$  is varied between -1 and 1. For convenience, the light shift is reported in two ways. First, on the left axis, the light shift of the Zeeman levels is given in relative units, divided by the large scalar light shift. This is useful if the scalar light shift in an experiment is known (e.g. from the side band spectrum) as it gives the shifts in terms of a fraction of the scalar shift. The right axis simply gives the relative shift of the Zeeman levels in units of frequency for the typical lattice depth  $U_0=35E_R$ , used in this work. Note that the two extreme cases  $\xi = \pm 1$  and  $\xi = 0$  are equivalent to the results in Figs. 4.4 and 4.5. We can see that the vector component of the light shift is dominant for most polarization ranges, such that the quantization axis is defined by the lattice propagation axis. The middle panel shows a close up of the HFS calculation for small deviations from perfect linear polarization. For values of  $\xi$  below  $10^{-4}$  the tensor effect is dominant and the

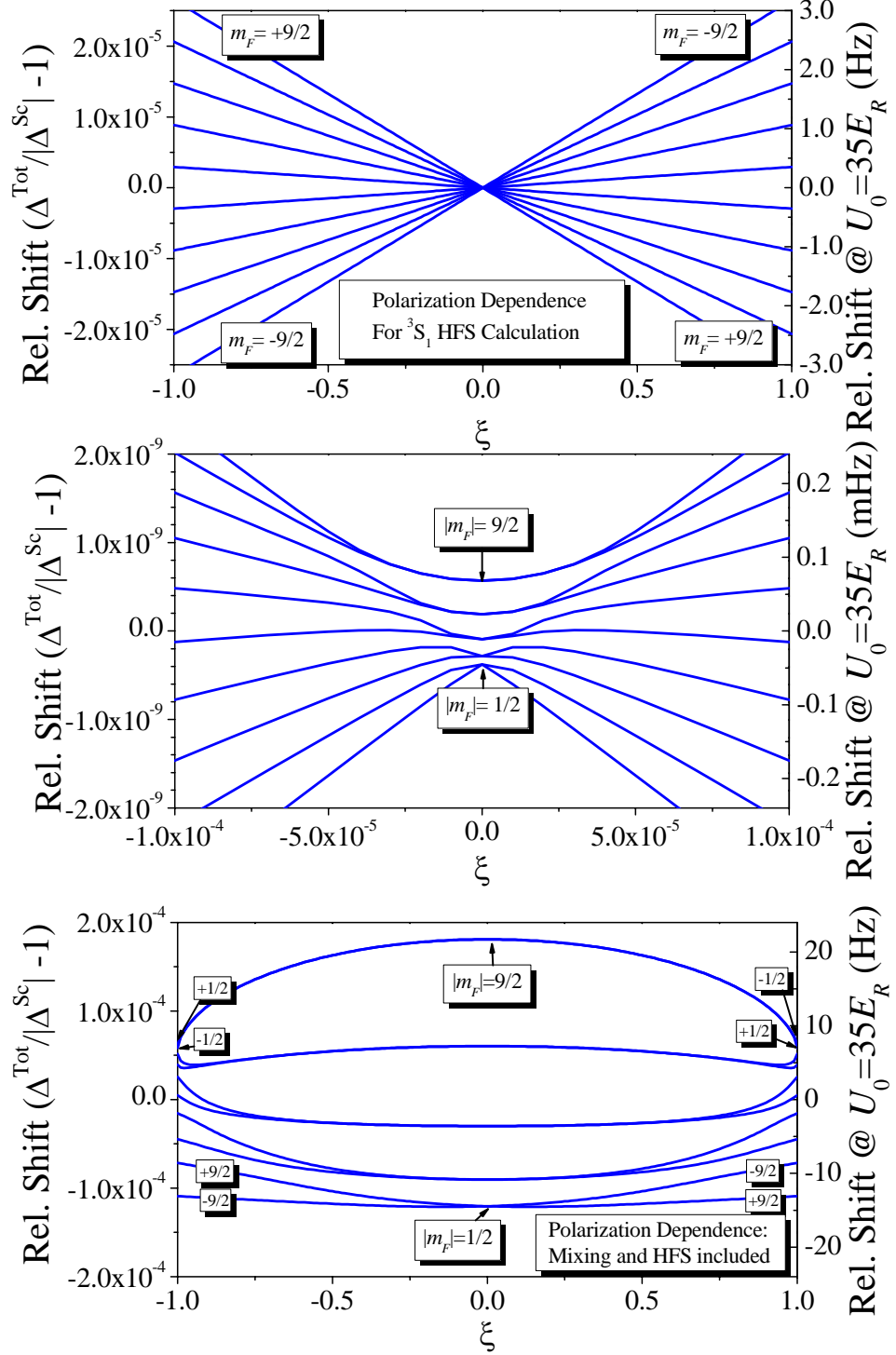


Figure 4.6: Shifts of the  $^3P_0$  sublevels are plotted vs. lattice ellipticity  $\xi$ . The shifts are given both in fractional units (relative to the scalar light shift), and in units of frequency for  $U_0 = 35E_R$ . The first two panels show the results for the HFS polarizability calculation while the lower panel includes the  $^3P_1$  state mixing.

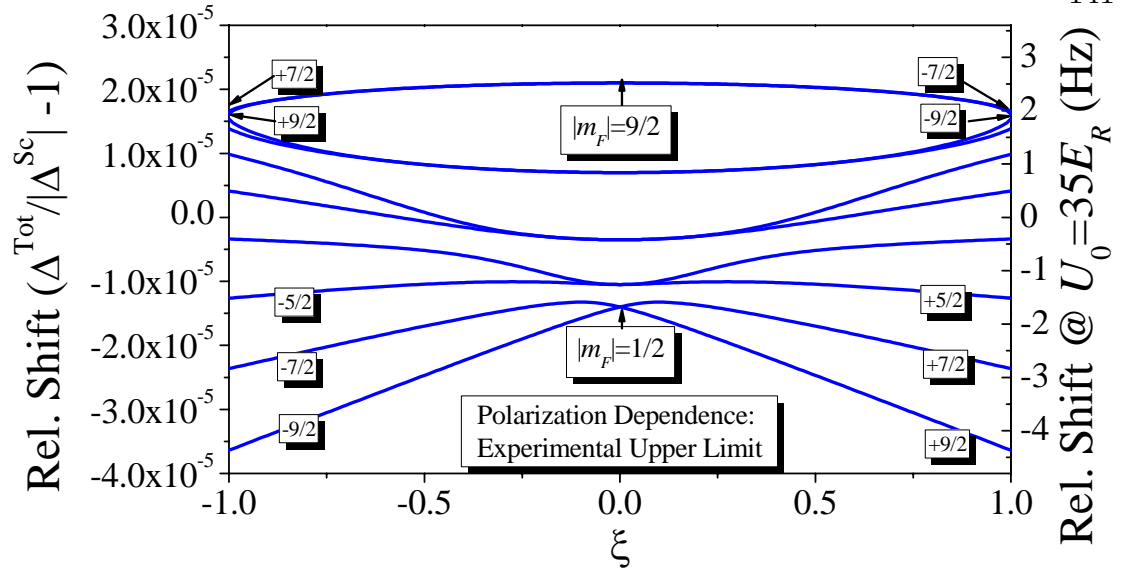


Figure 4.7: Calculation of the Zeeman-like light shifts when the experimental upper limit from this work is used for the tensor polarizability,  $\alpha^{\text{ten.}} = -0.006$ .

quantization axis is well defined by the linear lattice polarization. The magnetic sublevels are labeled at the special case polarizations where they are well defined ( $\xi = 0, \pm 1$ ).

The bottom panel in the Figure gives a similar calculation, this time using the polarizabilities obtained from the more complete evaluation which includes the state mixing. In this case we find the tensor contribution is dominant over a large range of polarizations. According to Fig. 4.6, the tensor shift is significant, as large as 20 Hz for the  $|m_F| = 9/2$  state. As mentioned earlier, this predicted shift is inconsistent with our experimental data. For example, the 5 Hz spectra presented in Fig. 3.19 was taken with nearly-zero field and with nearly-linear lattice polarization such that any  $m_F$ -dependent light shift is at most causing a 4 Hz broadening. From Fig. 4.6 we would expect the broadening to be 10s of Hz. Furthermore in the next section of this chapter (Section 4.4.2, we make direct measurements of the tensor shift which allow us to constrain the shift to an order of magnitude less than that predicted here. In light of this overestimate

from our theory, we also calculate the polarization dependence of the light shift assuming a worst-case scenario where the experimental upper limit for the tensor polarizability of  $-0.006$  a.u. is used along with the largest theoretically predicted (in this work) vector polarizability of  $0.0149$  a.u.. The result, plotted in Fig. 4.7 represents a more accurate estimate of the potential sublevel light shifts than that in Fig. 4.6.

We have now completely solved the state dependent light shift issue for arbitrary polarizations, in the absence of other external fields. In the future, when the polarizabilities have all been measured, we can return to this issue to plot the exact dependence.

#### 4.3.4 Case IV: Light Shift in the Presence of an External Magnetic Field

One final case which is useful to consider for realistic experiments, is the light shift sensitivity when a bias magnetic field is used to define the quantum axis. Here we will consider the special case where the bias field is orthogonal to the lattice propagation axis. If the quantum axis is well defined by a magnetic field, we know that by changing the polarization of the lattice we cannot completely change the quantum axis as we did before. The effective magnetic field  $d\vec{B}$  caused by any circular component of the polarization will now be orthogonal to the bias field  $B$ . For a large bias field,  $B \gg d\vec{B}$ , the quantum axis will be essentially unchanged. As Fig. 4.6 shows, for pure circular polarization at our typical trap depth, the contribution of the vector light shift for the stretched state is  $\sim 3\text{Hz}$ . Given the  $^3P_0$  total  $g$ -factor of  $295 m_F \text{ Hz/G}$ , the vector shift is equivalent to a magnetic field of  $2.2 \text{ mG}$ . Thus for fields on the order of  $100 \text{ mG}$ ,  $B \gg d\vec{B}$  is well satisfied. In this situation the effect of the vector shift is reduced by a geometric factor of  $\cos \varphi$ , where  $\varphi$  is the angle between the lattice propagation direction and

the bias magnetic field [133]. The tensor shift term is unchanged, still having the same  $3 \cos^2 \phi' - 1$  dependence, remembering that  $\phi'$  is the relative angle between the light polarization direction and the quantum axis, now defined by the bias field. In this case, the total light shift is given by

$$h\Delta\nu = - \left( \alpha^{sc.} + \alpha^{vect.} \xi \cos \varphi \frac{m_F}{2F} + \alpha^{ten.} \frac{3m_F^2 - F(F+1)}{F(2F-1)} \frac{3 \cos^2 \phi' - 1}{2} \right) \frac{E^2}{2}. \quad (4.24)$$

Careful consideration of Eq. 4.24 reveals that the Zeeman light shift sensitivities in a clock can be dramatically reduced with an appropriate choice of geometry and polarization. If the light is linearly polarized, we enjoy a reduction factor of  $\xi$  on the vector term, as we saw before. If the bias field is aligned orthogonally to the light propagation axis ( $\varphi \simeq \pi/2$ ), the vector contribution is further reduced by a factor  $\cos \varphi \approx \delta\varphi$ , where  $\delta\varphi$  is the misalignment relative to perfect orthogonal orientation. In this situation, the angle  $\phi'$  is the angle between the linear polarization and the bias magnetic field in the plane orthogonal to the light propagation. Note that if linear polarization is guaranteed, the tensor component can then in principle be eliminated if  $\phi' \simeq 57.4^\circ$  as  $(3 \cos^2[57.4^\circ] - 1) \rightarrow 0$  as pointed out in [133].

### 4.3.5 Summary of Nuclear-Spin Related Shifts

Now that we have explored the various nuclear spin-related shifts in the lattice clock, we will combine all the effects into one master equation which can be used to estimate frequency shifts when both electric and magnetic fields are present. For our experimental situation where the lattice field  $E$  is linearly polarized ( $\xi \simeq 0$ ) along the quantum axis ( $\phi' \simeq 0, \varphi \simeq \pi/2$ ) as defined by an external magnetic field  $B$  (see Fig. 4.8), the level shifts for the two clock states (from

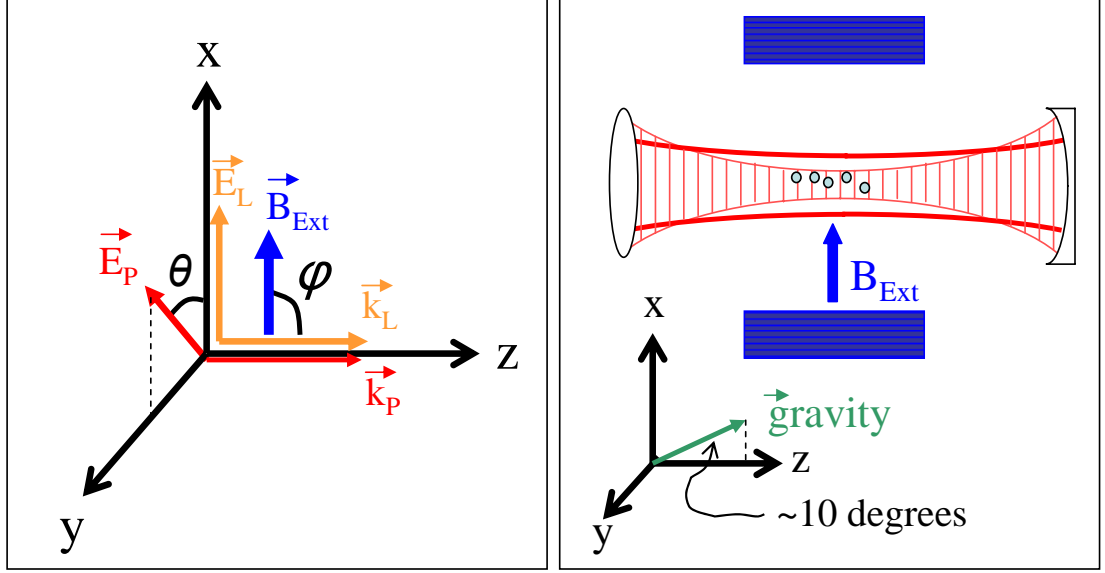


Figure 4.8: Setup for experimental investigation of nuclear spin effects. The lattice and probe propagate along the  $z$ -axis. The lattice polarization  $\vec{E}_L$  is fixed along the  $x$ -axis while the probe polarization  $\vec{E}_P$  can be varied by an angle  $\theta$  relative to the lattice polarization, in the  $xy$ -plane. The magnetic field  $\vec{B}_{ext}$  is aligned along the  $x$ -axis such that the angle  $\phi'$  between the quantum axis and lattice polarization is zero, and the angle  $\varphi$  between the quantum axis and light propagation axis is  $\pi/2$ . The right panel shows the orientation of the system relative to gravity, which is offset from  $z$ , in the  $yz$  plane, by about 10 degrees.

Eqs. 4.15 and 4.24) are given by  $h\Delta\nu$  with

$$\begin{aligned}\Delta\nu_e &= -m_F(g_I + \delta g)\mu_0 B - \left( \alpha_e^{sc.} + \alpha_e^{vec.} \xi \delta\varphi \frac{m_F}{2F} + \alpha_e^{ten.} \frac{3m_F^2 - F(F+1)}{F(2F-1)} \right) \frac{E^2}{2h} \\ \Delta\nu_g &= -m_F g_I \mu_0 B - \left( \alpha_g^{sc.} + \alpha_g^{vec.} \xi \delta\varphi \frac{m_F}{2F} + \alpha_g^{ten.} \frac{3m_F^2 - F(F+1)}{F(2F-1)} \right) \frac{E^2}{2h}\end{aligned}\quad (4.25)$$

Where the subscripts  $e$  and  $g$  refer to the excited ( $^3P_0$ ) state and ground ( $^1S_0$ ) state respectively. Here we have omitted the second order Zeeman shift  $\Delta_B^{(2)}$  for simplicity, and the reader is reminded that from the previous section, this effect has negligible dependence on  $m_F$ . Hyperpolarizability effects ( $\propto E^4$ ) [41, 39, 48, 47] are ignored as they are negligible in  $^{87}\text{Sr}$  at the level of  $10^{-17}$  for the range of lattice intensities used in current experiments [41].

As we are nearing the discussion of the measurement of some of these shifts

(finally), it is convenient to re-write Eq. 4.25 in terms of the lattice trap depth  $U_T$  in units of the energy of a lattice photon recoil  $E_R$ , where  $U_T/E_R$  characterizes the lattice intensity. This is a naturally way to describe the light shift effects as  $U_T$  can be directly measured using sideband spectroscopy. The light shift terms can then be written as shift coefficients for the scalar ( $\kappa^S$ ), vector ( $\kappa^V$ ), and tensor ( $\kappa^T$ ) interactions, with units of  $\text{Hz}/(U_T/E_R)$ .

$$\begin{aligned}\Delta\nu_e &= -m_F(g_I + \delta g)\mu_0 B - (\kappa_e^S + \kappa_e^V \xi \delta\varphi m_F + \kappa_e^T (3m_F^2 - F(F+1))) \frac{U_T}{E_R} \\ \Delta\nu_g &= -m_F g_I \mu_0 B - (\kappa_g^S + \kappa_g^V \xi \delta\varphi m_F + \kappa_g^T (3m_F^2 - F(F+1))) \frac{U_T}{E_R}.\end{aligned}\quad (4.26)$$

Using Eq. 4.26 we can then write the frequency of  $\pi$ -transitions ( $\Delta m_F = 0$ ) from a ground state sublevel  $m_F$  as

$$\begin{aligned}\nu_{\pi m_F} &= \nu_c - (\Delta\kappa^S - \Delta\kappa^T F(F+1)) \frac{U_T}{E_R} - (\Delta\kappa^V m_F \xi \delta\varphi + \Delta\kappa^T 3m_F^2) \frac{U_T}{E_R} \\ &\quad - \delta g m_F \mu_0 B,\end{aligned}\quad (4.27)$$

where the shift coefficients due to the differential polarizabilities are represented as  $\Delta\kappa$ , and  $\nu_c$  is the bare clock frequency. The basic principle of the lattice clock technique is to tune the lattice wavelength (and hence the polarizabilities) such that the intensity-dependent frequency shift terms are reduced to zero. Due to the  $m_F$ -dependence of the third term of Eq. 4.27, the Stark shifts cannot be completely compensated for all of the sublevels simultaneously. Or equivalently, the magic wavelength will be different depending on the sublevel used. The significance of this effect depends on the magnitude of the tensor and vector terms relative to the scalar term. The scalar shift coefficient is simple since the trap depth  $U_T$  is in fact *defined* by the scalar light shift of the ground state. Therefore, near the magic wavelength we have  $\kappa_{1S_0}^S \simeq \kappa_{3P_0}^S = 3.4 \times 10^3 \text{ Hz}/(U_T/E_R)$  (where 3.4 kHz is really just  $E_R/h$ ). Using our polarizability calculations from the previous section, along with the relevant scaling factors in Eq. 4.25, we find  $\kappa_{3P_0}^T = -2 \times 10^{-3} \text{ Hz}/(U_T/E_R)$

and  $\kappa_{3P_0}^V = 2 \times 10^{-2} \text{ Hz}/(U_T/E_R)$  where again we have used the experimental upper limit for the tensor shift. As before, we estimate that the state-dependent light shift of the clock transition will be dominated by the  $^3P_0$  contribution such that  $\Delta\kappa^T \simeq \kappa_{3P_0}^T$  and  $\Delta\kappa^V \simeq \kappa_{3P_0}^V$ .

The frequencies of  $\sigma^\pm$  ( $\Delta m_F = \pm 1$ ) transitions from a ground  $m_F$  state will also prove useful in our experimental analysis. They are similar to the  $\pi$ -transitions, given by

$$\begin{aligned} \nu_{\sigma_{m_F}^\pm} = & \nu_c - (\Delta\kappa^S - \Delta\kappa^T F(F+1)) \frac{U_T}{E_R} - ((\kappa_e^V(m_F \pm 1) - \kappa_g^V m_F) \xi \delta\varphi) \frac{U_T}{E_R} \\ & - (\kappa_e^T 3(m_F \pm 1)^2 - \kappa_g^T 3m_F^2) \frac{U_T}{E_R} - (\pm g_I + \delta g(m_F \pm 1)) \mu_0 B. \end{aligned} \quad (4.28)$$

#### 4.4 Experimental Determination of Nuclear Spin Effects

To explore the magnitude of the various  $m_F$ -dependent shifts in Eq. 4.27, a differential measurement scheme is used to eliminate the large shifts common to all levels. Using resolved sublevels one can extract  $m_F$  sensitivities by measuring the splitting of neighboring transitions. This is the approach taken here. To resolve the nuclear sublevels, a Helmholtz coil pair provides a field along the lattice polarization axis. Two other coil pairs are used along the other axes to zero the orthogonal fields. To explore both  $\pi$  and  $\sigma$  transitions, the probe laser is linearly polarized at an angle  $\theta$  relative to the quantum axis. The orientation of all of the relevant fields in the setup is shown in Fig. 4.8.

##### 4.4.1 Precision Measurement of $\delta g$

When the probe polarization is oriented parallel to the quantization axis ( $\theta = 0$  in Fig. 4.8), the ground state atoms undergo  $\pi$ -transitions ( $\Delta m_F = 0$ ). The large nuclear spin provides ten possible transitions, as shown in Fig. 4.2. The high spectral resolution provided by the lattice clock technique allows for the



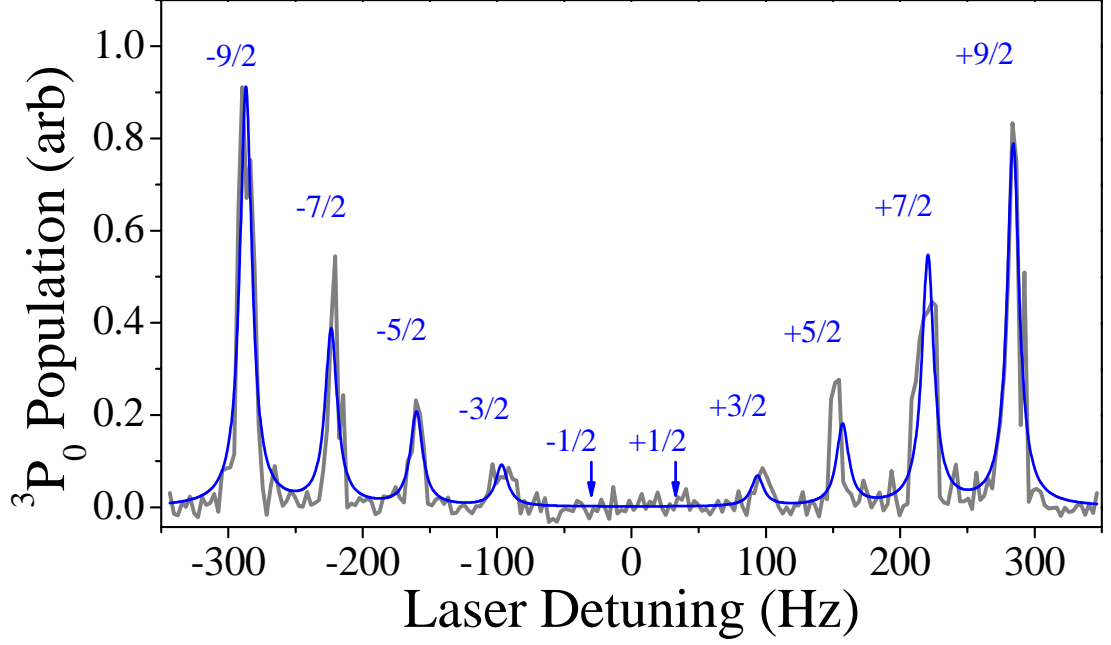


Figure 4.9: Observation of the  $^1S_0$ - $^3P_0$   $\pi$ -transitions ( $\theta = 0$ ) in the presence of a 0.58 G magnetic field. Data is shown in grey and a fit to the eight observable lineshapes is shown as a blue curve. The relative transition amplitudes for the different sublevels are strongly influenced by the Clebsch-Gordan coefficients. Here, Fourier limited transition linewidths of 10 Hz are used.

study of nuclear spin effects at small bias fields, as the ten sublevels can easily be resolved with a few hundred mG. An example of this is shown in Fig. 4.9, where the transitions are observed in the presence of a 0.58 G bias field. This is important for achieving a high accuracy measurement of  $\delta g$  as the contribution from magnetic-field-induced state mixing is negligible. To extract the desired shift coefficients we note that for the  $\pi$  transitions we have a frequency gap between neighboring lines of

$$f_{\pi, m_F} = \nu_{\pi m_F} - \nu_{\pi m_F - 1} = -\delta g \mu_0 B - \Delta \kappa^V \xi \delta \varphi \frac{U_T}{E_R} - \Delta \kappa^T 3(2m_F - 1) \frac{U_T}{E_R}. \quad (4.29)$$

From Eq. 4.29, we see that by measuring the differences in frequency of two spectroscopic features, the three terms of interest ( $\delta g$ ,  $\Delta \kappa^V$ , and  $\Delta \kappa^T$ ) can be determined independently. The differential  $g$  factor can be determined by vary-

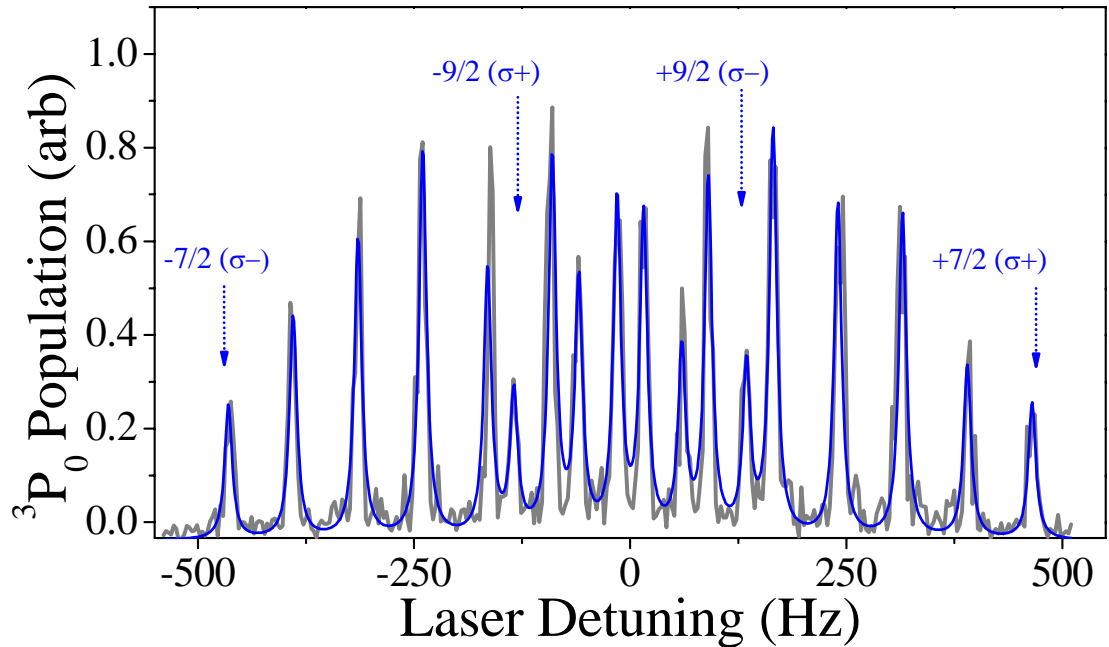


Figure 4.10: Observation of the 18  $\sigma$  transitions when the probe laser polarization is orthogonal to that of the lattice ( $\theta = \frac{\pi}{2}$ ). Here, a field of 0.69 G is used. Data is shown in grey and a fit to the eight observable lineshapes is shown as a blue curve. The peaks are labeled by the ground state sublevel of the transition and the relevant polarization. The relative transition amplitudes for the different sublevels are strongly influenced by the Clebsch-Gordan coefficients. Here, Fourier limited transition linewidths of 10 Hz are used.

ing the magnetic field. The contribution of the last two terms can be extracted by varying the intensity of the standing wave trap, and can be independently determined since only the tensor shift depends on  $m_F$ .

While the  $\pi$  transitions allow a simple determination of  $\delta g$ , the measurement requires a careful calibration of the magnetic field and a precise control of the probe laser frequency over the  $\sim 500$  seconds required to produce a scan such as in Fig. 4.9. Any linear laser drift will appear in the form of a smaller or larger  $\delta g$ , depending on the laser scan direction. Furthermore, the measurement can not be used to determine the sign of  $\delta g$  as an opposite sign would yield an identical spectral pattern.

In an alternative measurement scheme, we instead polarize the probe laser

perpendicular to the lattice polarization axis ( $\theta = \frac{\pi}{2}$ ) to excite both  $\sigma^+$  and  $\sigma^-$  transitions ( $\Delta m_F = \pm 1$ ). In this configuration, 18 spectral features are observed and easily identified (Fig. 4.10). For now we ignore small shifts due to the lattice potential,  $\delta g$  is then given by extracting the frequency splitting between adjacent transitions of a given polarization (all  $\sigma^+$  or all  $\sigma^-$  transitions) as  $f_{\sigma^\pm, m_F} = \nu_{\sigma_{m_F}^\pm} - \nu_{\sigma_{m_F-1}^\pm} = -\delta g \mu_0 B$ . If we also measure the frequency difference between  $\sigma^+$  and  $\sigma^-$  transitions from the same sublevel,  $f_{d, m_F} = \nu_{\sigma_{m_F}^+} - \nu_{\sigma_{m_F}^-} = -2(g_I + \delta g)\mu_0 B$ , we find that the differential  $g$ -factor can be determined from the ratio of these frequencies as

$$\delta g = \frac{g_I}{\frac{f_{d, m_F}}{2f_{\sigma^\pm, m_F}} - 1}. \quad (4.30)$$

In this case, prior knowledge of the magnetic field is not required for the evaluation, nor is a series of measurement at different fields, as  $\delta g$  is instead directly determined from the line splitting and the known  $^1S_0$   $g$  factor  $g_I$ . The field calibration and the  $\delta g$  measurement are in fact done simultaneously, making the method immune to some systematics which could mimic a false field, such as linear laser drift during a spectroscopic scan or slow magnetic field variations. Using the  $\sigma$  transitions also eliminates the sign ambiguity which persists when using the  $\pi$  transitions for measuring  $\delta g$ . While we can not extract the absolute sign, the recovered spectrum is sensitive to the relative sign between  $g_I$  and  $\delta g$ . This is shown explicitly in Fig. 4.11 where the positions of the transitions have been calculated in the presence of a  $\sim 1$  G magnetic field. Figure 4.11(a) shows the spectrum when the signs of  $g_I$  and  $\delta g$  are the same while in Fig. 4.11(b) the signs are opposite. The two plots show a qualitative difference between the two possible cases. Comparing Fig. 4.10 and Fig. 4.11 it is obvious that the hyperfine interaction **increases** the magnitude of the  $^3P_0$   $g$ -factor ( $\delta g$  has the same sign as  $g_I$ ). We state this point explicitly because of recent inconsistencies in theoretical

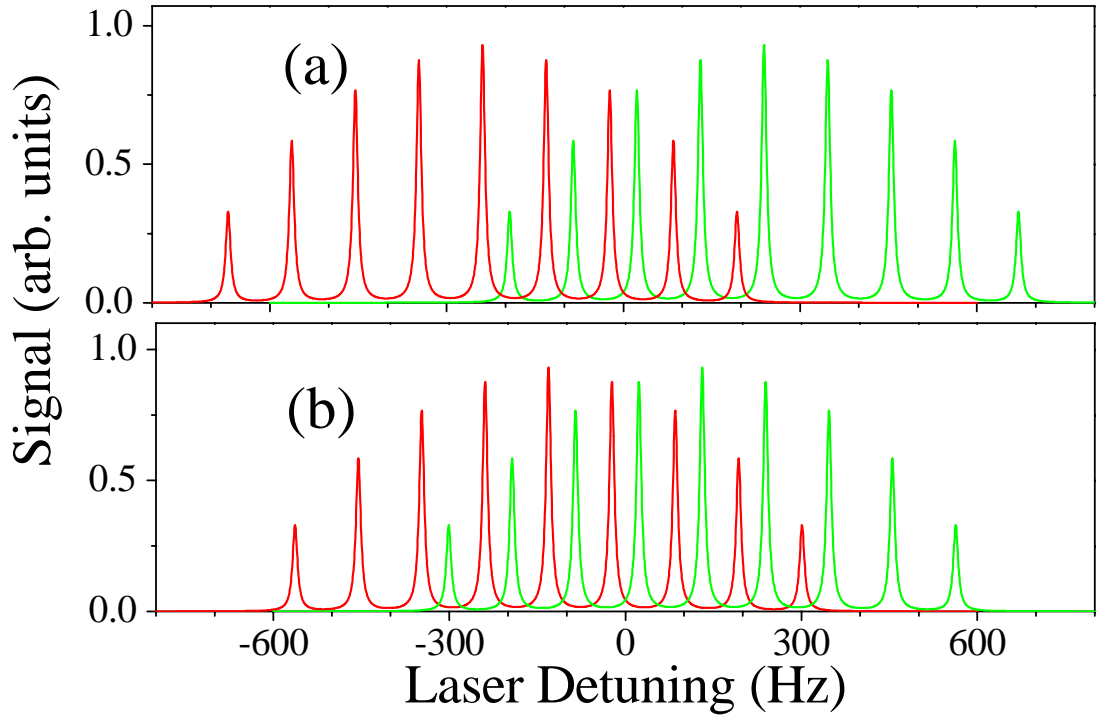


Figure 4.11: Calculation of the 18  $\sigma$  transition frequencies in the presence of a 1 G bias field, including the influence of Clebsch-Gordan coefficients. The green (red) curves show the  $\sigma^+$  ( $\sigma^-$ ) transitions. (a) Spectral pattern for  $g_I\mu_0 = -185$  Hz/G and  $\delta g\mu_0 = -109$  Hz/G. (b) Same pattern as in (a) but with  $\delta g\mu_0 = +109$  Hz/G. The qualitative difference in the relative positions of the transitions allows determination of the sign of  $\delta g$  compared to that of  $g_I$ .

estimates of the relative sign of  $\delta g$  and  $g_I$  in the  $^{87}\text{Sr}$  literature [46, 45].

To extract the magnitude of  $\delta g$ , data such as in Fig.4.10 are fit with eighteen Lorentzian lines, and the relevant splitting frequencies  $f_{d,m_F}$  and  $f_{\sigma^\pm}$  are extracted. Due to the large number of spectral features, each experimental spectrum yields 16 measurements of  $\delta g$ . A total of 31 full spectra was taken, resulting in an average value of  $\delta g\mu_0 = -108.4(4)$  Hz/G where the uncertainty is the standard deviation of the measured value. To check for sources of systematic error, the magnetic field was varied to confirm the field independence of the measurement. We also varied the clock laser intensity by an order of magnitude to check for Stark and line pulling effects. It is also necessary to consider potential measurement errors

due to the optical lattice since in general the splitting frequencies  $f_{d,m_F}$  and  $f_{\sigma\pm}$  will depend on the vector and tensor light shifts. For fixed fields, the vector shift is indistinguishable from the linear Zeeman shift (see Eqs. 4.27-4.29) and can lead to errors in calibrating the field for a  $\delta g$  measurement. In this work, a high quality linear polarizer ( $10^{-4}$ ) is used which would in principle eliminate the vector shift. However, any birefringence of the vacuum windows or misalignment between the lattice polarization axis and the magnetic field axis can lead to a non-zero value of  $\xi$  and  $\varphi$ . To measure this effect in our system, we varied the trapping depth over a range of  $\sim (0.6 - 1.7)U_0$  and extrapolated  $\delta g$  to zero intensity, as shown in Fig. 4.12. Note that this measurement also checks for possible errors due to scalar and tensor polarizabilities as their effects also scale linearly with the trap intensity. We found that the  $\delta g$ -measurement was affected by the lattice potential by less than 0.1%, well below the uncertainty quoted above.

The precise measurement of  $\delta g$  provides an opportunity to evaluate the validity of the state mixing theory in the first 4 sections of this chapter. This is important for determination of the  $^3P_0$  lifetime as we saw it depends strongly on the type of calculation performed. From the standard BW calculation we found  $\delta g\mu_0 = -109.1(1)$  Hz/G which is in excellent agreement with the experimental value of  $-108.4(4)$ . Using the mixing values in conjunction with Eq. 4.11 we found that the  $^3P_0$  lifetime is  $152(2)$  s. Since  $\delta g$  is determined mainly by the properties of the  $^3P_1$  state, it is not surprising that the theoretical and experimental values are in good agreement. Conversely, the lifetime of the  $^3P_0$  state depends nearly equally on the  $^1P_1$  and  $^3P_1$  characteristics, so in light of the poor prediction of the  $^1P_1$   $A$  value, the lifetime prediction deserves further investigation.

The MBW theory calculation resulted in  $\delta g\mu_0 = -117.9(5)$  Hz/G and  $\tau^{^3P_0} = 110(1)$  s. Here, the agreement with experiment is fair, but the uncertainties in experimental parameters used for the theory are too small to explain the 10%

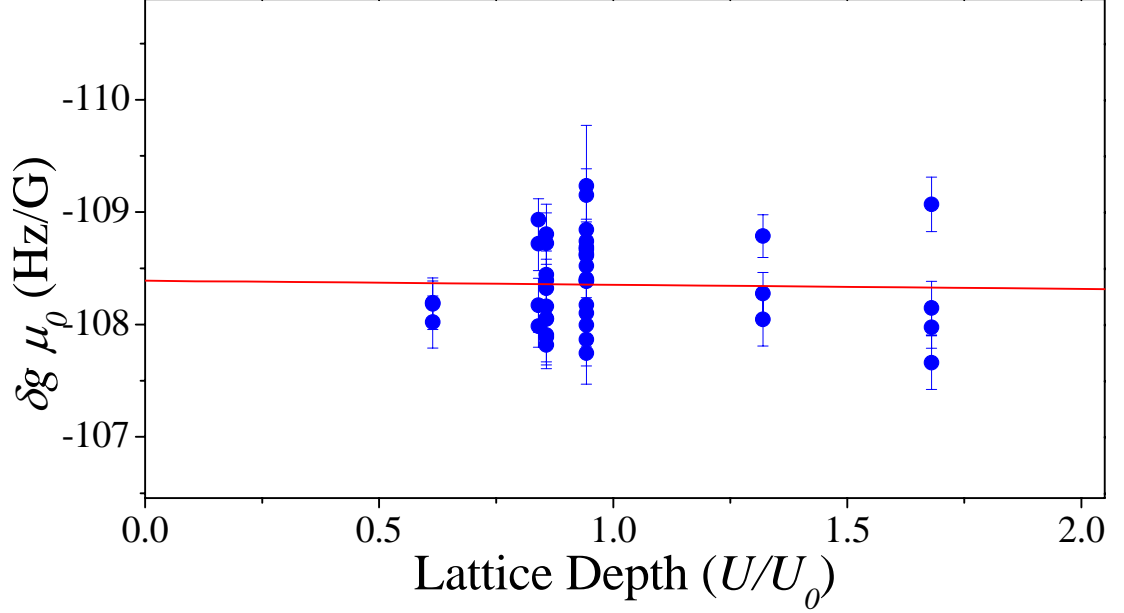


Figure 4.12: Summary of  $\delta g$ -measurements for different lattice intensities. Each data point (and uncertainty) represents the  $\delta g$  value extracted from a full  $\sigma^\pm$  spectrum such as in Fig. 4.10. Linear extrapolation (red line) to zero lattice intensity yields a value  $-108.4(1)$  Hz/G consistent with the mean value reported in the text. The slope of the line reveals that the  $\delta g$  measurement is effected by less than 0.1 Hz/G at our typical trap depth

discrepancy. The inability of the BW and MBW theory to simultaneously predict  $\delta g$  and  $A_{1P_1}$  seems to suggest that the theory is inadequate for  $^{87}\text{Sr}$ . A second possibility is a measurement error of some of the hfs coefficients, or the ground state  $g$ -factor. The triplet hfs is well resolved and has been confirmed with high accuracy in a number of measurements. An error in the ground state  $g$ -factor measurement at the 10% level is unlikely as it has been measured multiple times, however it could be tested in future measurements by calibrating the field in an independent way so that both  $g_I$  and  $\delta g$  can be extracted from our splitting data. On the other hand, the  $^1P_1$  hfs measurement has only been performed once using level crossing techniques, and is complicated by the fact that the structure is not resolved ( $\gamma=32$  MHz), and that the nearby  $^{88}\text{Sr}$  transition dominates the spectrum

for naturally abundant samples. Present  $^{87}\text{Sr}$  cooling experiments could be used to provide an improved measurement of the  $^1P_1$  data to check whether this is the origin of the discrepancy.

With the  $^1P_1$  splitting being the most likely source of experimental error for the calculation, we have also tried to perform a MBW calculation without using the  $^1P_1$   $A$  value. In Eq. 4.14,  $\delta g$  depends strongly on  $\tilde{\alpha}_0\tilde{\alpha}$  and only weakly ( $< 0.1\%$ ) on  $\tilde{\beta}_0\tilde{\beta}$ , therefore our  $\delta g$  measurement can be used to tightly constrain  $\tilde{\alpha}_0 = 2.35(1) \times 10^{-4}$ , and then we can use only the triplet hfs data to calculate  $\tilde{\beta}_0$  in the MBW theory framework (we'll call this MBW II). In this way we find  $\tilde{\beta}_0 = -3.2(1) \times 10^{-6}$ , yielding  $\tau^{3P_0} = 182(5)$  s. The resulting  $^1P_1$  hfs  $A$  coefficient is  $-15.9(5)$  MHz, which is an improvement compared to the standard BW calculation as it only disagrees with the experimental value by 12 MHz.

Although one can presumably predict the lifetime with a few percent accuracy (based on uncertainties in the experimental data), the large model-dependent spread in values introduces significant additional uncertainty. Based on the calculations above (and many other similar ones) and our experimental data, the predicted lifetime is  $145(40)$  s. A direct measurement of the natural lifetime would be ideal for constraining  $\tilde{\beta}_0$ , as has been done in similar studies with trapped ion systems such as  $\text{In}^+$  [35] and  $\text{Al}^+$  [30] or neutral atoms where the lifetime is shorter. For Sr this type of experiment is difficult due to trap lifetime limitations, and the measurement accuracy would be limited by blackbody quenching of the  $^3P_0$  state [68].

Table 4.4 summarizes the calculations of  $\delta g$  and  $\tau^{3P_0}$  discussed here including the HFI mixing parameters  $\tilde{\alpha}_0$  and  $\tilde{\beta}_0$ . Other recent calculations based on the BW theory [39, 46], *ab initio* relativistic many body calculations [134], and an effective core calculation [128] are given for comparison, with error bars shown when available.

Table 4.4: Theoretical estimates of  $\delta g$  and  $\tau^{3P_0}$  for  $^{87}\text{Sr}$ 

<i>Values used in Calculation</i>					
$\tilde{\alpha} = 0.9996 \quad \tilde{\beta} = -0.0286(3)$					
Calc.	$\tilde{\alpha}_0$	$\tilde{\beta}_0$	$\tau^{3P_0}$ (s)	$\delta g \mu_0$ $m_F(\text{Hz/G})$	$A^1P_1$ (MHz)
BW	$2.37(1) \times 10^{-4}$	$-4.12(1) \times 10^{-6}$	152(2)	-109.1(1)	-32.7(2)
MBW	$2.56(1) \times 10^{-4}$	$-5.5(1) \times 10^{-4}$	110(1)	-117.9(5)	-3.4(4) <sup>a</sup>
MBW II	$2.35(1) \times 10^{-4}$	$-3.2(1) \times 10^{-4}$	182(5)	-108.4(4) <sup>b</sup>	-15.9(5)
Ref [134]	—	—	132	—	—
Ref [128, 135]	$2.9(3) \times 10^{-4}$	$-4.7(7) \times 10^{-4}$	110(30)	-130(15) <sup>c</sup>	—
Ref [39, 46]	—	—	159	106 <sup>d</sup>	—
<sup>a</sup> Experimental value [87]					
<sup>b</sup> Experimental value from this work					
<sup>c</sup> Calculated using Eq. 4.14					
<sup>d</sup> Sign inferred from Figure 1 in Ref. [46]					

#### 4.4.2 Experimental Limits on the Sublevel-Dependent Light Shifts

In the previous section, we saw that the vector light shift was insignificant at our precision for the  $\delta g$  measurement (see Fig. 4.12). While we were able to confirm that the vector shift effect is small and consistent with zero in our system, it is difficult to report an upper limit for the vector shift coefficient  $\Delta\kappa^V$  due to uncertainty in the lattice polarization purity and orientation relative to the quantization axis. We can however constrain the quantity  $\Delta\kappa^V \xi \delta\varphi$  which at least gives an idea of what kind of shifts can be expected if reasonable care is taken in the experimental setup. The vector shift was found to effect the splitting by less than 0.1 Hz, even for the stretched states, therefore as an upper limit we report  $\Delta\kappa^V \xi \delta\varphi = 0(6) \times 10^{-4} \text{ Hz}/(U_T/E_R)$ . In terms of a pseudo-magnetic field  $d\vec{B}$ , the shift at  $U_0$  is equivalent to a field of  $0(2) \times 10^{-4} \text{ G}$ . In future measurements, the magnetic field could be aligned along the lattice propagation axis, and circular trap polarization could be used such that  $\xi \delta\varphi = 1$ , enhancing the measurement precision of  $\Delta\kappa^V$  by orders of magnitude. From our calculations, we would then



expect shifts at the few Hz level which would be easily observable if the experiments in the previous section were repeated (specifically Fig. 4.12).

Unlike the vector shift, the tensor contribution to the sublevel splitting is distinguishable from the magnetic contribution even for fixed fields. Adjacent  $\sigma$  transitions can be used to measure  $\Delta\kappa^T$  and  $\kappa_e^T$  due to the  $m_F^2$  dependence of the tensor shift. An appropriate choice of transition comparisons results in a measurement of the tensor shift without any contributions from magnetic or vector terms. To enhance the sensitivity of our measurement we focus mainly on the transitions originating from states with large  $m_F$ ; for example, we find that

$$\begin{aligned}\Delta\kappa^T &= -\frac{f_{\sigma^+,m_F=7/2} - f_{\sigma^+,m_F=-7/2}}{42\frac{U_T}{E_R}} \\ \kappa_e^T &= -\frac{f_{d,m_F=7/2} - f_{d,m_F=-7/2}}{84\frac{U_T}{E_R}},\end{aligned}\tag{4.31}$$

while similar combinations can be used to isolate the differential tensor shift from the  $\sigma^-$  data as well as the tensor shift coefficient of the  $^1S_0$  state. From the  $\sigma$  splitting data taken for the  $\delta g$  measurement, we find  $\Delta\kappa^T = 0.03(8)$  Hz/ $U_0$  and  $|\kappa_e^T| = 0.02(4)$  Hz/ $U_0$ . The error bars represent the standard deviation of many measurements, with the scatter in the data due mainly to laser frequency noise and slight under sampling of the peaks. The data for these measurements is shown in Fig. 4.13. Similarly, we extracted the tensor shift coefficient from  $\pi$  spectra, exploiting the  $m_F$ -dependent term in Eq. 4.29, yielding  $\Delta\kappa^T = 0.02(7)$  Hz/ $U_0$ .

The measurements here are all consistent with zero and were not found to depend on the trapping depth used for a range of 0.85–1.7  $U_0$ , and hence are interpreted as conservative upper limits to the shift coefficients. From the previous section, we expect that the total tensor shift would be dominated by the  $^3P_0$  state such that the limit here for  $\kappa_e^T$  can be interpreted as the tightest constraint for  $\Delta\kappa^T$ . In comparing the measurements here with the theory section, we find that the maximum size of the tensor polarizability constrained by our

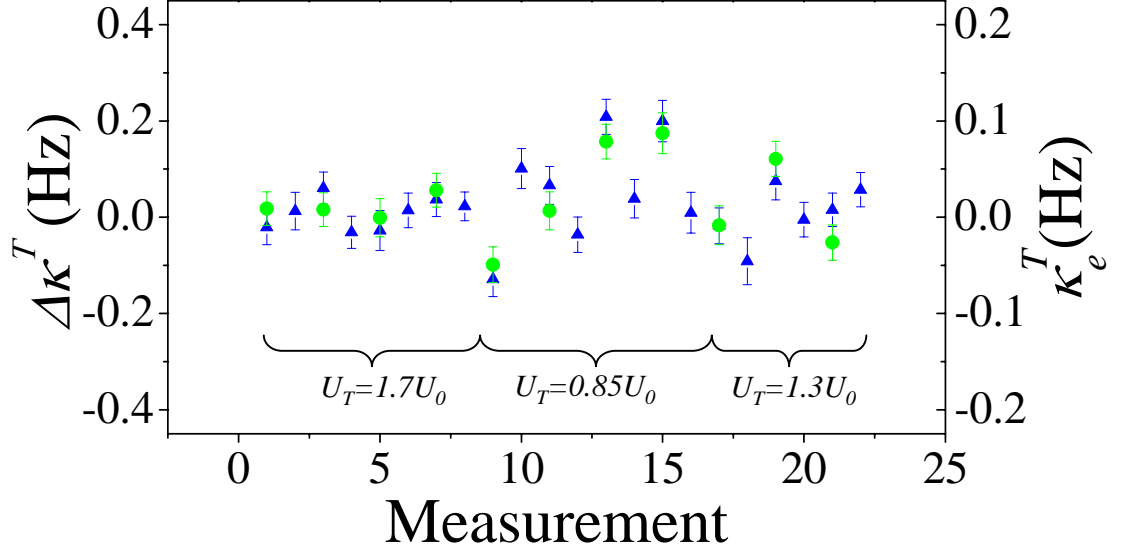


Figure 4.13: Measurement of the tensor shift coefficients  $\Delta\kappa^T$  (blue triangles), and  $\kappa_e^T$  (green circles), using  $\sigma$  spectra and Eq. 4.31. A given spectrum yields two measurements of  $\Delta\kappa^T$  (one for  $\sigma^+$  and one for  $\sigma^-$ ) and one value of  $\Delta\kappa^T$ . The measured coefficients show no statistically significant trap depth dependence while varying the depth from 0.85–1.7  $U_0$ .

data, 0.006 a.u., is roughly an order of magnitude smaller than that predicted by the state mixing calculation. While we can't rule out the importance of state mixing in the tensor shift, we can say that the simple calculation made here is insufficient for an accurate prediction. Improvements on the precision of these limits can be made by going to larger trap intensities to enhance sensitivity, as well as by directly stabilizing the clock laser to components of interest for improved averaging. It will be important to improve these measurements as the accuracy of lattice clocks increase, especially if a 3D lattice geometry is used in which the polarization depends strongly on the trap design.

Table 4.5 summarizes the measured sensitivities to magnetic fields and the lattice potential. The Stark shift coefficients for linear polarization at 813.4280(5) nm are given in units of  $\text{Hz}/(U_T/E_R)$ . For completeness, a recent measurement of the second order Zeeman shift using  $^{88}\text{Sr}$  has been included [57]. Although only upper

Table 4.5: Measured Field Sensitivities for  $^{87}\text{Sr}$ 

Sensitivity	Value	Units	Ref.
$\Delta_B^{(1)}/m_F B$	-108.4(4)	Hz/G	This work
$\Delta_B^{(2)}/B^2$	-0.233(5)	Hz/G <sup>2</sup>	[57] <sup>a</sup>
$\Delta\kappa^T$	$6(20) \times 10^{-4}$	Hz/( $U_T/E_R$ )	This work <sup>b</sup>
$\Delta\kappa^T$	$9(23) \times 10^{-4}$	Hz/( $U_T/E_R$ )	This work <sup>c</sup>
$\kappa_e^T$	$5(10) \times 10^{-4}$	Hz/( $U_T/E_R$ )	This work <sup>c</sup>
$\Delta\kappa^V \xi \delta\varphi$	$0(6) \times 10^{-4}$	Hz/( $U_T/E_R$ )	This work <sup>d</sup>
<sup>a</sup> Measured for $^{88}\text{Sr}$			
<sup>b</sup> Measured with $\pi$ spectra			
<sup>c</sup> Measured with $\sigma^\pm$ spectra			
<sup>d</sup> From Fig. 4.12			

limits are reported here for the tensor shift, the result can be used to estimate the accuracy and linewidth limitations for lattice clocks. In the absence of magnetic fields, the tensor shift can cause line broadening of the transition for unpolarized samples. Given the transition amplitudes in Fig. 4.9, the upper limit for line broadening, derived from the tensor shift coefficients discussed above, is 4 Hz at  $U_0$ . Therefore we cannot fully rule out the tensor shift as the broadening mechanism in Fig. 3.19, although residual magnetic fields are still a more likely suspect. The tensor shift also results in a different magic wavelength for different  $m_F$  sublevels, which is constrained here to the few picometer level or below. These should be considered conservative upper limits however, as in our more recent measurements (not discussed in this thesis) with spin polarized state we have so far not observed a change in the magic wavelength of even 1 pm. Of all of the sublevel shift effects explored here, the differential  $g$  factor will have by far the biggest impact on the clock.

#### 4.5 Implications For the $^{87}\text{Sr}$ Lattice Clock

In the previous sections, the magnitude of relevant shifts of the Zeeman levels were estimated. Here, we briefly discuss the feasibility of different routes

to reduce or eliminate the nuclear spin effects for development of a clock with an inaccuracy of less than  $10^{-17}$ .

#### 4.5.1 Method I: Degenerate Sublevels

The most straightforward approach for reducing nuclear spin effects is to have the relevant magnetic and optical fields under strict control. This is in fact the approach taken in the next chapter, in which the accuracy of the lattice clock is experimentally explored. Here we assume that the population is roughly equally distributed among the ground state sublevels, and  $\pi$  transitions are excited. To eliminate the linear Zeeman shift at the 1 mHz ( $2 \times 10^{-18}$ ) level for all of the  $m_F$  states, one needs to provide a field-free environment at the level of  $2 \times 10^{-6}$  G. This level of control could be challenging even if magnetic shielding is used in the apparatus, and would certainly require a careful design. In practice, the requirement would not be as stringent since the sublevels are shifted evenly about the zero field point causing lineshape deformation, the clock shift would then come into play depending on the imbalance of population in the sublevels, or the polarization of the probe laser.

For magnetic fields at the  $\mu\text{G}$  level the quantum axis of the system is defined by the lattice, so we expect the Zeeman-like light shifts to be in the worst case consistent with Fig. 4.7 for a trap depth of  $U_0 = 35E_R$ . Therefore to eliminate the vector light shift contribution at the  $10^{-18}$  level, the polarization ellipticity  $\xi$  should be at the  $10^{-4}$  level or below. This is easily achieved with commercially available polarizers, however, one must ensure that other optical components such as vacuum windows are not deteriorating the polarization purity. The remaining effect to consider is the tensor light shift. From the HFS calculation we expect the tensor interaction to broaden the Zeeman spectra by a few mHz. From our experimental upper limits it could be a few Hz, and the true values likely lies

somewhere in between. Unlike the magnetic and vector sensitivity, the shift is not symmetric in  $m_F$  so the shift will do more than broaden the line, even in the ideal case of perfect population distribution and probe polarization. This is exacerbated by the fact that the excitation fraction of the clock transition has a very strong  $m_F$  dependence (see Fig. 4.9) such that the line will be strongest for the  $|m_F|=9/2$  states. Therefore it's possible that the tensor shift can result in a clock shift as large as a few Hz. In real experiments, the lattice depth will always be varied to check that the scalar light shifts are well canceled. As the tensor shift is also proportional to the trap depth, this effect should be naturally accounted for in the scalar evaluation. The sensitivity of the tensor shift to population distribution will depend strongly on the actual size of the tensor polarizability, and hence to confidently reach the sub  $10^{-17}$  level of accuracy with this zero B-field scheme, the value of the tensor shift needs to be accurately measured. The tensor problem could be completely avoided if the atoms only populate one  $m_F$  state (or two states with the same  $|m_F|$  such that the tensor shift is completely absorbed in  $\lambda_m$  and does not deform the line.

One practical consideration worth mentioning for the case described here, is that the different excitation fractions for the different sublevels (due to Clebsch-Gordon coefficients) will limit the final signal size achievable for a given probe intensity. In our experiments for example we have found that we get a smaller excitation fraction when the sublevels are degenerate, but that can be increased if a resolved sublevel is used. This could be avoided if the atoms are spin-polarized before the measurement.

#### 4.5.2 Method II: Resolved Sublevels and Spin Polarized Samples

A second, more promising path to clock operation free of nuclear spin effects, is the use of resolved spin states in the presence of a bias magnetic field. In this

way one could average the positions of two  $\pm m_F$  states to eliminate the  $m_F$  dependent linear Zeeman shift. Then we can dramatically relax our demands on precise magnetic field control as the average frequency of the two measurements will only be affected by the Zeeman shift in second order. We found that the magnitude of the shift coefficient was  $0.233 \text{ Hz/G}^2$ , so for fields of a few hundred mG calibrating the shift to 1 mHz should be possible. As we saw in this chapter, application of a bias field can also reduce the overall sensitivity to light shifts and polarization. Moreover, according to Eq. 4.27, the vector shift depends on  $m_F$  so the averaging procedure should eliminate it in the same way that the linear Zeeman effect is removed. The remaining issue then is the tensor shift which will depend on  $|m_F|$  and hence will not be removed. This problem will be bypassed in a natural way, in that for the sake of efficiency, clock measurements will be focused on only one pair of  $\pm m_F$  states. Therefore when a magic wavelength is determined experimentally for the chosen  $m_F$ -pair, the effect of the tensor shift will be to slightly modify the cancellation wavelength if a different set of sublevels are employed. One should keep in mind the polarization axis when determining the magic wavelength in this way, since the magnitude of the tensor shift changes by a factor of  $-1/2$  as  $\xi$  goes from 0 to 1.

In the interest of increased  $S/N$ , and the reduction of line pulling effects from nearby transitions, the resolved sublevel technique is best suited for spin polarized samples. If the atoms are evenly distributed among the sub levels, they are essentially wasted as they are not used for clock operation, so we might as well try and push them all towards the useful states. Additionally, with spin polarized samples we avoid the issue of limited excitation fraction due to different Rabi frequencies. Figure 4.14 shows an example of a spin-polarized measurement using the  $m_F = \pm 9/2$  states for cancellation of the Zeeman and vector shifts. To polarize the sample, we optically pump the atoms using a weak beam resonant with the

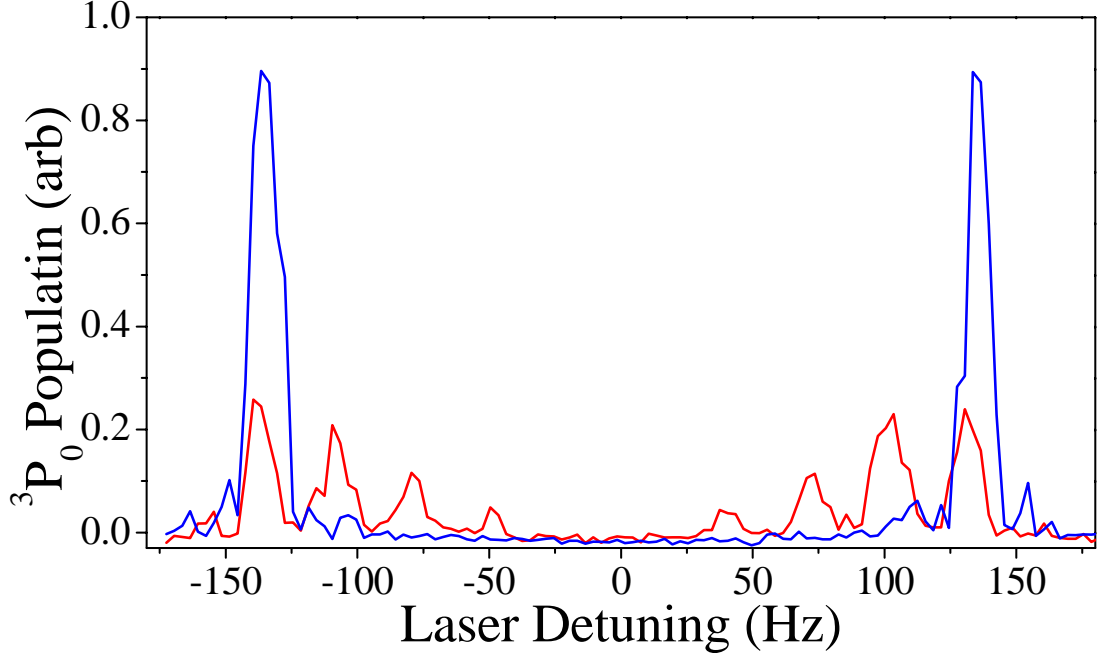


Figure 4.14: The effect of optical pumping via the  $^3P_1$  ( $F = 7/2$ ) state is shown via direct spectroscopy with  $\theta = 0$ . The red data shows the spectrum without the polarizing light for a field of 0.27 G. With the polarizing step added to the spectroscopy sequence the blue spectrum is observed. Even with the loss of  $\sim 15\%$  of the total atom number due to the polarizing laser, the signal size of the  $m_F = \pm 9/2$  states is increased by more than a factor of 4.

$^1S_0$ - $^3P_1$  ( $F = 7/2$ ) transition. The beam is co-aligned with the lattice and clock laser and linearly polarized along the lattice polarization axis ( $\theta = 0$ ), resulting in optical pumping to the stretched ( $m_F = 9/2$ ) states. Spectroscopy with (blue) and without (red) the polarizing step shows the efficiency of the optical pumping as the population in the stretched states is dramatically increased while excitations from other sublevels are not visible. Alternate schemes have been demonstrated elsewhere [91, 46] where the population is pumped into a single  $m_F = \pm 9/2$  state using the  $^1S_0$ - $^3P_1$  ( $F = 9/2$ ) transition. In our system, we have found the method shown here to be more efficient in terms of atom number in the final state and state purity. The highly efficient optical pumping and high spectral resolution should allow clock operation with a bias field of less than 300 mG for a 10 Hz

feature while keeping line pulling effects due to the presence of the other sublevels below  $10^{-17}$ . The corresponding second order Zeeman shift for such a field is only  $\sim 21$  mHz, and hence knowledge of the magnetic field at the 1% level is sufficient to control the effect to below  $10^{-18}$ . With the high accuracy  $\delta g$ -measurement reported here, real time magnetic field calibration at the percent level is trivial.

The use of spin polarized atoms also opens the door for some interesting physics. With the high precision optical clocks provide, one should be able to eventually see the effect of atomic collisions on the clock frequency. This effect is well known in Cs-fountain clocks, coming into play at the  $10^{-13}$  level. For  $J = 0$  states here, we expect the shift to be significantly smaller, but still non-zero. If the collisions between  $m_F=9/2$  and  $m_F=-9/2$  ground state atoms lead to a measurable frequency shift, then it would be interesting to see if the collision shift can be suppressed by polarizing the atoms into a single  $m_F$  state, such as the  $9/2$  state. (One would then occasionally alternate clock operation between  $9/2$  and  $-9/2$  to ensure the zeeman shifts are still under control.) In this case,  $s$ -wave collisions will be eliminated since the atoms are fermions in the same quantum state. This would be great for clock operation, as collision shifts are a long standing concern in the debate of ions vs. neutrals as the best frequency standards. Realistically, the collisions will not be completely removed because  $p$ -wave scattering can still take place, although this effect can be reduced dramatically if the atoms are at a temperature of  $1 \mu K$  in both the longitudinal and radial direction. The inhomogeneous Rabi excitation considerations (discussed in Chapter 3) will also likely degrade the suppression of  $s$ -wave scattering. One also must also take care in the state preparation to ensure pure polarization.



## 4.6 Man Made Clock Transition for Bosonic Isotopes

Here we discuss a third, drastically different approach to avoid nuclear spin effects in the lattice clock. Initial concerns that nuclear spin effects would limit the obtainable accuracy of a lattice clock have prompted a number of recent proposals to use bosonic isotopes in combination with external field induced state mixing [51, 52, 53, 54, 55] to replace the mixing provided naturally by the nuclear spin. The bosonic isotopes present a number of advantages in clock development, first of all, there are no magnetic sublevels in the clock states, so we can forget about the linear Zeeman effect, and the tensor and vector light shifts. Therefore, the constraints on field orientation and polarization purity are diminished. Secondly, the use of bosons opens up the possibility to use more isotopes in the lattice clock configuration, as most of the stable alkaline-earth isotopes in fact do not have nuclear spin. The bosonic isotopes typically are more naturally abundant, which in many experiments means more available atoms and a larger  $S/N$ . Furthermore in the case of Sr, the laser cooling complexity is reduced slightly for bosonic isotopes.

The basic principle of these ideas is to use external fields to mix the  $^3P_0$  clock state with the  $^1P_1$  state, such that  $^3P_0$  acquires a small  $E1$  lifetime. If we remember from Eq. 4.3, the spin orbit and hyperfine interaction provided this mixing as,

$$|^3P_0\rangle = |^3P_0^0\rangle + (\tilde{\alpha}_0\tilde{\alpha} - \tilde{\beta}_0\tilde{\beta})|^3P_1^0\rangle + (\tilde{\alpha}_0\tilde{\beta} + \tilde{\beta}_0\tilde{\alpha})|^1P_1^0\rangle + \tilde{\gamma}_0|^3P_2^0\rangle. \quad (4.32)$$

For the bosonic isotopes we have  $\tilde{\alpha}_0 = \tilde{\beta}_0 = \tilde{\gamma}_0 \equiv 0$ , so a new state mixing mechanism is needed to provide the desired effect of a finite lifetime. One can dream up a number of schemes to accomplish this, but since we are also worried about clock accuracy we should take care and consider the effect of the mixing on the clock frequency. From the nuclear spin mixing, we can take the lesson that

the  $^1P_1$  state is the most important to the interaction, as the natural lifetime of the  $^3P_0$  state was due to that of  $^1P_1$ , although mediated by the spin-orbit mixing between  $^1P_1$  and  $^3P_1$  (see section 4.1.2). Therefore, it should be the easiest to provide ample state mixing if the  $^1P_1$  state is used in any scheme. The  $^3P_1$  state can of course be used as well since it contains an admixture of  $^1P_1$ , but the required interaction will be much stronger since the admixture of  $^1P_1$  is so small, an effect that could be detrimental to the final clock accuracy.

#### 4.6.1 EIT Clock

The first approach to induce the state mixing which we shall examine is to apply an optical field which connects the  $^3P_0$  state directly with the  $^1P_1$  state. In this case we will have a modification of the  $^3P_0$  state given by

$$|^3P_0\rangle = |^3P_0^0\rangle + \varepsilon|^1P_1\rangle, \quad (4.33)$$

and the lifetime will be given by Eq. 4.11 by replacing  $(\tilde{\alpha}_0\tilde{\beta} + \tilde{\beta}_0\tilde{\alpha})^2$  with  $\varepsilon^2$ . For small detuning of the mixing laser, the mixing coefficient  $\varepsilon$  is given by the magnetic dipole coupling matrix element between  $^3P_0$  and  $^1P_1$  for a given laser intensity, and optical frequency. This has been evaluated for Sr [52], and for a 1 mHz linewidth (the same as provided by the nuclear spin in  $^{87}\text{Sr}$ ), a laser intensity of 3.9 mW/cm<sup>2</sup> is required for the magnetic-dipole transition. Based on the atomic polarizability of the clock states, this external field results in an ac Stark shift of -21 mHz. This seems like an acceptable trade off as the mixing laser intensity can be calibrated at the % level, providing uncertainty in the clock shift below  $10^{-18}$ , while eliminating any nuclear spin related issues that arise in  $^{87}\text{Sr}$ . This promising mixing scheme was first proposed [52] at JILA for a bosonic clock in an EIT configuration (shown in Fig. 4.15) where the state mixing can be detected on the  $^1S_0$ - $^1P_1$  transition as a mHz interference feature in the absorption spectrum.

This EIT clock however has one practical issue which needs to be addressed. The interaction is so weak ( $\sim 1$  mHz) that the evolution of the atomic population from  $^1S_0$  to  $^3P_0$  is very slow, taking hundred of seconds for the system to evolve. This is no different than the standard case in  $^{87}\text{Sr}$  where we have a 1 mHz width but actually use a Fourier limited width of a few Hz. In those experiments we speed up the process by simply cranking up the probe power, with the caveat that we suffer from some additional ac Stark shifts. The same thing can be done in the EIT case. If we want a width of 10 Hz, we need to increase the mixing laser by a factor of  $10^5$ , which increases the corresponding Stark shift by the same factor to about 200 Hz. This shift is larger than any of the expected shifts in the  $^{87}\text{Sr}$  clock. Ways around this problem have been proposed by our group at JILA [54] using a pulsed EIT sequence to reduce the Stark shift to the mHz level, but it remains to be seen if the complexity of the technique will be a problem experimentally. Another EIT clock proposal, in this case from the University of Washington [51], was made around the same time as the one reported here involving similar concepts.

#### 4.6.2 Magnetic Field Induced Clock

While the promising EIT proposal above has a few technical issues to consider, it seemed to get the clock community thinking harder about using the bosons for clocks. The next mixing proposal [53] came from our friends at NIST, which was to mix the  $^3P_0$  and  $^3P_1$  state with a DC magnetic field. Here we will have a modification of the  $^3P_0$  state given by

$$|^3P_0\rangle = |^3P_0^0\rangle + \varepsilon_{DC}|^3P_1\rangle = |^3P_0^0\rangle + \varepsilon_{DC}\tilde{\alpha}|^3P_1^0\rangle + \varepsilon_{DC}\tilde{\beta}|^1P_1^0\rangle, \quad (4.34)$$

such that the lifetime will be given by Eq. 4.11 by replacing  $(\tilde{\alpha}_0\tilde{\beta} + \tilde{\beta}_0\tilde{\alpha})^2$  with  $(\varepsilon_{DC}\tilde{\beta})^2$ . Here, the mixing coefficient  $\varepsilon_{DC}$  is given by the magnetic dipole operator and detuning between  $^3P_0$  and  $^3P_1$ . Since the interaction is with the  $^3P_1$  state, the

effectiveness of mixing in the  $^1P_1$  decay rate will be reduced by  $\tilde{\beta}^2$  compared to the optical case, however this is partially compensated by the fact that the energy difference between  $^3P_0$  and  $^3P_1$  is small (i.e. the mixing goes as the matrix element divided by the detuning). This proposal is very promising because of its simplicity, instead of using additional lasers, the state mixing is done with electromagnets. Of course, we still must consider clock shifts. For the magnetic scheme, one must consider the second order Zeeman effect and the Stark shift from the probe laser. To estimate the shifts, one should consider the required Rabi frequency needed in the experiment. For maximum excitation, one needs  $\Omega t = \pi$  where  $t$  is the length of the spectroscopic pulse. The usable probe time will be limited by the laser linewidth or other decoherences. If we assume a Fourier-limited linewidth then we have the situation  $\Omega \times (0.89/\gamma) = \pi$ . Assuming equal shifts from probe laser and second order Zeeman effect, the induced Rabi frequency for Sr is given by [56]  $\Omega/2\pi = 0.3 \delta\nu$  where  $\delta\nu = \delta\nu_{probe} = \delta\nu_{Zeeman}$ . For a Fourier-limited spectral width of 10 Hz, the required fields of  $B=9$  G and  $I_p=1$  W/cm<sup>2</sup> each contribute a shift of -19 Hz. Once again, this is not necessarily more desirable than our  $^{87}\text{Sr}$  situation in which none of the Zeeman(-like) shifts were even close to that level. However, the simplicity of this system is hard to ignore and may well be worth the effort of calibrating the relevant fields at the  $10^{-5}$  level.

### 4.6.3 State Mixing at the Magic Wavelength

A third scheme which has recently been discussed by the Tokyo group [55] is to use optical fields at the magic wavelength to perform the mixing. Here the optical field is not resonant with any states, the mixing comes about via the light (assumed circularly polarized) coupling with the vector component of the  $^3P_1$  polarizability. Since the field is at the magic wavelength, one doesn't have to worry about the effect of Stark shifts linear in intensity. It is also a convenient approach

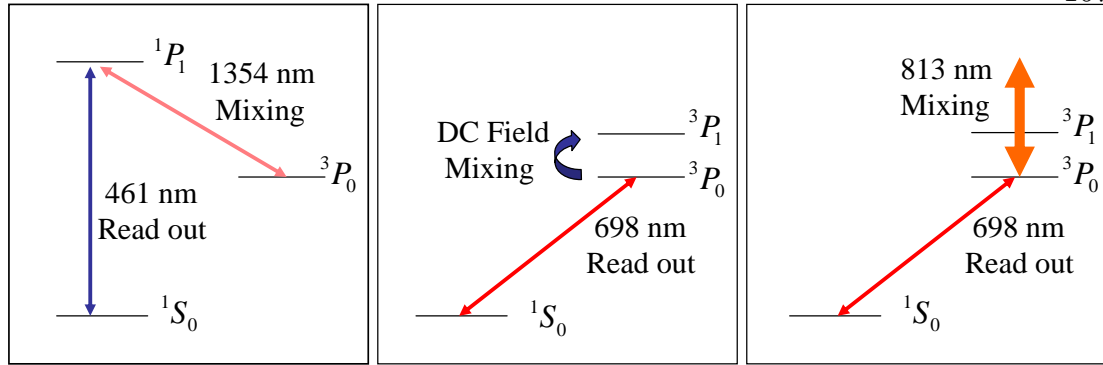


Figure 4.15: Proposed mixing schemes for use of the clock transition in bosonic isotopes.

because the light source will presumably be well developed at this wavelength since it is the same as the lattice potential. One still has to consider the clock probe effect, and more importantly, if the required mixing field grows large, the hyperpolarizability must be considered. In this mixing scheme the Rabi frequency is proportional to the mixing intensity, and the square root of the probe intensity. The light shifts scale linearly with the probe intensity and as the square of the mixing intensity. Therefore it is difficult to increase the mixing without drastically increasing the Stark shift. For example, one finds that for a linewidth of 10 Hz, the total stark shift is minimized at a probe intensity of  $1.8 \text{ W/cm}^2$  and mixing intensity of  $0.74 \text{ MW/cm}^2$ , each resulting in stark shifts of  $-33 \text{ Hz}$ .

In looking at these three schemes above we find some interesting differences. In the first scheme, the EIT method hand cuffs us into cranking up the mixing field (our only choice) which results in Stark shifts. Here the transition width is proportional to the mixing intensity  $I_{mix}$ , as is the Stark shift. In the second scheme, the mixing depends proportionally on the magnetic field  $B$  and as the square root of the probe intensity  $\sqrt{I_p}$ . The shifts on the other hand scale as  $B^2$  and  $I_p$ . This is similar to the third scheme where the width scales proportionately with the mixing intensity and as the square root of the probe intensity, while the

shifts scale as  $I_{mix}^2$  and  $I_p$ . We can see then that there is a real fundamental difference between the first method and the next two, in that in the magnetic and magic wave scheme, the mixing interactions cause quadratic frequency shifts while enhancing the mixing linearly. Furthermore, the second two mixing schemes use the  $^3P_1$  state as a source of  $^1P_1$  characteristic, resulting in significantly smaller mixing (compared to that of the nuclear spin effect) for a given frequency shift. This may sound counter intuitive based on the results above, so consider the following: In the EIT scheme, the mixing laser provides the same linewidth as the nuclear spin would, while shifting the clock by only 20 mHz. In the magnetic mixing case, the field mixes about three orders of magnitude less of the  $^1P_1$  characteristic for fields described here, and the clock shift from the mixing field is in the 10 Hz range. We must therefore conclude that the optical mixing of  $^1P_1$  is significantly more efficient as a means to create a desired state mixture while minimizing the clock shift. So why do we have bigger frequency shifts in the CW EIT case above?

The one thing we are forgetting is the effect of the probe laser. In the magnetic scheme for example, the Rabi frequency can get a big boost by using more power in the probe laser, therefore making up for the weaker mixing field, doing a bit of damage control if you will. This is just like in the case of  $^{87}\text{Sr}$  where a 1 mHz line is available but we use a stronger light intensity to push the Rabi frequency up to the Hz level. Fortunately in  $^{87}\text{Sr}$ , the linewidth is large enough that the needed intensity for broadening to 10 Hz only shifts the clock transition by a few mHz. In the magnetic scheme the mixing field does a poor job compared to the nuclear spin so the probe intensity has to be pushed harder, in the end resulting in tens of Hz level shifts. Now, in the EIT scheme, the probing mechanism is on the  $^1P_1$  line, and therefore does not help in broadening the transition, which is why we had to push the mixing effect harder. So we see now that the fault of the EIT mixing is not the mixing at all, but the detection.

Table 4.6: Field Sensitivities For Different Lattice Clock Schemes Using  $^{88}\text{Sr}$ . Relevant clock shift mechanisms and magnitudes are given for each scheme for both 0.5 and 10 Hz transition widths. When two significant shifts are present in a given system, field values are chosen which minimize the total shift. In the  $^{87}\text{Sr}$  case, it is assumed that the first order Zeeman shift and vector light shift are averaged out using alternating measurement, while the tensor shift is removed by convention of measuring the magic wavelength for the polarized states. All Zeeman shifts listed represent the second order Zeeman effect.

Spin ( $I$ )	Method( $\lambda_{det.}$ )	$\gamma=0.5$ Hz		$\gamma=10$ Hz	
		Fields	Shift $\delta\nu$	Fields	Shift $\delta\nu$
9/2	Spin Polarized(698) HFI Mixing	$I_p=100\text{nW/cm}^2$	$-5\mu\text{Hz}$	$I_p=41\ \mu\text{W/cm}^2$	$-2\ \text{mHz}$
		$B_{split}=0.3\text{G}$	$-21\ \text{mHz}$	$B_{split}0.3\text{G}$	$-21\ \text{mHz}$
0	CW EIT (461)	$I_{mix}=1.9\ \text{W/cm}^2$	$-10.5\ \text{Hz}$	$I_{mix}=39\ \text{W/cm}^2$	$-210\ \text{Hz}$
0	Pulsed EIT (461)	$I_{mix}=1.9\ \text{W/cm}^2$	$< 5\ \text{mHz}$	$I_{mix}=39\ \text{W/cm}^2$	$< 5\ \text{mHz}$
0	Magnetic (698) Mixing DC	$I_p=52\text{mW/cm}^2$	$-0.9\text{Hz}$	$I_p=1\ \text{W/cm}^2$	$-19\ \text{Hz}$
		$B_{mix}=2\text{G}$	$-0.9\ \text{Hz}$	$B_{mix}=9\text{G}$	$-19\ \text{Hz}$
0	Magic wave (698) Mixing 813 nm	$I_{mix}=0.16\ \text{MW/cm}^2$	$-1.6\ \text{Hz}$	$I_{mix}=0.74\ \text{MW/cm}^2$	$-33\ \text{Hz}$
		$I_p=98\ \text{mW/cm}^2$	$-1.6\ \text{Hz}$	$I_p=1.8\ \text{W/cm}^2$	$-33\ \text{Hz}$

This is precisely the effect addressed in the modified EIT scheme in Ref. [54].

#### 4.7 So What Should I Chose? Fermions or Bosons

Now that we have discussed a number of different approaches for lattice clockery, we can take more of a big picture view and try and sort out which scheme to choose. Table 4.6 summarizes some of the parameters of interest for Sr which should help give a fair ‘‘apples to apples’’ type comparison for different boson schemes, as compared to the fermion case with spin-polarized atoms. We have given the estimated frequency shifts for different schemes, for transition widths of 0.5 Hz, and the more realistic case of 10 Hz. The shift coefficients will be different for other species like Mg, Ca, Yb, and Hg, but the basic trends are the same.

In reality, the decision between fermion and boson approaches will depend on a number of issues. Laser stabilization seems to be the most critical one, for both accuracy and stability. For the accuracy of the boson clock, the achievable linewidth, assumed based mainly on the laser limitation, sets the requirement for the mixing fields, and therefore the size of the frequency shifts that need to be

calibrated. For the fermionic clock, one can use broader lines without inducing large shifts, reducing the demands on the laser. One might assume that the bosonic case will at least be superior for stability, even if the accuracy is reduced, due to the larger atom numbers possible. But in actuality, the  $10^4$  strontium atoms in our  $^{87}\text{Sr}$  system, along with the 2 Hz resonances we have observed, can in principle support a 1 s stability of a few parts in  $10^{-17}$ . This is well out of the range of current state of the art oscillators which would limit such a system. Therefore increasing the  $S/N$  by a factor of 3 (via an order of magnitude atom increase) with the bosons may not improve the stability of current clocks. Another major difference between the fermion and boson method is dealing with collision shifts. If atom-atom interaction is eventually the limiting systematic for the lattice clock, this can be dealt with differently for the two species. For spin polarized fermions, we may be able to enjoy the absence of  $s$ -wave scattering in a 1D lattice [136]. For bosons, one would have to isolate the atoms in a 3D lattice to remove the scattering process. Conversely, if line pulling due to radial motion in the trap becomes the dominant effect, one would desire a 3D lattice setup. A 3D lattice would suit the bosons well but could cause some problems for the fermions due to lattice polarization issues. If the situation is that the clock is finally limited by some other isotope independent shift that wouldn't depend on the lattice setup, such as the room temperature black body stark shift, then the choice of isotope could boil down to a popularity contest as it is very useful to have different labs exploring the same clock for standard development.

This author's taste is to stick with the fermion case until a limiting systematic arises, or until clock lasers can be developed which can take advantage of the improved  $S/N$  provided by the larger natural abundance. This is partially motivated by the possibility of eliminated collisions without the added complexity of a 3D lattice. Fortunately, the decision at hand for future lattice clock developers,



is a choice between very promising techniques. And it is a choice which can easily be changed as new information on systematic effects comes to light.

## Chapter 5

### Accuracy Evaluation of the $^{87}\text{Sr}$ Optical Lattice Clock

#### 5.0.1 So What Time Is It? How (un)Certain Are You?

In the last couple of chapters we have seen that the lattice clock technique can provide an unprecedented level of precision in spectroscopy with line  $Q$ 's exceeding  $2 \times 10^{14}$ . After exploring the effect of the hyperfine interaction, we can see that the differential  $g$ -factor and the vector and tensor light shifts do not present fundamental road blocks to clock performance. With the precision, and some interesting physics under our belt, we now turn to the issue of frequency metrology. To determine the frequency of the clock transition with high accuracy, we must verify experimentally that systematic shifts of the clock transition are well understood and controlled. While we have claimed that we expect uncertainties at the mHz level in the previous chapter, in a real world system we need direct measurements which show the shifts are under control.

At the end of the last chapter we discussed a few choices for developing an accurate clock. In this work, we pursue a measurement of  $^{87}\text{Sr}$  clock frequency using Method I, where we use degenerate sublevels. Here we have the drawback that the transition frequency will be sensitive to various Zeeman shifts, nonetheless we will find that with the high spectral resolution of the lattice clock, these effects can be characterized to high precision. There is no doubt that for the ultimate  $^{87}\text{Sr}$  lattice clock it would be better to use Method II where spin polarized samples

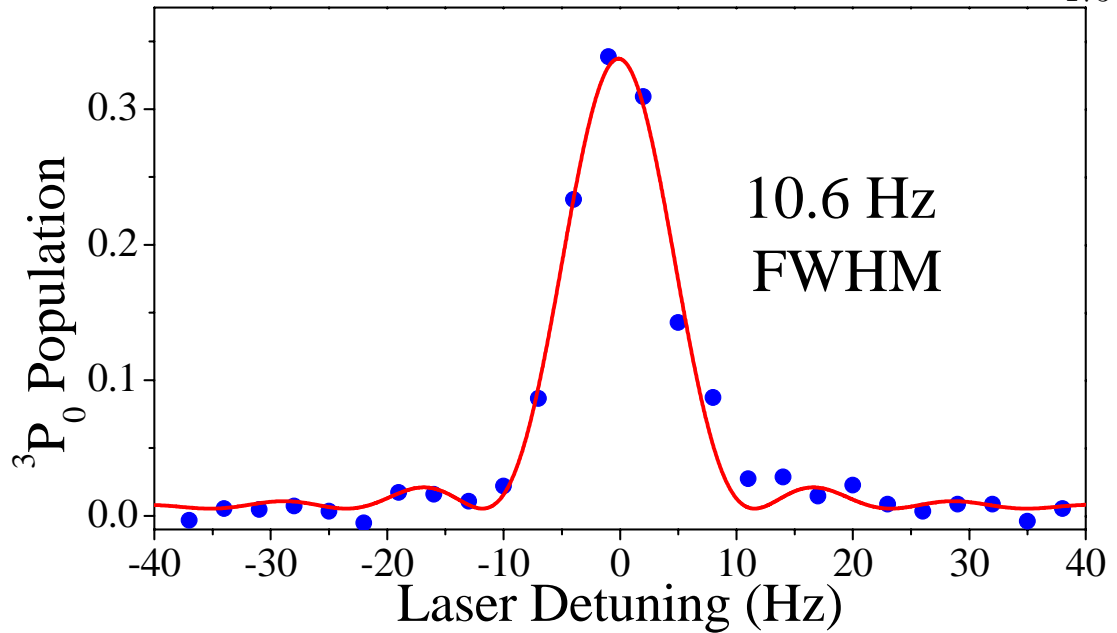


Figure 5.1: High resolution spectroscopy of the  $^1S_0$ - $^3P_0$  transition. A Fourier-limited resonance profile for typical operating parameters in the absolute frequency measurement experiment. A  $\text{sinc}^2$  fit is shown in red, giving a linewidth (FWHM) of 10.6(3) Hz ( $Q \simeq 4 \times 10^{13}$ ). The spectrum is taken without averaging or normalization.

are used to average  $m_F$ -dependent shifts, but at the time that this measurement was made, we had not yet implemented the polarizing scheme shown in Fig. 4.14. It is interesting to see how far the more simple measurement scheme can take us so that we know whether it is worthwhile to implement the additional complexity. Another important choice for the measurement is the spectral width. Ideally one wants to operate in a regime where the laser noise is small compared to the absorption feature such that laser fluctuations and drifts do not write noise or offsets onto the lineshape. One can imagine that trying to lock a laser to a peak with a width similar to the laser linewidth is not going to work well. Thus, instead of using our highest possible  $Q$  features we typically use shorter spectroscopy pulses of 80 ms to Fourier broaden the line to  $\sim 10$  Hz. At this width, the lineshape is very robust and the  $S/N$  is determined mainly from the

shot-to-shot atom number fluctuation and not the laser fluctuations. Figure 5.1 shows an absorption feature on an 80 ms pulse, revealing the expected  $\text{sinc}^2$  lineshape and width of 10.6(3) Hz.

The exploration of systematic spectroscopy shifts is not the only issue in determining the clock frequency, we also need a high accuracy frequency reference for comparison. This is where the fs-comb will come into play as we need a way to compare the optical frequency of our strontium atoms with the standard that defines frequency and time, the microwave ground state hyperfine transition in Cs. Fortunately for us, one of the highest accuracy Cs clocks in the world is located down the street from JILA, at the NIST Time and Frequency Division [5]. We are able to access the frequency of this standard by comparison with a NIST H-maser which is directly calibrated by the Cs fountain clock. The maser signal is transferred to JILA via an optical fiber link [117, 137, 138] providing an accurate frequency with a stability of  $\sim 3 \times 10^{-13}$  at 1 s. The comparison of two different high accuracy clocks can involve a whole different set of systematic errors which must be considered when reporting the final frequency.

This chapter is organized in two main sections. First, we explore the systematic effects associated with lattice spectroscopy of  $^{87}\text{Sr}$  atoms. This includes direct measurement of frequency shifts caused by magnetic fields, atomic collisions, the lattice potential, and the probe laser. Also included are relevant theoretical uncertainties based on measured parameters in our system. This component of the experiment tells us how accurate the Sr lattice clock is, or equivalently how accurate one would expect the clock frequency to be if one could measure the optical frequency with infinite accuracy. The second part of the chapter is devoted to an accurate measurement of the clock frequency. Here we discuss the fs-comb system used for optical to microwave conversion, accurate frequency transfer over a fiber link, and the frequency measurement of the Sr clock transition. This mea-

surement is interpreted differently, not as how accurate the Sr clock is, but how accurately we can measure the frequency of the clock (or any clock) with our setup. Based on the evaluation in these two sections (and previous chapters), we discuss the outlook for the strontium lattice clock, in terms of projected accuracy and stability, as well as an optical frequency standard for possible re-definition of the SI second.

## 5.1 Lattice Spectroscopy Accuracy Evaluation

The straight and narrow path to evaluating frequency shift systematics is to compare the clock of interest to a fixed reference clock, and vary some parameters to see if you can see a shift. In our lab, the best reference clock available is the Cs-calibrated hydrogen maser signal from NIST. While we can use this clock as a fixed reference, and in fact we did just that in our first lattice clock evaluation [44], the problem is that the stability of the maser signal limits how easily we can do the evaluation. The maser frequency uncertainty averages down as  $< 3 \times 10^{-13} \tau^{-1/2}$  for a measurement time  $\tau$  in seconds, such that if we want to study systematic effects at the level of  $10^{-16}$  we would have to average for  $10^6$  seconds (12 days) to get one data point. Unfortunately, none of the lasers this author built stay locked for *this* long so in practice it would take much more time to get that data point. This long averaging time is of course why we went into the optical clock business in the first place.

### 5.1.1 Interleaved Method for Evaluating Systematics

To speed up our evaluation process, instead of measuring systematic shifts against the microwave clock, we use our clock laser cavity as the reference frequency. The clock laser provides a short term stability of  $10^{-15}$  which should dramatically reduce the amount of averaging time we need to evaluate the shifts.

The big problem here is that the laser cavity drifts so if we measure the transition frequency under one condition we cannot compare that data to a later measurement because the reference frequency will have drifted. If we are to use the cavity as a reference we need some way to change the systematic parameters quickly and reduce biasing from linear drift. As a general approach for evaluating systematics, an interleaved scheme is used where the parameter of interest is cycled through different values, synchronized with each frequency step of the probe laser across the resonance. The interleaved data is then separated into resonance profiles corresponding to each parameter value, allowing the center frequency (relative to the laser cavity), and hence the slope of the frequency shift, to be measured for a variety of parameters in a short time. An example of the interleaved technique is shown in Fig. 5.2 where we scan the clock laser across the transition, while the atom number is being alternated between a high and low value, synchronized with the laser step. In this way the effect of atomic density on the clock frequency is measured. The top panel shows the resulting spectrum where every second frequency point on the spectrum is a high atom number point (blue points) and the other points (green) are data when a low atom number is used. The lower panels show the low and high atom number data plotted individually.

By interlacing two different experimental conditions during a single scan, we ensure that the entire spectrum for each condition is effectively taken within 1 s of each other (the time to take one point), drastically reducing the effect of cavity drift on the relative frequency between the two peaks. Any laser drift will be common to both spectra and the scan direction can be alternated to further reduce biasing. For a single trace of the transition this method is very powerful, but one still cannot trust the positions of the extracted peaks relative to those taken a few minutes earlier. The useful information we can take from the interleaved method is the slope of the frequency shift, in the case of Fig. 5.2 that would be  $d\nu/dN$ .

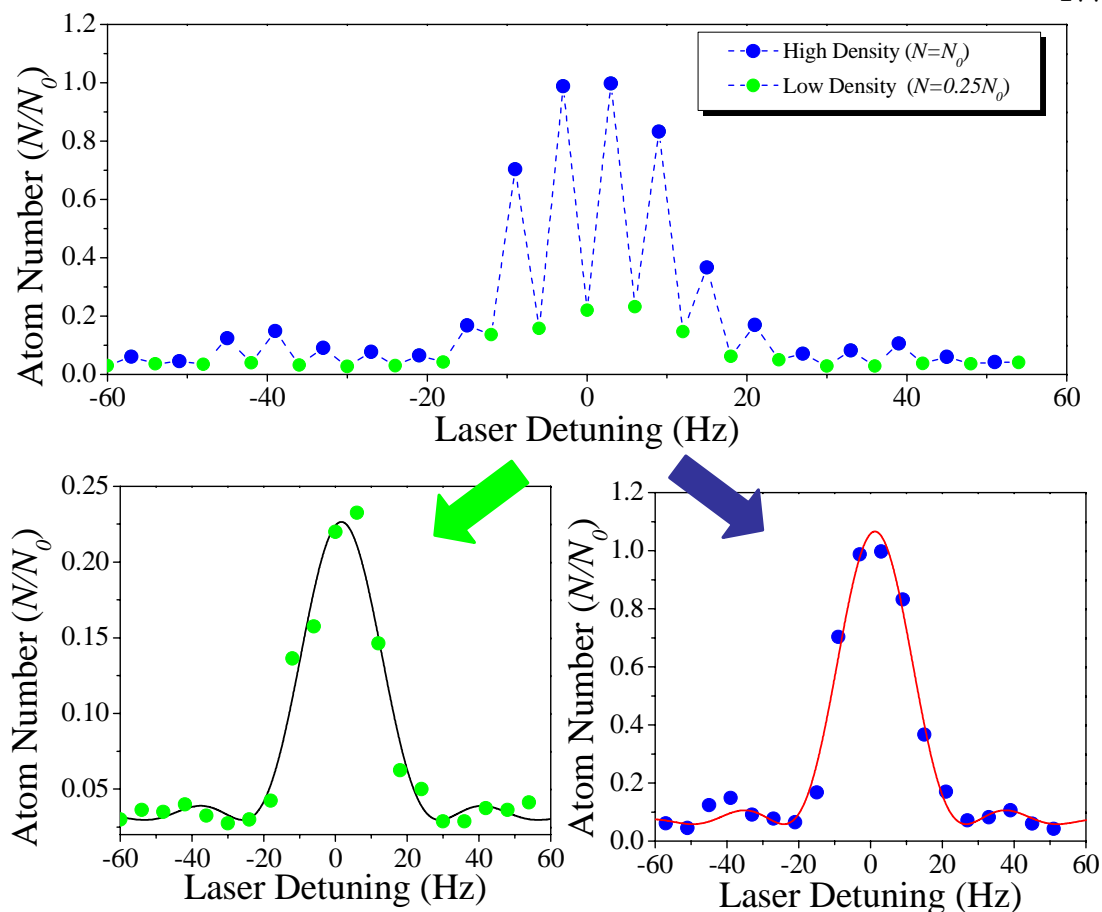


Figure 5.2: The interleaved measurement scheme for evaluation of systematic shifts. During a scan of the clock transition, the parameter of interest is varied. Here we illustrate the idea showing an interleaved scan (top graph) where the atom number in the lattice is alternated between a high (blue) and low (green) values synchronized with each experimental cycle. The data can then be separated into two lineshapes such that the resonant frequency can be determined for each condition. The useful information we take from such a measurement is the slope, or change in frequency versus the condition, as that does not depend on the actual frequency of the laser.

Use of the slope allows us to average many of these measurements together for improved precision, regardless of what the cavity frequency was at the time the data was taken. In this way we can take advantage of the high stability laser oscillator, and save ourselves some serious averaging time compared to the maser. One can also envision a more complex (but possibly more efficient) scheme where

a stage of locking the laser to the atomic transition under a fixed condition is interleaved with a scan or locking of the line under varied conditions. If the interleaving is fast compared to the laser drift, one could then extract the shift by looking at how the AOM frequency used for locking changes.

### 5.1.2 Polarizability Effects: Stark Shifts from the Lattice Laser

Of the many effects to be characterized for an optical lattice clock, the effect of the lattice laser itself remains a focal point. We have seen from our earlier discussion that there are a few different effects to consider. The dominant effect is that of the scalar light shift. Since we don't know the exact magic wavelength, we choose a value of 813.4280(5) (which was near the best reported value at the time of 813.428(1) [41]), and experimentally checked for clock shifts by varying the depth of the trap. Since the light shift is proportional to the trap depth, we can vary the trap and extrapolate the light shift to zero depth. An example of this is shown in Fig. 5.3 where four different values of the lattice intensity are interleaved during a single scan, taking less than one minute. The resulting shift coefficient for this scan, 0.4(4.4) Hz/ $U_0$ , is consistent with zero. To reduce the uncertainty in the shift, we have taken 776 single measurements (using 2, 4, or 8 interleaved intensity values), with the resulting shift coefficients shown in the right panel of the figure as a histogram. The distribution of values is gaussian, and provides an average value for the Stark shift, for a given trap depth  $U_T$ , of  $-108(257) \times (U_T/U_0)$  mHz. The mean value of the shift is consistent with zero, and based on our upper limit for the shift sensitivity of 350 Hz/nm at  $U_0$ , the value suggests that the lattice wavelength used in this work differs from the magic value by -0.3(7) picometers. The magic wavelength we can extract from this measurement is 813.4283(12) which is in excellent agreement with Ref. [41].

We also should consider the effect of the vector and tensor light shifts. Since



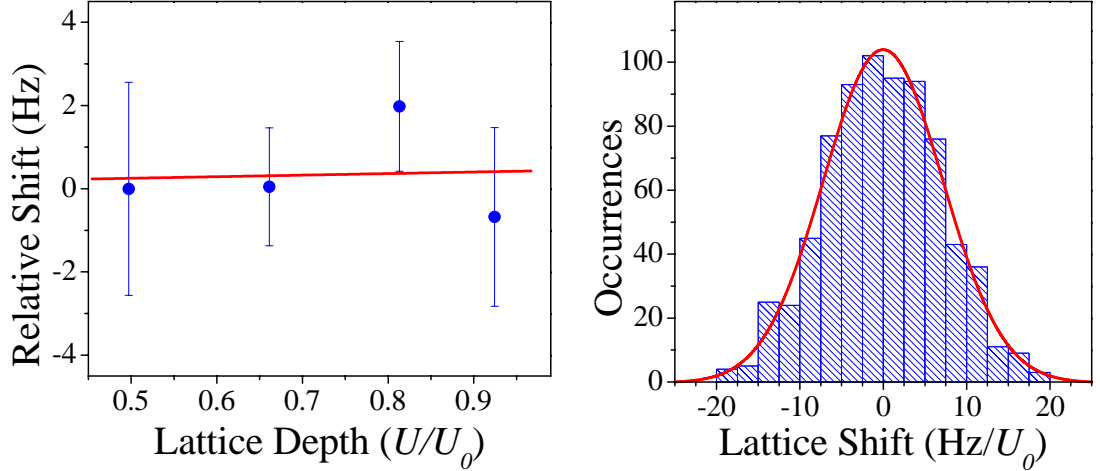


Figure 5.3: A measurement of the lattice Stark shift is achieved using four interleaved intensities during a scan of the clock transition. For this measurement the shift is  $0.4(4.4) \text{ Hz}/U_0$ . The Histogram summarizes the result of 776 single measurements (such as in the left plot) of the Stark shift for our typical intensity  $U_0$ .

in this measurement we are operating without a strong bias magnetic field the quantum axis is defined by the lattice polarization such that the zeeman-like light shifts can be predicted from our earlier calculations. In our system, the final polarizer for the lattice is expected to provide  $10^{-4}$  purity of linear polarization. From the polarization purity of the retro-reflected lattice beam we estimate the birefringence of the vacuum windows reduces the polarization purity by at most  $10^{-2}$ , which would result in a symmetric splitting equivalent to a fictitious magnetic field of  $60 \mu\text{G}$ . The shift from the symmetric splitting effect must be evaluated experimentally to take into account the realistic population distribution. From our magnetic field measurements below (5.1.6) we find Zeeman shift coefficients of roughly  $10 \text{ Hz}/\text{G}$ , such that we can expect the vector light shift to contribute at the sub mHz level. We show in 5.1.6 that the Zeeman shift uncertainty obtained here is on the 100 mHz level such that we can completely ignore the vector shift. While the exact size of the vector and tensor shift coefficients are only based on

theory and experimental upper limits, we note that the linear extrapolation to the zero-trap depth clock frequency performed above is sufficient to characterize the total Stark shift from scalar, vector, and tensor polarizabilities as the interaction for all of these effects depends linearly with the trap depth. We thus report only one total value of the light shift uncertainty based on the measurements above, which includes shifts from vector, tensor, and residual scalar light shifts. We also note that no systematic dependence of the lineshape on the lattice depth was observed again suggesting the tensor and vector contributions are small.

The linear extrapolation inherently assumes the hyperpolarizability effects are negligibly small. The best measurement for the fourth order electric field sensitivity is  $4.5(4.5) \mu\text{Hz}/(U_T/E_R)^2$  [41, 43] such that at our fields the shift is only  $1.3(1.3)\times 10^{-17}$ . This is orders of magnitude smaller than our scalar light shift uncertainty above, and can therefore be ignored.

### 5.1.3 Polarizability Effects: Stark Shifts from the Probe Laser

Systematics related to the probe laser were considered in two respects. First, the probe can cause Stark shifts of the clock states by coupling to external levels. This shift will depend on the achievable linewidth and can be estimated from the polarizability calculation, the probe time, and the saturation intensity for the clock transition. Assuming a 10 Hz feature ( $t=80$  ms) we can approximate the intensity needed to excited the atoms with a  $\Omega \times t = \pi$  pulse as

$$I = I_{sat} \frac{2\Omega^2}{\Gamma^2} \quad (5.1)$$

Where the saturation intensity is  $I_{sat} = 0.41 \text{ pW}/\text{cm}^2$ ,  $\Gamma=1/150$  s, and  $\Omega=\pi/(80ms)$ . The resulting intensity required is  $28 \mu\text{W}/\text{cm}^2$ . Based on our polarizability calculations the shift is less than -10 mHz. However, here we have neglected the effect of atomic motion in the trap on the Rabi frequency. The longitudinal and

radial motion will reduce the rabi frequency by a factor  $\langle n | e^{i\vec{k}\cdot\vec{x}} | n \rangle$  as discussed in Chapter 3. This reduction factor depends strongly on the atom temperature and trap parameters. Therefore, the linewidth and polarizability is not enough to predict the shift and it must be explored experimentally.

The second effect we considered was whether asymmetric motional sidebands could cause line pulling. This effect is minimal as the sidebands are well resolved (even the radial sidebands are detuned by more than ten times the transition width) and are only observed for large probe intensities.

Both of these effects were checked experimentally by varying the probe power by more than an order of magnitude during 77 measurements. The final value for the shift is 8(50) mHz. To eliminate Stark shifts from other sources, all lasers used for cooling, trapping, and detection are switched with both acousto-optic modulators and mechanical shutters.

#### 5.1.4 Polarizability Effects: Blackbody Radiation Shift

Systematic shifts from black body radiation (BBR) are another concern for clock accuracy [49]. Since the static polarizabilities ( $\alpha^{\text{tot.}}(\omega \rightarrow 0)$ ) of the clock states differ, we can expect that the radiation field from a black body emitter can provide a differential shift of the levels, which must be accounted for. The clock shift can be calculated for a temperature  $T$  if the differential static polarizability of the clock state is known, by

$$\delta\nu = -\frac{k_B^4}{60\epsilon_0\hbar^4c^3}\Delta\alpha^{\text{tot.}}(\omega = 0)T^4 \quad (5.2)$$

This formula is a good approximation if there are no atomic transitions within the BBR spectrum. The  $T^4$  dependence suggests that hot objects near the atoms can be a concern. Based on our polarization calculations we find that the static polarizability of the  $^3P_0$  and  $^1P_1$  states is 351.3 a.u. and 197.4 a.u. respectively.

This leads to a BBR clock shift of -1.39 Hz at  $T=300$  K, an effect large enough that we certainly can't ignore it. We can check the validity of using the simple static polarizability by performing a more correct calculation where the shift is determined by integrating the product of the black-body intensity spectrum with the differential polarizability over the relevant frequency range of the emission spectrum, as

$$\delta\nu = -\frac{1}{4\epsilon_0\pi^3c^3} \int \Delta\alpha^{tot.}(\omega) \frac{\omega^3}{e^{-\frac{h\omega}{k_B T}} - 1} d\omega \quad (5.3)$$

Here we find that for at  $T=300$  K we can expect a clock shift of -1.52 Hz. The small difference in the two calculations is attributed to the presence of the  $^3P_0$ - $^3D_1$  resonance in the polarizability at  $2.6 \mu\text{m}$  which is within the BBR spectrum at this temperature.

In comparing our values here with that of high accuracy atomic structure calculations in Ref. [49] we find a discrepancy in the final value of the BBR shift where a value of -2.354(32) Hz is reported for  $T=300$  K. The origin in the discrepancy is the calculation of the static polarizability, as they find  $\alpha(^3P_0)=458.3(3.6)$  a.u. and  $\alpha(^1S_0)=197.2(2)$  a.u.. While the values for the  $^1S_0$  state are in excellent agreement, the  $^3P_0$  state calculations disagree by 100 a.u.. The most significant difference between the two calculations of the polarizability is that in this work we have not included the effect of the continuum contribution [139]. It is expected that the  $^1S_0$  state will be much less sensitive to the continuum contribution due to its larger detuning, and the rapid convergence of the total Stark shift after including only the first few states (see Table 3.3). Therefore we expect that our  $^1S_0$  calculation would agree with that of [49], and it does. Convergence of the  $^3P_0$  state is much slower, and the state is closer in energy to the continuum state so we expect a poor agreement there. The interesting thing is that the continuum states appear to have a significant effect on the  $^3P_0$  polarizability in the DC limit, but

not at optical frequencies since our magic wavelength calculation was spot on. It is possible that at the magic wavelength we are artificially taking the continuum into effect by use of the  $^3S_1$  strength adapted from Stark shift measurements in [36], while at DC that state is not as dominant so the polarizability there will be wrong. For now, we take the calculations of Ref. [49] as the correct value since the continuum is included, resulting in a final BBR shift of

$$\delta\nu = -2.354(32) \left( \frac{T}{300K} \right)^4 \text{ Hz} \quad (5.4)$$

To estimate the shift of our clock due to the BBR we measure the temperature of the vacuum chamber during measurements (see for example Fig. 5.8). For the work reported below the temperature during the frequency measurement was 298.0(1.5) K where the uncertainty is twice the measured fluctuation of the chamber temperature during the frequency measurement. The frequency shift is then -2.292(45) Hz where the uncertainty includes the theoretical uncertainty in the shift coefficient. We also considered the effect of a nearby heated sapphire window in the experiment which is kept at 200 °C. The window is 15.24 cm from the atoms and had a diameter of 0.95 cm, such that the solid angle subtended on the atoms is small, as is the resulting shift of -0.045(31) Hz. Here in determining the uncertainty we have allowed the solid angle to vary by a factor of 2 to account for possible reflections of the BBR radiation within the vacuum chamber and emissivity variation of the materials, while the temperature was assumed to be known within only 10 °C. We consider this a conservative estimate of the window contribution to the total shift. A third concern is that of the nearby Sr oven in which the nozzle runs at a smoking 850 °C. Although the temperature is high the effect is considered negligible because of the distance to the atom (60 cm), small solid angle, and most importantly the mechanical shutter in the system which closes during spectroscopy blocking the radiation from traveling towards the

atoms. Based on the discussion here, the total BBR shift is  $-5.44(16) \times 10^{-15}$ .

### 5.1.5 Characterization of Collision Shifts

It is well known that atomic collisions can affect the measured frequency of a clock transition [15]. In Cs-fountains for example the collision shift in fractional frequency can be as large as  $10^{-13}$ . The frequency shift of the clock ground state due to elastic collisions in a cold atom sample is given by [140]

$$\delta\nu = \frac{4\pi\hbar^2\rho a_{scat}}{M} \quad (5.5)$$

where  $\rho$  is the atomic density and  $a_{scat}$  is the ground state scattering length. Assuming the scattering length of the two clock states was known, and only s-wave elastic scattering was taking place, we could predict the collision shift. For  $^{87}\text{Sr}$  the collision properties such as the scattering length are unknown. Furthermore we are simultaneously probing states with different nuclear spins which probably will have different collision properties between different spin states. For example, atoms in the same spin state will not have s-wave collisions (in addition p-wave collisions can be frozen out at low temperatures) since they are fermions in the same quantum state, on the other hand the shift for collisions between different spin states could be large. The bottom line is that we don't know enough about the collision properties to simply calculate the shift, so it must be measured. The effect of atomic density on the transition frequency is explored in a similar fashion as the light shift. Densities ranging within (0.2-1)  $\rho_0$  are interleaved by varying the number of atoms in the lattice (by altering the original blue MOT number) to create plots as in Fig. 5.4, where  $\rho_0$  is our typical operating density. A histogram of 422 measurements of the density effect is shown in the right panel, resulting in a shift coefficient of  $3(140) \times \rho/\rho_0$  mHz. To calibrate  $\rho_0$  we use the measured atom number from the spectroscopy sequence which is  $\sim 10^4$ . The

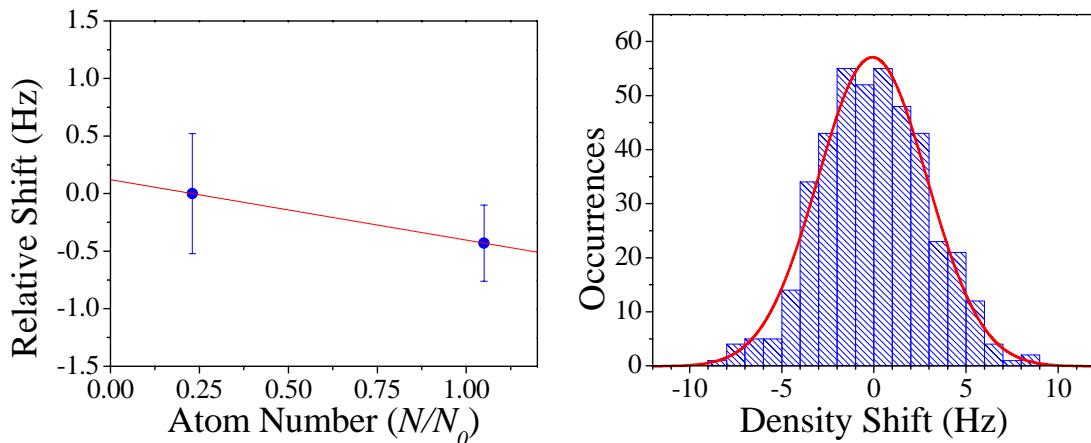


Figure 5.4: Measuring the effect of density changes on the transition frequency. The right plot shows a histogram of 422 measurements (such as the left plot) in which the atomic density is varied by up to a factor of 5 during spectroscopy. The measured shift is  $0.003(0.140)$  Hz at our typical operating density.

atoms are distributed into about 80 lattice sites, giving an average of about 100 atoms per site. The volume of each lattice site is determined from the measured trap frequencies and atom temperatures. We estimate our peak density to be  $\rho_0 \simeq 5 \times 10^{11} \text{ cm}^{-3}$ . Notably the upper limit of the density-related fractional frequency shift recorded here of  $5.6 \times 10^{-28} \text{ cm}^{-3}$  is  $\sim 10^6$  times smaller than for Cs [5, 6].

### 5.1.6 Characterization of Magnetic Effects

The ten nuclear-spin sublevels of the clock transition result in systematic effects related to magnetic and optical fields. For example, the asymmetric distribution of population among the sublevels can be a central systematic issue when using unpolarized atomic samples, as any  $m_F$ -dependent magnetic or optical interaction can cause a frequency shift, even if the sub-levels are shifted symmetrically about the center. As discussed in Chapter 4, the differential  $g$ -factor of the clock states provides the most significant effect as it leads to a sensitivity to magnetic fields of nearly 500 Hz/G for the stretched states. This large splitting can cause

clock shifts if the population is not symmetric or if the probe polarization excites  $\sigma$  transitions as well the  $\pi$  transitions. Three orthogonal sets of Helmholtz coils are used to characterize frequency shifts caused by the Zeeman sensitivity of the nuclear-spin sublevels. The orientation of the fields relative to the lattice is as follows. Field-1 is exactly parallel to the polarization axis of the lattice, such that application of the field does not change to quantum axis of the experiment. The broadening of the transition on this axis is therefore the most efficient as is our resolution in field calibration. Field-2 is nearly orthogonal to both the lattice polarization axis and the lattice propagation axis, while Field-3 is nearly parallel to the lattice propagation axis. For these axes the broadening is less severe for small fields than the Field-1 axis. For each direction, the transition linewidth is used to find the field minimum as shown in Fig. 5.5. For small fields, the data is well described by a parabola, and the field minimum can typically be determined within  $\pm 3$  mG. Due to the broadening mechanism, the use of narrow 10 Hz resonances allows the field zero to also be monitored in real time within  $\pm 5$  mG for Field-1 and  $\pm 10$  mG for Fields 2 and 3. This is a nice feature as we will notice right away if the background field in the lab changes at the few mG level, just by looking at the spectral lineshape. Frequency shift sensitivity is explored using the interleaved scheme with the results shown for Field-3, (which we found causes the largest frequency shift). Here the average values for 112 measurements on that axis are shown, yielding a slope of  $26(4)$  Hz/G. Similar measurements were performed for the other two axes yielding  $22(7)$  Hz/G for Field-1 and  $12(3)$  Hz/G for Field-2. Based on the broadening and shift data, observation of a 10 Hz spectra then guarantees that the frequency shift from axis 1, 2, and 3 are  $110(35)$  mHz,  $120(30)$  mHz, and  $260(40)$  mHz respectively. Since, the Field-3 shift is not as tightly constrained, we also do an occasional full field calibration of that axis to reduce the field uncertainty to less than 5 mG. In our standard operation the



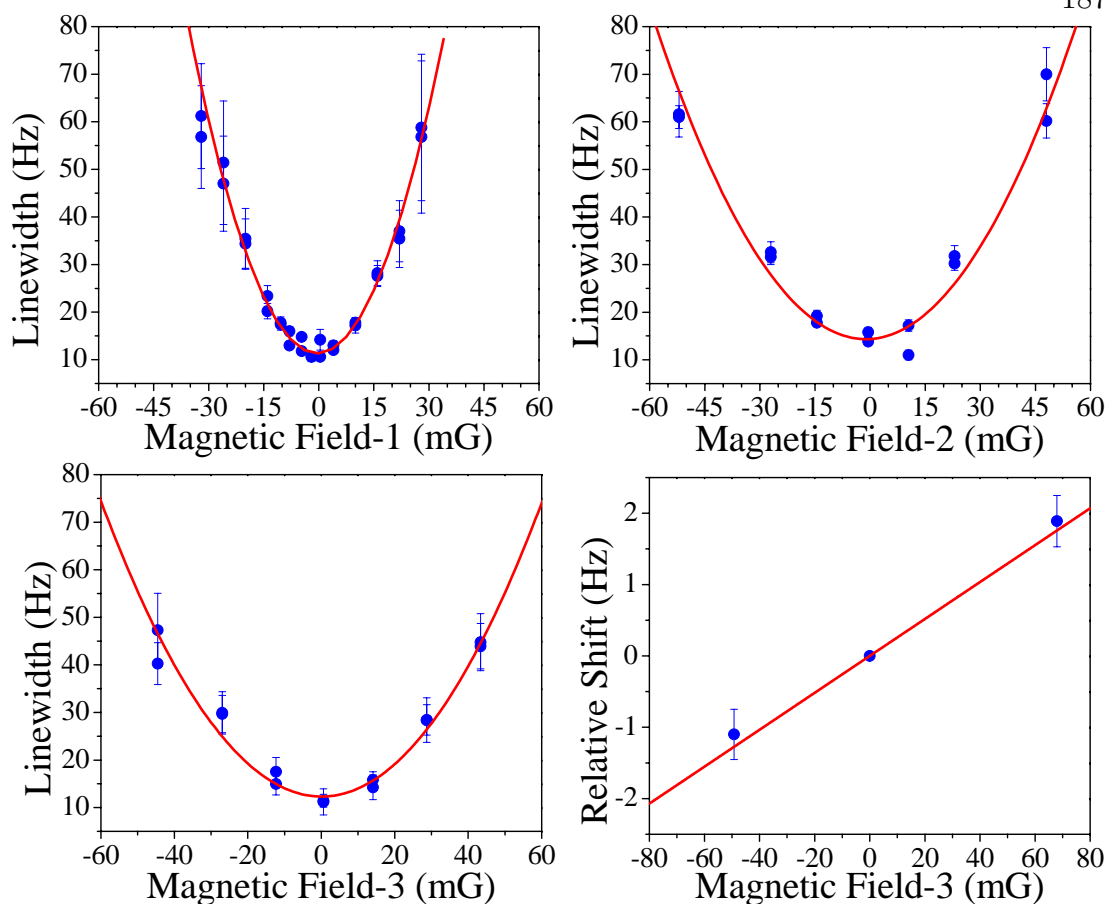


Figure 5.5: Effect of a magnetic field on the transition linewidth and frequency. The magnetic field for each axis is calibrated using the width of the narrow resonance. The data is fit to a parabola, determining the field zero typically to within 3 mG. The result of 112 interleaved measurements where the field-3 is varied during spectroscopy is shown. The frequencies of the zero field values are used as a reference for presentation purposes. The slope of all the measurements for this axis yields an average value of 26(4) Hz/G.

upper limit for the magnetic field shift is then  $5.3 \times 10^{-16}$ . Again, this gives insight into the minimal effect of the vector light shift which we discussed was equivalent to a field of less than  $100 \mu\text{G}$  in our system. Since we are operating near zero magnetic field, the second order Zeeman shift is also very small, on the order of  $2 \times 10^{-19}$ .

Table 5.1: Error budget for the  $^{87}\text{Sr}$  lattice clock discussed in the text. Here the uncertainties are given for our typical operating parameters,  $U_T=U_0=35E_R$ ,  $\rho=\rho_0=5\times 10^{11}\text{ cm}^{-3}$ ,  $\lambda_L=813.4280(5)$ .

Contributor	Correction ( $10^{-16}$ )	Uncertainty ( $10^{-16}$ )
AC Stark–Lattice (sca., vec., and ten.)	2.5	6.0
AC Stark–Probe and Line pulling	-0.2	1.2
AC Stark–BBR	54.4	1.6
Atomic Density	-0.1	3.3
Linear Zeeman	0	5.3
Second Order Zeeman	0	0.002
Second Order Doppler	0	< 0.001
Fourth Order Light Shift	-0.13	0.13
Total	56.5	8.8

### 5.1.7 Summary of Clock Systematics

Table I summarizes the dominant systematic uncertainties for spectroscopy of the clock transition, reported in terms of fractional frequency. A total uncertainty of  $0.88 \times 10^{-15}$  is achieved, representing the first experimental verification that the lattice technique can reach inaccuracies below the  $10^{-15}$  level, comparable with Cs fountains. The largest uncertainties are limited by technical issues such as a small dynamic range on the lattice intensity and sensitivity to stray magnetic fields. The 50-fold reduction of the systematic uncertainty from our previous work [44] is mainly due to the improved line  $Q$  and direct use of the stable optical reference.

## 5.2 Absolute Frequency Measurement of the $^1S_0$ - $^3P_0$ Transition

With the spectroscopy systematics well characterized, we now turn to the issue of measuring the optical clock frequency. In this section we describe the fs-comb setup used for the absolute frequency measurement, as well as the remote clock comparison system used to link our lab at JILA with the Time and Frequency Division at NIST. This frequency measurement includes a extra set of potential

systematics which are discussed here.

### 5.2.1 The Frequency Comb

A number of excellent reviews are available detailing the principles and uses of fs-comb lasers in optical frequency metrology [141, 142, 21]. Here we only briefly discuss some of the relevant details of the comb system used in this work, which is described at length elsewhere by Foreman [143], and is very similar to the comb previously reported in [144]. Our fs-comb system has some non-traditional features which simplify some operational issues. The comb offset frequency is stabilized in the usual  $f-2f$  self-referenced way [19], with the caveat that in this system the use of microstructure fiber is unnecessary to achieve the full octave spectrum required for stabilization. Elimination of the alignment sensitive microstructure fiber allows operation of the comb over many hours without any tweaking by the operator. The repetition rate ( $\sim 100$  MHz) is stabilized by heterodyning the 698 nm clock laser with a near by comb mode and stabilizing the beat via feed back to the comb cavity length. Since the repetition rate is stabilized at an optical frequency, the accuracy requirements for the synthesizers and counters used are dramatically relaxed as the microwave noise does not get scaled up by the large comb mode number. With the offset and repetition frequencies locked, the frequency of all the comb modes are known (relative to the clock laser frequency) in terms of a mode number and the different beat frequencies in the locking scheme. Comparison of the optical frequency with a high accuracy microwave standard can then be done by measuring the repetition rate of the comb relative to the high accuracy RF reference.

Stabilizing the repetition rate via the clock laser also allows transfer of the clock stability over the entire comb spectrum as the comb linewidth is now determined by that of the clock laser. By comparing of our stabilized comb to

an independent clock laser at 1064 nm we have shown [143, 138] that the sub Hz linewidth of the clock is transferred across the spectrum (see for example Fig. 5.11 where this is done in a more complicated situation with the clock lasers separated by a long fiber link). This optical transfer is a crucial capability of the comb, as comparison of different high accuracy optical clocks require direct comparison of different optical frequencies without precision degradation.

### 5.2.2 Microwave Reference and Transfer

With the frequency comb in place, the next issue is comparison of the comb to the microwave reference at NIST. The general approach taken in this work is to use the microwave reference to apply amplitude modulation on a transfer laser which can then be transmitted to our lab via an optical fiber where the modulation frequency is detected and compared to the comb repetition rate. Fortunately in our lab we have access to the Boulder Research and Administration Network (BRAN) [145] fiber link which connects JILA to a number of buildings on campus, and most importantly the NIST Time and Frequency Division  $\sim 3.5$  km away.

A detailed schematic of the frequency measurement setup is shown in Fig. 5.6. A commercial RF synthesizer at NIST is stabilized to the 10 MHz H-maser signal which is calibrated by the Cs fountain primary standard. The synthesizer provides a 950 MHz signal which is used for amplitude modulation of a CW transfer laser at 1320 nm. The laser passes through a fiber optic circulator and then into the 3.5 km BRAN fiber towards our lab at JILA [117, 137]. On the JILA end, our self-referenced fs-comb is tightly locked to the clock laser by stabilizing the beat at 698nm and feeding back to the cavity length of the comb (and thus the rep. rate). The comb repetition rate is then detected on a photodetector and is compared to the 950 MHz transfer signal. The difference between these two microwave frequencies is then recorded, such that the frequency of the clock laser relative to

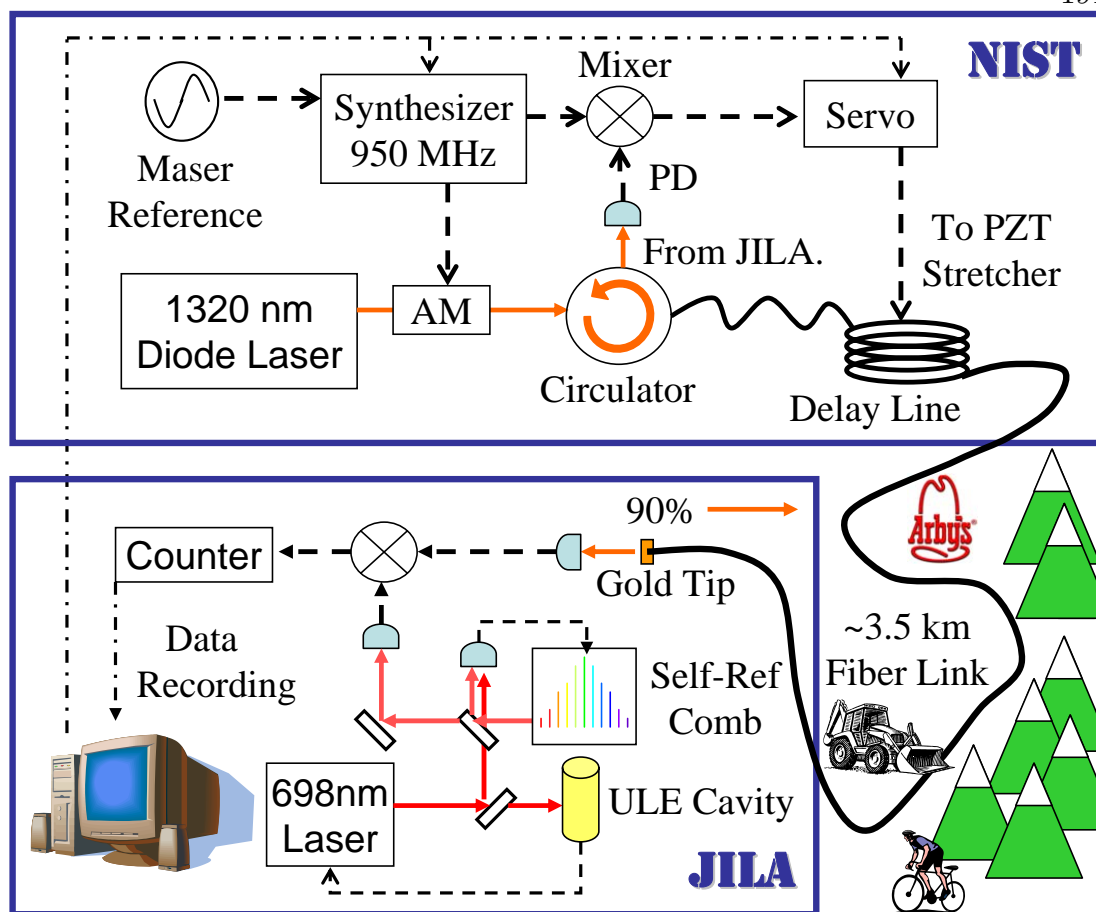


Figure 5.6: Cartoon diagram of the absolute frequency measurement setup. The Cs calibrated H-maser signal stabilizes the RF synthesizer used for amplitude modulation of the transfer laser. The laser is sent through the 3.5 km BRAN fiber which travels through an urban environment before coming to the JILA lab. The microwave transfer can be phase stabilized as discussed in the text. On the JILA end, the amplitude modulation on the transfer laser is compared with the repetition rate of a self referenced fs-comb, which is phase locked to the 698nm clock laser.

the Cs standard can be determined. The NIST synthesizer is computer controlled from the JILA lab such that the modulation frequency can be set to a convenient frequency, depending on the repetition rate of the laser. The maser and transfer system provide a 1 s instability of  $2.5 \times 10^{-13}$ , and for the work reported here, the maser is calibrated to  $1.7 \times 10^{-15}$  by the Cs fountain. Thus we can hope to measure our Sr frequency to a similar accuracy level if the transfer does not

degrade the microwave frequency.

To check the accuracy of the fiber transfer, the fiber tip at the JILA end is coated with a thin gold layer such that nearly 90% of the light is reflected back to NIST. The return light is then extracted from the fiber optic circulator and round trip modulation signal can be detected on a photo diode. This round trip signal is compared to the output of the synthesizer with a mixer, providing an error signal proportional to the phase difference between the two signals. To test the accuracy of the transfer we monitored the output of the mixer over a period of a few days, with the results shown in Fig. 5.7. The passive transfer of the microwave reference using the fiber is seen to introduce phase changes specifically related to periodic stretching and compressing of the fiber length which are strongly correlated to daily temperature variations. This effect results in frequency offsets as large as  $10^{-14}$ , with the sign of the correction depending on whether the fiber is expanding or contracting (i.e. morning or evening). This kind of effect is certainly a concern for our clock measurement since it can cause frequency biases which are correlated to the weather and time of day the data was taken. Given that much of our data is typically taken in the evening when the rest of the lab empties out, this bias is unacceptable.

To eliminate this effect, the fiber length is stabilized using a PZT fiber stretcher which is controlled by the output of the comparison mixer which measures the local microwave phase at NIST compared to that of modulated light reflected back from JILA [137]. Since the round trip light passes through the fiber stretcher twice the phase is stabilized at both the JILA and round trip ends. The locking is fairly robust, providing accurate frequency transfer at the level of a few parts in  $10^{17}$  according to in-loop measurements. Since we have not yet made out-of-loop measurements of the system performance we artificially increase the uncertainty by an order of magnitude to  $10^{-16}$ , which is conservative considering

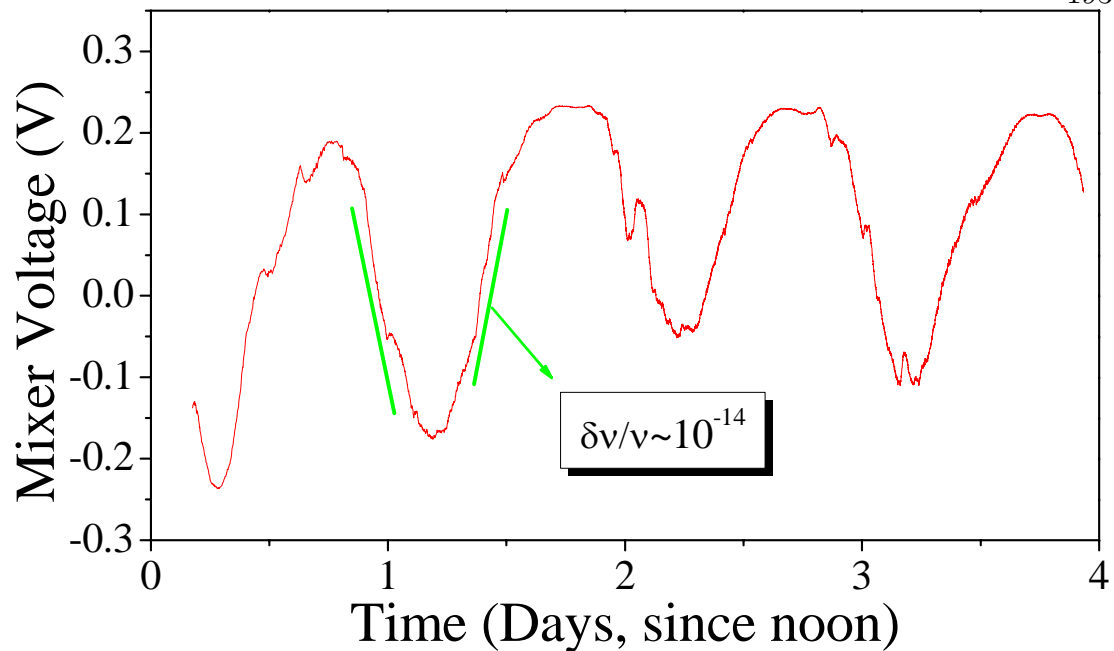


Figure 5.7: Measurement of the phase error resulting from passive microwave transfer via the BRAN link over a four day period. The phase error is strongly correlated with daily temperature swings and can result in large frequency errors of up to  $1 \times 10^{-14}$  if measurements are taken during the same time every day.

other potential problems should not cause any shifts at this level [146]. It should be noted that to achieve this level of stabilization it was necessary to replace any connectorized links in the fiber path with fusion splices, as we found that the connectors reflected an unacceptable amount of light, degrading the locking signal. The main limitation of this system is the dynamic range of the fiber stretcher which cannot compensate for the changing BRAN length for longer than about an hour. Because of this, the fiber servo is occasionally disengaged via computer control at JILA, and the transfer modulation frequency is slightly changed to allow a re-set of the fiber servo offset near zero.

The reference synthesizer for the transfer can also cause frequency errors [147] as we have measured that drifts in the synthesizer's temperature result in referencing errors leading to fractional shifts at the level of  $4 \times 10^{-14} \text{ (K/Hour)}^{-1}$ .

For the measurements reported here, the synthesizer is placed in a temperature stabilized enclosure and the temperature inside and outside the enclosure is monitored. For the data set below, the resulting correction was  $-1.7(7) \times 10^{-15}$ .

All synthesizers and counters used in the experiment which can effect the measured frequency were referenced to a commercial Cs clock in our lab which guarantees accuracy of the RF frequency to better than  $10^{-10}$ . These include any AOM drivers, or fiber noise cancelation setups for the spectroscopy laser, as well as the counters and reference synthesizers for the comb. Since these various microwave frequencies in the experiment are small offsets on optical frequencies, the precision provided by the commercial Cs clock is sufficient. For example an 80 MHz AOM offset which is controlled by a RF synthesizer with  $10^{-10}$  accuracy provides mHz level control, which at our optical frequencies is negligible. The exception to this rule, in some experiments, is the comb repetition rate, in which the fraction noise in the microwave regime gets multiplied up to the optical regime by the mode number  $n$ . However, in our case the repetition rate is stabilized by an optical heterodyne beat with the clock laser such that the microwave noise is not scaled up, and is therefore negligible.

### 5.2.3 Gravitational Correction

The final systematic issue that we consider for the clock comparison here is that of gravity. In a gravitational potential, we expect the clock frequency to deviate from its natural value. This can cause a problem if labs at different elevations want to compare frequencies. The standard way of reporting frequencies of this precision to the international community is to correct the recorded frequency for one's elevation relative to the earth's geoid. In this way all clock frequencies will be reported for the same gravitational potential. For example when NIST reports the Cs-based timescale to the international community (BIPM), the mea-



sured value requires some correction to account for the gravitational potential in Boulder. In our setup on the other hand, we are using Sr and Cs clocks which are both in Boulder such that the gravitational potential is nearly equal. More simply, the two clocks are in the same potential and the frequency ratio will not depend on what that potential is. We therefore only need to consider effects due to the difference in elevation of the Cs and Sr clocks. The position of the Cs fountain is well known (for these gravitational reasons), and the elevation of our strontium clock has been calibrated using a nearby GPS receiver in the JILA building. The difference in elevation between the two clocks is 11.3(2) m. Since the Sr clock is at a lower elevation, the frequency runs slow, such that we should apply a positive correction of  $1.25(2) \times 10^{-15}$  where we have used the fractional frequency shift coefficient of  $1.09 \times 10^{-16} \text{ m}^{-1}$  [148].

#### 5.2.4 Absolute Frequency Measurement

With our frequency measurement system in place, we should be able to measure the  $^1S_0$ - $^3P_0$  transition frequency with an accuracy similar to that of the calibrated maser. Based on the maser stability of  $< 3 \times 10^{-13} \tau^{-1/2}$ , we can expect that we will need 24 hours of measurement to average down to the maser uncertainty. To avoid any time of day bias, we measured the frequency continuously over a full 24 hour period. For a measurement of this length, we need to be sure that the strontium systematics in Table 5.1 do not fluctuate. The lattice shift is not a problem over this time scale as the laser intensity is servoed and the wavelength is easily monitored in realtime with a high precision wavemeter that has been calibrated by the clock laser. The density shift is also not a concern because the value of  $\rho_0$  is the peak density we achieve, and over such a long time, a drop in atoms is a bigger concern than a sudden gain. Furthermore, the atom number is naturally recorded in each spectrum taken. The biggest concern is that

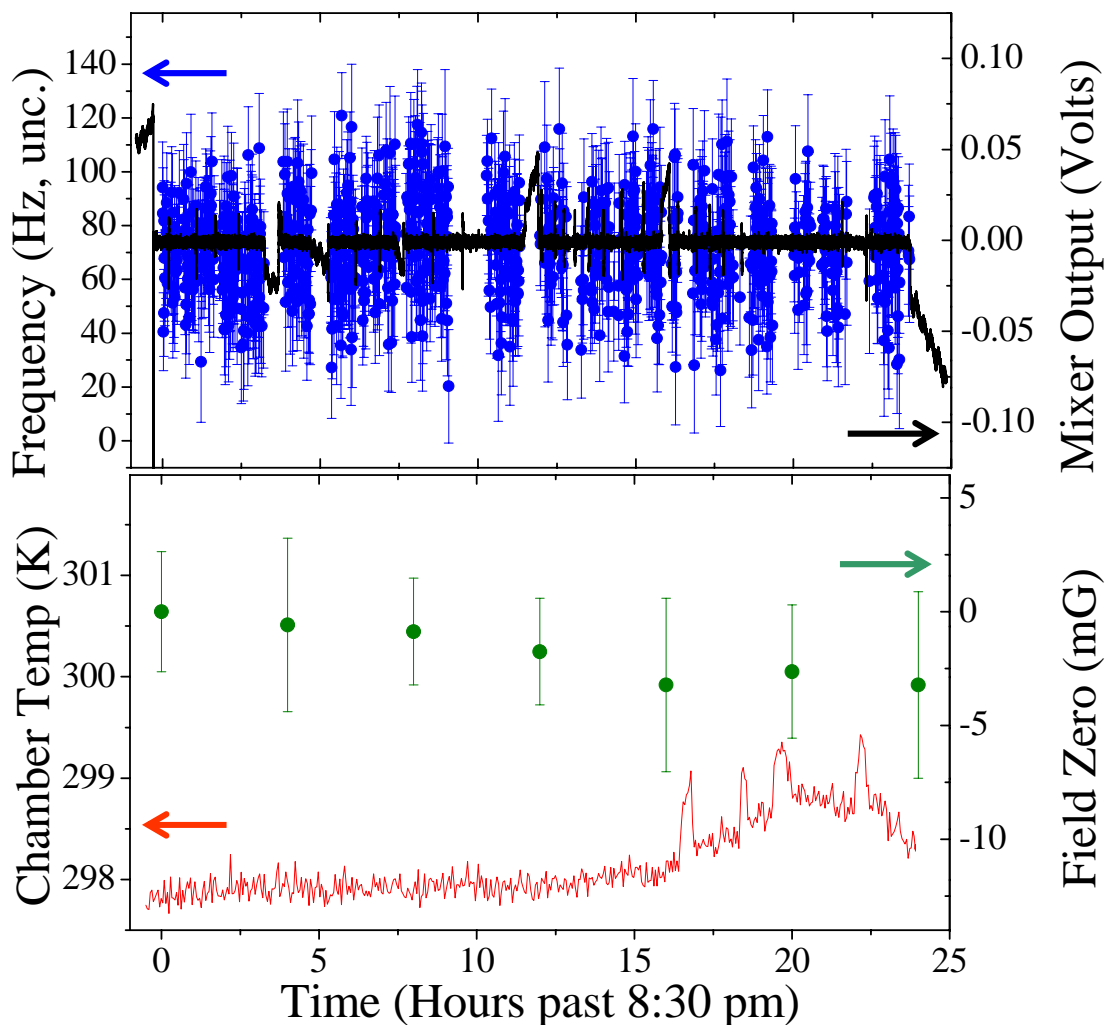


Figure 5.8: Data record for the absolute frequency measurement discussed in the text. The top panel shows the frequency measurement (including the maser calibration) resulting from each line scan (blue). The black line shows the fiber link stabilization signal. The bottom panel show the occasional field-3 calibrations (green) and the recorded temperature of the vacuum chamber (red).

magnetic fields in the room can drift. To monitor this we look at the transition width which depends on the field, for example on the most sensitive axis we can constrain the stray field to within a few mG if the linewidth is 10 Hz. As a second check we repeat the zero calibration once every few hours for the axis which effects the linewidth the least. The temperature of the chamber is also monitored during the entire measurement.

Figure 5.8 shows the raw frequency measurements over a 24 hour period. Here the measured frequency (including the maser offset calibration of  $-401.0 \times 10^{-15}$ ) is given relative to a convenient value of  $\nu_0 = 429,228,004,229,800$  Hz. Each data point (blue) corresponds to a scan of the transition using 11 Hz features, as in Fig. 5.1. The frequency uncertainty for the measurement is typically  $\sim 20$  Hz, consistent with the maser allan deviation for the 30 second measurement. The breaks in the data correspond to measurements being stopped for various reasons such as laser unlocks, fiber transfer unlocks, field calibrations, etc. The recorded mixer voltage for the stabilized BRAN fiber is given on the same plot (black), showing that the phase problem in Fig. 5.7 is well controlled with the fiber stabilization. The lower panel of the figure shows our monitoring of the spectroscopy systematics during the measurement. The magnetic field is monitored by the transition widths of each measurement, and also by occasional complete field calibrations shown as green data points in the lower panel. Over the 24 hour period it was found that the field did not drift significantly compared to our tolerances of 5-10 mG. The temperature of the vacuum chamber was also monitored as shown in the red data of the lower panel. The four large peaks in the temperature data are times when the atom cooling cycle was stopped for optimization. When this is done the MOT coils are run constantly, which heats up the surrounding air and vacuum chamber. After about 10 minutes of running in the typical sequence mode the chamber cools off again. The temperature data here is used to determine the systematic in Table 5.1. Note the unfortunate nature of our lab as the baseline of the temperature data is very steady for the first 12 hours (8pm-8am) but is much less stable when JILA comes to life in the morning, causing unlocks which require re-tweaking of the cooling setup.

The graph in Fig. 5.9 shows the same frequency data, after removing data points in which the fiber transfer was unstabilized, the chamber temperature had

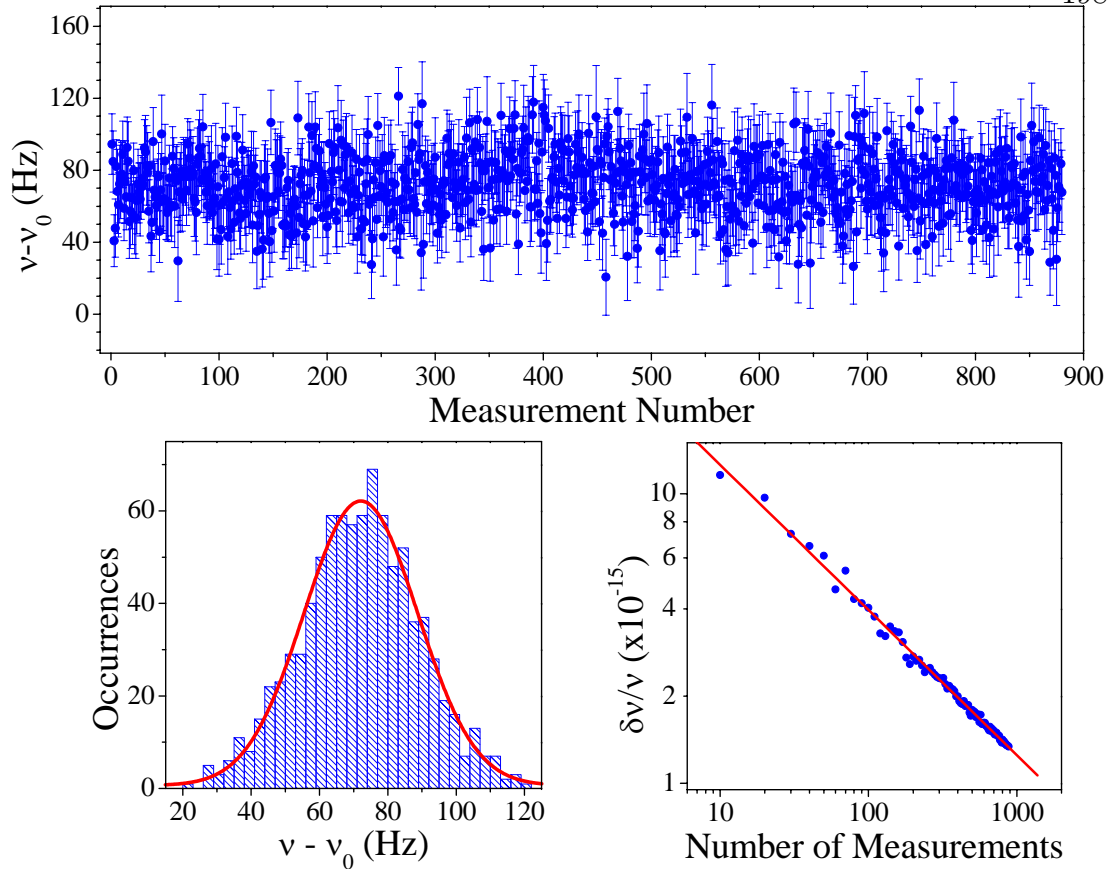


Figure 5.9: Absolute frequency measurement of the  $^1S_0 - ^3P_0$  transition. (Top) Counting record of 880 measurements taken over a 24 hour period yields a mean value of 71.8(6) Hz (corrected for only the maser offset). The uncertainty averages down as  $N^{-0.501(4)}$ , where  $N$  is the number of measurements (randomized), reaching  $1.4 \times 10^{-15}$ . A histogram of the frequency measurements with a gaussian fit (red) of the data is also shown. Here the offset frequency,  $\nu_0$ , is 429,228,004,229,800 Hz.

spiked, and one group of data where the temperature of the transfer synthesizer had been poorly controlled. This final data set contains 880 absolute frequency measurements which span a the full 24 hour period fairly evenly. The mean value of the frequency (relative to  $\nu_0$ ) is 71.8 Hz. The histogram in the figure attests to the gaussian nature of the measurement and the third panel in the figure shows how the uncertainty averages down versus the number of measurements (randomized). The data averages down as  $N^{-0.501(4)}$ , to give a final statistical uncertainty

Table 5.2: Error budget for the absolute frequency measurement of the  $^{87}\text{Sr}$  clock transition. The measured frequency, preadjusted by  $-401.0 \times 10^{-15}$  for the maser calibration, is corrected by the Sr spectroscopy offset (Table 5.1), and other small correction factors. The final frequency of the transition is reported relative to a convenient offset frequency  $\nu_0 = 429,228,004,229,800$  Hz. The total uncertainty for the frequency is  $2.5 \times 10^{-15}$ , or 1.1 Hz, which is dominated by the maser calibration uncertainty.

Contributor	Correction ( $10^{-15}$ )	Uncertainty ( $10^{-15}$ )
Sr (Table 5.1)	5.65	0.88
Maser Calibration	–	1.7
Synth. Temp. Drift	-1.7	0.7
Fiber Transfer	0	0.1
Gravitational shift	1.25	0.02
Total Systematic	5.2	2.0
Total Statistical	0	1.4
Total	5.2	2.5
$\nu_{Sr} - \nu_0$	74.0 Hz	1.1 Hz

of 0.6 Hz or  $1.4 \times 10^{-15}$ . This is consistent with the maser allan deviation for the measurement time of the 880 line scans. The measured frequency is then corrected by the systematic offsets listed in Table 5.2. The Sr correction, given in Table 5.1, is  $5.65(0.88) \times 10^{-15}$ . The synthesizer correction is calculated based on the mean rate of temperature change during the entire measurement. Applying the correction locally instead of globally does not change the final frequency within the uncertainty reported. The only significant corrections in Tables 5.1 and 5.2 not determined by direct frequency measurements here are the BBR shift and the gravitational shift arising from the difference in elevation of the NIST Cs fountain and the JILA Sr lattice. With all of the corrections applied, the frequency of the  $^{87}\text{Sr } ^1S_0\text{-}^3P_0$  transition is  $429,228,004,229,874.0(1.1)$  Hz, with the uncertainty mainly limited by the maser calibration. At the time of the measurement the final absolute frequency uncertainty of  $2.5 \times 10^{-15}$  corresponds to the most accu-

rate optical frequency measurement for neutral atoms, falling short of only the recent  $\text{Hg}^+$  ion result [29] as the most accurate absolute optical measurement of any system.

### 5.2.5 An International Effort

The precision and accuracy enhancement provided by the lattice clock has led to investigations by a number of labs around the world. This type of competition is very healthy for the development of a frequency standard as independent results can be compared between different groups with different systems. A summary of the  $^{87}\text{Sr}$  clock transition measurements in an optical lattice is shown in Fig. 5.10, with the same relative offset  $\nu_0$  as before. The record spans reported values from 2005 to present, attesting to the intense pursuit of the lattice clock. Due to the rapid progress in the field, the measurements are given in order of the date the research was presented in final form, via journal submission or arxiv pre-print date. Not shown is the first absolute measurement of the transition frequency, taken with a free space cloud of atoms, reported by the Paris group [149]. The value is in agreement with the measurements shown, having a large uncertainty (on this scale) of 15 kHz.

One can imagine that some uneasiness set in among the community with the announcement of the first two measurements by the group in Tokyo [58] and our group [44], as the frequency value disagreed by a few sigma. The first value was made public while our measurement was under way, causing us to go back and check, double check, and triple check our frequency (and lose some sleep along the way). No matter what "knob" we turned, we could not induce a frequency change in the lattice clock at anywhere close to the disagreement, so we published the number we were getting. The main difference between the measurements was that our group was using the Cs-calibrated maser reference whereas the Tokyo group

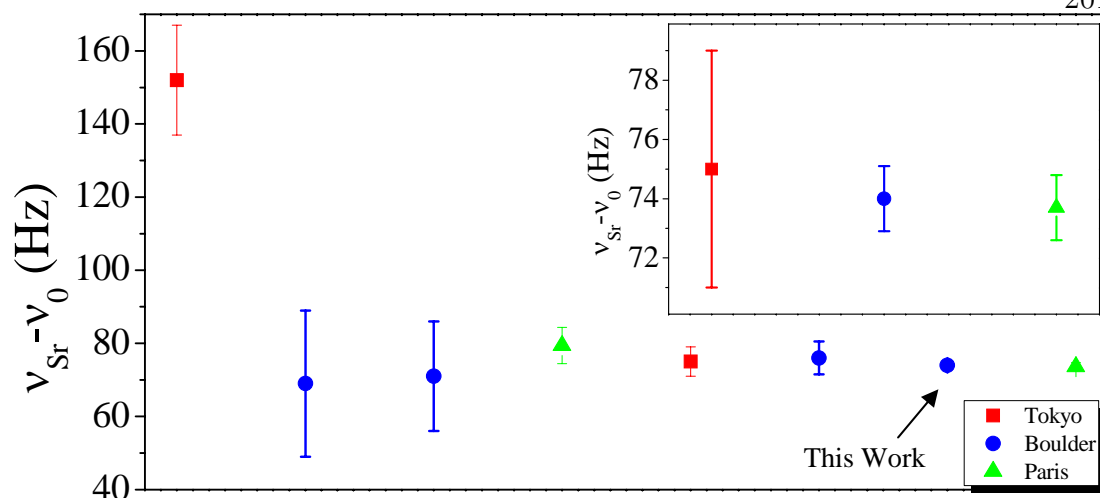


Figure 5.10: International measurement record for the  $^{87}\text{Sr}$  lattice clock. Published data is shown from our group [44, 150, 151, 42] (blue circles) as well as the groups in Tokyo [58, 46] (red squares) and Paris [45, 43] (green triangles). Aside from the first measurement, the agreement between the three labs is excellent, as can be seen in the inset which shows a closer view of the most recent measurement from each group. Notably, the last two measurements agree at the level of  $7 \times 10^{-16}$ .

was employing a commercial Cs clock calibrated by a GPS signal. The latter method provides a measurement stability orders of magnitude worse than the maser system, requiring  $10^5$  seconds of integration to reach the level of precision of 20 Hz (while the maser requires only 30 seconds). This reference was thought by us to be the cause of the discrepancy, even more so as we repeated the measurement six months later and found the same clock frequency [150] as our original value. These thoughts were validated by a third independent measurement by the Paris group [45] which was in perfect agreement with our value and involved direct comparison to a Cs-fountain. A revised value was published from Tokyo shortly thereafter (although close enough in time, not to have been influenced by the Paris result) where they had employed a maser for the comparison [46]. With the  $4\sigma$  disagreement resolved, measurements by all the groups continue with high confidence.

The measurement described in this work  $\nu_{Sr} - \nu_0 = 74.0(1.1)$  Hz [42] is in excellent agreement with our original value, and provides an accuracy improvement of about a factor of 5 compared to the other measurements. More recently, the Paris group announced an improved number of  $\nu_{Sr} - \nu_0 = 73.7(1.1)$  Hz [43]. The agreement between our two labs is remarkable, at the level of  $7 \times 10^{-16}$ . The agreement is even more exciting if one considers how different the two lattice experiments are. In our system we used a degenerate sublevel, a line width of 10 Hz, a relatively shallow trap of  $35 E_R$ , and scans of the transition to determine the frequency. In the Paris experiment resolved spin polarized samples were used to eliminate the Zeeman shift, line widths greater than 30 Hz were used, an order of magnitude deeper trap depth was employed, and the clock laser was locked to the transition. The Sr-Cs comparison setups were also quite different in two labs as the Paris group used a nearby Cs-fountain and our group used a Cs-calibrated H-maser signal transferred from a remote location with an optical fiber. Thus two very different measurement schemes yielded the same result. This speaks volumes for not only the lattice clock as a frequency standard, but also the Cs fountains, as comparison between two sets of clocks on different continents yield the same value to 15 digits. As pointed out by P. Lemonde, the agreement between the two Sr-Cs measurements is actually too good, given the agreement between the Cs-fountain results reported to BIPM over the same time period. This could be explained in a few ways. One possibility is that the agreement was somewhat coincidental in that different systematics of some of these clocks could be under estimated or compensating one another. Another, more interesting possibility, is that the ratio of the Cs-Sr frequencies is in better agreement than the raw Cs frequencies reported to BIPM because some of the correction terms, such as the gravitational shift, may not be known as well as we think. Only more measurements with better and better clocks can answer these questions.



The inset of Fig. 5.10 shows a zoom in of the most recent measurements from the three Sr lattice clock groups. The agreement between the three groups (on three different continents) speaks strongly for the lattice clock as a future candidate for redefinition of the SI second. The repeatability of the Sr frequency measurements is also now at a useful level, in combination with the results of Ref. [8], for constraining the drifts of fundamental constants and local position invariance [152].

The outlook for the Sr lattice clock is quite promising as experiments are currently being developed by groups in Florence, PTB, and NPL, and other labs. So we can expect to see plots similar to Fig. 5.10 to include measurements from five or six standards labs in the near future. This kind of attention puts the strontium lattice clock in a special class, as no other optical frequency standard is being pursued by so many groups.

### 5.3 Outlook for The $^{87}\text{Sr}$ Lattice Clock: Current Progress

While the prospects for the  $^{87}\text{Sr}$  lattice are very encouraging, work must continue to improve the clock accuracy and stability. With the line  $Q$ 's shown in this work, the lattice clock should eventually surpass the ions in term of stability as the clock laser is improved. For accuracy concerns, the evaluation here is still an order of magnitude away from that which has been achieved with the Hg ion [29]. To make further progress on clock precision and accuracy, it is desirable to use another optical clock for comparison. Comparison of Sr to the maser for example is limited by the maser stability such that we cannot say with high confidence what the Sr stability actually is. It would also be useful to have an optical clock for comparison, to avoid the interleaved scheme used here. In light of this, we again turn to our colleagues at the NIST Time and Frequency Division where a number of high accuracy high precision optical clocks are available, including a

Hg [29] and an Al [30] ion clock, a neutral Ca clock [24], and a Yb [56] optical lattice clock. In this section we briefly discuss our progress towards all optical clock comparisons.

To make clock comparisons we again take advantage of the BRAN fiber link. Since the 698nm light cannot be directly transferred through the fiber, we instead use the comb to coherently transfer the clock information across the optical spectrum to a more convenient wavelength. The comb is locked to the 698 nm laser to provide sub-Hz linewidth across the spectrum to 1064nm where a transfer laser is phase locked to the comb. The transfer laser is then sent to NIST via the BRAN fiber. To stabilize the fiber link, we follow the same principle as in the microwave transfer, only in this case an AOM is used as the actuator. A gold tip at the NIST end of the BRAN reflects most of the light back to JILA where we can detect and servo out the phase noise added by the fiber transfer. We have shown that for BRAN fiber of a few km length, the transfer technique is coherent with stability better than  $1 \times 10^{-17} \tau^{-1/2}$  for averaging times as long as 1000 seconds [138]. Thus the noise floor for the transfer is negligible given our laser performance. Using the link we can make direct laser comparisons with NIST as our transfer laser can be beat against a fs-comb on the NIST end of the link, which is stabilized to the laser of interest. We therefore can make a beat between two highly stabilized clock lasers in different labs, using the fiber link, and two frequency combs to bridge the gap (both in spatial, and frequency dimensions) This complexity may make one suspect that the narrow linewidth may not be preserved, so we have tested the system using our clock laser at 698 nm and the 1126 nm laser which acts as the oscillator for the NIST Hg ion clock [153]. The results are shown in Fig. 5.11 where a beat note between the transfer laser (stabilized to the JILA comb and clock laser) and the NIST comb (stabilized to the Hg clock laser) reveal a RBW limited linewidth of 1 Hz, showing that

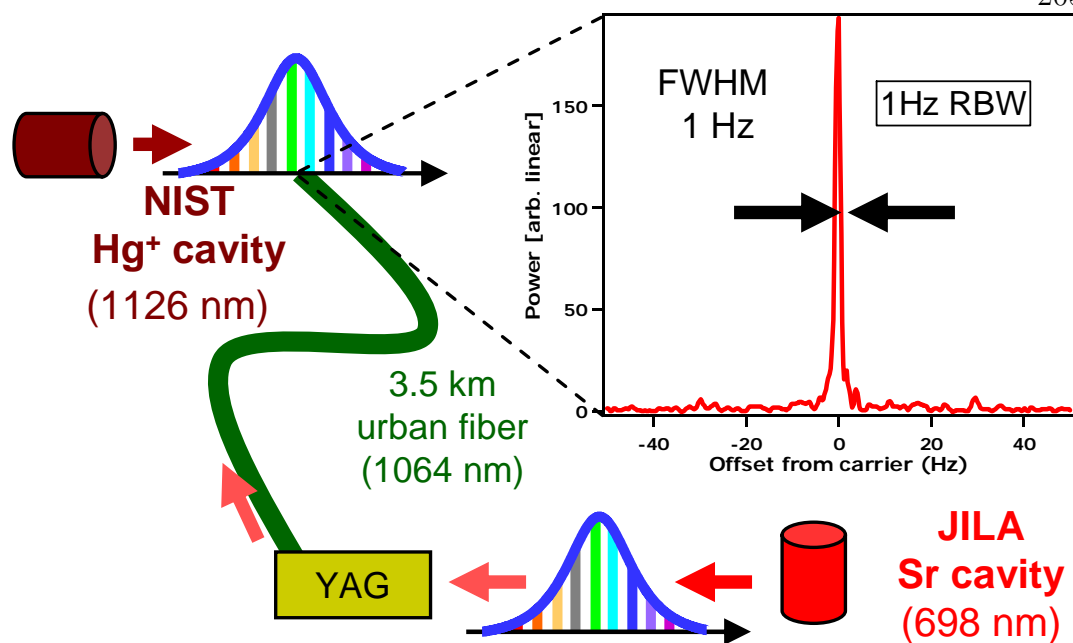


Figure 5.11: Comparison of the Sr and Hg<sup>+</sup> clock lasers using the (AOM) stabilized BRAN fiber link. The beat between the JILA transfer laser and the NIST comb reveals the laser linewidth is not deteriorated by the 3.5 km urban fiber, or the use of two fs-combs.

the complexity of the transfer and 2 frequency combs does not degrade the laser linewidth.

With the possibility of high precision optical comparisons we have also made some improvements to the Sr clock system. In looking at Table 5.1 we see that most of the systematics were statistically limited, such that the optical comparison should allow further reduction. To further improve the systematic evaluation we now injection lock the Ti:Sapphire [154] using a ECDL at 813 nm to increase the output power, and thus the available dynamic range for evaluation. The lattice wavelength is also stabilized to the comb for improved measurement of the magic wavelength (or frequency at this level). To eliminate the largest systematic, the Zeeman sensitivity, we now use Method II where the atoms are spin polarized to the  $m_F = \pm 9/2$  states and the average frequency is measured, such that the shift

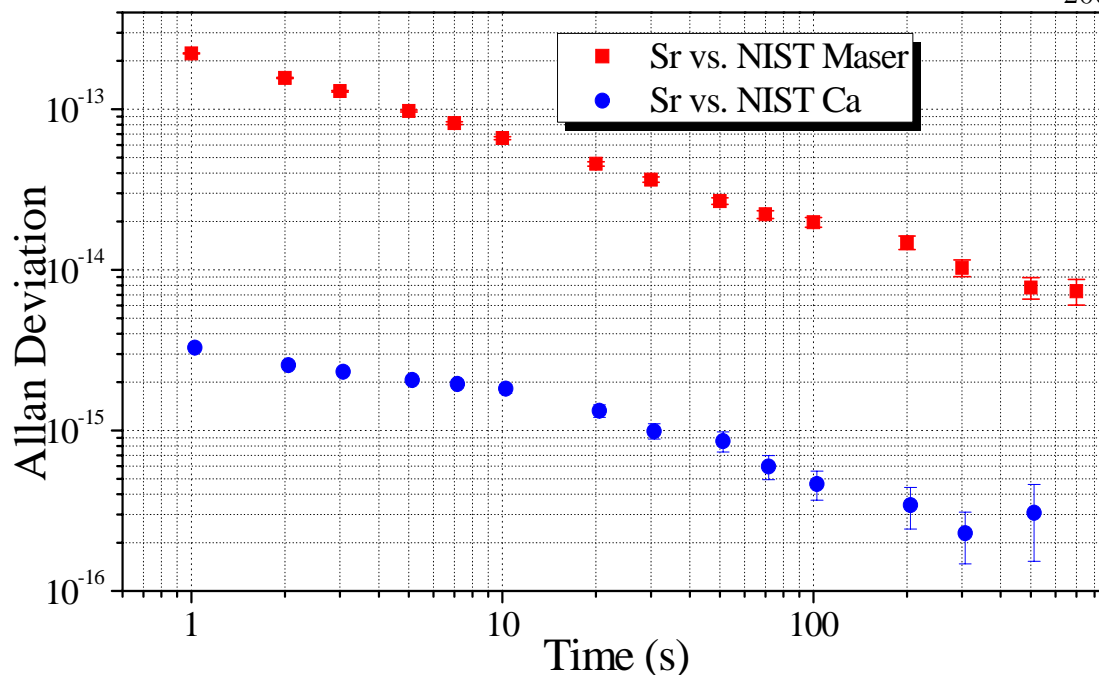


Figure 5.12: Measurement of the Sr clock stability using the NIST H-maser (red) and the NIST Ca optical clock (blue). The advantages of optical clock comparison are significant in that the stability is nearly two orders of magnitude better for the timescale shown, meaning a reduction in averaging time of nearly four orders of magnitude to achieve a given precision level.

from magnetic and optical Zeeman shifts are nominally removed (but still must be checked). We have also developed locking protocol such that the clock laser no longer scans the transition but is locked to it. With these improvements in place, and some preliminary measurements, we expect the clock uncertainty to be at about  $1 \times 10^{-16}$  by the end of 2007. This value would surpass even the best Cs fountains and nearly catch the best ion results. The expected limitation in the next round of measurement is the uncertainty in the BBR shift coefficient and the temperature distribution of the vacuum chamber.

We have begun re-evaluation of the clock accuracy using an optical comparison with the NIST Ca clock. The Ca clock frequency is not known with as high of accuracy as the Sr clock, but provides us with a number of advantages. The

Ca clock provides an excellent stability, and the system can be operated on an hours notice with robust performance. Figure 5.12 shows a stability measurement of the Sr clock (in the higher accuracy setup discussed here) compared to the H-maser and the NIST Ca clock. The Sr-Ca comparison provides a 1 s stability of  $3 \times 10^{-15}$  which is limited by the Ca laser. The stability typically averages down as  $< 5 \times 10^{-15} \tau^{-15}$  providing frequency comparison at the  $3 \times 10^{-16}$  level in 200 s. To reach the same level with the maser comparison requires  $10^6$  s of averaging. So while we can't use the the Ca clock to improve the absolute frequency measurement, it is incredibly useful for evaluation of our spectroscopy systematics. The stability shown here is by no means a fundamental limit to the Sr lattice clock stability. The data here is likely limited by the Ca system as the Sr stability is estimated to be limited by laser noise at  $\sim 2 \times 10^{-15} \tau^{-1/2}$ . If we assume adequate laser pre-stabilization, use of 2Hz spectra (which we have already observed), and quantum projection noise limited measurement of our  $10^5$  atoms (which seem possible to reach with improvements to the loading process), we expect to achieve stability in the  $1 \times 10^{-17}$  range for 1 s. The biggest hurdle here is getting the laser pre-stabilization to that level. Hopefully, the prospects of sub  $10^{-17}$  stability in a second will provide sufficient motivation for oscillator development to that level. To improve the absolute frequency value we can eventually compare the Sr frequency with that of the Hg ion which is known from Cs calibration to  $9 \times 10^{-16}$ . Beyond that point we are running out of room with the Cs clock and can only measure frequency ratios between optical clocks until one species is chosen as the next standard for the SI second.

## Chapter 6

### On the Horizon

In this final chapter, some future experiments and applications of the lattice clock system are discussed. Specifically, a few thoughts are given related to improving the  $^{87}\text{Sr}$  accuracy and the prospects of using other atomic species in a lattice clock.

#### 6.1 Future $^{87}\text{Sr}$ Clockwork

Even with the rapid progress on the  $^{87}\text{Sr}$  lattice clock system in the past four years, there is still much work to do if we wish to catch the accuracy levels of those elusive ion clocks across the road at NIST. The anticipated accuracy limitation in our next round of measurements, for example, is that of the BBR shift. To reduce the uncertainty of this effect in the future, a two pronged attack is likely needed. The first issue is the actual size of the BBR shift, that is, improving (and confirming) the theoretical value which currently has a fractional uncertainty of  $7 \times 10^{-17}$ . Futures measurement of the relevant excited state lifetimes (especially the lowest  $^3S_1$  and  $^3D_1$  state), possibly by photoassociation experiments, will certainly help in determining the polarizability with high accuracy. One can also envision a more direct measurements in which the lattice clock is operated in a variable temperature environment. The second issue is control of the environment in order to keep the temperature stable. At 300 K, the sensitivity of the clock transition

to temperature fluctuations is  $\sim 7 \times 10^{-17}/^\circ\text{K}$ . Therefore uniform environmental control at the 0.1 K level is needed to reach below  $10^{-17}$  in accuracy.

Atomic collisions in the lattice are also becoming of great interest. As the clock precision improves we should be able to explore the various collision properties of the different nuclear spin states. It may even be possible to eliminate *s*-wave collisions all together if single spin-states are used in clock operation. However it remains an open question on whether the same Rabi inhomogeneity effects that limit the excitation fraction will degrade the “fermionic purity”. If indeed the Rabi dephasing does limit the collision suppression, than the natural course of action will be to try and cool the atoms further, or to move on to a 3D lattice.

Three dimensional lattice clocks may eventually be more accurate than their 1D counterparts, as collisions can be essentially removed by giving each atom its own well. For atoms with nuclear spin, the size of the tensor and vector light shift will be more of a concern in the 3D lattice, due to the polarization dependence. Therefore, it will be important to improve on the measured upper limits presented in this work. If the shifts are too large, than EIT or DC field mixing approach with the bosonic isotopes will be more desirable.

## 6.2 Other Lattice Clock Candidates

While in this work Sr has been the main focus, Yb and Hg certainly are intriguing candidates for the lattice clock system. Although not directly in the sights of our lab, these systems are certainly interesting and will play (are playing) a role in the future of this lattice clock business. To this author, the most intriguing Yb property is the existence of an  $I = 1/2$  isotope  $^{171}\text{Yb}$ . Though the NIST group has focused mainly on the bosonic isotopes. It will fun to see what happens if/when they play with an  $F = 1/2$  clock transition, where the tensor shift should be absent and the atoms are “naturally” in the stretched (and only)

magnetic states from the get go. Neutral Hg also has an attractive  $I = 1/2$  isotope, and is now under development by P. Lemonde and S. Bize in Paris [155]. The main benefit in going to a Hg lattice clock, is that the electric dipole transitions are much further into the UV than Sr or Yb, such that the clock frequency is larger, and, more importantly, the BBR shift may be significantly smaller. It will be interesting to see if this systematic gain, is worth the cost (effort and \$\$\$!) of operating a lattice at 350 nm, and cooling and clock lasers around 257 nm.

Earlier in this thesis the different methods for lattice clocks were discussed (in terms of bosons vs. fermions), however this author has, somewhat intentionally, reserved any discussion of using different elements for this more speculative section. Not that use of other species is speculative, but more that this author feels it's a bit too early in this young field to be pointing fingers at one element or another, and instead just focused on the gritty details of the Sr system. But since it is useful to critically compare the different possibilities, I'll concede and quickly give my thoughts on the current situation. In comparing Yb and Sr, one can go back and forth a number of times on which would ultimately be better. Shift  $A$  (hyperfine splitting, BBR shift uncertainty, ...), might be larger in Yb than in Sr, and shift  $B$  might be smaller (BBR shift, second order Zeeman, ...), but nominally most of the field sensitivities are close enough that it won't be a deal breaker either way. The difference may then come down to practicality, although even here the issue is still somewhat debatable. For example, the laser cooling in Sr is much more efficient than in Yb, but also more complex. From our discussion of Rabi frequency effects in lattice spectroscopy we can assume that the colder the better, especially if it allows use of shallower traps. Sr seems to have the edge here, in that both Doppler and sideband cooling on the  $^3P_1$  transition work better than in the Yb case. Another practical difference is in the laser sources, where in Sr they can all be generated from diode sources, but in Yb the wavelengths are



more challenging. Then again Yb offers more stable isotopes than Sr which may provide a nice exit strategy if one of those species has its mind set on bullying neighboring atoms in that awful phase-shifting collisional way.

For now, it seems the international momentum is on the side of Sr, and with the results in Fig. 5.10 it's tough to argue that anyone currently pursuing Sr should make a detour. Admittedly, that momentum may have more to do with laser colors, cooling, and the already large number of labs pursuing Sr, than any particular systematic advantages. So we should expect to see similar results from Yb labs in the near future.

## Bibliography

- [1] S. A. Diddams, J. C. Bergquist, S. R. Jefferts, and C. W. Oates, Standards of Time and Frequency at the Outset of the 21st Century, *Science* **306**, 1318 (2004).
- [2] N. F. Ramsey, in *Laser Physics at the Limit*, edited by H. Figger, D. Meschede, and C. Zimmermann (Spinger, Berlin, 2002), pp. 3–8.
- [3] <http://www.bipm.org/>.
- [4] J. L. Hall, Optical Frequency Measurement: 40 Years of Technology Revolutions, *IEEE Journ. Sel. Top. Quant. Electr.* **6**, 1136 (2000).
- [5] T. P. Heavner, S. R. Jefferts, E. A. Donley, J. H. Shirley, and T. E. Parker, NIST-F1: recent improvements and accuracy evaluations, *Metrologia* **42**, 411 (2005).
- [6] S. Bize *et al.*, Cold atom clocks and applications, *Journal of Physics B: Atomic, Molecular and Optical Physics* **38**, S449 (2005).
- [7] T. Damour and J. H. Taylor, Strong-field tests of relativistic gravity and binary pulsars, *Phys. Rev. D* **45**, 1840 (1992).
- [8] T. M. Fortier *et al.*, Precision Atomic Spectroscopy for Improved Limits on Variation of the Fine Structure Constant and Local Position Invariance, *Phys. Rev. Lett* **98**, 070801 (2007).
- [9] J. L. Hall, Nobel Lecture: Defining and measuring optical frequencies, *Rev. Mod. Phys.* **78**, 1279 (2006).
- [10] T. W. Hansch, Nobel Lecture: Passion for precision, *Rev. Mod. Phys.* **78**, 1297 (2006).
- [11] <http://www.gps.gov>.
- [12] L. Hollberg *et al.*, Optical Frequency Standards and Measurements, *IEEE Journ. Quant. Electro.* **37**, 1502 (2001).

- [13] F. Chapeletet, J. Guena, D. Rovera, P. Laurent, P. Rosenbusch, G. Santarelli, S. Bize, A. Clairon, M. E. Tobar, and M. Abgrall, in *Proceedings of the Joint IEEE-FCS and EFTF Meeting* (Geneva, Switzerland, May 29–June 1, 2007), pp. 467–472.
- [14] G. Santarelli, P. Laurent, P. Lemonde, A. Clairon, A. G. Mann, S. Chang, A. N. Luiten, and C. Salomon, Quantum Projection Noise in an Atomic Fountain: A High Stability Cesium Frequency Standard, *Phys. Rev. Lett.* **82**, 4619 (1999).
- [15] K. Gibble and S. Chu, Laser-cooled Cs frequency standard and a measurement of the frequency shift due to ultracold collisions, *Phys. Rev. Lett.* **70**, 1771 (1993).
- [16] R. J. Rafac, B. C. Young, J. A. Beall, W. M. Itano, D. J. Wineland, and J. C. Bergquist, Sub-dekahertz Ultraviolet Spectroscopy of  $^{199}\text{Hg}^+$ , *Phys. Rev. Lett.* **85**, 2462 (2000).
- [17] M. M. Boyd, T. Zelevinsky, A. D. Ludlow, S. M. Foreman, S. Blatt, T. Ido, and J. Ye, Optical Atomic Coherence at the 1-Second Time Scale, *Science* **314**, 1430 (2006).
- [18] D. J. Jones, S. A. Diddams, J. K. Ranka, A. Stentz, R. S. Windeler, J. L. Hall, and S. T. Cundiff, Carrier-Envelope Phase Control of Femtosecond Mode-Locked Lasers and Direct Optical Frequency Synthesis, *Science* **288**, 635 (2000).
- [19] S. A. Diddams, D. J. Jones, J. Ye, S. T. Cundiff, J. L. Hall, J. K. Ranka, R. S. Windeler, R. Holzwarth, T. Udem, and T. W. Hansch, Direct Link between Microwave and Optical Frequencies with a 300 THz Femtosecond Laser Comb, *Phys. Rev. Lett.* **84**, 5102 (2000).
- [20] T. Udem, R. Holzwarth, and T. W. Hansch, Optical frequency metrology, *Nature* **416**, 233 (2002).
- [21] *Femtosecond Optical Frequency Comb: Principle, Operation, and Applications*, edited by J. Ye and S. T. Cundiff (Springer, NewYork, (2004)).
- [22] J. L. Hall, M. Zhu, and P. Buch, Prospects for using laser-prepared atomic fountains for optical frequency standards applications, *J. Opt. Soc. Am. B* **6**, 2194 (1989).
- [23] W. Ertmer, R. Blatt, and J. L. Hall, Some Candidate Atoms and Ions for Frequency Standards Research using Laser Radiative Cooling Techniques, *Prog. Quant. Electr.* **8**, 248 (1984).

- [24] G. Wilpers, C. Oates, and L. Hollberg, Improved uncertainty budget for optical frequency measurements with microkelvin neutral atoms: Results for a high-stability  $^{40}\text{Ca}$  optical frequency standard, *Applied Physics B: Lasers and Optics* **85**, 31 (2006).
- [25] C. Degenhardt *et al.*, Calcium optical frequency standard with ultracold atoms: Approaching  $10^{-15}$  relative uncertainty, *Phys. Rev. A* **72**, 062111 (2005).
- [26] U. Sterr, C. Degenhardt, H. Stoehr, C. Lisdat, H. Schnatz, J. Helmcke, F. Riehle, G. Wilpers, C. Oates, and L. Hollberg, The optical calcium frequency standards of PTB and NIST, *Comptes Rendus Physique* **5**, 845 (2004).
- [27] K. Sengstock, U. Sterr, J. H. Muller, V. Rieger, D. Bettermann, and W. Ertmer, Optical Ramsey spectroscopy on laser-trapped and thermal Mg atoms, *Appl. Phys. B* **59**, 99 (1994).
- [28] T. Ido, T. H. Loftus, M. M. Boyd, A. D. Ludlow, K. W. Holman, and J. Ye, Precision Spectroscopy and Density-Dependent Frequency Shifts in Ultracold Sr, *Phys. Rev. Lett.* **94**, 153001 (2005).
- [29] W. H. Oskay *et al.*, Single-Atom Optical Clock with High Accuracy, *Phys. Rev. Lett.* **97**, 020801 (2006).
- [30] T. Rosenband *et al.*, Observation of the  $^1S_0 \rightarrow ^3P_0$  Clock Transition in  $^{27}\text{Al}^+$ , *Phys. Rev. Lett.* **98**, 220801 (2007).
- [31] H. S. Margolis, G. P. Barwood, G. Huang, H. A. Klein, S. N. Lea, K. Szymaniec, and P. Gill, Hertz-Level Measurement of the Optical Clock Frequency in a Single  $^{88}\text{Sr}^+$  Ion, *Science* **306**, 1355 (2004).
- [32] P. Dube, A. A. Madej, J. E. Bernard, L. Marmet, J.-S. Boulanger, and S. Cundy, Electric Quadrupole Shift Cancellation in Single-Ion Optical Frequency Standards, *Phys. Rev. Lett.* **95**, 033001 (2005).
- [33] T. Schneider, E. Peik, and C. Tamm, Sub-Hertz Optical Frequency Comparisons between Two Trapped  $^{171}\text{Yb}^+$  Ions, *Phys. Rev. Lett.* **94**, 230801 (2005).
- [34] P. J. Blythe, S. A. Webster, H. S. Margolis, S. N. Lea, G. Huang, S.-K. Choi, W. R. C. Rowley, P. Gill, and R. S. Windeler, Subkilohertz absolute-frequency measurement of the 467-nm electric octupole transition in  $^{171}\text{Yb}^+$ , *Phys. Rev. A* **67**, 020501 (2003).
- [35] T. Becker, J. v. Zanthier, A. Y. Nevsky, C. Schwedes, M. N. Skvortsov, H. Walther, and E. Peik, High-resolution spectroscopy of a single  $\text{In}^+$  ion: Progress towards an optical frequency standard, *Phys. Rev. A* **63**, 051802 (2001).

- [36] T. Ido and H. Katori, Recoil-Free Spectroscopy of Neutral Sr Atoms in the Lamb-Dicke Regime, *Phys. Rev. Lett.* **91**, 053001 (2003).
- [37] J. Ye, D. W. Vernooy, and H. J. Kimble, Trapping of Single Atoms in Cavity QED, *Phys. Rev. Lett.* **83**, 4987 (1999).
- [38] H. Katori, in *Proceedings of the 6th Symposium on Frequency Standards and Metrology*, edited by P. Gill (World Scientific, Singapore, 2002), pp. 323–330.
- [39] H. Katori, M. Takamoto, V. G. Palchikov, and V. D. Ovsiannikov, Ultra-stable Optical Clock with Neutral Atoms in an Engineered Light Shift Trap, *Phys. Rev. Lett.* **91**, 173005 (2003).
- [40] M. Takamoto and H. Katori, Spectroscopy of the  $^1S_0$ – $^3P_0$  Clock Transition of  $^{87}\text{Sr}$  in an Optical Lattice, *Phys. Rev. Lett.* **91**, 223001 (2003).
- [41] A. Brusch, R. L. Targat, X. Baillard, M. Fouche, and P. Lemonde, Hyperpolarizability Effects in a Sr Optical Lattice Clock, *Phys. Rev. Lett.* **96**, 103003 (2006).
- [42] M. M. Boyd, A. D. Ludlow, S. Blatt, S. M. Foreman, T. Ido, T. Zelevinsky, and J. Ye,  $^{87}\text{Sr}$  Lattice Clock with Inaccuracy below  $10^{-15}$ , *Phys. Rev. Lett.* **98**, 083002 (2007).
- [43] P. Lemonde, in *Proceedings of the Joint IEEE-FCS and EFTF Meeting* (Geneva, Switzerland, May 29–June 1, 2007).
- [44] A. D. Ludlow, M. M. Boyd, T. Zelevinsky, S. M. Foreman, S. Blatt, M. Notcutt, T. Ido, and J. Ye, Systematic Study of the  $^{87}\text{Sr}$  Clock Transition in an Optical Lattice, *Phys. Rev. Lett.* **96**, 033003 (2006).
- [45] R. L. Targat, X. Baillard, M. Fouche, A. Brusch, O. Tcherbakoff, G. D. Rovera, and P. Lemonde, Accurate Optical Lattice Clock with  $^{87}\text{Sr}$  Atoms, *Phys. Rev. Lett.* **97**, 130801 (2006).
- [46] M. Takamoto, F.-L. Hong, R. Higashi, Y. Fujii, M. Imae, and H. Katori, Improved Frequency Measurement of a One-Dimensional Optical Lattice Clock with a Spin-Polarized Fermionic  $^{87}\text{Sr}$  Isotope, *J. Phys. Soc. Jpn.* **75**, 104302 (2006).
- [47] S. G. Porsev, A. Derevianko, and E. N. Fortson, Possibility of an optical clock using the  $6^1S_0 \rightarrow 6^3P_0$  transition in  $^{171,173}\text{Yb}$  atoms held in an optical lattice, *Phys. Rev. A* **69**, 021403 (2004).
- [48] V. D. Ovsiannikov, V. G. Pal'chikov, H. Katori, and M. Takamoto, Polarisation and dispersion properties of light shifts in ultrastable optical frequency standards, *Quantum Electronics* **36**, 3 (2006).

- [49] S. G. Porsev and A. Derevianko, Multipolar theory of blackbody radiation shift of atomic energy levels and its implications for optical lattice clocks, *Phys. Rev. A* **74**, 020502 (2006).
- [50] M. M. Boyd, T. Zelevinsky, A. D. Ludlow, S. Blatt, T. Zanon-Willette, S. M. Foreman, and J. Ye, Nuclear spin effects in optical lattice clocks, *Phys. Rev. A* **76**, 022510 (2007).
- [51] T. Hong, C. Cramer, W. Nagourney, and E. N. Fortson, Optical Clocks Based on Ultranarrow Three-Photon Resonances in Alkaline Earth Atoms, *Phys. Rev. Lett.* **94**, 050801 (2005).
- [52] R. Santra, E. Arimondo, T. Ido, C. H. Greene, and J. Ye, High-Accuracy Optical Clock via Three-Level Coherence in Neutral Bosonic  $^{88}\text{Sr}$ , *Phys. Rev. Lett.* **94**, 173002 (2005).
- [53] A. V. Taichenachev, V. I. Yudin, C. W. Oates, C. W. Hoyt, Z. W. Barber, and L. Hollberg, Magnetic Field-Induced Spectroscopy of Forbidden Optical Transitions with Application to Lattice-Based Optical Atomic Clocks, *Phys. Rev. Lett.* **96**, 083001 (2006).
- [54] T. Zanon-Willette, A. D. Ludlow, S. Blatt, M. M. Boyd, E. Arimondo, and J. Ye, Cancellation of Stark Shifts in Optical Lattice Clocks by Use of Pulsed Raman and Electromagnetically Induced Transparency Techniques, *Phys. Rev. Lett.* **97**, 233001 (2006).
- [55] V. D. Ovsianikov, V. G. Pal'chikov, A. V. Taichenachev, V. I. Yudin, H. Katori, and M. Takamoto, Magic-wave-induced  $^1\text{S}_0$ - $^3\text{P}_0$  transition in even isotopes of alkaline-earth-metal-like atoms, *Phys. Rev. A* **75**, 020501 (2007).
- [56] Z. W. Barber, C. W. Hoyt, C. W. Oates, L. Hollberg, A. V. Taichenachev, and V. I. Yudin, Direct Excitation of the Forbidden Clock Transition in Neutral  $^{174}\text{Yb}$  Atoms Confined to an Optical Lattice, *Phys. Rev. Lett.* **96**, 083002 (2006).
- [57] X. Baillard, M. Fouch, R. Le Targat, P. G. Westergaard, A. Lecallier, Y. Le Coq, G. D. Rovera, S. Bize, and P. Lemonde, Accuracy evaluation of an optical lattice clock with bosonic atoms, *Opt. Lett.* **32**, 1812 (2007).
- [58] M. Takamoto, F.-L. Hong, R. Higashi, and H. Katori, An optical lattice clock, *Nature* **435**, 321 (2005).
- [59] C. W. Hoyt, Z. W. Barber, C. W. Oates, A. V. Taichenachev, V. I. Yudin, and L. Hollberg, in *Proceedings of the 20th European Frequency and Time Forum* (Braunschweig, Germany, March 27-30, 2006), pp. 324–328.
- [60] H. J. Metcalf and P. van der Straten, *Laser Cooling and Trapping* (Springer-Verlag, New York, 1999), (and references therein).

- [61] F. Dalfovo, S. Giorgini, L. P. Pitaevskii, and S. Stringari, Theory of Bose-Einstein condensation in trapped gases, *Rev. Mod. Phys.* **71**, 463 (1999).
- [62] S. Giorgini, L. P. Pitaevskii, and S. Stringari, Theory of ultracold Fermi gases, 2007, arxiv/0706.3360.
- [63] G. K. Woodgate, *Elementary Atomic Structure* (Clarendon Press, Oxford, 2000).
- [64] T. E. Barrett, S. W. Dapore-Schwartz, M. D. Ray, and G. P. Lafyatis, Slowing atoms with  $\sigma^-$  polarized light, *Phys. Rev. Lett.* **67**, 3483 (1991).
- [65] A. Noble and M. Kasevich, UHV optical window seal to conflat knife edge, *Rev. Sci. Instrum.* **65**, 3042 (1994).
- [66] K. Liu and M. G. Littman, Novel geometry for single-mode scanning of tunable lasers, *Opt. Lett.* **6**, 117 (1981).
- [67] M. Bode, I. Freitag, A. Tnnermann, and H. Welling, Frequency-tunable 500-mW continuous-wave all-solid-state single-frequency source in the blue spectral region, *Opt. Lett.* **22**, 1220 (1997).
- [68] X. Xu, T. H. Loftus, J. L. Hall, A. Gallagher, and J. Ye, Cooling and trapping of atomic strontium, *J. Opt. Soc. Am. B* **20**, 968 (2003).
- [69] D. Hansen and A. Hemmerich, Doppler-free spectroscopy of metastable calcium in a discharge heat pipe, *Phys. Rev. A* **72**, 022502 (2005).
- [70] T. Loftus, J. R. Bochinski, and T. W. Mossberg, Magnetic trapping of ytterbium and the alkaline-earth metals, *Phys. Rev. A* **66**, 013411 (2002).
- [71] T. H. Loftus, T. Ido, M. M. Boyd, A. D. Ludlow, and J. Ye, Narrow line cooling and momentum-space crystals, *Phys. Rev. A* **70**, 063413 (2004).
- [72] M. Yasuda and H. Katori, Lifetime Measurement of the  $^3P_2$  Metastable State of Strontium Atoms, *Phys. Rev. Lett.* **92**, 153004 (2004).
- [73] S. B. Nagel, C. E. Simien, S. Laha, P. Gupta, V. S. Ashoka, and T. C. Killian, Magnetic trapping of metastable  $^3P_2$  atomic strontium, *Phys. Rev. A* **67**, 011401 (2003).
- [74] D. P. Hansen, J. R. Mohr, and A. Hemmerich, Magnetic trapping of metastable calcium atoms, *Phys. Rev. A* **67**, 021401 (2003).
- [75] V. Kokoouline, R. Santra, and C. H. Greene, Multichannel Cold Collisions between Metastable Sr Atoms, *Phys. Rev. Lett.* **90**, 253201 (2003).
- [76] A. Derevianko, S. G. Porsev, S. Kotochigova, E. Tiesinga, and P. S. Julienne, Ultracold Collision Properties of Metastable Alkaline-Earth Atoms, *Phys. Rev. Lett.* **90**, 063002 (2003).

- [77] D. Hansen and A. Hemmerich, Observation of Multichannel Collisions of Cold Metastable Calcium Atoms, *Phys. Rev. Lett.* **96**, 073003 (2006).
- [78] R. W. P. Driver, J. L. Hall, F. V. Kowalski, J. Hough, G. M. Ford, A. J. Munley, and H. Ward, Laser Phase and Frequency Stabilization Using an Optical Resonator, *Appl. Phys. B* **31**, 97 (1983).
- [79] T. H. Loftus, T. Ido, A. D. Ludlow, M. M. Boyd, and J. Ye, Narrow Line Cooling: Finite Photon Recoil Dynamics, *Phys. Rev. Lett.* **93**, 073003 (2004).
- [80] K. R. Vogel, T. P. Dinneen, A. Gallagher, and J. L. Hall, Narrow-Line Doppler Cooling of Strontium to the Recoil Limit, *IEEE Trans. on Inst. and Meas.* **48**, 618 (1999).
- [81] H. Katori, T. Ido, Y. Isoya, and M. Kuwata-Gonokami, Magneto-Optical Trapping and Cooling of Strontium Atoms down to the Photon Recoil Temperature, *Phys. Rev. Lett.* **82**, 1116 (1999).
- [82] N. Poli, R. E. Drullinger, G. Ferrari, J. Leonard, F. Sorrentino, and G. M. Tino, Cooling and trapping of ultracold strontium isotopic mixtures, *Phys. Rev. A* **71**, 061403 (2005).
- [83] E. A. Curtis, C. W. Oates, and L. Hollberg, Quenched narrow-line laser cooling of  $^{40}\text{Ca}$  to near the photon recoil limit, *Phys. Rev. A* **64**, 031403 (2001).
- [84] T. Binnewies, G. Wilpers, U. Sterr, F. Riehle, J. Helmcke, T. E. Mehlstübler, E. M. Rasel, and W. Ertmer, Doppler Cooling and Trapping on Forbidden Transitions, *Phys. Rev. Lett.* **87**, 123002 (2001).
- [85] Y. Castin, H. Wallis, and J. Dalibard, Limit of Doppler cooling, *J. Opt. Soc. Am. B* **6**, 2046 (1989).
- [86] N. Poli, private communication.
- [87] H.-J. Kluge and H. Sauter, Levelcrossing Experiments in the First Excited  $^1\text{P}_1$  States of the Alkaline Earths, *Z. Physik* **270**, 295 (1974).
- [88] G. zu Putlitz, Bestimmung des elektrischen Kernquadrupolmomentes des ungeraden stabilen Strontium-87-Kerns, *Z. Physik* **175**, 543 (1963).
- [89] S. M. Heider and G. O. Brink, Hyperfine structure of  $^{87}\text{Sr}$  in the  $^3\text{P}_2$  metastable state, *Phys. Rev. A* **16**, 1371 (1977).
- [90] I. Courtillot, Première observation de la transition fortement interdite  $^1\text{S}_0$ - $^3\text{P}_0$  du strontium, pour une horloge optique à atomes piégés, Ph.D. thesis, L'Université De Paris VI, 2003.



- [91] T. Mukaiyama, H. Katori, T. Ido, Y. Li, and M. Kuwata-Gonokami, Recoil-Limited Laser Cooling of  $^{87}\text{Sr}$  Atoms near the Fermi Temperature, *Phys. Rev. Lett.* **90**, 113002 (2003).
- [92] R. H. Dicke, The Effect of Collisions upon the Doppler Width of Spectral Lines, *Phys. Rev.* **89**, 472 (1953).
- [93] D. J. Wineland and W. M. Itano, Laser cooling of atoms, *Phys. Rev. A* **20**, 1521 (1979).
- [94] D. J. Wineland, W. M. Itano, J. C. Bergquist, and R. G. Hulet, Laser-cooling limits and single-ion spectroscopy, *Phys. Rev. A* **36**, 2220 (1987).
- [95] J. C. Bergquist, W. M. Itano, and D. J. Wineland, Recoilless optical absorption and Doppler sidebands of a single trapped ion, *Phys. Rev. A* **36**, 428 (1987).
- [96] H. Katori, T. Ido, and M. Kuwata-Gonokami, Optimal Design of Dipole Potentials for Efficient Loading of Sr Atoms, *J. Phys. Soc. Jpn.* **68**, 2479 (1999).
- [97] J. J. Sakuri, *Modern Quantum Mechanics* (Addison Wesley Longman, New York, 1994).
- [98] S. Friebel, C. D'Andrea, J. Walz, M. Weitz, and T. W. Hänsch,  $\text{CO}_2$ -laser optical lattice with cold rubidium atoms, *Phys. Rev. A* **57**, R20 (1998).
- [99] B. H. Bransden and C. J. Joachain, *Physics of Atoms and Molecules* (Prentice Hall, Harlow, England, 2003).
- [100] H. G. C. Werij, C. H. Greene, C. E. Theodosiou, and A. Gallagher, Oscillator strengths and radiative branching ratios in atomic Sr, *Phys. Rev. A* **46**, 1248 (1992).
- [101] H. J. Andra, H.-J. Plohn, W. Wittmann, A. Gaupp, J. O. Stoner, Jr., and M. Gaillard, Lifetimes of levels in neutral strontium (Sr I), *J. Opt. Soc. Am.* **65**, 1410 (1975).
- [102] D. A. Miller, L. You, J. Cooper, and A. Gallagher, Collisional energy transfer between excited-state strontium and noble-gas atoms, *Phys. Rev. A* **46**, 1303 (1992).
- [103] P. G. Mickelson, Y. N. Martinez, A. D. Saenz, S. B. Nagel, Y. C. Chen, T. C. Killian, P. Pellegrini, and R. Cote, Spectroscopic Determination of the s-Wave Scattering Lengths of  $^{86}\text{Sr}$  and  $^{88}\text{Sr}$ , *Phys. Rev. Lett.* **95**, 223002 (2005).

- [104] W. H. Parkinson, E. M. Reeves, and F. S. Tomkins, Neutral calcium, strontium and barium: determination of  $f$  values of the principal series by the hook method, *Journal of Physics B: Atomic and Molecular Physics* **9**, 157 (1976).
- [105] C. E. Moore, *Atomic Energy Levels: As Derived From the Analyses of Optical Spectra* (National Bureau of Standards, Washington D. C., 1971), Vol. 2, circular 467.
- [106] S. Blatt, Master's thesis, Fakultät für Mathematik, Informatik und Physik der Leopold-Franzens Universität, Innsbruck, (2005).
- [107] N. Poli, R. J. Brecha, G. Roati, and G. Modugno, Cooling atoms in an optical trap by selective parametric excitation, *Phys. Rev. A* **65**, 021401 (2002).
- [108] R. Juregui, N. Poli, G. Roati, and G. Modugno, Anharmonic parametric excitation in optical lattices, *Phys. Rev. A* **64**, 033403 (2001).
- [109] R. Grimm, M. Weidemüller, and Y. B. Ovchinnikov, in *Advances in Atomic, Molecular, and Optical Physics*, edited by B. Bederson and H. Walther (Academic Press, September, 1999), Vol. 42, pp. 95–170, (eprint arXiv:physics/9902072).
- [110] P. Lemonde and P. Wolf, Optical lattice clock with atoms confined in a shallow trap, *Phys. Rev. A* **72**, 033409 (2005).
- [111] A. Quessada, R. P. Kovacich, I. Courtillot, A. Clairon, G. Santarelli, and P. Lemonde, The Dick effect for an optical frequency standard, *Journal of Optics B: Quantum and Semiclassical Optics* **5**, S150 (2003).
- [112] A. D. Ludlow, X. Huang, M. Notcutt, T. Zanon-Willette, S. M. Foreman, M. M. Boyd, S. Blatt, and J. Ye, Compact, thermal-noise-limited optical cavity for diode laser stabilization at  $1 \times 10^{-15}$ , *Opt. Lett.* **32**, 641 (2007).
- [113] K. Numata, A. Kemery, and J. Camp, Thermal-Noise Limit in the Frequency Stabilization of Lasers with Rigid Cavities, *Phys. Rev. Lett.* **93**, 250602 (2004).
- [114] M. Notcutt, L.-S. Ma, A. D. Ludlow, S. M. Foreman, J. Ye, and J. L. Hall, Contribution of thermal noise to frequency stability of rigid optical cavity via Hertz-linewidth lasers, *Phys. Rev. A* **73**, 031804 (2006).
- [115] M. Notcutt, L.-S. Ma, J. Ye, and J. L. Hall, Simple and compact 1-Hz laser system via an improved mounting configuration of a reference cavity, *Opt. Lett.* **30**, 1815 (2005).

- [116] L.-S. Ma, P. Jungner, J. Ye, and J. L. Hall, Delivering the same optical frequency at two places: accurate cancellation of phase noise introduced by optical fiber or other time-varying path, *Opt. Lett.* **19**, 1777 (1994).
- [117] J. Ye *et al.*, Delivery of high-stability optical and microwave frequency standards over an optical fiber network, *J. Opt. Soc. Am. B* **20**, 1459 (2003).
- [118] J. C. Bergquist, S. A. Lee, and J. L. Hall, Saturated Absorption with Spatially Separated Laser Fields: Observation of Optical "Ramsey" Fringes, *Phys. Rev. Lett.* **38**, 159 (1977).
- [119] C. J. Bordé, C. Salomon, S. Avrillier, A. van Lerberghe, C. Bréant, D. Bassi, and G. Scoles, Optical Ramsey fringes with traveling waves, *Phys. Rev. A* **30**, 1836 (1984).
- [120] G. Breit and L. A. Wills, Hyperfine Structure in Intermediate Coupling, *Phys. Rev.* **44**, 470 (1933).
- [121] A. Lurio, M. Mandel, and R. Novick, Second-Order Hyperfine and Zeeman Corrections for an (sl) Configuration, *Phys. Rev.* **126**, 1758 (1962).
- [122] T. Zelevinsky, M. M. Boyd, A. D. Ludlow, T. Ido, J. Ye, R. Ciurylo, P. Naidon, and P. S. Julienne, Narrow Line Photoassociation in an Optical Lattice, *Phys. Rev. Lett.* **96**, 203201 (2006).
- [123] S. Tojo, M. Kitagawa, K. Enomoto, Y. Kato, Y. Takasu, M. Kumakura, and Y. Takahashi, High-Resolution Photoassociation Spectroscopy of Ultracold Ytterbium Atoms by Using the Intercombination Transition, *Phys. Rev. Lett.* **96**, 153201 (2006).
- [124] R. Ciurylo, E. Tiesinga, S. Kotochigova, and P. S. Julienne, Photoassociation spectroscopy of cold alkaline-earth-metal atoms near the intercombination line, *Phys. Rev. A* **70**, 062710 (2004).
- [125] M. V. Romalis, W. C. Griffith, J. P. Jacobs, and E. N. Fortson, New Limit on the Permanent Electric Dipole Moment of  $^{199}\text{Hg}$ , *Phys. Rev. Lett.* **86**, 2505 (2001).
- [126] B. Lahaye and J. Margerie, The  $g$ -Factor of the Metastable  $6\ ^3\text{P}_0$  Level of Odd Isotopes of Mercury, *Journal de Physique* **36**, 943 (1975).
- [127] A. Lurio, Configuration Interaction and the hfs of the sl Configuration, *Phys. Rev.* **142**, 46 (1966).
- [128] R. Santra, K. V. Christ, and C. H. Greene, Properties of metastable alkaline-earth-metal atoms calculated using an accurate effective core potential, *Phys. Rev. A* **69**, 042510 (2004).

- [129] L. Olschewski, Messung der magnetischen Kerndipolmomente an freien  $^{43}\text{Ca}$ -,  $^{87}\text{Sr}$ -,  $^{135}\text{Ba}$ -,  $^{137}\text{Ba}$ -,  $^{171}\text{Yb}$ -, und  $^{173}\text{Yb}$ -Atomen mit optischem Pumpen, *Z. Physik* **249**, 205 (1972).
- [130] H. Kopfermann, *Nuclear Moments* (Academic Press, New York, 1958).
- [131] J. R. P. Angel and P. G. H. Sandars, The hyperfine structure Stark effect: I. Theory, *Proc. Roy. Soc. A* **125** (1968).
- [132] A. Khadjavi, A. Lurio, and W. Happer, Stark Effect in the Excited States of Rb, Cs, Cd, and Hg, *Phys. Rev.* **167**, 128 (1968).
- [133] M. V. Romalis and E. N. Fortson, Zeeman frequency shifts in an optical dipole trap used to search for an electric-dipole moment, *Phys. Rev. A* **59**, 4547 (1999).
- [134] S. G. Porsev and A. Derevianko, Hyperfine quenching of the metastable  $^3\text{P}_{0,2}$  states in divalent atoms, *Phys. Rev. A* **69**, 042506 (2004).
- [135] R. Santra, private communication.
- [136] M. W. Zwierlein, Z. Hadzibabic, S. Gupta, and W. Ketterle, Spectroscopic Insensitivity to Cold Collisions in a Two-State Mixture of Fermions, *Phys. Rev. Lett.* **91**, 250404 (2003).
- [137] S. M. Foreman, K. W. Holman, D. D. Hudson, D. J. Jones, and J. Ye, Remote transfer of ultrastable frequency references via fiber networks, *Rev. Sci. Instrum.* **78**, 021101 (2007).
- [138] S. M. Foreman, A. D. Ludlow, M. H. G. de Miranda, J. E. Stalnaker, S. A. Diddams, and J. Ye, Coherent optical phase transfer over a 32-km fiber with 1-s instability at  $10^{-17}$ , 2007, (eprint arxiv:0707.096).
- [139] A. Derevianko, private communication.
- [140] P. J. Leo, P. S. Julienne, F. H. Mies, and C. J. Williams, Collisional Frequency Shifts in  $^{133}\text{Cs}$  Fountain Clocks, *Phys. Rev. Lett.* **86**, 3743 (2001).
- [141] S. T. Cundiff, J. Ye, and J. L. Hall, Optical frequency synthesis based on mode-locked lasers, *Rev. Sci. Instrum.* **72**, 3749 (2001).
- [142] S. T. Cundiff and J. Ye, Colloquium: Femtosecond optical frequency combs, *Rev. Mod. Phys.* **75**, 325 (2003).
- [143] S. M. Foreman, Femtosecond Frequency Combs for Optical Clocks and Timing Transfer, Ph.D. thesis, JILA and the Department of Physics, University of Colorado, Boulder CO, 2007.

- [144] T. M. Fortier, D. J. Jones, and S. T. Cundiff, Phase stabilization of an octave-spanning Ti:sapphire laser, *Opt. Lett.* **28**, 2198 (2003).
- [145] <http://www.branfiber.net>.
- [146] F. Narbonneau, M. Lours, S. Bize, A. Clairon, G. Santarelli, O. Lopez, C. Daussy, A. Amy-Klein, and C. Chardonnet, High resolution frequency standard dissemination via optical fiber metropolitan network, *Rev. Sci. Instrum.* **77**, 064701 (2006).
- [147] J. E. Stalnaker *et al.*, in *Proceedings of the 2006 IEEE International Frequency Control Symposium* (Miami, FL, 2006), pp. 462–469.
- [148] T. Parker, private communication.
- [149] I. Courtillot, A. Quessada, R. P. Kovacich, A. Brusch, D. Kolker, J.-J. Zondy, G. D. Rovera, and P. Lemonde, Clock transition for a future optical frequency standard with trapped atoms, *Phys. Rev. A* **68**, 030501 (2003).
- [150] M. M. Boyd, A. D. Ludlow, T. Zelevinsky, S. M. Foreman, S. Blatt, T. Ido, and J. Ye, in *Proceedings of the 20th European Frequency and Time Forum* (Braunschweig, Germany, March 27-30, 2006), pp. 314–318.
- [151] J. Ye *et al.*, in *Atomic Physics 20, Proceedings of the XX International Conference on Atomic Physics; ICAP*, edited by C. Roos, H. Hafner, and R. Blatt (AIP, Innsbruck, 2006), pp. 80–91.
- [152] S. Blatt *et al.*, in preparation.
- [153] B. C. Young, F. C. Cruz, W. M. Itano, and J. C. Bergquist, Visible Lasers with Subhertz Linewidths, *Phys. Rev. Lett.* **82**, 3799 (1999).
- [154] E. A. Cummings, M. S. Hicken, and S. D. Bergeson, Demonstration of a 1-W injection-locked continuous-wave titanium:sapphire laser, *Appl. Opt.* **41**, 7583 (2002).
- [155] M. Peterson *et al.*, in *Proceedings of the Joint IEEE-FCS and EFTF Meeting* (Geneva, Switzerland, May 29-June 1, 2007), pp. 649–653.